

ADVANCES IN TECHNIQUES FOR THE CHARACTERISATION OF TARGETS IN METAL DETECTION AND ULTRAWIDE BAND ELECTROMAGNETIC SCREENING APPLICATIONS

A THESIS SUBMITTED TO THE UNIVERSITY OF MANCHESTER
FOR THE DEGREE OF DOCTOR OF PHILOSOPHY
IN THE FACULTY OF SCIENCE AND ENGINEERING

2022

TOYKAN ÖZDEĞER

DEPARTMENT OF ELECTRICAL AND ELECTRONIC ENGINEERING

Table of Contents

Abstract.....	12
Declaration.....	13
Copyright.....	14
Acknowledgements.....	15
The Author.....	16
List of Publications.....	17
Journal Articles	17
Conference Articles.....	17
Other Outcomes	18
Abbreviations	19
1. Introduction.....	23
1.1. Aims and Objectives	26
1.2. Research Contributions	28
1.3. Thesis Structure.....	31
2. Using the Magnetic Polarizability Tensor For Reducing False Alarm Rate ...	33
2.1. Introduction	33
2.2. MPT Theory	34
An Alternative Way to Derive the MPT Equation.....	37
2.3. Previous Work.....	39
Summary	43
3. Magnetic Polarizability Tensor Measurement System.....	47
3.1. System Overview	48
3.2. Coil Arrangement.....	49
Receive Coil Balancing.....	51
3.3. System Electronics	53
Transmit Electronics	53

Receive Electronics	54
Microcontroller	55
3.4. Target Orientation Manipulator.....	55
Single Axis Rotation	56
Three-Axis Measurement.....	56
Higher Order MPT Characterisation.....	58
3.5. Software.....	59
Control Routines	59
Post-Processing Algorithm	61
Graphical User Interface	63
3.6. Methodology	64
3.7. Coil Characterisation and System Performance	66
Field Uniformity	66
Measurement Noise.....	67
Measurement Drift	68
Experiment Repeatability.....	69
MPT Characterisation Performance	70
3.8. Large Coil Arrangement.....	73
3.9. Summary	75
4. Magnetic Polarizability Tensor Case Studies	77
4.1. British Pound and United States Dollar Coins	77
4.2. Minimum Metal Anti-Personnel Landmines.....	79
4.3. MPT for Faster and More Reliable Security Screening	83
Non-Threat Objects.....	85
Datasets	87
Clustering Results	88
4.4. Measuring the Generalised MPT of Cone Shaped Targets	93

4.5. Summary	94
5. Ground Penetrating Radar	97
5.1. Introduction	97
5.2. Principles of GPR.....	98
5.3. Previous Work.....	101
5.4. Simulation Models	104
Landmine Models.....	104
Clutter Models.....	106
Soil Models	107
Dataset.....	108
5.5. Summary and Future Work	110
6. Conclusion and Future Work	113
6.1. Conclusion.....	113
6.2. Future Work	117
References	120
Publications.....	132
Publication 1	135
Publication 2	137
Publication 3	139
Publication 4	141
Publication 5	143

Word Count: 65,223

List of Tables

Table I – Showing countries with the most child casualties in 2020. Data from [3].	24
Table II – List of publications with a short summary for each paper describing the achievements and how the paper relates to the research.	30
Table III – Basic settings that can be set by the user for each experiment in the control algorithm.	60
Table IV – NRMSE of differences between maximum and minimum transimpedance eigenvalues of the copper disk compared to the average.	70
Table V – NRMSE of differences between measured MPT eigenvalues compared to the previously published measured and simulated MPT eigenvalues.	79
Table VI – Characterised Anti-Personnel Landmines	80
Table VII – Summary of tested standard threat objects.	84
Table VIII – Object types involved in the datasets generated. Numbers in each cell under the dataset columns indicate the number of specific objects in that sub-group of the dataset.	87
Table IX – Main parameters of the simulation models.	108

List of Figures

Figure 1-1 – Map showing countries who are signatories of The Mine Ban Treaty. Data from [3].....	24
Figure 3-1 – System schematic showing coils, electronics and the data acquisition PC.	49
Figure 3-2 – Coil geometry of the coil arrangement. (a) is transmit and receive coils separately and (b) is both coils put together showing their relative positions.....	51
Figure 3-3 – The coil arrangement. (a) is the mechanical drawing and (b) is the completed version.....	51
Figure 3-4 – Coil impedances measured between 1 kHz and 1 MHz. (a) is individual receive coil impedances before and after balancing. (b) is the transimpedance between transmit and receive coils before and after balancing the receive coils.	52
Figure 3-5 – The aluminium, 19-inch rack electronics box of the instrument.....	53
Figure 3-6 – Transmit amplifier circuit diagram. The diagram shows one inverting and one non-inverting amplifier. However, in reality, there are 10 of each, which are identical.....	54
Figure 3-7 – Receive amplifier circuit diagram.	55
Figure 3-8 – Target orientation manipulator for single axis rotation. (a) is the three-dimensional design of the TOM. (b) is the built version of the TOM with a Type-72 AP landmine placed on the rotating plate.	56
Figure 3-9 – Computer Aided Design (CAD) models and built version of the Target Orientation Manipulator. (a) and (c) showing closed CAD and built versions. (b) and (d) showing CAD and built versions where the two halves are separated.	57
Figure 3-10 – TOM capable of rotating cone shaped objects around one axis outside of the region with uniform magnetic field. (a-b) are the CAD drawings and (c-d) are the manufactured TOM using 3D printing techniques.	58

Figure 3-11 – The control routine’s main workflow.....	61
Figure 3-12 – The post-processing algorithm’s main workflow.....	62
Figure 3-13 – Screenshot of the main tab of the GUI, where the experiments are controlled.	63
Figure 3-14 – Cone shaped target objects used for rank 2 and rank 3 MPT characterisations. (a) copper, (b) aluminium, (c) brass cone.....	65
Figure 3-15 – Simulations of the magnetic field inside the coil system for the non-target case when transmit and receive coils are individually driven by an electric current. (a) transmit coil and (b) receive coil excitation. The measurement region is between the red vertical lines shown in the figure. The subplots within the figure show the field data within the measurement region at an enhanced scale.	66
Figure 3-16 – Magnetic Field plots for transmit and receive coils. (a) transmit coil, (b) receive coil.	67
Figure 3-17 – MPT measurement noise floor compared to the real and imaginary transimpedance values of a copper disk across the operating frequency spectrum. The transimpedances are shown in dB scale instead of mm^3 for easy comparison.	68
Figure 3-18 – Measurement drift of real and imaginary transimpedance values at 50 kHz plotted versus time for 120 minutes.	68
Figure 3-19 – Average of the transimpedance values of ten consecutive experiments with error bars showing the range of maximum and minimum values for each transimpedance. Plots show (a) real and (b) imaginary transimpedance values. The deviation in the data is approximately two orders of magnitude smaller compared with the absolute transimpedance values, which gives the appearance of single horizontal tick lines for the plotted error bars in the main plots. The upper right insert region in the plots shows the typical small deviation across the experiments, which is not easily discernible in the main plots.	69
Figure 3-20 – Example target objects showing copper cuboid with a hole, ‘L’ shape and three legged ‘L’ shape. Object (a) and (b) copper cuboids with a hole, (c)	

and (d) copper ‘L’ shapes, (e) three legged ‘L’ shape. All five objects have a thickness of 10 mm where the three legged ‘L’ shape’s third leg is 19 mm.....	70
Figure 3-21 – Measured real and imaginary MPT eigenvalues of target objects, compared with results from FEM simulations, MPT Calculator and measurements using the previous TOM. Plots (a-b) small ‘L’ shape, (c-d) large ‘L’ shape, (e-f) small cuboid with hole, (g-h) large cuboid with hole. “Expt 1” represents values from experiments done using the single axis TOM while “Expt 2” represents values taken using the multi axis one. “FEM” represents values from FEM simulations while “MPT Calculator” represents values acquired using the MPT Calculator.	71
Figure 3-22 – Real and imaginary MPT eigenvalues for a three legged ‘L’ shape measured using the new object orientation manipulator, compared with results from FEM simulations and MPT Calculator. “Expt 2” represents values taken using the multi axis TOM. “FEM” represents values from FEM simulations while “MPT Calculator” represents values acquired using the MPT Calculator. Plots show (a) real and (b) imaginary MPT eigenvalues.	72
Figure 3-23 – The large-scale coil arrangement showing; (a) design concept cut away along with simplified inner receive coil and (b) constructed coil arrangement on the bespoke mounting platform	74
Figure 3-24 – CAD model and built version of the large-scale TOM; (a) design concept and (b) constructed TOM with mounting plate. The TOM is approximately 360 mm in diameter.....	74
Figure 4-1 – Measured real and imaginary rank 2 MPT eigenvalues for US coinage, compared with simulated and previously published rank 2 MPT results are shown. Plots (a-b) one cent, (c-d) dime, (e-f) half dollar and (g-h) nickel. Expt 1 and Sim are values for experimental and simulated results from [63] while Expt 2 is experimental data from the instrument described in this thesis.....	78

Figure 4-2 – Real and imaginary MPT eigenvalues of M14 anti-personnel landmine and its components. (a-b) are M14 anti-personnel landmine. (c-d) are detonator and pin of M14.	81
Figure 4-3 – Real and imaginary MPT eigenvalues of Type-72 anti-personnel landmine and its components. (a-b) are Type-72 anti-personnel landmine. (c-d) are detonator, pin, spring, and igniter of Type-72.....	81
Figure 4-4 – Real and imaginary MPT eigenvalues of VS50 AP landmine and its components. (a-b) are VS50 AP landmine. (c-d) are detonator, pin, spring, and top plate of VS50.	82
Figure 4-5 – Real and imaginary MPT eigenvalues of PMN anti-personnel landmine and its components. (a-b) are PMN anti-personnel landmine. (c-d) are detonator, pin, striker spring, plunger spring and igniter of PMN.	82
Figure 4-6 – MPT eigenvalues of normal and rusted pins of M14 anti-personnel landmine. (a) is real and (b) is imaginary MPT eigenvalues.....	83
Figure 4-7 – Example tested firearm types; (a) polymer framed self-loading pistol (Glock 43), (b) metal framed handgun (Beretta 92FS), (c) revolver (Smith and Wesson, model 547), (d) Uzi 9 mm SMG, (e) mini revolver (NAA .22), (f) hollow battery casing with 9 mm cartridges inside, (g) Example concealed knives.....	84
Figure 4-8 – Real (a) and imaginary (b) eigenvalue MPT data for example tested objects; polymer (Glock 17) and metal framed pistols (Sig Sauer 9mm P225) and revolver (Colt 0.455).	85
Figure 4-9 – Example non-threat test objects; (a) subset of circulated British coins (circa 2015) and (b) typical UK mortice and domestic door keys.	86
Figure 4-10 – Real (LHS) and imaginary (RHS) eigenvalue MPT data for example tested objects; (a)-(b) one pound coin and domestic key, (c)-(d) polymer pistol and domestic key.	86
Figure 4-11 – PCA visualization and three different clustering algorithms applied to the datasets with 168 features per object; (a-d) is dataset 1 and (e-h) is dataset 2.	91

Figure 4-12 – PCA visualization and three different clustering algorithms applied to the datasets with 2 features per object; (a-d) is dataset 1 and (e-h) is dataset 2.	92
Figure 4-13 – Rank 2 and rank 3 MPT of the steel cone. (a)-(b) are the measured and simulated rank 2 MPT of the cone, respectively. (c)-(d) are the measured and simulated rank 3 MPT of the cone.....	94
Figure 5-1 – An A-Scan recorded for around 5 nanoseconds, where the direct interaction between transmit and receive antennas, the wave bounce back from the air/ground boundary and the responses from the dielectric discontinuities in the soil are shown.	99
Figure 5-2 – A B-Scan made up of 62 A-Scans recorded on a straight line with 4 mm steps.	100
Figure 5-3 – Simulation model of a PMA-1 AP landmine. (a) is the landmine with the top lid closed and (b) the top lid open, revealing the components inside.	104
Figure 5-4 – Simulation model of a PMA-2 AP landmine. (a) is the landmine view from outside and (b) is the cross-sectional view from the side.....	105
Figure 5-5 – Simulation model of a PMA-3 AP landmine. (a) is the landmine view from outside and (b) is the cross-sectional view from the side.....	105
Figure 5-6 – Model of the 7.62×51 mm NATO standard ammunition cartridge. (a) is the unfired cartridge as a whole, (b) is the cartridge case and (c) is the bullet.	106
Figure 5-7 – Two soil models generated using gprMax. (a) is a soil model with inhomogeneous material distribution and rough surface. In addition to the features in (a), (b) also introduces clutter and grass.....	107
Figure 5-8 – A snapshot of the GPR waves propagating through a simulation model, where reflections from the grass, soil surface, and the PMA-2 landmine are visible.	107
Figure 5-9 – Example B-Scan before and after applying post processing. (a) the raw B-Scan, (b) after background removal, (c) after applying time varying gain, and (d) after magnitude normalisation.	109

Abstract

Metal detection (MD) has been commonly used in humanitarian demining since MD can detect the metal components in Anti-Personnel landmines. However, land in post-conflict areas contain metal clutter such as shrapnel or bullets, resulting in a high false alarm rate (FAR). MD has been augmented with ground penetrating radar (GPR) in recent years to reduce FAR caused by metal clutter. However, GPR is also prone to FAR, caused by other clutter in the soil such as burrows, water pockets or rocks. A better discrimination for both MD and GPR could help speed up humanitarian demining by reducing FAR.

The Magnetic Polarizability Tensor (MPT) is a representative electromagnetic property of a metal object, which depends on the size, material, shape, and excitation frequency of the object. If an MPT library of threat and non-threat metal objects was generated, an MD capable of measuring the MPT of the target objects could utilise this library to improve classification performance and reduce FAR. This thesis describes advances in techniques for characterising electromagnetic response of metallic targets using by exploiting their tensor description. The major contribution of this research is as follows. (i) This research has realised a new instrument and the associated measurement methodology for measuring the rank 2 tensor of typical metal objects encounter in landmine detection and security screening. The instrument utilises a novel coil geometry capable of generating a uniform magnetic field over a specific region containing the target object to accurately measure the rank 2 MPT. (ii) A novel methodology for fast and reliable measurement of the rank 2 MPT was also established. Performance of the instrument has been validated by comparing the measured rank 2 MPTs with previously published simulated and experimental data, where good agreement has been observed. (iii) The instrument was used to study the rank 2 MPT of four AP landmines and their metal components. (iv) Rank 2 MPT of 200 firearms and non-threat metal objects were measured to generate an MPT library with the motivation to improve classification on walk-through metal detectors. Clustering in the data was then studied using unsupervised machine learning (ML) techniques.

This thesis has also considered how ML techniques can be used to advance the characterisation of buried non-metallic targets that would normally be inspected using GPR. Unlike MD, the GPR responses are more complex. Therefore, a large training set is required. However, a large training dataset is required to achieve high accuracy. To obtain the dataset, a real GPR dataset could be augmented with simulated data. The major contribution from this research in GPR is establishing a methodology for generating synthetic data representing real life scenarios. A methodology for generating a synthetic data representing real life scenarios is presented. A simulated GPR dataset involving AP landmines and clutter was then generated. Preliminary performance evaluation of two ML classifiers were tested using the simulated GPR data. The established methodology and the dataset can be used to augment a real GPR dataset in the future when the real data becomes available.

Declaration

No portion of the work referred to in this thesis has been submitted in support of an application for another degree or qualification of this or any other university or other institute of learning.

Copyright

- i. The author of this thesis (including any appendices and/or schedules to this thesis) owns certain copyright or related rights in it (the “Copyright”) and s/he has given the University of Manchester certain rights to use such Copyright, including for administrative purposes.
- ii. Copies of this thesis, either in full or in extracts and whether in hard or electronic copy, may be made only in accordance with the Copyright, Designs and Patents Act 1988 (as amended) and regulations issued under it or, where appropriate, in accordance with licensing agreements which the University has from time to time. This page must form part of any such copies made.
- iii. The ownership of certain Copyright, patents, designs, trademarks and other intellectual property (the “Intellectual Property”) and any reproductions of copyright works in the thesis, for example graphs and tables (“Reproductions”), which may be described in this thesis, may not be owned by the author and may be owned by third parties. Such Intellectual Property and Reproductions cannot and must not be made available for use without the prior written permission of the owner(s) of the relevant Intellectual Property and/or Reproductions.
- iv. Further information on the conditions under which disclosure, publication and commercialisation of this thesis, the Copyright and any Intellectual Property and/or Reproductions described in it may take place is available in the University IP Policy (see <http://documents.manchester.ac.uk/DocuInfo.aspx?DocID=24420>), in any relevant Thesis restriction declarations deposited in the University Library, the University Library’s regulations (see <http://www.library.manchester.ac.uk/about/regulations/>) and in the University’s policy on Presentation of Theses.

Acknowledgements

I would like to take this opportunity to express my thanks to all those who have supported me during my PhD.

First of all, I would like to express my sincere gratitude to my supervisor Prof. Anthony Peyton for his incredible support, guidance and encouragement throughout my PhD. You have inspired me as a person and as an engineer. Thank you for giving me the opportunity to be part of this incredible research.

My genuine thanks to Dr John Davidson who not only has been a great colleague to work together, but also supported me in every part of my journey as a mentor. Your advice about engineering, science and life has been valuable and will always be with me.

I would like to thank everyone in the Electromagnetic Sensing Group for welcoming me to the group and for the good friendships which we made. Each one of you has helped me on at least something during my PhD. In addition, I would like to thank Dr Liam Marsh, Michael O'Toole, Daniel Conniffe, Prof. Bill Lionheart and Prof. Paul Ledger for playing a crucial role on the progress of my research. My special thanks goes to Dr Wouter van Verre, who has helped me on everything from the start and sometimes even stayed with me in the labs until late to help make things work.

I wouldn't be here without the support of my parents Sergül and Tayfun, who have dedicated their lives and sacrificed a lot for me and my little brother, Boran. I will never be able to repay what you have done for me. I wish to make you feel proud for the rest of my life. My little brother Boran also has always been by my side through my whole journey. Thank you for enjoying all the ups with me and being there for me during all the downs. I am proud of you for who you have become and for the things you have achieved. My incredible girlfriend Dilem has supported me through every part of my life for the last 11 years we have been together. Thank you for being by my side and helping me become the person I am today. I am excited for our future and to enjoy the good memories awaiting us. Last but not least, I would like to thank all my friends who always have supported me and thankfully are too many to mention here. We have made a lot of good memories together. Thank you for making my life enjoyable.

Emotion without action is irrelevant. - Jody Williams

The Author

Toykan Özdeğer was born in Nicosia, Cyprus. He received the M.Eng. (Hons.) degree in Electrical and Electronics Engineering (with Industrial Experience) from the University of Manchester with first class in 2018. He was also awarded the Rolls Royce Best Third Year Individual Project Award for the project named “Position Sensor Fusion for AUVs” under the supervision of Dr Frank Podd. He worked as an Instrumentation, Control and Automation Engineering placement student in Phillips 66 between 2016-2017 for one year during his degree. He is currently pursuing a PhD at the University of Manchester.

He started his PhD in 2018 at the University of Manchester. His research interests include Metal Characterization using Magnetic Induction Spectroscopy, Landmine Detection and applications of Machine Learning to threat classification. The projects he was involved with include landmine detection and next generation smart walk-through metal detectors.

List of Publications

Journal Articles

The following list of published or accepted articles, presented in chronological order, have resulted from this research:

- **Özdeğer, T.**, Davidson, J. L., van Verre, W., Marsh, L. A., Lionheart, W. R. B., Peyton, A. J., "Measuring the Magnetic Polarizability Tensor Using an Axial Multi-Coil Geometry," *IEEE Sensors Journal*, vol. 21, no. 17, pp. 19322-19333, 2021.
- **Özdeğer, T.**, Ledger, P. D., Lionheart, W. R. B., Davidson, J. L., Peyton, A. J., "Measurement of GMPT Coefficients for Improved Object Characterisation in Metal Detection," *IEEE Sensors Journal*, vol. 22, no. 3, pp. 2430-2446, 2022.
- **Özdeğer, T.**, Davidson, J. L., Ledger, P. D., Conniffe, D., Lionheart, W. R. B., Peyton, A. J., "Measuring the Magnetic Polarizability Tensor of Non-Symmetrical Metallic Objects," *IEEE Sensors Journal*, Submitted, Under Review.
- Davidson, J. L., **Özdeğer, T.**, Conniffe, D., Murray-Flutter, M., Peyton, A. J., "Classification of Threat and Non-Threat Objects Using the Magnetic Polarizability Tensor and a Large-Scale Multi-Coil Array," *IEEE Sensors Journal*, Submitted, Accepted.
- Elgy, J., Ledger, P. D., Davidson, J. L., **Özdeğer, T.**, "Computation and Measurement of Magnetic Polarizability Object Characterisations of Highly Conducting and Permeable Objects", *Journal to be decided*.

Conference Articles

The following conference articles, listed in chronological order, have resulted from this research. The name of the presenting author has been underlined:

- van Verre, W., **Özdeğer, T.**, Gupta, A., Podd, F.J.W., Peyton, A. J., "Threat Identification in Humanitarian Demining Using Machine Learning and Spectroscopic Metal Detection," in Yin H., Camacho D., Tino P., Tallón-

Ballesteros A., Menezes R., Allmendinger R. (eds) Intelligent Data Engineering and Automated Learning – IDEAL 2019, Lecture Notes in Computer Science, vol 11871. Springer, Cham.

- **Özdeğer, T.**, Ledger, P. D., Peyton, A. J., "A Study on the Magnetic Polarizability Tensors of Minimum Metal Anti-Personnel Landmines," *2022 IEEE International Instrumentation and Measurement Technology Conference (I2MTC)*, pp. 1-6, 2022.

Other Outcomes

The following publication in a non-peer-reviewed conference has resulted from this research:

- **Özdeğer, T.**, Ledger, P. D., Peyton, A. J., "Quantifying the Metal Detection Signatures of Minimum Metal Anti-Personnel Landmines," *18th International Symposium – Mine Action*, 2022.

Abbreviations

ANN	Artificial Neural Network
AP	Anti-Personnel
AT	Anti-Tank
AVG	Average
CAD	Computer Aided Design
CNN	Convolutional Neural Network
DAC	Digital-to-Analogue Converter
DNN	Deep Neural Network
DSP	Digital Signal Processing
EIT	Electrical Impedance Tomography
EMI	Electromagnetic Induction
ERW	Explosive Remnants of War
EPSRC	Engineering and Physical Sciences Research Council
FAR	False Alarm Rate
FDTD	Finite-Difference Time-Domain
FEM	Finite Element Method
FPGA	Field-Programmable Gate Array
GMPT	Generalised Magnetic Polarizability Tensor
GPR	Ground Penetrating Radar
GUI	Graphical User Interface
IACS	International Annealed Copper Standard
ICBL	International Campaign to Ban Landmines
IOT	Internet of Things

IR	Infra-Red
IUK	Innovate United Kingdom
KNN	K-Nearest Neighbours
LHS	Left Hand Side
LR	Logistic Regression
MD	Metal Detection
MDF	Medium Density Fibreboard
ML	Machine Learning
MP	Machine Pistol
MPT	Magnetic Polarizability Tensor
MPV	Man-Portable Vector Sensor
MQTT	Message Queuing Telemetry Transport
MTADS	Multi-Sensor Towed Array Detection System
NDT	Non-Destructive Testing
NFC	National Firearms Centre
NN	Neural Network
NRMSE	Normalised Root-Mean-Square Error
NUFFT	Non-Uniform Fast Fourier Transform
PBT	Polybutylene Terephthalate
PCA	Principal Component Analysis
PCB	Printed Circuit Board
PLA	Polylactic Acid
PSU	Power Supply Unit
PVC	Polyvinyl Chloride

RF	Random Forest
RHS	Right Hand Side
ROM	Reduced Order Model
RX	Receive
SMD	Smart Metal Detector
SMG	Sub-Machine Gun
SNR	Signal-to-Noise Ratio
SOC	System on Chip
SVD	Singular Value Decomposition
SVM	Support Vector Machine
TI	Truncated Icosahedron
TNT	Trinitrotoluene
TOM	Target Orientation Manipulator
TX	Transmit
UWB	Ultra-Wideband Radar
UXO	Unexploded Ordnance
WTMD	Walk-Through Metal Detector

1. Introduction

Landmines are explosive devices typically concealed underground with the aim of destroying or disabling enemy targets such as vehicles, tanks and military personnel as they pass over them. However, landmines can still pose a threat for many years after military conflicts have ended to civilians and economies around the world. A landmine is typically a cylindrical or box shaped container housing an explosive substance. They are generally designed to explode when triggered by the victim, for instance when pressure is applied from the top. There are around 600 types of Anti-Personnel (AP) landmines with the purpose of injuring or killing humans, while Anti-Tank (AT) landmines aim to disable vehicles [1], [2]. Landmines are indiscriminate weapons with most killings taking place in peace times and with the highest proportion of the civilian casualties being children [3].

Landmines can remain armed for decades, meaning they stay active until long after the conflict has ended. This renders large areas of land unusable, preventing use of the land for agriculture, socio-economic activity, or housing [4]. Although this causes substantial damage to the society around the contaminated land, the most significant damage is caused by the landmines' inability to discriminate between soldiers, civilians, or children. People inadvertently enter contaminated areas and accidentally stand on landmines, which usually result in serious injury or death. Treatment costs of these accidents also further decrease the economic strength of the community [2], [4].

Although, the use, stockpiling and production of AP landmines are prohibited by The Mine Ban Treaty (Ottawa Treaty) [5]-[7] which has been agreed by 164 state parties, production is still being carried out by 12 non-signatory states including the United States, Russia, China, and India [3], [7]. A map displaying the current states who have signed the Treaty is shown in Figure 1-1. According to "The Landmine Monitor," published by the International Campaign to Ban Landmines (ICBL), 55 million stockpiled AP landmines have been destroyed by signatory states of The Mine Ban Treaty since 1997. However, tens of millions of active landmines remain deployed around the world to this day [2], [3]. A minimum of 7,073 casualties caused by AP landmines and explosive remnants of war (ERW) were reported in 2020, with around 80% of these victims being civilians. This was an increase compared to the previous years, where 6,897 and 5,554 casualties were reported in 2018 and 2019, respectively. Of the civilian casualties,

around 50% of them were children in all three years. Table I displays the countries with the most child casualties in 2020 caused by landmines and Explosive Remnants of War. Although, more than 356,000 AP landmines were cleared between years 2018-2020, this is a very small number, compared to the size of worldwide landmine contamination [3], [8], [9].



Figure 1-1 – Map showing countries who are signatories of The Mine Ban Treaty. Data from [3].

Table I – Showing countries with the most child casualties in 2020. Data from [3].

Country	Child Casualties	Percentage of total global child casualties in 2020
Afghanistan	706	37%
Syria	537	29%
Yemen	130	7%
Myanmar	76	4%
South Sudan	56	3%
Burkina Faso	49	3%
Iraq	42	2%
Pakistan	30	2%

Common methods of landmine clearance include the use of mechanical methods and Metal Detectors (MD). The clearance process is very slow when landmine detectors utilizing MD are used, as well as dangerous when human workers are involved [10]-[12]. Mechanical methods are fast but costly when excavation vehicles are used [11], [12]. Although, the use of MD results in a high detection rate, it suffers from a high False Alarm Rate (FAR) where the rate of a true positive alarm ranges from only 1 in 100 to 1 in 1000 alarms (FAR of above 99%) [10], [11]. This is mostly caused by the metal clutter buried in the soil such as, shrapnel, grenade pins, bullets and bullet cartridges which exist in post-conflict areas, and everyday objects, such as soda cans or metal bottle caps. Another cause of FAR is the use of modern, minimum-metal AP landmines where the metal content is only a few grams. This brings the need of using high signal gain in the MD, which in turn results in detection of even very small items of metal clutter in the soil, further increasing FAR [10], [11]. Detection performance of MD also significantly drops when used on mineralized soil, which is usually termed as “uncooperative soil” [13], [14]. This is caused by the very high electromagnetic response from the soil itself, which dwarfs the response from target objects [13]-[16]. Therefore, using only MD is not an ideal method for landmine detection, as the method can be very slow and expensive, depending on the characteristics of the land that is being cleared.

In addition to MD, other methods have been used for the purpose of demining. These include Ground Penetrating Radar (GPR) [11], [17], biological methods such as dogs, rats or bacteria [11], [17]-[19], mechanical clearance [11], [17], and acoustic sensors [17]. Like MD, each of these methods has their own strengths and limitations.

In recent years, MD has been augmented with Ground Penetrating Radar (GPR) to reduce the high FAR. GPR can detect dielectric discontinuities in the ground, meaning the method can detect objects with different dielectric properties compared to the soil they are buried in. This feature of GPR is useful since the casing of a landmine results in a dielectric discontinuity in the ground, which, in theory, can be detected by GPR. Parts of a landmine, including metal parts and the explosive, also results in dielectric discontinuity inside the landmine. Advanced GPR systems are also able to measure these specific signatures to also improve detection performance. However, rocks, water concentrations, air cavities such as burrows and other materials also cause dielectric discontinuities in the ground. This means landmine detectors utilizing GPR can also be prone to FAR, caused

by these clutter sources [20]-[22]. Clearly, there is room for improvement for the discrimination performance of these systems between clutter and AP landmines.

1.1. Aims and Objectives

The main aim of the research reported in this thesis is to investigate novel characterisation techniques to aid reducing FAR on dual-mode landmine detectors utilizing both GPR and MD. However, the larger portion of the work is concerned with characterisation techniques for MD, since this is the most common method used for humanitarian demining and as per the industrial partners' interests.

A library involving electromagnetic signatures of landmines and other target objects of interest may help reduce FAR generated by metal clutter on MD. Such libraries could be utilised by MDs capable of using multiple excitation frequencies and measuring the electromagnetic signatures of target objects for better target classification. For this reason, building a coil sensor capable of characterising electromagnetic signatures of metal objects is necessary, including the design and manufacturing of necessary electronics and control software to drive the sensor, as well as processing algorithms for received data. The Magnetic Polarizability Tensor (MPT) is a representative electromagnetic property of a metal object, which depends on the size, material, shape of the object as a function of the excitation frequency. Spectroscopic data from the sensor can be used to characterise MPT of metal objects, including AP landmines.

Machine Learning (ML) algorithms such as Artificial Neural Network (ANN) perform well for classification when trained by a large dataset covering a wide range of scenarios [23]. Training ML algorithms with synthetic datasets use models that represent real life scenarios. For the research presented in this thesis, this means generating simulated training sets which attempt to model realistic soil, landmine and clutter which could potentially improve our understanding of FAR generated by GPR on dual-mode landmine detectors. Therefore, generating and optimizing such datasets in addition to ML algorithms is a necessary part of this research.

Considering the above aims, the following objectives were set for this research:

1. To understand the requirements for characterizing electromagnetic signatures of metal objects, as well as any related work that has been undertaken by previous research. This also includes understanding possible proven ways of such

characterizations, including the application of the Magnetic Polarizability Tensor (MPT). Hence, designing, optimizing, and building an instrument system which can measure the MPT appropriately. Such an instrument system should have an appropriate level of performance which generates high quality data that can be utilized confidently by any further research. A larger and a smaller version of the same coil design is required to be built to cover a wide range of benign, clutter and threat objects with different sizes. The larger, less sensitive coil arrangement could be used to characterize large objects with a significant amount of metal, while the smaller, more sensitive coil arrangement could be used to characterize small objects with minimum metal content, such as minimum metal AP landmines.

2. To design, optimize, and build electronics within the instrument system that are capable of providing quality raw measurement data that can be processed to produce accurate MPT data. Such a system should be robust and built to a 'commercial' level, enabling the system to be reliable and consistent. Additionally, the system will be constructed in such a way that it can be transported for measurements undertaken outside the university laboratories.
3. To understand the methods of metal characterization and the underlying mathematical theory of the MPT. From this, develop an advanced signal processing algorithm capable of undertaking MPT inversion, using simple voltage measurements from the coils. Additionally, a hardware control algorithm will be developed enabling the system to automatically acquire measurement data in a robust and repeatable manner. Both the control and processing algorithms will be combined and wrapped around a Graphical User Interface (GUI) that enables the system to be used by people without advanced knowledge of the underlying theory. Data structure of the MPT characterizations should also be standardized in such a way which will lend itself to the development of a searchable MPT library in the future.
4. Similar to landmine detection, the MPT can also be utilised by walk-through metal detectors, where non-threat metal objects can be rejected, increasing throughput of people. If a library of threat objects (e.g., knives and guns) and non-threat objects (e.g., keys and coins) were to be generated, an ML classifier could be trained to have less false alarms. Therefore, one objective of this research is to collect MPT signatures of threat and non-threat objects, and prove the difference of MPT signatures.

5. Training ML algorithms with synthetic datasets which are useful in real applications require the generation of large number of unique models that represent real life scenarios. A pre-requisite of this is to understand soil and landmine materials and how they should be modelled. These can then be modelled and simulated in appropriate simulation software. Generating many different models to create a dataset also requires automation of the model generation process within set variable ranges. The generated GPR datasets can be divided into train and test datasets for training and testing the performance the ML algorithms.

Therefore, one objective of this research is to generate GPR simulation models and create datasets in an automated manner with variable ranges set in a way, so the models represent real life scenarios.

1.2. Research Contributions

This research is funded by the Engineering and Physical Sciences Research Council (EPSRC) and by the Sir Bobby Charlton Foundation. The research contributes to humanitarian demining by evaluating novel methods to aid target classification performance of dual mode landmine detectors utilizing both MD and GPR. One major outcome of this research is the construction and development of two (a larger and a smaller) novel MPT measurement systems utilizing a novel coaxial, multi-coil geometry. In addition, electronics and control software required to control the measurement system were also developed. The advantage of the novel coil geometry is the generation of a uniform electromagnetic field at a specific region inside the coil arrangements. This enables the accurate measurement of rank 2 MPTs of objects. The rank 2 representation assumes a simple dipole response from the metal object.

Difficulty of accurately manipulating an object's orientation inside a coil arrangement has been a problem in previous research, which made the previously reported systems either very slow or unable to characterize non-symmetrical, irregular, or non-homogenous objects. This research introduces a novel method for characterizing rank 2 MPTs of non-symmetrical objects. This has been achieved using a novel target orientation manipulator and an advanced post-processing algorithm for MPT inversion.

Using the system mentioned above, rank 2 MPTs of four real landmines and their components were characterized for the first time, to the best of the author's knowledge.

This uniquely proved the performance and the usefulness of the developed system for the humanitarian demining application, which was another major outcome of this research.

By utilising both the larger and the smaller coil arrays, rank 2 MPTs of around 200 threat (pistols, sub-machine guns etc.) and non-threat (belt buckles, mobile phones, coins etc.) objects were characterised. Unsupervised Machine Learning algorithms were applied to datasets generated using the MPT characterisations of the objects. Clustering of the threat and non-threat objects by the ML algorithms, as well as performance of the algorithms were evaluated and reported, which was another major outcome of this research.

Although rank 2 MPTs provide a good level of object characterization, the number of independent coefficients in the rank 2 MPT is limited. The Generalized Magnetic Polarizability Tensor (GMPT) includes higher order terms in the asymptotic expansion of MPT, which represents the object's properties more accurately and has more independent coefficients. Therefore, measuring the GMPT of objects has the potential of providing better target classification and identification. Undertaking experiments using non-uniform electromagnetic fields to prove the GMPTs can, for the first time, be measured in practice is another major outcome of this research.

The final major outcome of this research is the generation of synthetic GPR datasets to train Artificial Neural Network (ANN) and Convolutional Neural Network (CNN) type classifiers. This has involved simulations to generate datasets of realistic soil models, in addition to accurate models of three landmines and clutter items commonly found in soil contaminated by previous conflicts.

All publications authored and co-authored have been included in the Publications Chapter of this thesis, with the exception of publications where the author did not do a considerable contribution to the work. However, all publications involving the author can be found in the publications list at the start of this thesis. The author has taken the decision not to include the publications as separate chapters since in some cases there is significant overlap of the work from publication to publication. For this reason, all publications are included as a single chapter within this thesis. For conciseness, the publications which are included as part of this thesis are listed in Table II below with a summary of each paper in relation to the aims and objectives of this research.

Table II – List of publications with a short summary for each paper describing the achievements and how the paper relates to the research.

Title	Authors	Journal/ Conference	Summary
Measuring the Magnetic Polarizability Tensor Using an Axial Multi-Coil Geometry	Toykan Özdeğer, John L. Davidson, Wouter van Verre, Liam A. Marsh, William R. B. Lionheart, Anthony J. Peyton	IEEE Sensors Journal (Published, Volume: 21, Issue: 17, Sept. 2021)	This paper describes the MPT measurement system built as part of the research. A novel coil arrangement, system electronics and software are discussed in detail. This ties in with the three objectives which are related to building a system capable of characterizing MPTs of metal objects. However, this paper provides a method which can only characterize symmetrical objects.
Measuring the Magnetic Polarizability Tensor of Non-Symmetrical Metallic Objects	Toykan Özdeğer, John L Davidson, Paul D. Ledger, Daniel Conniffe, William R. B. Lionheart, Anthony J. Peyton	IEEE Sensors Journal (Under Review)	This paper follows up from the previous paper above, by providing a novel method for characterizing MPTs of non-symmetrical objects. This enables the system to be used to characterize any metal object, independent to its shape and material.
Measurement of GMPT Coefficients for Improved Object Characterisation in Metal Detection	Toykan Özdeğer, Paul D. Ledger, William R. B. Lionheart, John L. Davidson, Anthony J. Peyton	IEEE Sensors Journal (Published: Volume: 22, Issue: 3, Feb. 2022)	This paper describes methods to synthetically generate and measure higher rank MPT characterizations of metal objects. This proves that higher rank MPTs can be measured experimentally, which can be applied to various problems to improve classification.
A Study on the Magnetic Polarizability Tensors of Minimum Metal Anti-Personnel Landmines	Toykan Özdeğer, Paul D. Ledger, Anthony J. Peyton	The International Instrumentation & Measurement Technology Conference (Published: May 2022)	This conference paper reports MPT characterizations of four landmines and their components. These measurements were the first time the system was put into its intended use aimed by the research.
Classification of Threat and Non-Threat Objects Using the Magnetic Polarizability Tensor and a Large-Scale Multi-Coil Array	John L Davidson, Toykan Özdeğer, Daniel Conniffe, Mark Murray-Flutter, Anthony J. Peyton	IEEE Sensors Journal (Accepted)	This paper describes a larger coil array which was built using the same coil configuration as above. MPTs of small to medium sized firearms and a set of non-threat objects were measured using the instrument described. Two datasets were generated using the data and clustering in the data was evaluated by applying unsupervised machine learning.

1.3. Thesis Structure

Chapter 2 discusses background theory of MPT as well as existing previous work published on the subject, including previously proposed experimental instruments. Chapter 3 introduces the MPT measurement system that has been built as part of this research and presents the performance test results of the system. Chapter 4 then presents the results obtained from the case studies done using the instrument. Chapter 5 describes the GPR simulation models built for generating train datasets for ML training, as well as the ML test results. Finally, Chapter 6 concludes the thesis discussing the main outcomes of the research and possible areas of future work.

As this thesis is in Journal Format, Publications Chapter presents all major outcomes of this research in the form of journal or conference papers which have either been published or are under review.

2. Using the Magnetic Polarizability Tensor For Reducing False Alarm Rate

This chapter describes the basic principles of the Magnetic Polarizability Tensor (MPT) and discusses previous relevant work found via a comprehensive literature review. These principles serve as background to the work discussed in Chapter 3, as well as the publications produced by the author. Section 2.1 briefly introduces the MPT and its potential uses. Section 2.2 describes the Magnetic Polarizability Tensor and the underlying mathematical theory. Section 2.3 concludes with an overview of the relevant work that has been previously published on characterising the MPT of metal objects.

2.1. Introduction

The Magnetic Polarizability Tensor (MPT) is a characterisation of a metal object. The MPT of an object is defined by its shape, size, material and the applied excitation frequency. The induced voltage in a metal detection system is due to the eddy currents that are generated in a metal object and the magnetic polarisation within ferrous materials when the object is present in a time-varying low-frequency background field. The induced voltage can be expressed in terms of an integral over an appropriate surface involving the perturbed magnetic field due to the presence of the conducting object. An asymptotic expansion of this perturbed field characterises an object by MPT, which is independent of the object's position. This is particularly relevant to Metal Detection (MD) applications where False Alarm Rates (FAR) are high, such as landmine detection or walk-through metal detectors, as well as where object classification is necessary, such as scrap metal sorting. Application of the MPT to these areas are described in detail in Section 2.3. If a library describing characterisations of objects of interest and objects that need to be rejected is generated for an application, a classification algorithm can utilise this library to improve classification performance and reduce the FAR of the system. For example, this has recently been proved using synthetically generated MPT data in [24], where several types of metal objects were classified using MPT eigenvalues or MPT invariants by ML algorithms. Section 2.3 gives a detailed description of previous work in the area of classification algorithms applied to MD systems.

2.2. MPT Theory

In the presence of an object, B_α with high conductivity σ and permeability of μ , the interaction of magnetic and electric fields in metal detection can be described by the eddy current equations (1) and (2), where $j = \sqrt{-1}$ and $\omega = 2\pi f$.

$$\nabla \times \mathbf{E}_\alpha = j\omega\mu\mathbf{H}_\alpha \quad (1)$$

$$\nabla \times \mathbf{H}_\alpha = \mathbf{J}_0 + \sigma\mathbf{E}_\alpha \quad (2)$$

For a conducting permeable object described as $B_a = aB + z$, where B is the unit size object placed at the origin, scaled by a and translated by z from the origin, the object characterisation is provided by the rank 2 MPT in the leading order term of the asymptotic expansion of the perturbed magnetic field [25]-[31]. The rank 2 tensor composition comes from the MPT coefficients within the leading order term. Higher rank tensor composition can be obtained by including higher order terms of the asymptotic expansion in the equation, which describe the object's electromagnetic characteristics in more detail. However, it is possible to approximate the object's characterisation to rank 2 MPT, which can be accurately measured when a uniform magnetic field is applied to the target object. The asymptotic expansion is in the form of (3), which holds if $a \rightarrow 0$ meaning the object's size should be negligible compared to the generated field.

$$(\mathbf{H}_\alpha - \mathbf{H}_0)(\mathbf{x})_i = (\mathbf{D}_x^2 G(\mathbf{x}, \mathbf{z}))_{ij} (\mathcal{M})_{jk} (\mathbf{H}_0(\mathbf{z}))_k + \mathbf{R}(\mathbf{x})_i \quad (3)$$

$\mathbf{H}_0(\mathbf{z})$ in (3) represents the background magnetic field (or the primary magnetic field) present at the object's position. \mathbf{H}_α represents sum of the primary incident field and the secondary magnetic field generated by the eddy currents at position \mathbf{x} by an object where \mathbf{x} is external to the object. The magnetic field perturbation can then be expressed as $(\mathbf{H}_\alpha - \mathbf{H}_0)(\mathbf{x})$ at position \mathbf{x} . The object has a conductivity of σ_* and permeability of μ_* . $\mathbf{D}_x^2 G(\mathbf{x}, \mathbf{z})$ is the hessian of the free space Laplace Green function describing the background field where $G(\mathbf{x}, \mathbf{z}) = 1/(4\pi|\mathbf{x} - \mathbf{z}|)$. In addition, $(\mathbf{u})_i$ represents the i th component of vector \mathbf{u} and repeated indices imply summation. The residual $\mathbf{R}(\mathbf{x})$ has a known form as shown in [24]-[31] and includes the higher order terms of the asymptotic expansion. Finally, $(\mathcal{M})_{jk}$ is the complex symmetric rank 2 MPT expressed as in (4) and transforms as the coordinate system is rotated, i.e., $(\mathcal{M})'_{ij} = (\mathbf{R})_{ip} (\mathbf{R})_{jq} (\mathcal{M})_{pq}$.

$$\mathcal{M} = (\mathcal{M})_{ij} \mathbf{e}_i \otimes \mathbf{e}_j \quad (4)$$

where orthonormal coordinate basis vectors are described as $\mathbf{e}_i, i = 1, 2, 3$. Equation (5) also shows the complex symmetric MPT matrix at a frequency f where the coefficients with the same colour are the same. The MPT is complex symmetric with 6 independent coefficients.

$$\mathcal{M}(f) = \begin{bmatrix} \mathcal{M}'_{xx} + j\mathcal{M}''_{xx} & \mathcal{M}'_{xy} + j\mathcal{M}''_{xy} & \mathcal{M}'_{xz} + j\mathcal{M}''_{xz} \\ \mathcal{M}'_{yx} + j\mathcal{M}''_{yx} & \mathcal{M}'_{yy} + j\mathcal{M}''_{yy} & \mathcal{M}'_{yz} + j\mathcal{M}''_{yz} \\ \mathcal{M}'_{zx} + j\mathcal{M}''_{zx} & \mathcal{M}'_{zy} + j\mathcal{M}''_{zy} & \mathcal{M}'_{zz} + j\mathcal{M}''_{zz} \end{bmatrix} \quad (5)$$

For a case where a small coaxial transmit and receive coil pair placed away from a conductive permeable object, it has been shown in [26] that the change in the induced voltage in the receive coil caused by presence of the object is:

$$V_{ind} \approx \mathbf{m} \cdot (\mathbf{H}_\alpha - \mathbf{H}_0)(\mathbf{x}) \quad (6)$$

where \mathbf{m} is the magnetic dipole moment of the receive coil. For the case where a large coaxial coil pair is placed close to the target object, it has been shown in [26] that the induced voltage takes the form:

$$V_{ind} = \int_S \mathbf{n} \cdot (\mathbf{H}_\alpha - \mathbf{H}_0)(\mathbf{x}) d\mathbf{x} \quad (7)$$

where integral of the (6) over cross-sectional surfaces of the coils with unit normal \mathbf{n} predicts the induced voltage. For both (6) and (7), it has been proven that the equations can reduce to the form:

$$V_{ind} \approx -\frac{j\omega\mu_0}{I_r} \mathbf{H}^{Rx} \cdot (\mathcal{M}\mathbf{H}^{Tx}) \quad (8)$$

where I_r is the current that would flow through the receive coil, if it was to be used as the transmit coil. \mathbf{H}^{Tx} represents the magnetic field at the target object's position, generated by the transmit coil, and \mathbf{H}^{Rx} represents the pseudo magnetic field at the target object's position, if the receive coil was used as the transmit coil. To arrive at (8) from (3), it is necessary to have a uniform magnetic field over the region a target object occupies. In this case, the residual $\mathbf{R}(\mathbf{x})$ in (3) vanishes, which then enables the use of (8) with \mathcal{M} representing the complex symmetric rank 2 MPT. Therefore, a target object can be rotated inside the uniform magnetic field which would cause a change in the induced voltage, depending on the object's properties. The receive and transmit fields can also be rotated

accordingly using (9) to represent the change in orientation of the magnetic fields applied on the object.

$$\mathbf{H}_1 = \mathbf{R}\mathbf{H}_0 \quad (9)$$

where \mathbf{H}_0 is the initial magnetic field orientation, which can be rotated by the rotation matrix \mathbf{R} to find the rotated field \mathbf{H}_1 . Using 6 unique orientations and measuring the induced voltage at each orientation, 6 linear equations from (8) can be constructed. The linear equations can then be solved using the least-squares method to arrive at the MPT. Although using 6 unique orientations is enough to calculate the MPT, more are used in practice to achieve a better posed solution, as well as better Signal-To-Noise-Ratio (SNR).

The MPT is frequency dependent, which means using a wide frequency spectrum will result in a better characterisation of the object. In addition, the rank 2 MPT calculated using (8) is orientation dependent. However, it is important to have orientation independence for characterising MPT where the orientation of the object is unknown. To gain orientation independence, eigenvalues of the MPT matrix can be calculated. The resulting 3 complex eigenvalues represent the responses that would be generated if the target object's principal axes were aligned with the primary field [32]. The complex MPT eigenvalues are shown by the diagonal matrix in (10):

$$\mathbf{\Lambda}(f) = \begin{bmatrix} \mathbf{\Lambda}'_{xx} + j\mathbf{\Lambda}''_{xx} & 0 & 0 \\ 0 & \mathbf{\Lambda}'_{yy} + j\mathbf{\Lambda}''_{yy} & 0 \\ 0 & 0 & \mathbf{\Lambda}'_{zz} + j\mathbf{\Lambda}''_{zz} \end{bmatrix} \quad (10)$$

The MPT can be expressed in terms of the diagonalised MPT eigenvalues, $\mathbf{\Lambda}$, and the eigenvectors, \mathbf{Q} , that rotate them, i.e., $\mathcal{M}(f) = (\mathbf{Q}')\mathbf{\Lambda}(\mathbf{Q}')^T + j(\mathbf{Q}'')\mathbf{\Lambda}''(\mathbf{Q}'')^T$.

An Alternative Way to Derive the MPT Equation

The equation (8) relating the MPT to the voltage induced on the receive coil can also be derived by combining the Biot-Savart Law, Faraday's Law and the equation for the magnetic dipole moment. Using the Biot-Savart Law in (11), magnetic field strength generated by a circular coil at any point in space can be calculated [33].

$$\mathbf{H} = \frac{I}{4\pi r^2} \oint_c d\mathbf{l} \times \hat{\mathbf{r}} \quad (11)$$

where I is the filamentary current flowing through the coil, r is the distance between the coil segment and the observation point, $d\mathbf{l}$ represents the length of the coil segment used to generate the magnetic field, and $\hat{\mathbf{r}}$ is the unit vector from the coil segment to the observation point. The unit for \mathbf{H} is Amps per meter (A/m). A map of the magnetic field strength around a circular coil can therefore be generated by applying the equation at discrete points in three-dimensional space. Using the \mathbf{H} calculated by (11), the magnetic flux density can be calculated at the same points in space by multiplying the magnetic field strength with permeability of free space, where the unit for magnetic flux density, \mathbf{B} is Tesla:

$$\mathbf{B} = \mu_o \mathbf{H} \quad (12)$$

When there is a varying magnetic flux density through a circular coil, the voltage that is induced on the coil can be calculated using the Faraday's law in (13), where $d\mathbf{s}$ is the surface area in m^2 and t is time in seconds [34].

$$V_{ind} = - \iint \frac{\partial \mathbf{B}}{\partial t} \cdot d\mathbf{s} \quad (13)$$

Magnetic dipole moment of a planar circular coil can be described by (14) where I is the current flowing through the coil and S is the coil's area [35]-[37].

$$\mathbf{m} = SI \quad (14)$$

Equation (14) can be modified to cover three-dimensional space which takes the form in (15), where \mathbf{r} is the position vector, \mathbf{J} is the current density, and dv is the volume element in m^3 .

$$\mathbf{m} = \frac{1}{2} \int_v \mathbf{r} \times \mathbf{J} dv \quad (15)$$

Vector potential in (16) is generated in the presence of a magnetic dipole moment [35]-[37], where $\mathbf{B} = \nabla \times \mathbf{A}$.

$$\mathbf{A} \approx \frac{\mu_0 \mathbf{m} \times \hat{\mathbf{r}}}{4\pi r^2} \quad (16)$$

When the generated magnetic field is sinusoidal and time varying, the vector potential in (16) can be substituted for \mathbf{B} in (13), where the time derivative can also be written as $j\omega$.

$$V_{ind} = - \oint_c \frac{j\omega\mu_0}{4\pi r^2} \mathbf{m} \times \hat{\mathbf{r}} \cdot d\mathbf{l} \quad (17)$$

Equation (11) can be used to substitute for \mathbf{H} in (17) which simplifies to the form in (18).

$$V_{ind} = - \frac{j\omega\mu_0}{I_r} \mathbf{m} \cdot \mathbf{H}^{Rx} \quad (18)$$

Where I_r and \mathbf{H}^R represent the pseudo current and magnetic field that would be present if the receive coil was to be used as the transmit coil, same as in (8). Finally, by utilising the relationship between the magnetic dipole moment and the MPT in (19), we can arrive at the relationship between the induced voltage and the MPT in (20), which is the same formula as (8) [36].

$$\mathbf{m} = \mathcal{M} \mathbf{H}^T \quad (19)$$

$$V_{ind} \approx - \frac{j\omega\mu_0}{I_r} \mathbf{H}^{Rx} \cdot (\mathcal{M} \mathbf{H}^{Tx}) \quad (20)$$

2.3. Previous Work

This section provides an overview of the previous work that has been published on characterisation and the use of MPTs, which are relevant to the research in this thesis.

Research in [38]-[40] applied the use of the MPT in Unexploded Ordnance (UXO) detection. In [38], Fernandez *et al* introduced the Man-Portable Vector Sensor (MPV) which is a handheld sensor for characterising and detecting buried UXO. The sensor utilises five coils mounted at different positions, and the whole sensor is moved around above the target object to get the rotation information for characterising the MPT of the target object. Norton and Won used the GEM-3 handheld sensor to characterise spectroscopic electromagnetic induction (EMI) data of symmetrical objects at three orientations in [39]. The EMI data (collected using a frequency range from 30 Hz to 20 kHz) was used to characterise the MPTs of the objects. Additionally, a small library involving eigenvalues of MPT characterisations of nine cylinders were built. A fitting algorithm was used to see if an object could be detected when buried in soil. Finally, the same methodology was applied on the MPT characterisations of four UXOs. Similarly, Grzegorzczak *et al* attempted to simultaneously identify multiple UXO targets buried at different depths in [40] by using the MPV sensor from [38] and the Multi-Sensor Towed Array Detection System (MTADS) reported in [41] (which works at 50 Hz) by Nelson and McDonald. Similar to the MPV sensor in [38], the MTADS uses multiple coils to collect the orientation information, the MPT eigenvalues are then computed to arrive at the orientation independent characterisations. However, both systems operate slowly and are heavy. In addition, there are error contributions to the MPT characterisations from positioning errors. The sensors are also optimised only for UXO detection.

Research in [42]-[47] discusses the characterisation and application of MPT for walk-through metal detector applications in order to classify threat and non-threat objects potentially carried by people. In [42], Marsh *et al* describe a walk-through metal detector portal capable of characterising MPTs of objects passed through the portal at frequencies around 12 kHz. Multiple coils are used in the system to achieve orientation information of the object. Makkonen *et al* describes a method to determine target object properties using the MPT in [43] and to discriminate between cylinders and strips made from several materials. Decision borders between several types of materials are also shown. In [44]-[46], Makkonen *et al* evaluate the performance and attempt to improve the reliability for

classification of objects using the MPT collected by the system described in [42]. A K-Nearest Neighbours (KNN) method is used to classify a set of threat and non-threat objects passed through the portal. The classification performance is also improved by implementing noise and bias countering in the classifier, as well as object path detection and analysis. The classifier was reported to have over 95% success rate for classifying threats, and over 85% success rate of correctly classifying objects.

A conveyor belt system utilising magnetic induction spectroscopy was proposed in [48] to discriminate between metals made from different materials for metal recycling. 16 coils, each working at 6 frequencies (from 2 kHz to 64 kHz), were placed under the conveyor belt to collect spectral magnetic signature of the metal pieces going through the belt. A sample matching classifier was tested on spectral signatures of 117 test pieces where 95% classification accuracy was achieved.

Tao *et al* proposed a system for workpiece recognition in [49] where eight coils were positioned under the object bed in a circular array. Instead of rotating the object to recover the full MPT, orientation information was gathered by utilising the different position of each individual coil with respect to the target object. MPT of the target object was characterised partially using this method at a single frequency of 10 kHz. The system was tested using 26 target objects made from 4 different types of materials. The objects were clustered into their respective 4 material categories correctly using the partial MPT characterised using the circular coil array.

A handheld metal detector utilising a novel coil array was reported by Marsh *et al* in [50], where one transmit and four receive coils were used at different positions. The handheld detector was swept above a target object to retrieve orientation information, which was then used to characterise the MPT of the target object. The MPT characterisation error was reported to be from 10 dB to 20 dB with the SNR being 6%.

Ambrus *et al* evaluated the MPT characterisation performance of seven simulated planar coil arrangements in [51]. The coil arrangements ranged from a single transmit and single receive coil to single transmit and nine receive coils. The coil arrangements utilising multiple receive coils were optimised to best interrogate the three-dimensional space to characterise the target object's shape and orientation. MPT characterisation performance of three inversion methods including non-linear least squares, differential evolution and HAP (magnetic field \mathbf{H} , vector magnetic potential \mathbf{A} , and magnetic scalar potential, \mathbf{P})

methods were evaluated using synthetic data. The study concluded that planar coil arrangements utilising multiple receive coils have performed better for MPT characterisation of buried cylinders, irrespective of the inversion algorithm used.

Zhao *et al* used multiple coil arrangements, measurement and inversion methods to synthetically characterise MPTs of metal objects in [52]. The evaluated coil arrangements involved planar (one transmit, one receive coil) and coplanar (one transmit, two receive coil) metal detector swept above the target object, an inline metal detector utilising single transmit, two receive coils, and a balanced coaxial coil array utilising one transmit and two receive coils. For the coaxial coil array case, target orientation information was obtained by rotating the object inside the coils. Gaussian Elimination, Singular Value Decomposition (SVD) and Regularised Gauss Newton Method were used to arrive at the MPT characterisations of the target objects from the synthetic data. Simulations involving a brass wire in each sensor at 800 kHz were done. It was found that for the single transmit, single receive coil case, sufficient orientation information about the object could not be obtained to calculate the full rank MPT. For rest of the sensors, all inversion methods resulted in MPTs close to the analytical results.

Dekdouk *et al* applied linear least squares method in [53] to arrive at the MPT characterisation of target objects from both measured and simulated data. In addition, a non-linear optimisation algorithm was used to arrive at the MPT when the object's location was not known, which was also used to estimate the object's position. A tri-axial coil arrangement was used for obtaining the synthetic data, which is assumed as the true MPT of the target object, whilst a planar electromagnetic induction sensor and a coaxial coil arrangement producing a uniform magnetic field were used for obtaining the experimental data. The experimentally obtained MPTs of a spherical target object and an AP landmine detonator analogue were reported to be within 5% and 12% of the true MPTs, while the objects' locations were localised within a few centimetres.

Ambrus *et al* propose a circular mono-coil EMI sensor in [54] for characterising MPTs of target objects in time domain. The sensor is moved above the target object and measurements are taken at discrete positions to obtain orientation and shape information. A non-linear inversion method is used to arrive at the MPT characterisations from the EMI data, where the inversion method is not specified. The non-linearity of the problem is caused by the object's location being unknown.

Dalichaouch *et al* used a coil arrangement utilising a magneto-resistive sensor in [55] to characterise two minimum metal AP landmines. Although the MPT characterisations of the AP landmines were not calculated, spectroscopic responses from 100 Hz to 150 kHz were measured and reported.

Scott describes a coil array in [56] which is attached on a cart type arrangement to measure responses of AP landmines and metal clutter, such as bottle tops or ammunition shells. The coil array utilises a single transmit and three receive coils. The system uses 21 discrete frequencies separated logarithmically from 300 Hz to 90 kHz. The arrangement is pushed over the buried metal targets and the spectral magnetic responses are recorded. Scott and Larson later utilise the coil array described in [56] to establish a measurement facility for characterising MPTs of metal objects, described in [57]-[59]. A laboratory positioner is used to rotate the target objects within a known field generated by the coil array, which was held stationary during the experiments. The custom-made positioner is described to have three automated translational stages, two automated rotational stages (yaw and pitch), and one manually adjusted roll stage. The target objects were rotated in steps around one axis, where the rotation around the other two axes were stepped once a full rotation around the first axis is complete. Consequently, this results in having many orientations to measure with each experiment typically lasting 19 hours. A least squares method was used to arrive at the MPT characterisations of the target objects from the experiment data. Objects involving AP landmines, metal clutter such as rifle cartridges and still nails, as well as coplanar metal loops were characterised during the experiments. Good agreement between experimental and analytical MPT characterisations was reported for the case of single and triple conducting metal loops. Scott and Larson also describe the dipole expansion and inversion methods developed for calculating the MPT from measurement data in [58]. Scott and McFadden further describe the inversion method in [60] which is applied to the magnetic susceptibility measurement of soils and MPT characterisation of metal objects.

Rehim *et al* described a coil arrangement in [61] utilising one transmit and two receive coils, as well as custom electronics. A frequency spectrum from 1 kHz to 100 kHz was used with logarithmically spaced discrete frequencies. A custom target orientation manipulator capable of rotating target objects around one horizontal axis was reported in the paper. Least squares method was used to arrive at the MPT characterisations of the target objects from the measurement data. Later, the system was utilised [62] to

characterise metal clutter commonly found in post-conflict areas, as well as AP landmine surrogates. Davidson *et al* also utilised the system described in [61] to characterise the MPTs of the US coinage in [63]. The MPT characterisations of the coins were also calculated using data generated by Finite Element Method (FEM) type simulations. Although, compared to the experimental setup, a wider frequency spectrum from 1 Hz to 1 MHz was used for the simulations, resulting MPT characterisations from both simulations and experiments were reported to have a good agreement between 1 kHz and 100 kHz.

Research in [24], [31], [64]-[66] are the most recent and relevant to this research. Noteworthy progress is done both for the underlying mathematics and the application of the MPT for better object classification. In [31], Wilson and Ledger have reported a novel way of speeding up Finite Element Method (FEM) type simulations for synthetically characterising MPTs of metal object. An open-source simulation software under the name of “MPT-Calculator” was published as part of the paper. Amad *et al* in [64] has provided MPT characterisations of four objects as a benchmark which can be used to evaluate performance of new systems built for MPT measurement. Ledger and Lionheart discuss the theory for characterising multiple metal objects placed close to each other in [65] as well as characterising shape and material of buried objects in [27]. In addition, Ledger and Wilson discuss possible pre-processing methods in [66] or MPT datasets to be used in ML applications. The paper also provides a set of synthetically obtained object MPTs to build the dataset. Finally, Wilson and Ledger evaluate the performance of several ML algorithms in [24] on the dataset produced with synthetic MPT data.

Summary

From the literature it can be seen that a significant amount of research has resulted in the measurement and simulation of MPTs. To achieve this, several distinct types of approaches have been adopted, such as moving a coil arrangement above a buried object, rotating the target object inside a coil arrangement, or using multiple coils at the same time to obtain the orientation information. Overall, more than 25 coil geometries were explored in the literature reviewed in this section. However, the literature strongly suggests that the current experimental methods of acquiring the MPT are slow and, in some cases, inaccurate. In addition, some of the approaches are only able to characterise symmetrical metal objects, which can’t be applied to real life scenarios. A comprehensive

set of real threat and benign objects have also not been either produced or reported in the literature.

In line with the Research Contributions Section, the originality and novelty of this research relating to the measurement and use of the MPTs come from the following:

- Introduction of an MPT measurement system with two coil arrangements utilising a novel coil geometry for generating a uniform magnetic field inside the coils. This work has been published in IEEE Sensors Journal with the title “Measuring the Magnetic Polarizability Tensor Using an Axial Multi-Coil Geometry”.
- Introduction of a fast and accurate procedure for characterising rank 2 MPTs of non-symmetrical, irregular metal objects. This work has been submitted to IEEE Sensors Journal with the title “Measuring the Magnetic Polarizability Tensor of Non-Symmetrical Metallic Objects”.
- Measurement of higher rank MPTs of cone shaped metal objects for the first time, to the best of the author’s knowledge. This work has been published in IEEE Sensors Journal with the title “Measurement of GMPT Coefficients for Improved Object Characterisation in Metal Detection”.
- Measurement of the rank 2 MPT characterisations of four landmines for the first time, to the best of the author’s knowledge. This work was presented in the 2022 IEEE International Instrumentation and Measurement Technology Conference (I2MTC) with the title “A Study on the Magnetic Polarizability Tensors of Minimum Metal Anti-Personnel Landmines” and was published in the conference’s proceeding.
- Measurement of the rank 2 MPT characterisations of firearms ranging from small pistols to sub-machine guns.
- Measurement of the rank 2 MPT characterisations of an extensive set of non-threat objects, such as belt buckles, mobile phones and watches.
- Application of unsupervised ML algorithms to datasets generated using the experimental data to interrogate the clustering between the threat and non-threat objects. The work mentioned in the last three bullet points have been accepted for publication the in IEEE Sensors Journal with the title “Classification of Threat

and Non-Threat Objects Using the Magnetic Polarizability Tensor and a Large-Scale Multi-Coil Array”.

As discussed in the Introduction Chapter, a problem with metal detectors used in landmine Detection and walk-through metal detectors, is solely the detecting the presence of a metal object. If more information could be obtained about the detected metal target, a smart classification could be made on the targets, reducing FAR and increasing application speed both for landmine detection and security screening. The instrument and the methodology described in Chapter 3 shows that the MPT can be used to measure the electromagnetic properties of the target object, and this information can be used to discriminate between different types of targets.

The reason for building coil arrays which can generate a uniform magnetic field to measure the rank 2 MPT of metal targets as part of this research is the sufficient approximation of the target object’s electromagnetic properties by the rank 2 MPT. However, coils used in most practical applications (e.g., landmine detection and walk-through metal detection) do not generate uniform magnetic fields, where there is more contribution from higher order terms to the MPT. The higher rank MPT of the targets in these applications can be measured by knowing the exact magnetic field generated by these coils at the target’s position, as well as recording the object’s location with respect to the sensor. This can lead to more accurate measurement of the target object’s MPT with potential to further improve the target classification performance by the sensors.

3. Magnetic Polarizability Tensor Measurement System

In Chapter 1 the high occurrence rate of false alarms in landmine detection, and the need for an improvement were discussed. In Chapter 2, the MPT theory, how MPT can be used for better target classification, and how this was done in the literature were discussed. By utilising recent advances in mathematical theory and developing measurement techniques capable of characterising the electromagnetic properties of target objects, it is possible to accurately obtain the MPTs of a range of metal objects. If a library of MPT measurements of landmines and metal clutter was built, classification software, such as curve fitting or supervised machine learning algorithms, could be trained and deployed to better classify the target objects. This could help considerably reduce FAR by rejecting the objects with high possibility of being clutter. This chapter describes a laboratory instrument capable of measuring rank 2 MPT data of metal objects. The instrument was designed and built as part of this research with the motivation of paving the way towards building such a library.

Section 3.1 gives an overview of the instrument including the coil array, system electronics and the software. Section 3.2 describes the geometry of the coil array and the mechanical details. Section 3.3 then discusses the system electronics including the transmit and receive amplifier circuits and the microcontroller used for signal acquisition. The target orientation manipulators and their applications were mentioned in Section 3.4. Section 3.5 describes the control and post-processing routines necessary for running the experiments, as well as the Graphical User Interface of the software. Experiment methodology and the instrument's MPT characterisation performance were evaluated in detail in Sections 3.6 and 3.7, respectively. Section 3.8 then describes the larger coil arrangement built to work with the existing electronics and software for characterising MPTs of firearms. Finally, Section 3.9 summarises the key points about the design and development of the instrument discussed in this chapter.

3.1. System Overview

To measure the rank 2 MPT of objects containing small amount of metal (e.g., AP landmines), an instrument utilising a coil array capable of generating a uniform magnetic field at the position of the target object is required. In addition, the generated field must be strong enough to achieve a high Signal-to-Noise ratio for small metal objects (e.g., the small amount of metal in AP landmines). Finally, a bespoke software with experiment control and data post-processing capabilities is required to run the instrument.

The instrument described in this chapter consists of three main parts, which are the coil arrangement, system electronics and the control software. The Graphical User Interface (GUI) of the control software allows users to choose experiment settings, such as transmit voltage, frequency range, number of frequencies per decade, the target orientation manipulator used in the experiment, etc. The control software uses the settings to send control signals to a microcontroller inside the electronics box, which then generates the excitation signal for the transmit electronics. The resulting voltage and current on the coils are measured using two sets of receive electronics which filter and amplify the signals. The measured signals are acquired by the microcontroller and Digital Signal Processing (DSP) techniques are applied before converting the measured values to transimpedances and sending these values back to the control software, where the values are stored. Averaging, MPT calculation and result plotting are then done by the control software. The coil arrangement is made up of a transmit coil and two oppositely wound receive coils which are balanced to give near zero output when no metal object is placed near or in the coils. The instrument was designed to work in the frequency range from 100 Hz to 100 kHz. The frequency spectrum was chosen to capture the most characteristic information from metal objects with similar size to metal components within a minimum metal AP landmine, as well as metal objects relevant to walk-through metal detection. The excitation frequency range used for mine detectors and walk-through detectors typically extends from a few hundred Hz to a hundred kHz. This choice of frequency range is influenced by several factors as follows. At the lower end of the range, the detector system must output data at a rate consistent with the relative movement of the target. For instance, for a target moving at 1 m/s, with an output frame rate of 100 Hz, would give a spatial sampling rate of 1 cm, sufficient to capture several frames of data during the passage of most targets. The upper frequency is limited either by parasitic signals from the ground (landmine detection) or the person (WTMD), which typically

increase with frequency, or by the effects of unwanted resonances within the inductive coils of the detector. Of course, the frequency range must also be compatible with the response of the target, which is one of the main themes of this study. A schematic of the instrument is shown in Figure 3-1. The instrument is the subject of a peer reviewed and published journal paper entitled "Measuring the Magnetic Polarizability Tensor Using an Axial Multi-Coil Geometry" which is given in Publications – Publication 1 of this thesis.

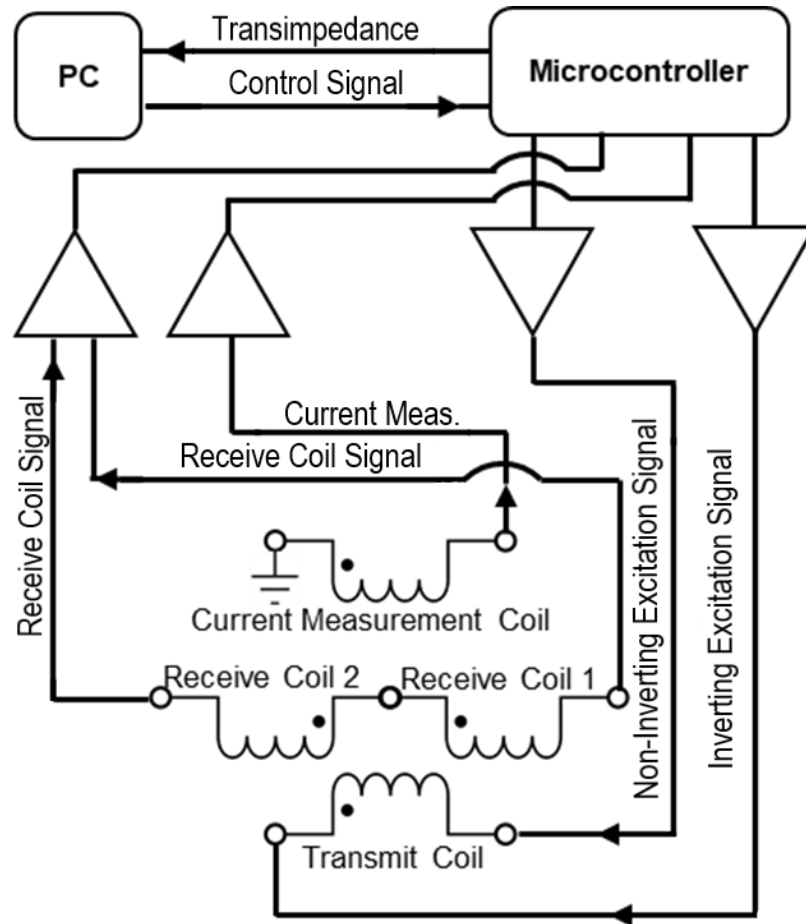


Figure 3-1 – System schematic showing coils, electronics and the data acquisition PC.

3.2. Coil Arrangement

To characterise the rank 2 MPTs of metal objects, a uniform magnetic field needs to be applied to the target object. The primary goal of constructing such instrument was to characterise minimum metal AP landmines. Therefore, a uniform field covering a volume of 13x13x13 cm was decided to be necessary as the region represents the size of common AP landmines [67]. A coil arrangement capable of generating a uniform magnetic field over such region was designed and optimised using Helmholtz coil principles. According to the Biot-Savart Law in (1), a magnetic field \vec{B} is produced when a current I passes

through a conductor with small segment $d\vec{L}$, where \vec{r}^2 is the displacement vector between point of observation and midpoint \hat{r} . As circular coils can be represented by a number of linear segments, (21) can be used to calculate the magnetic field generated by circular coils.

$$\vec{B} = \frac{\mu_0 I}{4\pi} \oint \frac{d\vec{L} \times \hat{r}}{r^2} \quad (21)$$

A coil geometry that satisfies the requirement of generating a uniform field across the specified region was found by an MEng team as part of their final year team project. They used a bespoke optimiser in MATLAB utilising Biot-Savart law and Helmholtz coil principles. The optimiser iteratively calculated the generated field over the specified region by varying a number of parameters including the number of coil sections, coil section positions and the number of turns.

The built coil arrangement consists of a transmit coil made up of 9 coil sections (turns: 11:3:5:5:5:5:3:11) and two receive coil halves, each made up of 4 coil sections (turns: 27:18:18:49 and 49:18:18:27 respectively), where the 4 coil sections are connected in series addition to form a single complete receiver coil. The two receive coil halves are connected in series opposition to give near zero output when there is no metal object in or near the coils. The coil geometry and the relative positions of the coils to each other are shown in Figure 3-2. The transmit coil is 240 mm in diameter and made up of a 2.1 mm enamelled copper wire. The receive coil is 220 mm in diameter and is made up of 1.2 mm PVC insulated wire. The coils are wound around two fiberglass reinforced plastic hollow tubes, one for the transmit, and one for the receive coils. A third fiberglass tube is used as the cover of the coil arrangement which fits around the transmit coil. A two-turn, current pick-up coil is present at the bottom of the coil arrangement to measure the current passing on the transmit coil. The current pick-up coil's position is chosen to have minimal interference over the generated magnetic field by the coils. For thermal and mechanical stability, and to preserve the relative positions of the coils to each other for keeping the coils balanced, the coil arrangement was encapsulated with epoxy resin. The built coil arrangement and the mechanical drawing are shown in Figure 3-3. To minimise the effects of any capacitive coupling between the coils and a target object placed in the coils, inner surface of the coil arrangement is covered with a conductive paint (Bare Conductive – Conductive Paint – SKU0216). The conductive paint is grounded to the system's

common ground and has a surface resistance of 55 Ω /Square for a sheet of thickness 50 microns.

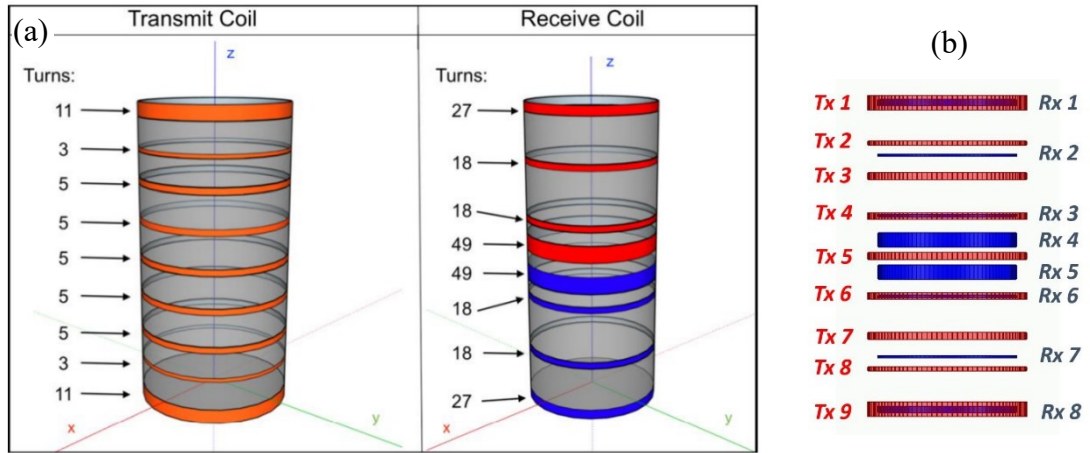


Figure 3-2 – Coil geometry of the coil arrangement. (a) is transmit and receive coils separately and (b) is both coils put together showing their relative positions.

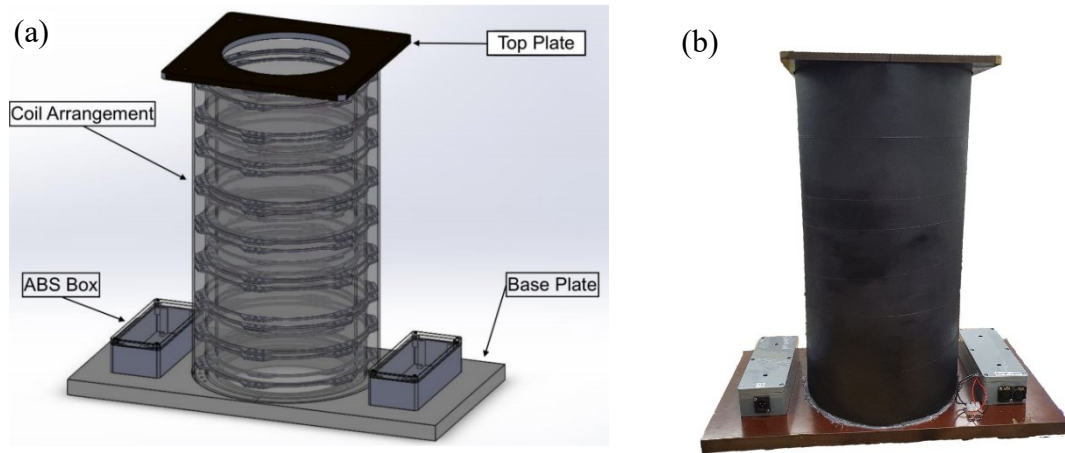


Figure 3-3 – The coil arrangement. (a) is the mechanical drawing and (b) is the completed version.

Receive Coil Balancing

Although, both receive coils were designed to be identical, in practice, there was a slight difference of the coils' impedances over the operating frequency spectrum. This was mainly caused by the receive coil at the top having longer connection wires compared to the one at the bottom, as the junction boxes were fixed to the base plate of the coil arrangement (see Figure 3-3). As a result, the receive coil at the top had a resonant frequency at 478 kHz while the receive coil at the bottom had a resonant frequency at 371 kHz. To reduce the impedance mismatch between the receive coils, parallel resistances of 56 k Ω and 43 k Ω were added to the top and the bottom receive coils, respectively. In addition, a parallel capacitance of 15 pF was added to the top receive coil. As a result, both receive coils' resonant frequencies were around 300 kHz with minimal impedance

differences within the operating frequency spectrum (100 Hz to 100 kHz). Impedance plots of the receive coils before and after impedance balancing are shown in Figure 3-4 (a). Balancing the impedances of the receive coils has effectively increased the linearity of apparent transimpedance between the transmit and the receive coils (connected in series opposition) within the operating frequency spectrum, which can be seen in Figure 3-4 (b). As can be seen from the figure, the resonant frequency of the transimpedance is at around 250 kHz, which is above the upper limit of the designed operating frequency.

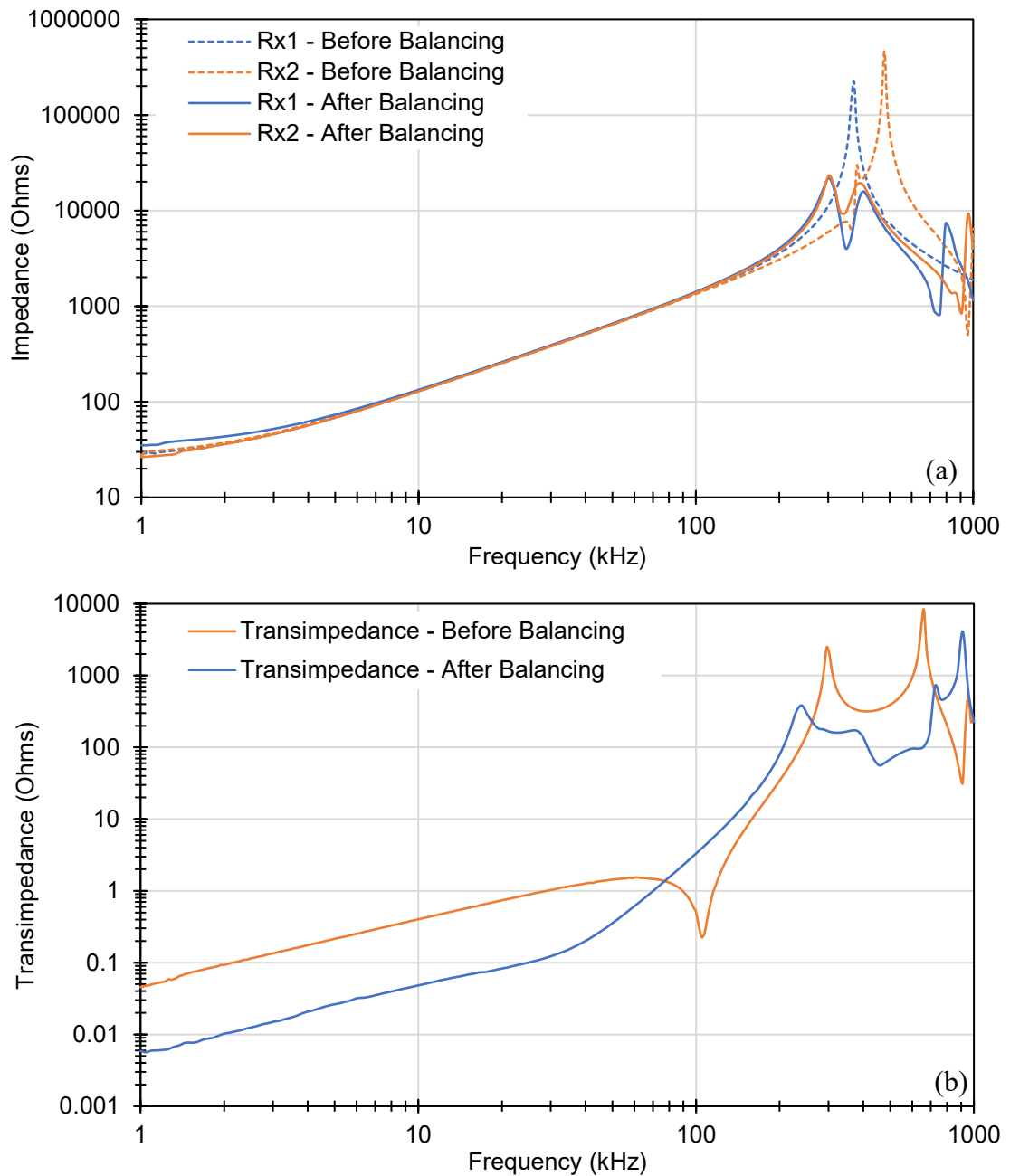


Figure 3-4 – Coil impedances measured between 1 kHz and 1 MHz. (a) is individual receive coil impedances before and after balancing. (b) is the transimpedance between transmit and receive coils before and after balancing the receive coils.

3.3. System Electronics

System electronics are made up of power supply units (PSUs), the microcontroller, and transmit and receive amplifier circuits. All electronics are housed in an aluminium 19-inch rack enclosure which is fitted with two cooling fans. There are a total of three medical grade PSUs powering the system electronics. Two of the PSUs (XP Power SMP350PS18) are used to power transmit and receive electronics and are able to output ± 18 V at 350 W each. Another 12 V, 80 W PSU is used to power the microcontroller and the cooling fans of the enclosure. The electronics box is shown in Figure 3-5.



Figure 3-5 – The aluminium, 19-inch rack electronics box of the instrument

Transmit Electronics

The transmit electronics are built on a four-layer printed circuit board (PCB) which consists of twenty power amplifiers (Analog Devices LT1210), an instrumentation amplifier (Texas Instruments AD8429) and a passive band pass filter at the input for removing AC and Digital-to-Analogue Converter (DAC) switching noises as well as any DC bias. The instrumentation amplifier interfaces the output from the microcontroller to the power amplifiers by amplifying the ± 1 V excitation signal to ± 32 V. The twenty power amplifiers are divided into two groups of ten as inverting and non-inverting configurations. Each power amplifier is powered with ± 18 V and can output over a range 32 V peak-to-peak. By having ten inverting and ten non-inverting power amplifiers, the transmit coil can be driven in a differential configuration to achieve a maximum peak-to-peak voltage of 64 V. To achieve the differential configuration, both ends of the transmit coil are excited with sine waves 180 degrees out of phase from each other, with no

common ground connection. By utilising the differential configuration of the power amplifiers, the transmit amplifier circuit is able to output 64 V peak-to-peak at 10 A (640 W reactive power) to the transmit coil. The transmit amplifier circuit diagram is shown in Figure 3-6.

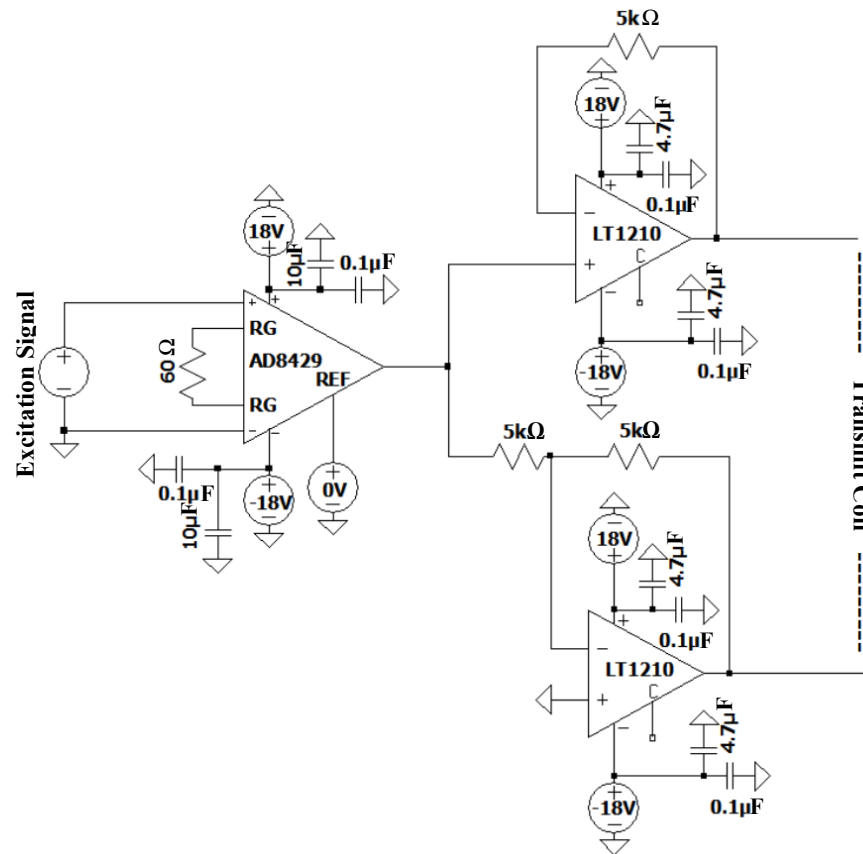


Figure 3-6 – Transmit amplifier circuit diagram. The diagram shows one inverting and one non-inverting amplifier. However, in reality, there are 10 of each, which are identical.

Receive Electronics

There are two identical receive amplifier circuits built on two-layer PCBs. Each receive amplifier circuit has an instrumentation amplifier (Texas Instruments AD8429) at the input interfacing with the coils. Output from the instrumentation amplifier is then input to an active band pass filter to attenuate any signals outside of the operating frequency spectrum. The cut-off frequencies of the band pass filters are chosen to be from just below 100 Hz to 200 kHz. This ensures any AC noise is eliminated, as well as any high frequency parasitic noise. One of the receive amplifier circuits is used for interfacing the receive coils to one of the inputs of the microcontroller, while the other receive amplifier circuit is used for interfacing the current pick-up coil for the transmit coil. The receive amplifier circuit diagram is shown in Figure 3-7.

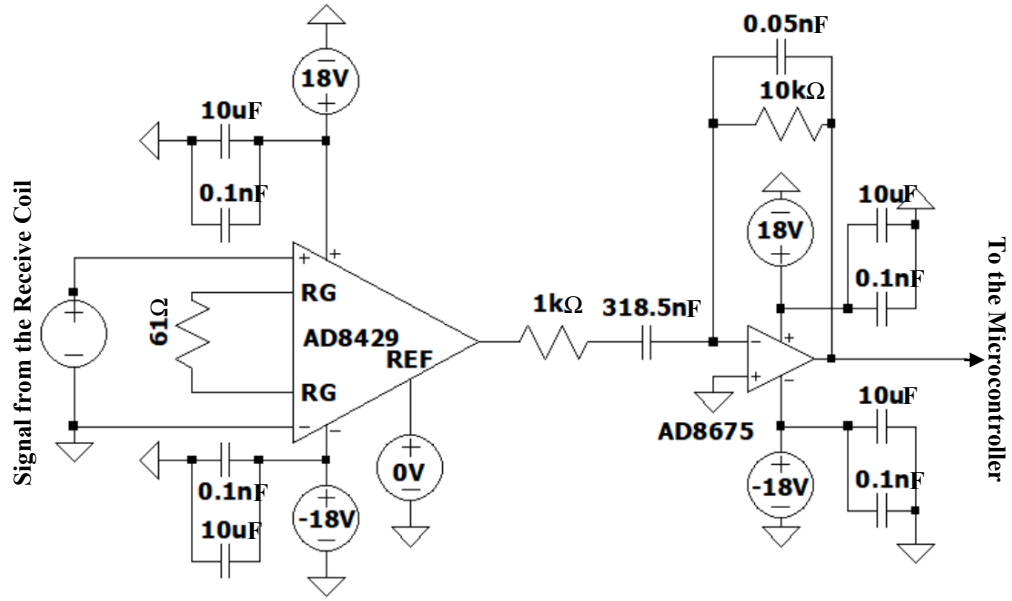


Figure 3-7 – Receive amplifier circuit diagram.

Microcontroller

A Red Pitaya model (STEMlab 125-14) is used as the microcontroller for data acquisition, digital signal processing and excitation signal generation. One of the two output ports of the microcontroller is used as the excitation source, which is connected to the input of the transmit amplifier circuit. Both input ports are also used as data acquisition points which interface with the two receive amplifier circuits for measuring the voltage and current induced on the coils.

3.4. Target Orientation Manipulator

To obtain all independent coefficients of the MPT, the target object has to be rotated inside the generated magnetic field. For the rank 2 MPT, a minimum of 6 independent orientations inside a uniform magnetic field are required to recover all 6 independent MPT coefficients, however more orientations may help with averaging and noise reduction. A higher number of independent orientations in a non-uniform magnetic field are required for characterising higher order MPT, e.g., rank 3. To rotate target objects inside the generated field by the instrument, three target orientation manipulators (TOM) have been built as follows:

- i. For characterising rank 2 MPTs of symmetrical metal objects.
- ii. For characterising rank 2 MPTs of non-symmetrical, irregular metal objects.

- iii. For characterising higher order MPTs of symmetrical objects.

These are described in the following sub-sections respectively.

Single Axis Rotation

Rotation around one axis is sufficient to fully characterise the rank 2 MPT of symmetrical objects if the axis of symmetry is known. A TOM capable of rotating target objects around a single axis was designed and built. This was mainly used during the initial stages of the instrument development. Symmetrical test objects were characterised as part of the development stage to understand the system and develop the necessary calibration and measurement methods. This meant that the required mathematical theory and the complexity of the control software were simpler. Target objects were rotated 360 degrees in typically 15-degree steps during experiments with this TOM. The TOM built for single axis rotation for characterising symmetrical metal objects is shown in Figure 3-8.

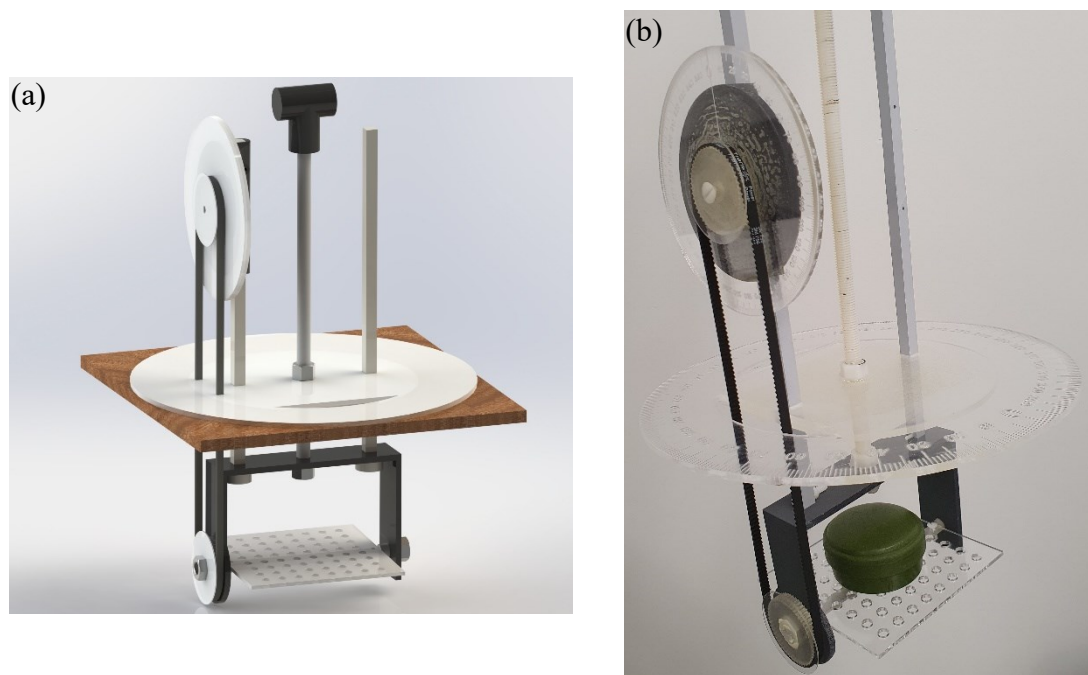


Figure 3-8 – Target orientation manipulator for single axis rotation. (a) is the three-dimensional design of the TOM. (b) is the built version of the TOM with a Type-72 AP landmine placed on the rotating plate.

Three-Axis Measurement

For characterising the rank 2 MPT of non-symmetrical objects, a minimum 6 independent rotations, which involves rotation around all three axes, inside a uniform magnetic field is necessary. A TOM similar to a three-axis gimbal could be built for this purpose. However, this would involve several complex moving parts, and must be built with no metal parts. Therefore, a simpler method of rotating objects in all three-axis was sought.

A truncated Icosahedron (tI) shaped TOM was designed and built for this purpose, which is the shape of a traditional football (soccer ball). This shape has 32 faces, which gives 16 unique orientations, because of the reciprocity caused by the uniform magnetic field. The tI shaped TOM is built in two parts, which can be opened to place the target object on a mounting plate inside. It also has keyed holes on each of the faces, which are numbered for reference. The TOM can then be placed on one of its faces on a keyed table inside the coil arrangement. The target object can be rotated by placing the TOM on its different reference faces which has known rotations compared to the starting orientation. The tI shaped TOM is shown in Figure 3-9. A larger version of the tI was built for measuring larger objects, such as firearms, which is described in Section 3.8. The work in this section has been further described in the peer reviewed (currently under review) journal paper entitled "Measuring the Magnetic Polarizability Tensor of Non-Symmetrical Metallic Objects" given in Publications – Publication 2 of this thesis.

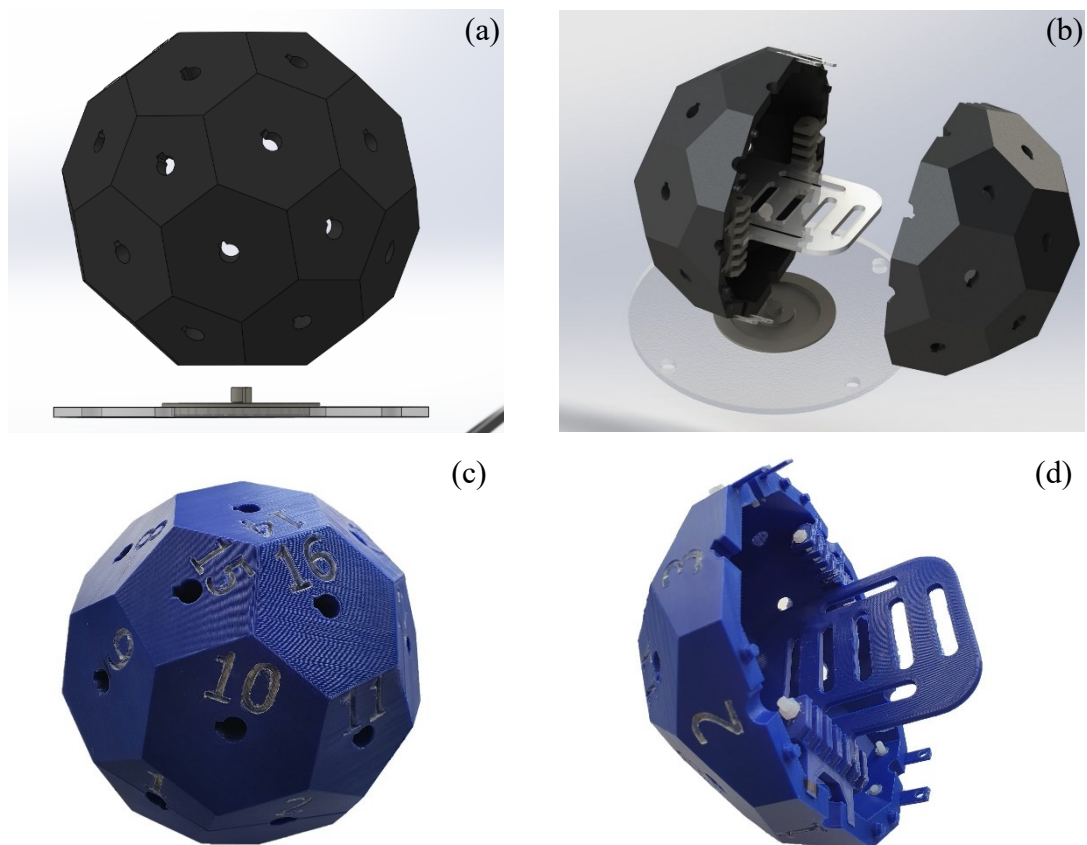


Figure 3-9 – Computer Aided Design (CAD) models and built version of the Target Orientation Manipulator. (a) and (c) showing closed CAD and built versions. (b) and (d) showing CAD and built versions where the two halves are separated.

Higher Order MPT Characterisation

As described in Chapter 2, the rank 2 approximation of the MPT holds when the target object is placed in a uniform magnetic field. The higher order MPT of the object (e.g., rank 3) can be characterised by placing and rotating the object outside of the region with uniform magnetic field. To characterise rank 3 MPT of cone shaped objects, a TOM capable of rotating the objects around an axis outside of the region with uniform magnetic field was built. The TOM, shown in Figure 3-10, can be placed on top of the coil arrangement, where the magnetic field is non-uniform, and the target objects can be rotated around an axis at different horizontal and vertical positions. More detail about the theory and measurement of higher rank MPTs are provided in a peer reviewed journal paper, which is given as part of this thesis, see Publications – Publication 4.

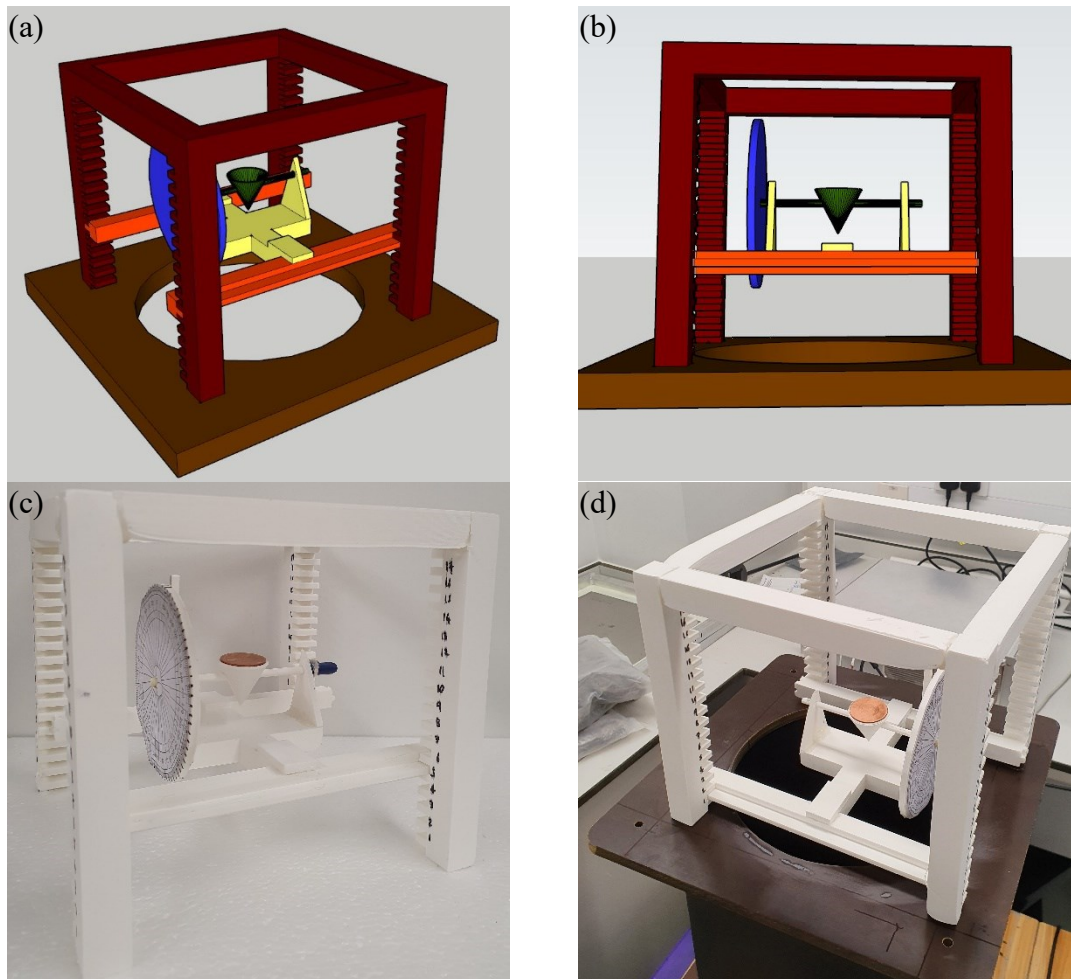


Figure 3-10 – TOM capable of rotating cone shaped objects around one axis outside of the region with uniform magnetic field. (a-b) are the CAD drawings and (c-d) are the manufactured TOM using 3D printing techniques.

3.5. Software

The software used to run the instrument consists of three different components which are:

- i. The control routines that run on the host PC.
- ii. The post-processing algorithm that also runs on the PC.
- iii. The algorithm that runs on the Red Pitaya microcontroller.

The control and post-processing routines are written in the Python programming language and are combined together into one with a GUI, which was also written in Python. The Red Pitaya microcontroller uses a previously developed algorithm which is written in combination of C++ programming language and Field-Programmable Gate Array (FPGA) programming. The algorithm for the microcontroller is written for operating conventional metal detector systems and has more features than required for this instrument.

Control Routines

The control routines allows the user to choose the experimental settings, perform a calibration, and display measurement plots in real time. It sends commands to the microcontroller in real time using Message Queuing Telemetry Transport (MQTT) communication protocol, which is generally used for Internet of Things (IoT) applications [68]. The basic settings that can be chosen by the user are shown in Table III.

The control algorithm also simultaneously receives messages from the microcontroller in real time, which carry the acquired and digitally filtered signal readings, as well as warning messages (e.g., input saturation). The control algorithm then averages, stores and displays the received inputs as per the experiment settings. The workflow of the control algorithm is shown in Figure 3-11. The control algorithm also enables users to change some important variables of the algorithm running on the microcontroller. Although the optimal settings are set for normal operations by default, these can be changed to adapt the process for different types of future experiments which might use the same software. Full code of the software used for this experiment is provided in Appendix 1.

Table III – Basic settings that can be set by the user for each experiment in the control algorithm.

Setting	Range	Setting	Range
Peak-to-Peak Voltage	1 – 64 V	File Name	N/A
Starting Frequency	0.1 – 10 kHz	Starting Position	1 – 16
Ending Frequency	1 – 100 kHz	Position Steps	1/2/4/8
Points Per Decade	1 – 100	Number of orientation steps before another background measurement	1/2/4/8/16
Sweep Type	Linear/ Logarithmic	Target Orientation Manipulator	Single/Multi Axis
Number of readings to average before moving to the next frequency	1 – 10	Calibration Mode	On/Off
Number of full sweeps to average per orientation	1 – 20	Sweep Mode	Single Frequency, Continuous Sweep

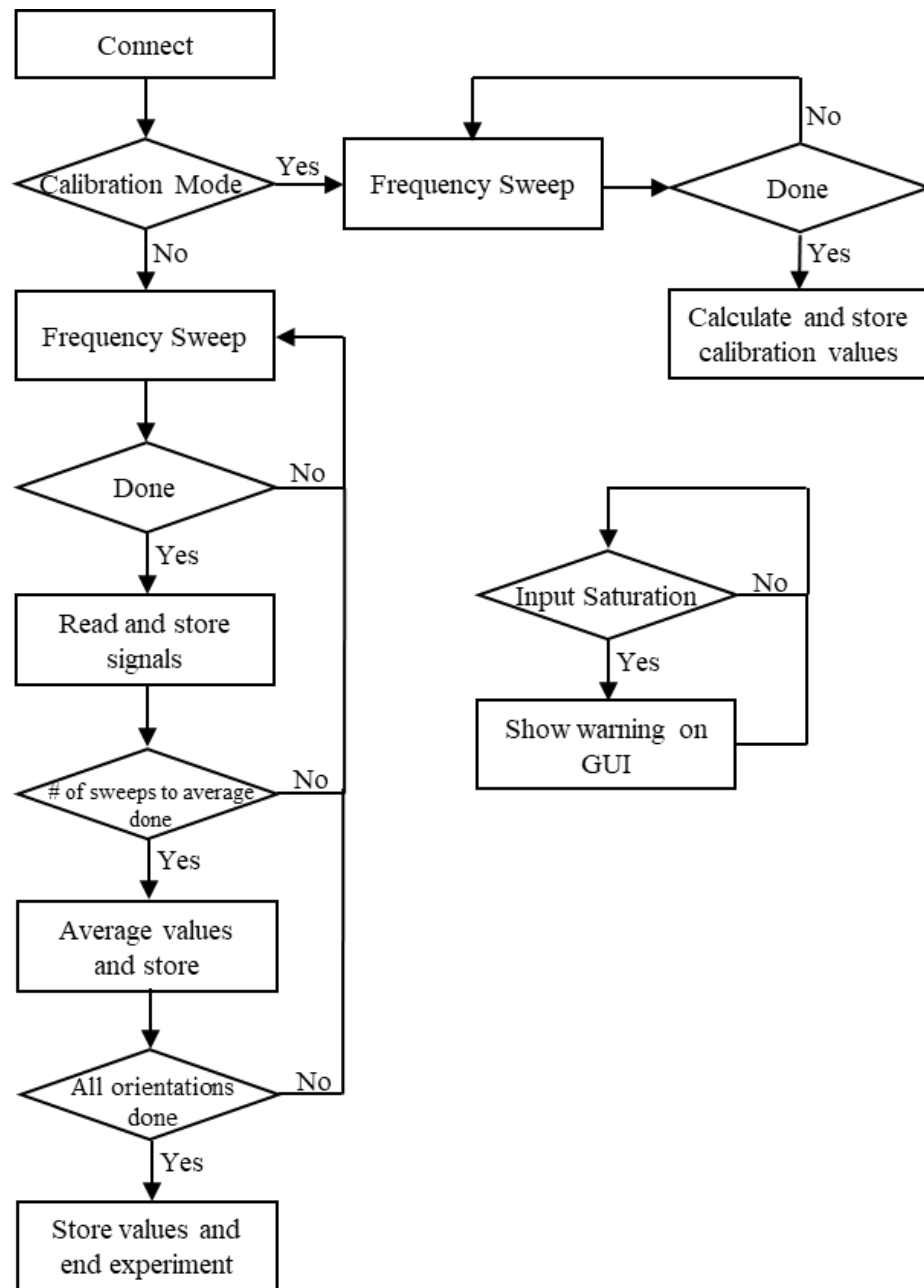


Figure 3-11 – The control routine's main workflow.

Post-Processing Algorithm

The post-processing algorithm lets the user convert the measured induced voltages into a rank 2 MPT of the object and extract its eigenvalues. The algorithm has manual and automatic modes, where the user can either use the default settings and process the most recent experiment's data or process any other experiment's data by using the manual mode. The post-processing algorithm first removes the background measurements from the measurements taken with the target object present in the coil arrangement to arrive at the field perturbation. The algorithm assumes linear drift between two consecutive

background measurements and generates a straight-line equation of the drift between them using the timestamps of the measurements. Phase calibration and scaling to the resulting values are applied using the values generated from the reference ferrite rod measurement. The algorithm then calculates the 6 MPT coefficients of the rank 2 MPT using the calibrated measurement data and orientation information. Finally, the algorithm calculates the MPT eigenvalues and plots the results. Basic workflow of the post-processing algorithm is shown in Figure 3-12 and the full code is given in Appendix 1.

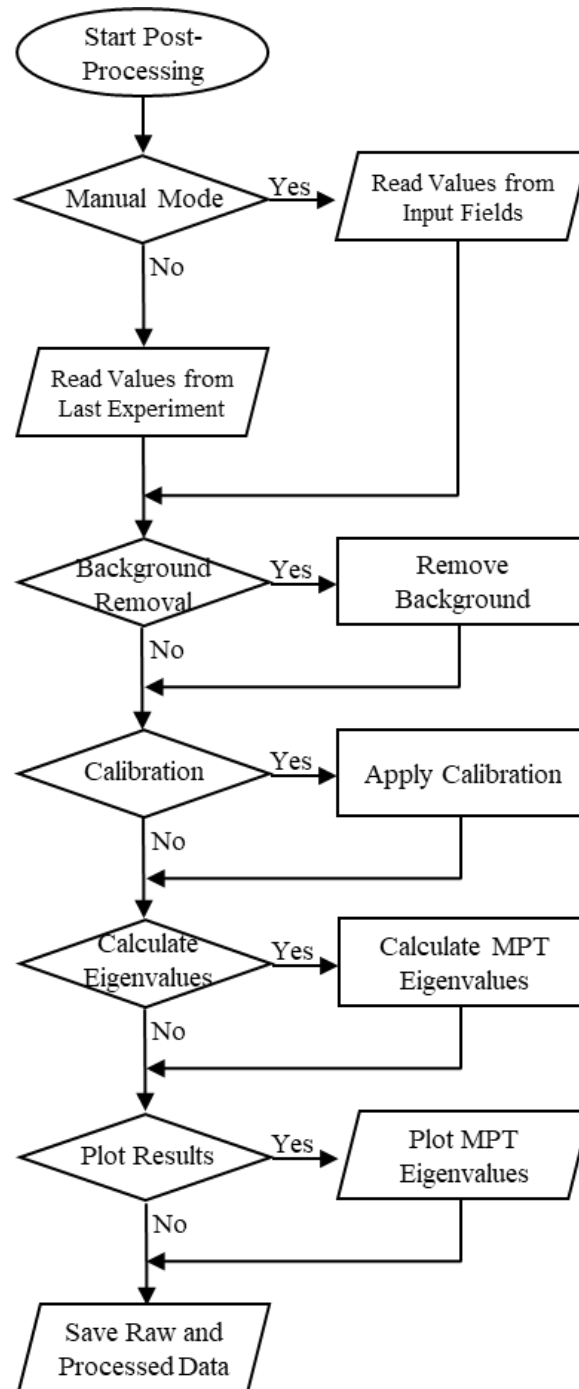


Figure 3-12 – The post-processing algorithm's main workflow.

Graphical User Interface

The control and post-processing algorithms are wrapped up in a GUI which combines both algorithms together. The GUI is written using a Python library called PyQt5, which has functions to generate the individual parts e.g., user input buttons. The GUI has three tabs; one houses the control algorithm's settings and some outputs, a second one houses some settings and variables of the microcontroller's algorithm, and finally, one for the post processing algorithm's settings. Figure 3-13 shows the main tab of the GUI.

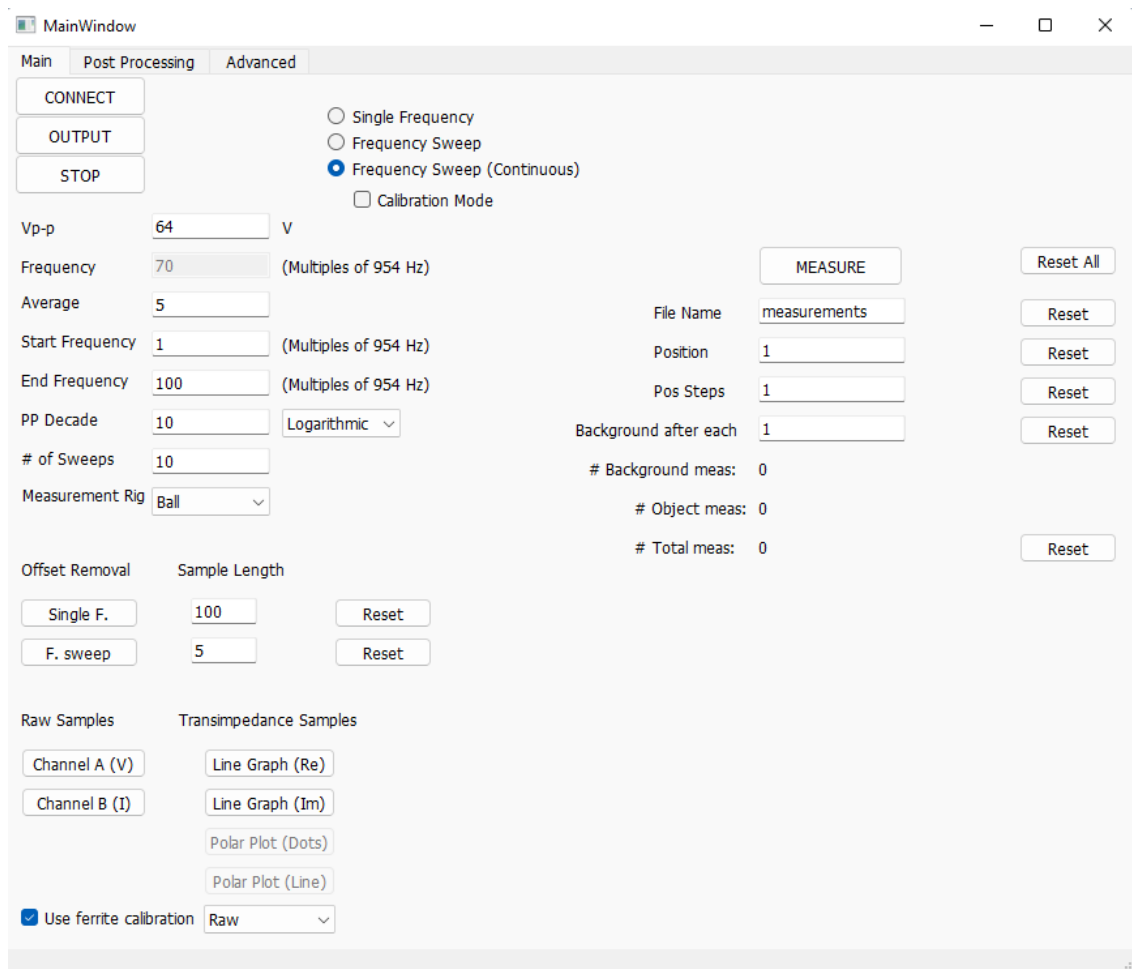


Figure 3-13 – Screenshot of the main tab of the GUI, where the experiments are controlled.

3.6. Methodology

Before starting an experiment, all output settings were set, and the instrument was left running for a minimum of half an hour to reach steady state temperature. The experiments were also conducted in a temperature-controlled laboratory to minimise thermal drift. These measures ensured that any measurement drift caused by temperature changes was minimised. A background measurement was taken with no object present inside the coils and stored. These values were then subtracted from the subsequent measurements with an object present in the coils. The object was then placed and rotated to the 16 different orientations inside the coil using the truncated icosahedron shaped TOM (for the rank 2 MPT characterisation). Depending on the level of averaging applied during an experiment, more background measurements were taken between different orientations and the background was updated. This ensured that drift in the measurements was further reduced.

Before characterising an object, a NiZn ferrite rod (Ferroxcube ROD10/40-4B2-L) was measured for calibration as a pure real (reactive) and constant frequency response is expected from the ferrite rod across the operating frequency of the instrument. Phase correction for each frequency was calculated according to the ferrite rod using (22), where Z_0 is the uncalibrated and $Z_{calibrated}$ is the calibrated transimpedance values, $|Z_0|$ is the absolute value and the θ is the angle of the complex number when in polar form. The correction values were then stored and applied to all subsequent target object characterisations.

$$Z_{calibrated} = Z_0 \times \frac{e^{-j\theta}}{|Z_0|} \quad (22)$$

For the rank 3 MPT measurement, three cone shaped metal objects in Figure 3-14 were used. The cones were made up of aluminium, copper and brass. The cones were placed in the TOM shown in Figure 3-10 and were rotated 360 degrees in 5-degree increments. The cones were rotated on top of the coil arrangement at different heights and horizontal positions. This meant that the magnetic fields applied to the cones at each position were different, revealing more information about the target object's characteristics. The MPT characterisations measured at the top of the coil arrangement also involved the rank 2 MPT, as well as the higher order terms. To only characterise the higher order terms, cones were also characterised inside the uniform magnetic field to measure only the rank 2 MPT

of the cones. The rank 2 MPT characterisations were then subtracted from the MPT characterisations made outside of the coil arrangement to reveal only the higher order terms in the MPT. Further detail about the theory and measurement of higher rank MPTs are provided in a peer reviewed and published journal paper entitled “Measurement of GMPT Coefficients for Improved Object Characterisation in Metal Detection,” which is given as part of this thesis, see Publications – Publication 4.

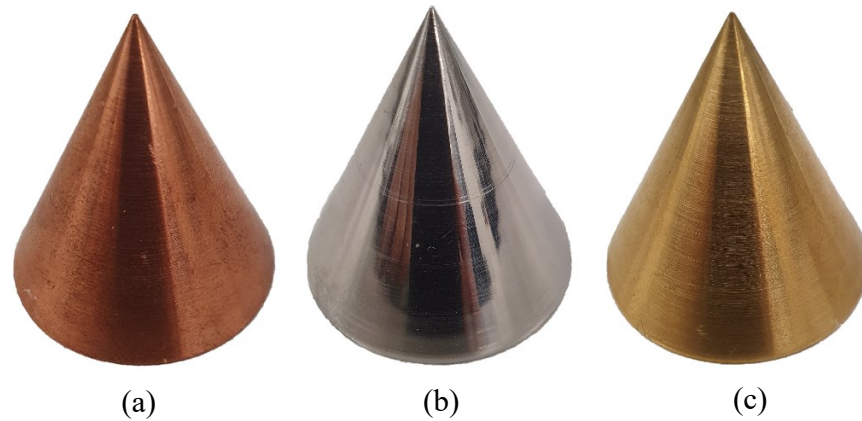


Figure 3-14 – Cone shaped target objects used for rank 2 and rank 3 MPT characterisations. (a) copper, (b) aluminium, (c) brass cone.

3.7. Coil Characterisation and System Performance

The system's performance was measured by evaluating the generated magnetic field uniformity, measurement noise and drift, experiment repeatability and the difference between various experimental and simulation methods.

Field Uniformity

The uniformity of the generated magnetic field was characterised by simulating the field strength along the vertical axis at different horizontal positions inside the coil arrangement. The simulations were made using the commercial FEM solver, Maxwell, (Ansys Electromagnetics Suite, Release 19.2). The simulated magnetic field strength for transmit and receive coils were used to generate field strength plots, shown in Figure 3-15, and field strength maps shown in Figure 3-16.

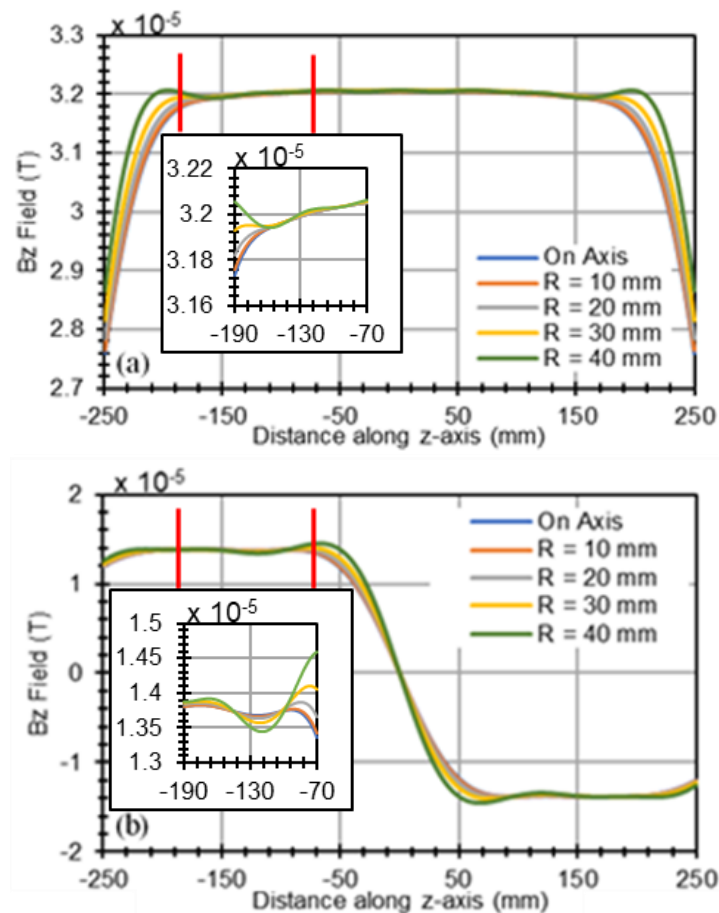


Figure 3-15 – Simulations of the magnetic field inside the coil system for the non-target case when transmit and receive coils are individually driven by an electric current. (a) transmit coil and (b) receive coil excitation. The measurement region is between the red vertical lines shown in the figure. The subplots within the figure show the field data within the measurement region at an enhanced scale.

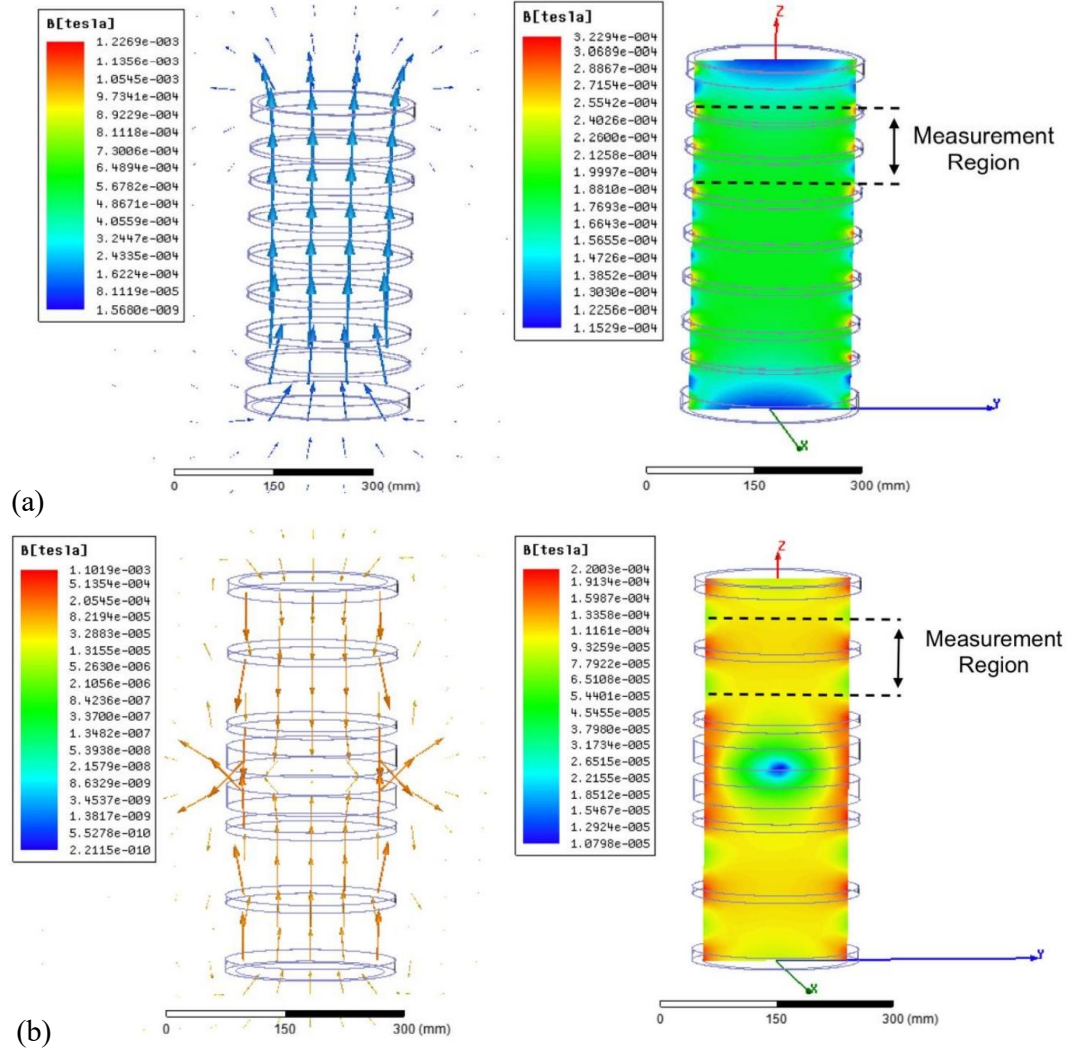


Figure 3-16 – Magnetic Field plots for transmit and receive coils. (a) transmit coil, (b) receive coil.

Measurement Noise

The measurement noise was quantified by comparing transimpedance values of a copper disk of 30 mm diameter and 2 mm thickness to the noise floor across the operating frequency spectrum. The comparison is shown in Figure 3-17 after the calibration process described in the previous section and plotted on a dB scale which is useful for providing a clear comparison. As seen from the figure, there is a minimum of 20 dB difference between the transimpedance values of the copper disk and the noise floor. The variance in the noise floor of MPT measurements is between -78 dB and -100 dB, which correlates to approximately 15 mm³. It should be noted that these values are at minimum signal averaging and the SNR can be improved by increasing the signal averaging during the experiments. However, this increases the time it takes to run each experiment.

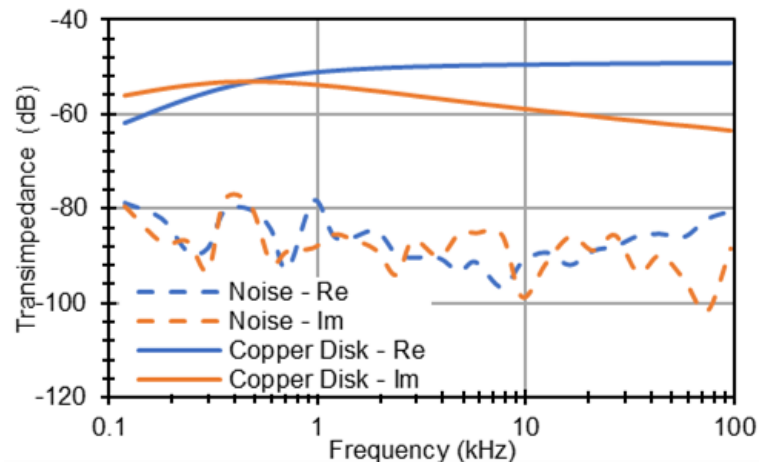


Figure 3-17 – MPT measurement noise floor compared to the real and imaginary transimpedance values of a copper disk across the operating frequency spectrum. The transimpedances are shown in dB scale instead of mm^3 for easy comparison.

Measurement Drift

Measurement drift was recorded at 50 kHz for two hours and plotted to determine the duration of the initial “warm-up” period. In addition, the amount of measurement drift during steady state conditions were used to decide on the interval between subsequent background measurements during an experiment. Figure 3-18 shows the measurement drift of real and imaginary transimpedance values plotted from when the instrument was initially turned on from cold until it reached steady state working condition. From the figure, it can be seen that the measurement drift stabilises after 60 minutes.

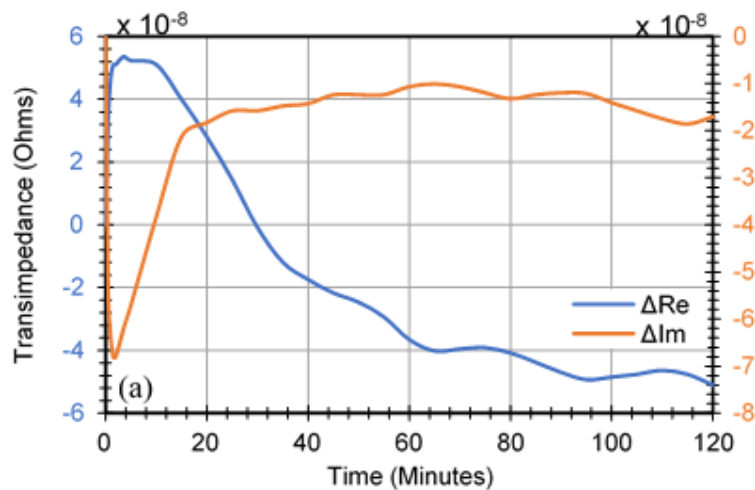


Figure 3-18 – Measurement drift of real and imaginary transimpedance values at 50 kHz plotted versus time for 120 minutes.

Experiment Repeatability

To evaluate the experiment repeatability of the instrument, transimpedance values from a copper disk at a single orientation were measured 10 times. Then, average values for each frequency of the 10 experiments were plotted with error bars showing the minimum and maximum values for each frequency, which is shown in Figure 3-19. It was found that a typical measurement had only 0.54% of average difference between minimum and maximum real transimpedance values and 0.62% for imaginary transimpedance values across the operating frequency spectrum. This shows excellent results in terms of measurement repeatability.

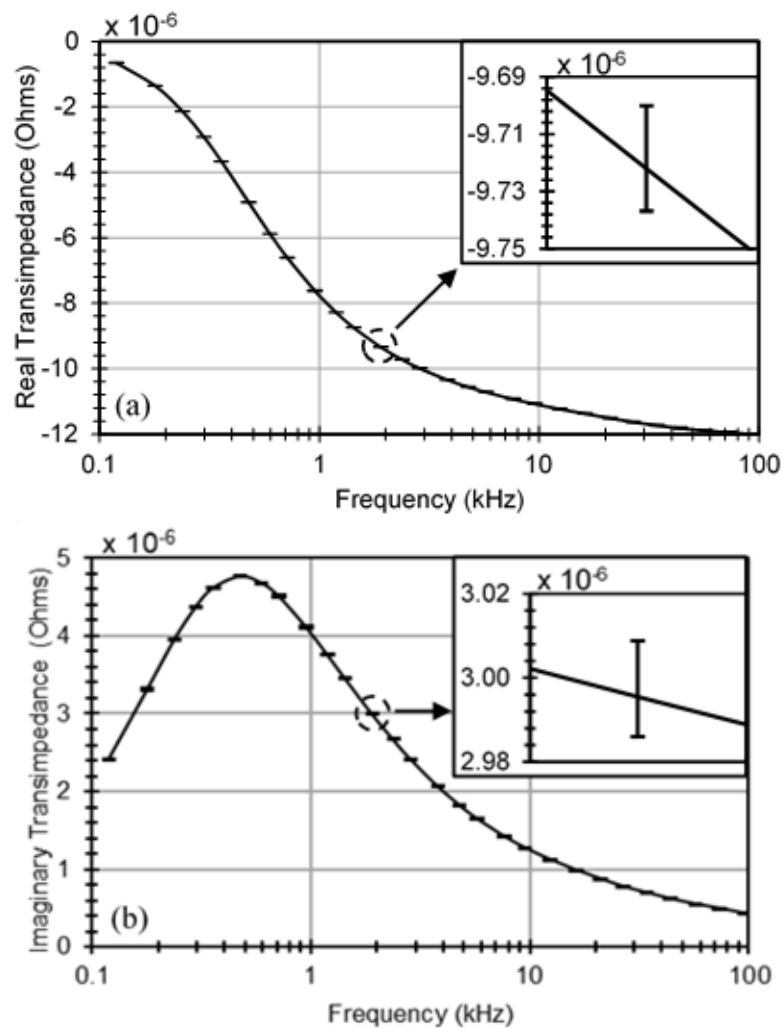


Figure 3-19 – Average of the transimpedance values of ten consecutive experiments with error bars showing the range of maximum and minimum values for each transimpedance. Plots show (a) real and (b) imaginary transimpedance values. The deviation in the data is approximately two orders of magnitude smaller compared with the absolute transimpedance values, which gives the appearance of single horizontal tick lines for the plotted error bars in the main plots. The upper right insert region in the plots shows the typical small deviation across the experiments, which is not easily discernible in the main plots.

The repeatability was further quantified using the Normalised Root Mean Square Error (NRMSE), shown in (23).

$$\text{NRMSE} = \frac{\sqrt{\frac{\sum_{i=1}^n (\text{Expt}_i - \text{Expt}(\text{Avg})_i)^2}{n}}}{\overline{\text{Expt}(\text{Avg})}} \quad (23)$$

In the NRMSE equation, n is number of measurement frequencies, Expt_i is the maximum or minimum transimpedance value at frequency i , $\text{Expt}(\text{Avg})_i$ is the average of the transimpedance values for frequency i and $\overline{\text{Expt}(\text{Avg})}$ is the average of average transimpedance values for all frequencies. The NRMSE values for a copper disk is shown in Table IV, where lower NRMSE values mean better experimental repeatability.

Table IV – NRMSE of differences between maximum and minimum transimpedance eigenvalues of the copper disk compared to the average.

Real Transimpedance		Imaginary Transimpedance	
Minimum	Maximum	Minimum	Maximum
0.0017	0.0023	0.0033	0.0037

MPT Characterisation Performance

A set of non-symmetrical copper test objects shown in Figure 3-20 were manufactured to test MPT characterisation performance of the instrument. The test objects' rank 2 MPTs were characterised using both the single and multi-axis TOMs. The test objects' MPTs were also acquired by simulations using the aforementioned FEM method and also using an optimized dedicated open source MPT-Calculator package [69] which employs the NGSolve FEM library [70]-[72].

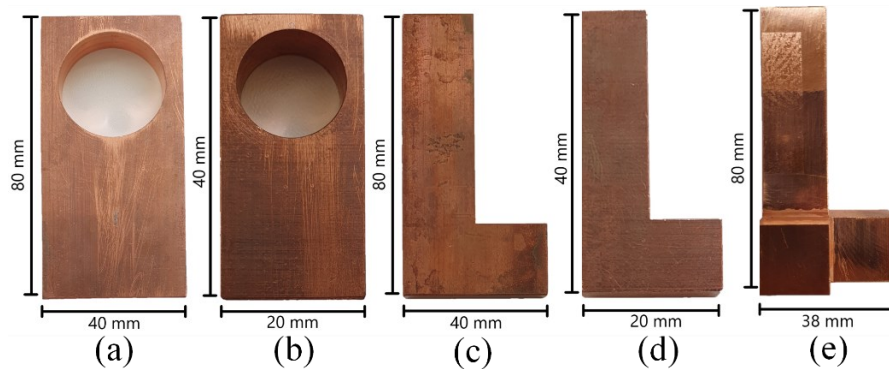


Figure 3-20 – Example target objects showing copper cuboid with a hole, 'L' shape and three legged 'L' shape. Object (a) and (b) copper cuboids with a hole, (c) and (d) copper 'L' shapes, (e) three legged 'L' shape. All five objects have a thickness of 10 mm where the three legged 'L' shape's third leg is 19 mm.

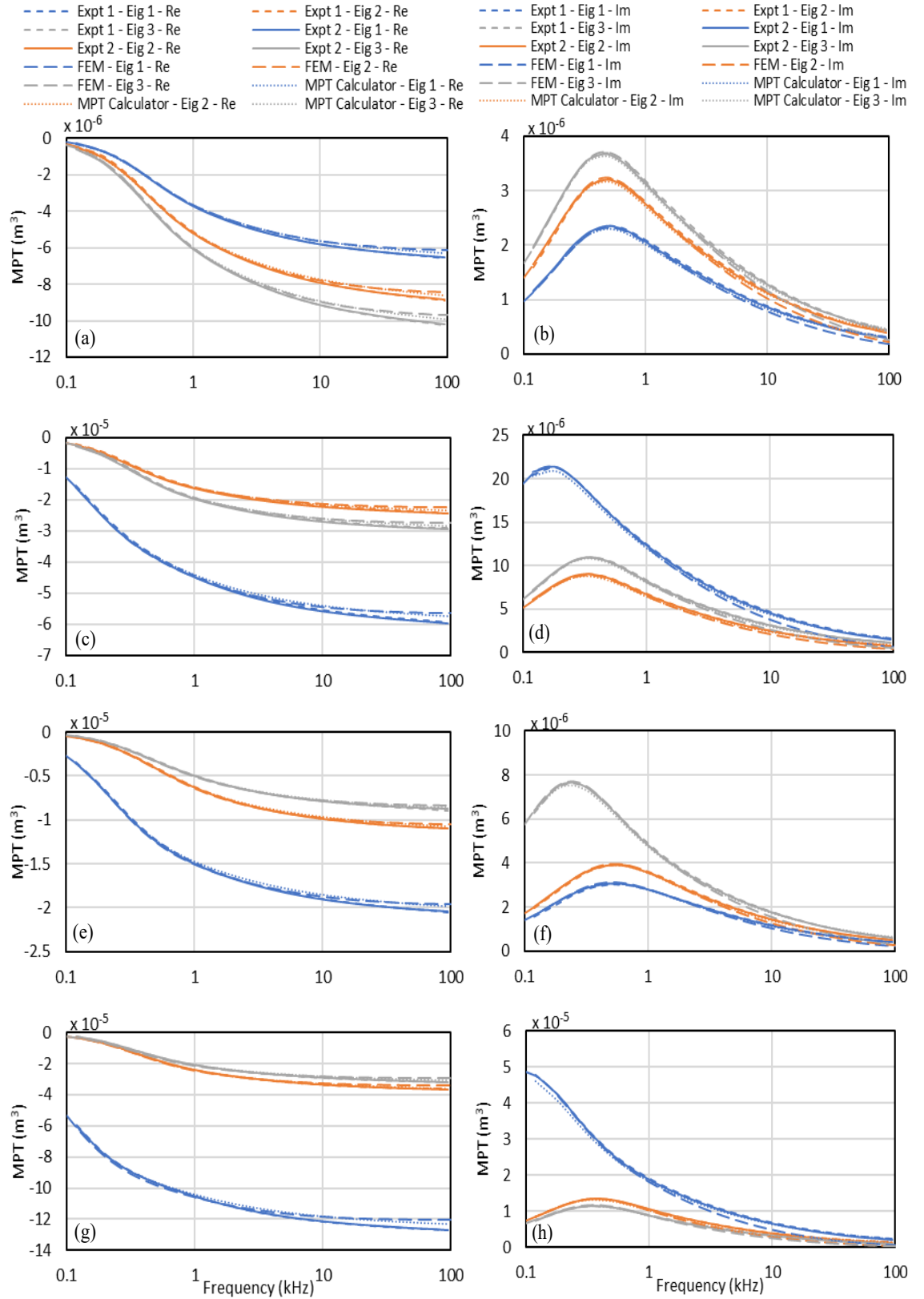


Figure 3-21 – Measured real and imaginary MPT eigenvalues of target objects, compared with results from FEM simulations, MPT Calculator and measurements using the previous TOM. Plots (a-b) small ‘L’ shape, (c-d) large ‘L’ shape, (e-f) small cuboid with hole, (g-h) large cuboid with hole. “Expt 1” represents values from experiments done using the single axis TOM while “Expt 2” represents values taken using the multi axis one. “FEM” represents values from FEM simulations while “MPT Calculator” represents values acquired using the MPT Calculator.

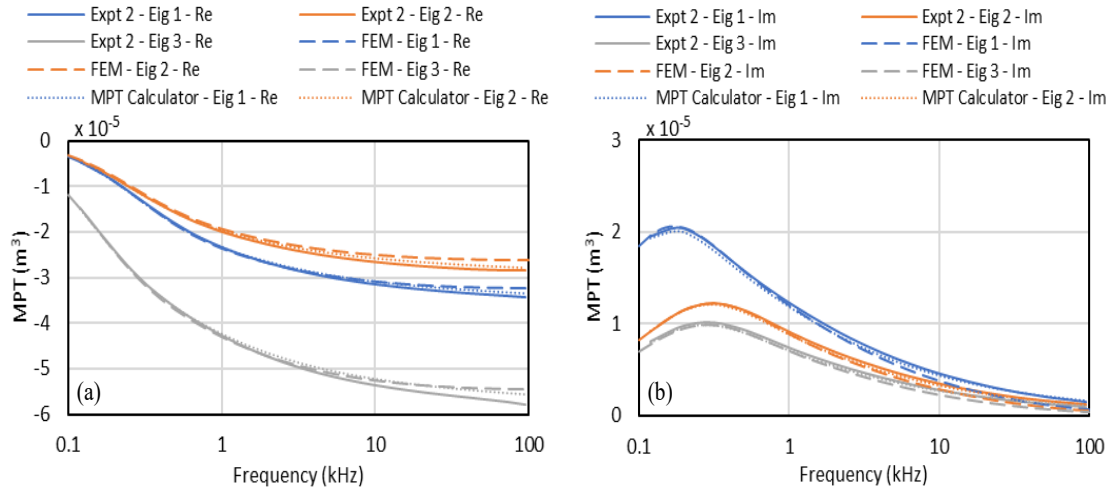


Figure 3-22 – Real and imaginary MPT eigenvalues for a three legged ‘L’ shape measured using the new object orientation manipulator, compared with results from FEM simulations and MPT Calculator. “Expt 2” represents values taken using the multi axis TOM. “FEM” represents values from FEM simulations while “MPT Calculator” represents values acquired using the MPT Calculator. Plots show (a) real and (b) imaginary MPT eigenvalues.

As can be seen from Figure 3-21 and Figure 3-22, there is a good agreement between the results acquired from all four methods. For all four test objects characterised using both TOMs in Figure 3-21, MPT eigenvalues’ loss-peak magnitude and frequencies were within less than one percent of each other, and five percent at worst when the simulations were also included. The three legged ‘L’ shape was not characterised using the single axis TOM as that was not possible given its non-symmetrical shape. However, the practical (multi axis TOM) and simulated (FEM and MPT Calculator) data in Figure 3-22 for the three legged ‘L’ shape still have their loss-peak magnitudes and frequencies within five percent of each other at worst. The main source of error between the two TOMs was the difference in orientation accuracy. The single axis TOM has around 1 degree orientation accuracy while the multi axis one has better than 1 degree accuracy, dictated by the ridges on the 3D printed surfaces which are below 0.2 mm. The FEM process involves several sources of error, including the inability to exactly model coil positions in the coil arrangement due to differences between the design and actual winding positions and the difficulty of representing eddy currents in thin surface layers across the full frequency spectrum of individual targets. Additionally, a further source of error between the practical and the simulation methods were because of the homogenous modelling of the target objects. In practice, this is not the case due to target materials having both small quantities of minor alloying metals and a level of unknown surface impurities or surface oxidation.

3.8. Large Coil Arrangement

Given the MPT characterisation performance of the coil arrangement described in this chapter, a larger coil arrangement with the same coil configuration was built for characterising larger target objects. Specifically, this coil arrangement was utilised to characterise small to medium sized firearms, such as pistols and sub-machine guns (SMGs) and larger non-threat objects, such as large mobile phones, battery power banks, etc. The large coil arrangement, shown in Figure 3-23, was built by scaling all dimensions from the smaller one by two. The external height of the large coil arrangement is 1.1 m, with a 0.44 m inner and 0.8 m outermost diameter. The transmit coil has an inner diameter of 495 mm and the two receive coils have an inner diameter of 430 mm.

Using fiberglass and encapsulating with epoxy resin at this size would not be possible given the weight concerns. Therefore, the large coil arrangement was built using 6 mm flexible Medium-density fibreboard (MDF) to provide the necessary tubular formers. The tubes holding the coils were fixed by using 12 mm MDF annuli lids on both top and the bottom with inserts, where the tubes slide in and keep in position. The transmit and receive coils were built using 12 AWG and 14 AWG PVC insulated copper wire wound around the MDF Tubes.

Given the larger size of the coil arrangement, a large multi axis TOM shown in Figure 3-24 was also built which utilises the same principle as the small multi axis TOM but is built with 3D printed parts and PBT (polybutylene terephthalate) pipe, rather than being fully 3D printed.

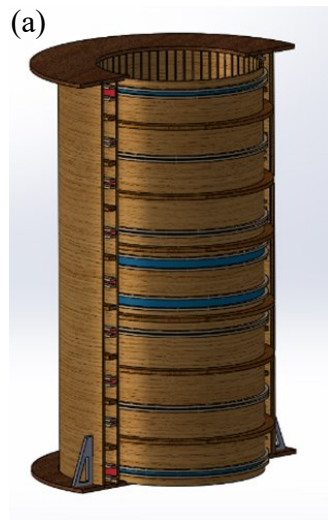


Figure 3-23 – The large-scale coil arrangement showing; (a) design concept cut away along with simplified inner receive coil and (b) constructed coil arrangement on the bespoke mounting platform

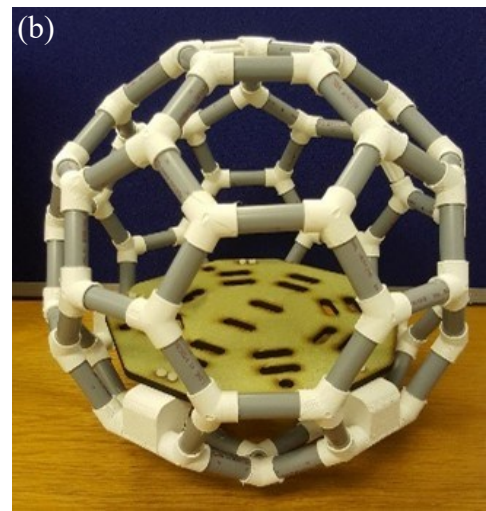
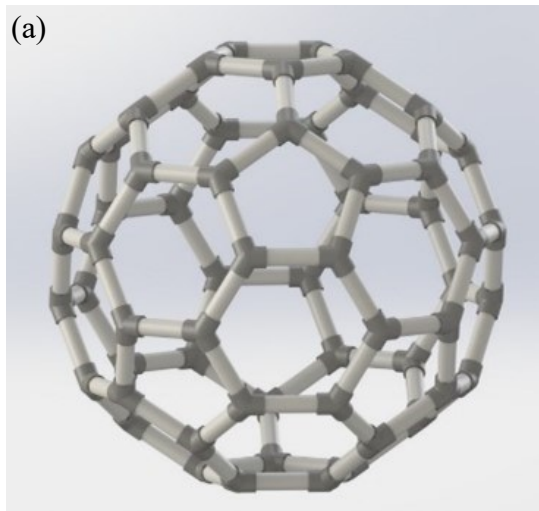


Figure 3-24 – CAD model and built version of the large-scale TOM; (a) design concept and (b) constructed TOM with mounting plate. The TOM is approximately 360 mm in diameter.

3.9. Summary

This chapter described an instrument capable of measuring the rank 2 MPT of metal targets. A coil array was developed using Helmholtz Coil principles to generate a uniform magnetic field over the region of the target, which is necessary for the rank 2 case. System electronics to drive the coil and for signal filtering were designed and built into a 19-inch rack enclosure. The transmit electronics were designed to have a high-power output (640 W) to achieve a high SNR when measuring small targets. To control the experiments and to automatically process the acquired data for MPT calculation, a software was written using Python, which also has a GUI for easy operation. Three TOMs were developed for different types of targets and applications. One of the TOMs were built for measuring rank 3 MPT of cone shaped objects outside of the uniform magnetic field region of the coils. This was for an experiment to prove that higher rank MPTs can be measured experimentally. The performance tests such as field uniformity, measurement noise and experiment repeatability showed good results, which proved the ability of the instrument to accurately measure rank 2 MPTs of the targets. Two journal papers were published about the instrument and the methodology used for acquiring the rank 2 MPTs. A larger coil array with the same coil geometry was also built for measuring the rank 2 MPT of larger objects (e.g., firearms) to extend the scope of the project to security screening applications.

4. Magnetic Polarizability Tensor Case Studies

Using both the smaller and the larger coil arrays described in Chapter 3, a range of objects were characterised over the course of this research, as part of different case studies. The case studies are described in separate sub-sections with subset of the results shown in each section. The complete results data covering all the objects that were characterised are given in Appendix 2. Most of the results shown in this section have been published in peer reviewed journals or have been submitted for publication and currently are under review, see Publications Chapter.

4.1. British Pound and United States Dollar Coins

Experimental and simulated rank 2 MPT of US Coinage were published previously in [63] by Davidson et al. Due to the symmetrical shape of coins, these targets were characterised again using the single-axis TOM in the small coil array. The results were compared with the previously published MPT characterisations to quantify the system's MPT characterisation accuracy using the single axis TOM. In addition, UK Coinage were also characterised using the multi-axis TOM to be included in a dataset described in Section 4.3. A subset of the results are shown in Figure 4-1, where the measured rank 2 MPT characterisations of the coins are compared with previously published experimental and simulated data. Overall, the experimental coin MPTs are in good agreement with the previously published experimental and simulated data, and NRMSE of the differences are given in Table V.

The main sources of error between experimental results and previously published experimental MPTs are from lower SNR and orientation accuracy of the previous system. Minor imperfections, difficulty of accurately modelling the faces and minor material inhomogeneities of the coins are the main reasons of differences between experimental and previously published simulated MPTs. Accurately modelling the coins' faces is difficult and requires a high resolution (which increase simulation complexity), so the coins are assumed to be perfect cylinders with smooth faces. In addition, the FEM simulations assume homogenous distribution of material throughout the coins, which is not the case in practice as the coins are made from alloys. The inability of the FEM process to accurately describe the true physical and electrical nature of coins is more fully described in [63].

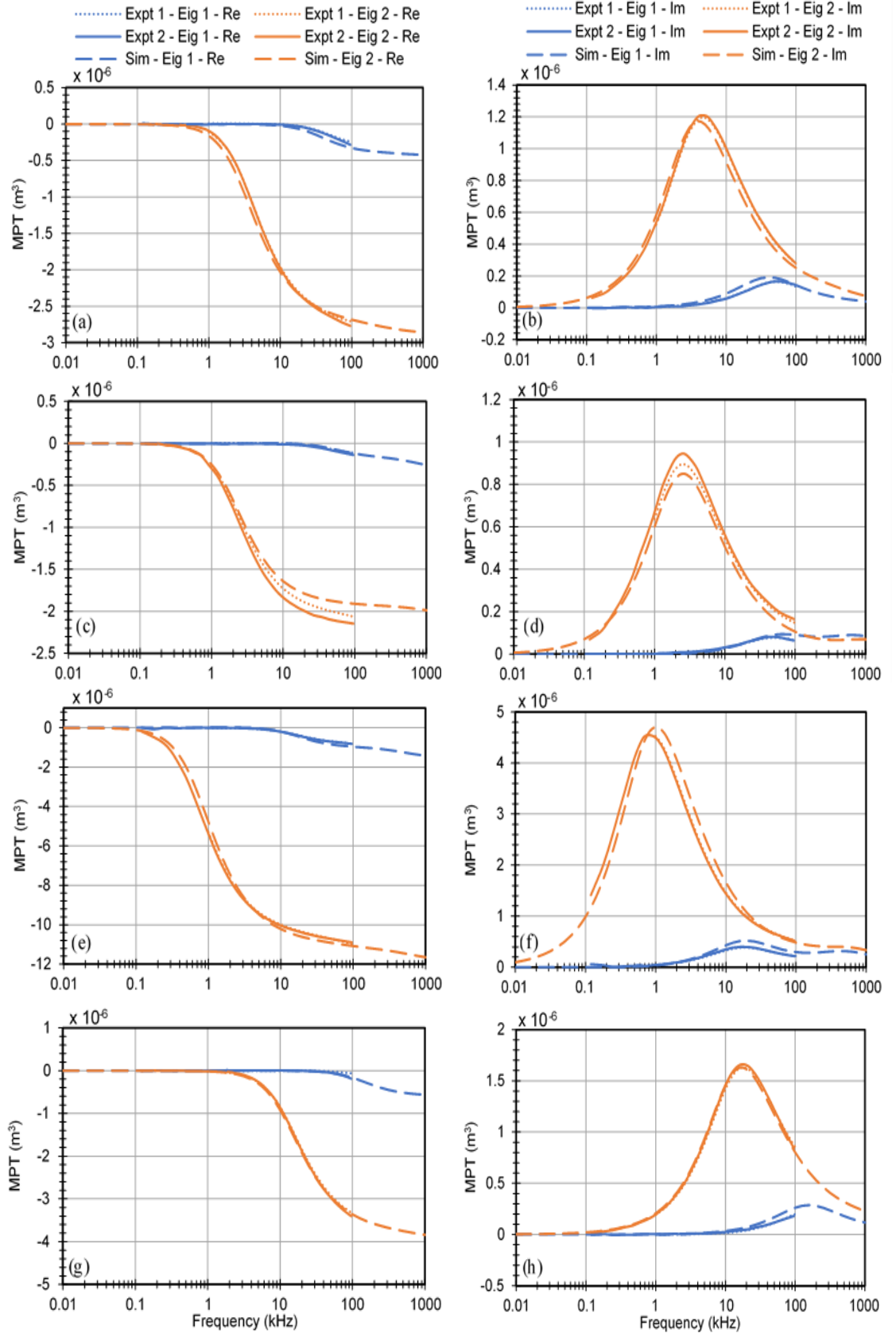


Figure 4-1 – Measured real and imaginary rank 2 MPT eigenvalues for US coinage, compared with simulated and previously published rank 2 MPT results are shown. Plots (a-b) one cent, (c-d) dime, (e-f) half dollar and (g-h) nickel. Expt 1 and Sim are values for experimental and simulated results from [63] while Expt 2 is experimental data from the instrument described in this thesis.

Table V – NRMSE of differences between measured MPT eigenvalues compared to the previously published measured and simulated MPT eigenvalues.




	Experimental Eigenvalues				Simulated Eigenvalues			
	Eigenvalue 1		Eigenvalue 2		Eigenvalue 1		Eigenvalue 2	
	Re	Im	Re	Im	Re	Im	Re	Im
One Cent	0.270	0.052	0.023	0.025	0.516	0.300	0.073	0.091
Nickel	3.290	0.138	0.044	0.025	0.367	0.535	0.046	0.042
Dime	0.618	0.061	0.059	0.066	0.755	0.304	0.146	0.142
Half Dollar	0.072	0.043	0.009	0.021	0.273	0.305	0.042	0.108

4.2. Minimum Metal Anti-Personnel Landmines

A range of AP landmines and AP landmine surrogates were measured using the multi-axis TOM and the small coil array, which was the main purpose of the instrument. The landmines were provided by Fenix Insight Ltd. The AP landmines which were measured are shown in Table VI. Each landmine, real or surrogate, was first measured as a whole, in the fully assembled state. The landmine was then taken apart and each metal component was characterised individually. Similarity of the real and surrogate landmines' MPT characterisations were then compared. Feedback about the similarities and differences of the real and surrogate landmines were provided. The rank 2 MPT characterisations of the landmines and their metal components are shown in Figure 4-2 – Figure 4-5. For all four landmines, the springs were found to be ferrous. This can be understood from the real MPT eigenvalues being above 0 m^3 towards the lower end of the frequency spectrum for the springs. The firing pins were also found to be ferrous except for the PMN. Firing and striker pins of the PMN landmine had the largest response amongst its components, which was the opposite of what was observed for the other three landmines. From these, it can be concluded that the firing and striker pins of the PMN landmine are made up of a different material compared to the other three landmines. Compared to M14 and Type-72 landmines, PMN and VS-50 landmines have 10 to 100 times higher response magnitude. This makes the latter ones more detectable, especially in soil with high magnetic content. Top plate of the VS-50 landmine, which is larger than the other components, mostly dominated the response of the landmine. MPT eigenvalues of normal and rusted firing pins of M14 landmine were also compared to assess the effects of rusting of metal components. The results are shown in Figure 4-6. The motivation of this comparison is that the landmines' components may rust after they have been left under the soil for long

time. It was found that the MPT eigenvalues between normal and rusted firing pins had minimal difference. However, the imaginary MPT eigenvalue 2 had a lower magnitude for the rusted pin towards the higher end of the frequency spectrum, compared to the normal pin. Although the difference is visible at this scale, it is still ten times smaller compared to the imaginary MPT eigenvalue 2 of the whole landmine's MPT characterisation. This means that the difference between normal and rusted pins would be difficult to discriminate in real world conditions, with higher noise and soil effects. Therefore, it can be concluded that rusting of the components of a minimum metal AP landmine may not have a significant impact of the landmines overall MPT characterisation. This reduces the possibility of a false classification of any potential target due to the components' rusting. The work in this section has been further described in the peer reviewed published conference paper entitled "A Study on the Magnetic Polarizability Tensors of Minimum Metal Anti-Personnel Landmines" and given in Publications – Publication 3 of this thesis.

Table VI – Characterised Anti-Personnel Landmines

Name	Image	Metal Components
M14		Detonator, Pin
Type-72		Detonator, Spring, Igniter, Pin
VS50		Detonator, Spring, Pin, Top Plate
PMN		Detonator, 2 Springs, Firing Pin, Lid Strap

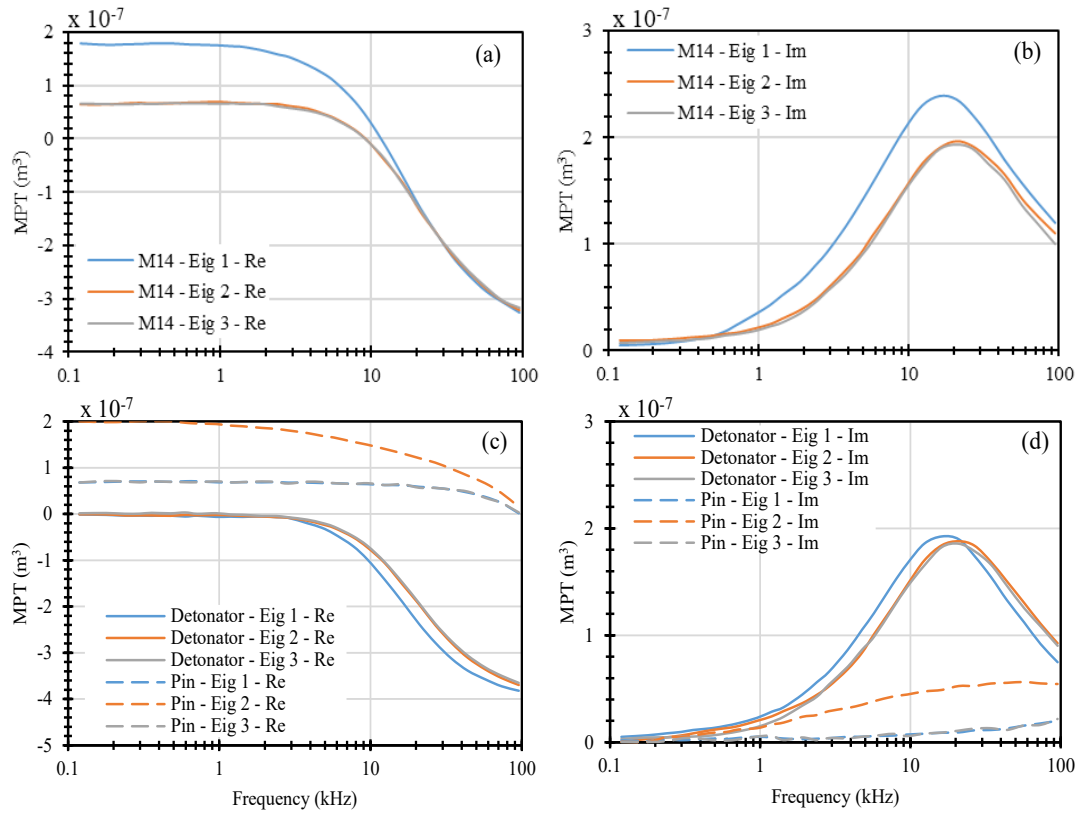


Figure 4-2 – Real and imaginary MPT eigenvalues of M14 anti-personnel landmine and its components. (a-b) are M14 anti-personnel landmine. (c-d) are detonator and pin of M14.

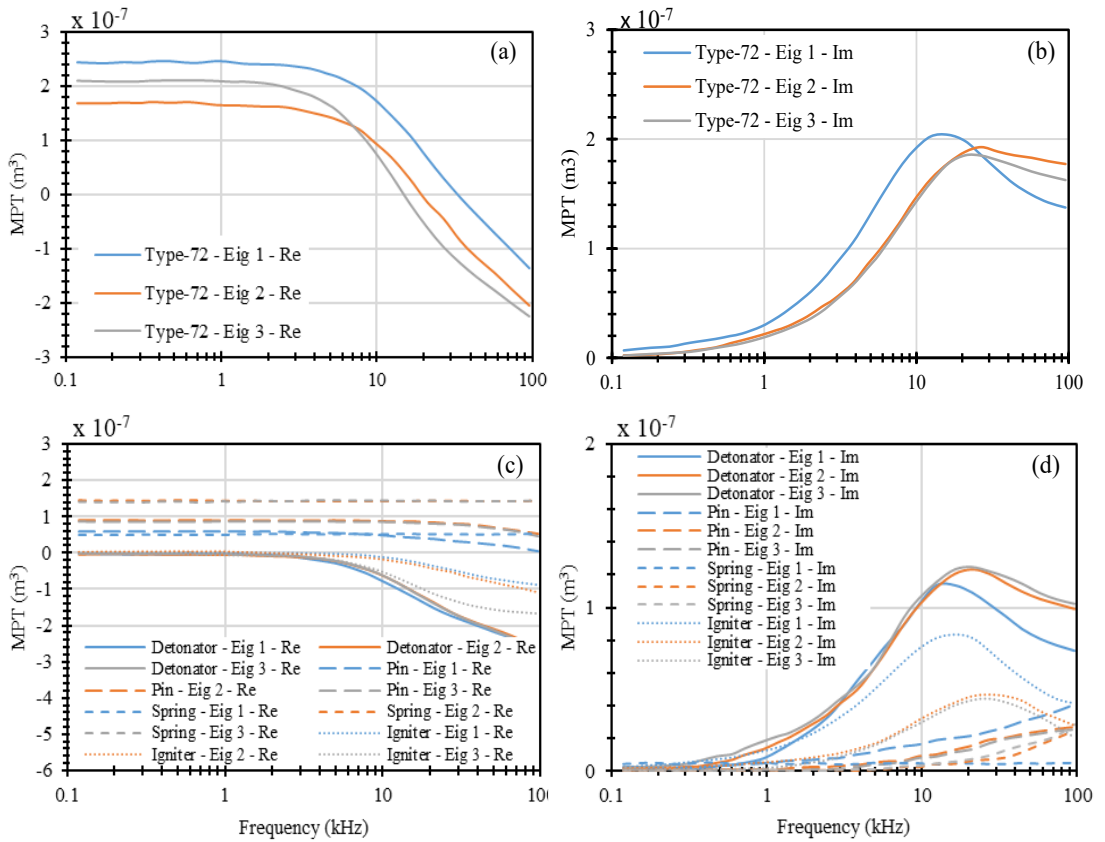


Figure 4-3 – Real and imaginary MPT eigenvalues of Type-72 anti-personnel landmine and its components. (a-b) are Type-72 anti-personnel landmine. (c-d) are detonator, pin, spring, and igniter of Type-72.

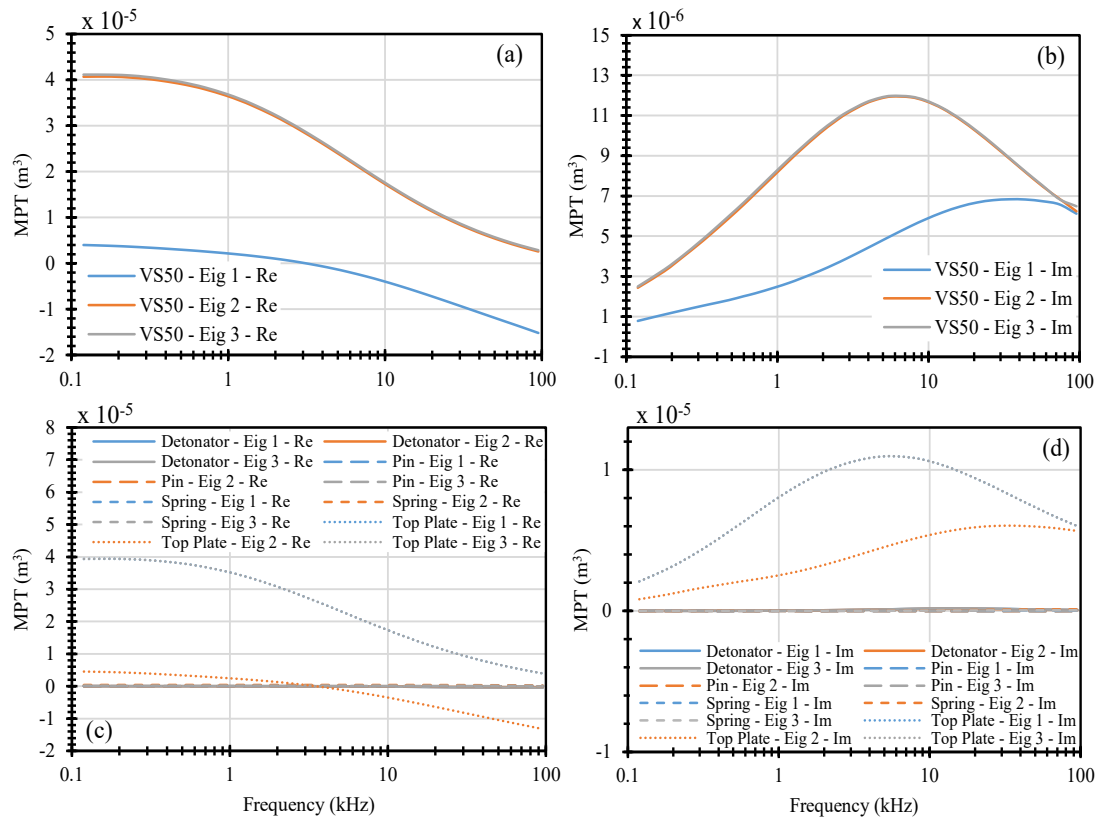


Figure 4-4 – Real and imaginary MPT eigenvalues of VS50 AP landmine and its components. (a-b) are VS50 AP landmine. (c-d) are detonator, pin, spring, and top plate of VS50.

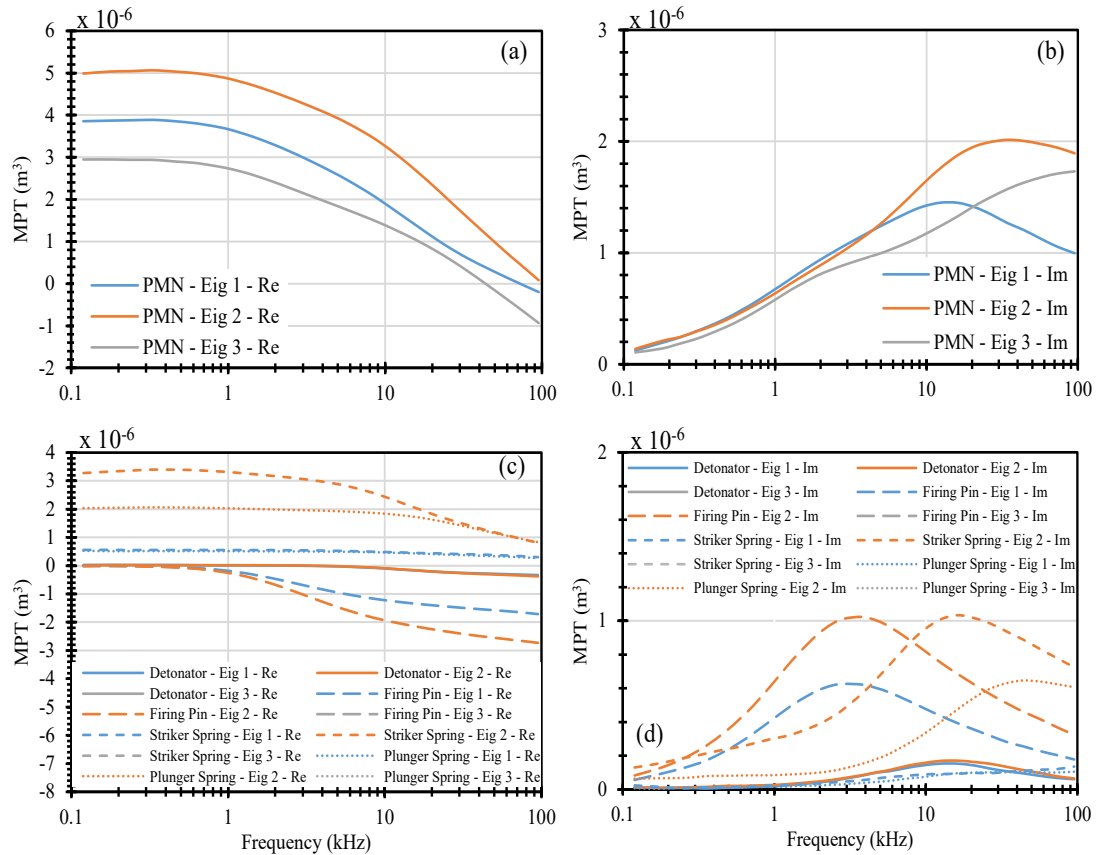


Figure 4-5 – Real and imaginary MPT eigenvalues of PMN anti-personnel landmine and its components. (a-b) are PMN anti-personnel landmine. (c-d) are detonator, pin, striker spring, plunger spring and igniter of PMN.

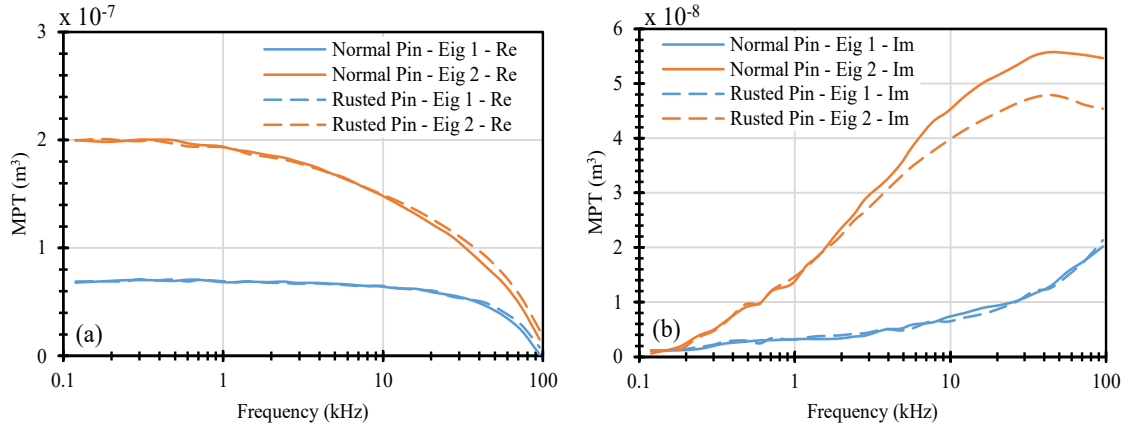


Figure 4-6 – MPT eigenvalues of normal and rusted pins of M14 anti-personnel landmine. (a) is real and (b) is imaginary MPT eigenvalues.

4.3. MPT for Faster and More Reliable Security Screening

Using walk-through metal detectors (WTMD) is currently the main method for screening people for metal threat objects (e.g., concealed guns and knives) at security checkpoints [73], [74]. Although, several new technologies have been proposed for classifying concealed targets in the recent years, WTMDs still cannot discriminate between potential threat and non-threat objects [75]. This means that each person is usually required to remove all metal possessions before going through a WTMD. This results in reduced throughput and long queues especially at big venues such as airports or stadia. If an MPT library of common threat and non-threat objects were to be built, smart classification algorithms could be trained to look for these signatures in the measurement data to better classify the targets and speed up the security screening process. Under the Innovate UK Smart Metal Detector (SMD) project (IUK project ref: 39814), and with collaboration of Rapiscan Systems (www.rapiscansystems.com) and Metrasens (www.metrasens.com), two separate measurement campaigns (lasting approximately 1 week each) were performed at the UK's National Firearms Centre (NFC). During the measurement sessions, around 120 threat objects' rank 2 MPTs were measured by utilising both the small and the large coil arrays described earlier, depending on the target object's size. In addition to the standard firearms, such as pistols and sub-machine guns, several unconventional threat objects were characterised, such as concealed knives. A subset of the measured firearm types are shown in Figure 4-7. The threat object groups are also shown in Table VII, except for the unconventional type objects, which are non-standard and do not form a group. Details of the inert fillings which are used in the deactivated grenades are also unknown and may affect the overall electromagnetic signatures of the

grenades if the fillings are metal based. An MPT comparison between a revolver, a polymer framed pistol and a metal framed pistol is shown in Figure 4-8.



Figure 4-7 – Example tested firearm types; (a) polymer framed self-loading pistol (Glock 43), (b) metal framed handgun (Beretta 92FS), (c) revolver (Smith and Wesson, model 547), (d) Uzi 9 mm SMG, (e) mini revolver (NAA .22), (f) hollow battery casing with 9 mm cartridges inside, (g) Example concealed knives.

Table VII – Summary of tested standard threat objects.

Group / Type	Details / Manufacturers
Glock Group	9m Self Loading Polymer Framed
Miscellaneous 9 mm Pistols	Smith and Wesson, Heckler and Koch, Beretta, Jennings Firearms
Revolver Group	Colt, Webley, Smith and Wesson, 0.38 and 0.45 Calibres
SMG	Uzi, Ingram, Scorpion, Steyr Arms
Pistol Pairs	Same manufacturer (and model); different material finishes Sig Sauer, Smith and Wesson, Sigma, Ruger
Mini Pistol Group	A set of mini pistols, mostly manufactured in mid 1900s
Grenades	Drill type with inert filling e.g., Arges Type HG84, ‘Mills’ British No. 5

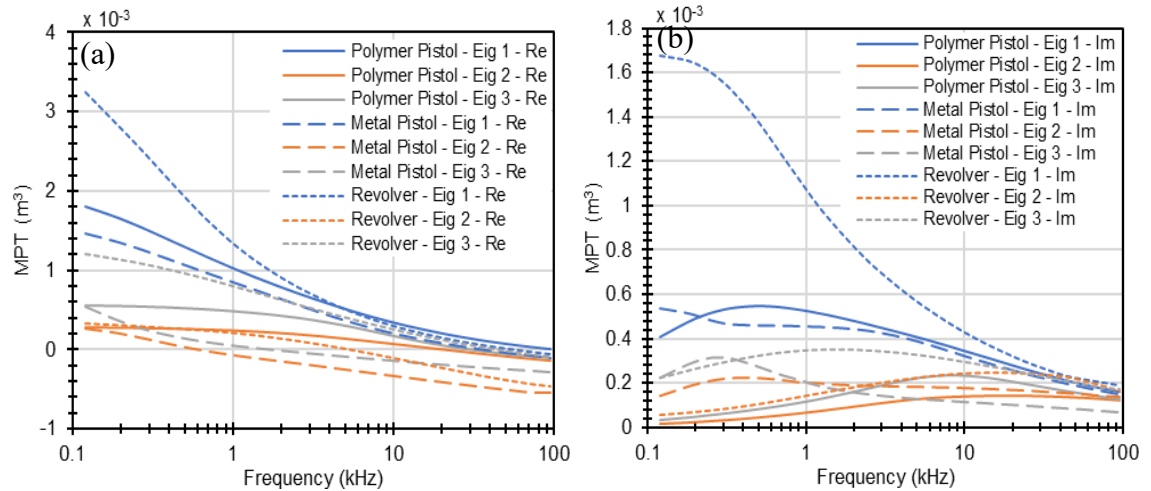


Figure 4-8 – Real (a) and imaginary (b) eigenvalue MPT data for example tested objects; polymer (Glock 17) and metal framed pistols (Sig Sauer 9mm P225) and revolver (Colt 0.455).

From the MPT comparison plot, it is apparent that the electromagnetic signatures of different types of pistols are dissimilar. The most significant difference is the imaginary eigenvalue 1 of the revolver, which has a very large magnitude at the loss-peak, compared to the other pistols. This is consistent with the properties of the revolver, as it has the highest amount of metal amongst the pistol types involved. However, the shapes of the curves (e.g., position and magnitude of the resonant peaks) are also different between all three pistols, which is very important for target classification purposes. All three pistols had three different MPT eigenvalue plots, which was consistent with their asymmetrical shapes. MPT eigenvalue 1 for all pistols were the largest one, which corresponds to the axial direction along the barrel of the pistols.

Non-Threat Objects

To assess their differences to the threat objects, and to form datasets for classification tests, a set of non-threat objects were also characterised in the University of Manchester laboratories. Some examples are coins, belt buckles, keys, mobile phones, vapes and headphones. A total of 90 non-threat objects were characterised which meant 210 object MPT eigenvalues were collected using the instrument for dataset creation. A subset of the non-threat objects are shown in Figure 4-9. An MPT comparison between a key and a one-pound coin, as well as a polymer pistol and a key is also shown in Figure 4-10. The one-pound coin in Figure 4-10(a-b) has two unique MPT eigenvalues instead of three compared to the key, caused by the symmetrical shape. When compared to a polymer framed pistol in Figure 4-10(c-d), the key has three orders of magnitude smaller response

size compared to the polymer framed pistol, which is the type of pistol with less metal, hence smaller response. Therefore, the magnitude difference would possibly be higher when compared with a metal framed pistol.

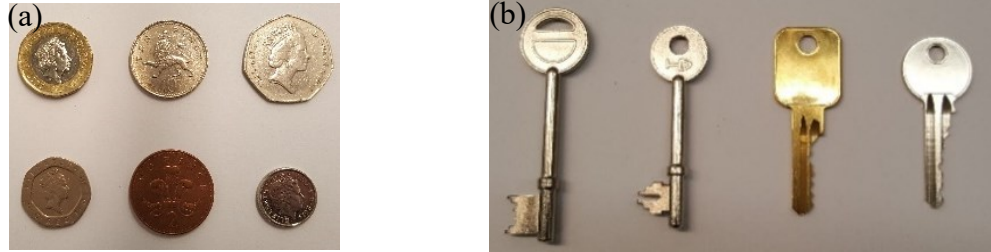


Figure 4-9 – Example non-threat test objects; (a) subset of circulated British coins (circa 2015) and (b) typical UK mortice and domestic door keys.

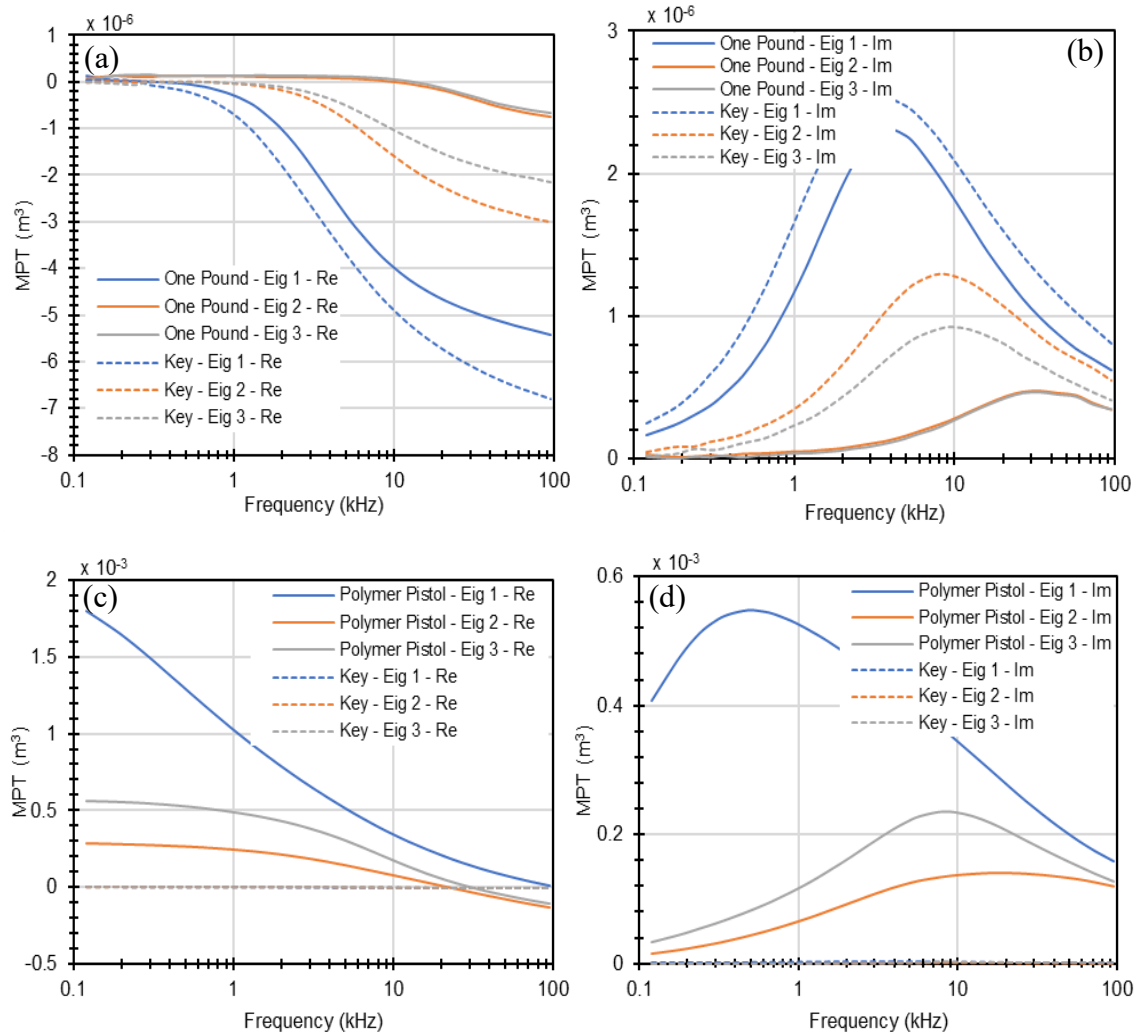


Figure 4-10 – Real (LHS) and imaginary (RHS) eigenvalue MPT data for example tested objects; (a)-(b) one pound coin and domestic key, (c)-(d) polymer pistol and domestic key.

Datasets

Two datasets were generated using the threat and non-threat object data described in sections above. The datasets were specifically generated to be used with unsupervised clustering algorithms, a form of unsupervised machine learning. Therefore, the types of objects and the potential groups they would form were considered when choosing the objects. One of the datasets involved a subset of the characterised firearms, which were expected to form clusters. The other dataset involved most of the firearms in the first dataset, except for the mini pistols and the grenades. Mini pistols were taken out as they are non-standard and formed a very small group, the grenades were removed as there is not enough information about the inert filling material, meaning they may not represent the real live grenades' signatures. The dataset also involved groups of non-threat objects (coins, keys, belts). Both datasets and the object groups are shown in Table VIII.

Table VIII – Object types involved in the datasets generated. Numbers in each cell under the dataset columns indicate the number of specific objects in that sub-group of the dataset.

	Dataset 1	Dataset 2
Metal Frame Pistol	11	11
Polymer Frame Pistol	18	18
Revolver	7	7
Mini Pistol	2	-
Sub-Machine Gun (SMG)	4	4
Grenade	4	-
Key	-	12
Coin	-	13
Belt	-	11
Total Number of Objects	46	76

From three complex MPT eigenvalues and 28 frequency points, 168 data points/features were recorded per object. Using the MPT eigenvalues, MPT invariants were calculated as per [24] and [66], which results in the same amount of data points but removes any possible error arising from arbitrary allocation of eigenvalues. Principal Component Analysis (PCA) was applied to each object's data to reduce the number of features per each object from 168 to 2. The dimensionality reduced data was found to still hold 95% of the information of the original 168 feature data. The data of each object was also normalised so that the minimum and the maximum values were between 0 and 1. This

removed the possibility of any classification bias caused by the response size of the object, such as a pistol versus a coin. A decision bias caused by the response size (which is a feature of an object) is desirable in a commercial, deployed system as a large magnitude signal is not expected from most of the non-threat objects (e.g., coins, mobile phones). However, for this case, it would not be feasible to plot the results without normalising the data as most of the small objects would appear as a single dot on the screen compared to the larger objects, which would make it impossible to evaluate the clusters in the data. This way, the objects are scattered across the two-dimensional plots showing the clusters in the data, decided by only looking at the shapes of the MPT eigenvalue curves and not the magnitudes. This means that the objects' shapes and materials are the deciding factor for the clusters. For evaluating the impact of dimensionality reduction of the data on the clustering performance, both datasets were used in their original form with 168 features, and also as processed form with 2 features per object. After applying the clustering algorithms, the datasets with 168 features/dimensions were also reduced to 2 dimensions by applying PCA to be presented on to dimensional plots.

Clustering Results

K-Means Clustering, Spectral Clustering and Agglomerative Clustering algorithms were used to evaluate the clustering in the datasets. The number of clusters for the clustering algorithms were set to 5, which was found to give the best performance for these datasets after initial tests. Other clustering algorithms (e.g., Meanshift Clustering and DBSCAN) were also tested on the datasets but found to give limited performance. Therefore, the afore mentioned three clustering algorithms were used for the actual performance evaluation and optimisation.

Clustering results for the datasets with original 168 features per target object are shown in Figure 4-11 and results for the dimensionality reduced datasets with 2 features per target object are shown in Figure 4-12. As K-Means Clustering uses decision boundaries to cluster data, the decision boundaries were plotted together with the results in Figure 4-12 for the datasets with 2 features per target object. However, it was not possible to draw the boundaries in Figure 4-11 for the datasets with 168 features per target object as the decision boundaries are not two-dimensional lines.

For dataset 1 in Figure 4-11, most firearm types were correctly grouped in separate clusters by all three algorithms. All revolvers and metal pistols were correctly in single

clusters for their own. However, two metal pistols were classified together with polymer pistols, and another one metal pistol together with a mixed firearm cluster of SMGs and Grenades. These metal pistols were converted ‘blank’ firing pistols, where the original ‘blank’ firing pistols were modified to fire real bullets. Because of that, these pistols possibly had different metal parts made from various materials, which made them appear more like other firearms rather than a metal pistol. All polymer framed pistols were also grouped into their own cluster, except for the Spectral Clustering algorithm, where the polymer framed pistols were divided into two separate clusters and one of them was in revolvers cluster. The grenades and the SMGs did not form a strong cluster together and were either clustered together with the polymer framed pistols or together in their own cluster. However, they would probably be clustered correctly if the datasets were not normalised, given the higher amount of metal in both types.

Most threat and non-threat objects in dataset 2 were grouped into separate clusters by all clustering algorithms. Most of the threat objects are positioned towards the left-hand side (LHS), while the non-threat ones are on the right-hand side (RHS) of the two-dimensional plots. Although, the separation between different firearm types was not as obvious as the dataset 1, the threat objects were grouped closely together, and the metal pistols were clearly separated into a different cluster for all three clustering algorithms. The reason for having different firearm types in one cluster in this dataset is possibly caused by having non-threat objects with very different characteristics to the firearms (e.g., they have less ferrous steel and more non-ferrous alloys), which makes different types of firearms appear very similar to each other compared to a coin or a key.

In some cases, some ferrous non-threat objects were clustered together with the threat objects, meaning some false positive classification. For example, in Figure 4-11(f), two ferrous coins were clustered together with the threat objects, and in Figure 4-11(g), two belts and a coin were again clustered with the threat objects. However, no threat object in any case was clustered together with the non-threat objects. This means that the clustering algorithms did not produce any false negative classification. The false classification of some non-threat objects as threat objects would possibly not happen if the data was not normalised, as a firearm would generally have a much larger response compared to a non-threat object (e.g., a coin or a belt). However, the normalisation was necessary for this specific application for the purpose of clearly presenting the results, as described previously.

The performance of the clustering algorithms, when applied to data with 2 features, were still considerably good but slightly worse than when they were applied to data with 168 features. This was an expected result given that 5% of the information was lost when the dimensionality was reduced by applying PCA. For example, in Figure 4-12(d), one of the grenades was incorrectly clustered together with the metal pistols, which was correctly clustered in Figure 4-11(d), when the dataset with 168 features per target object was used. In addition, the metal pistols were clustered together with the other firearm types in Figure 4-12(h), where they were clustered in their own cluster in Figure 4-11(h), when the dataset with 168 features per target object was used.

The performance of the clustering algorithms in this application was limited and had some errors, caused by the normalisation of the data and the small size of the datasets. However, the purpose of this application was to prove that different types of threat and non-threat objects could be clustered separately with the application of Unsupervised ML algorithms. For a commercial system, or to test the real-life performance of object classification using MPT, a Supervised ML algorithm trained with a large, non-normalised dataset would possibly be used. The Supervised ML algorithm would also be able to classify different types of threat and non-threat objects. However, it would still perform better at classifying an object as threat or non-threat compared to classifying the individual type of the objects. This work is the subject of a recently accepted peer review journal paper provided in Publications – Publication 5.

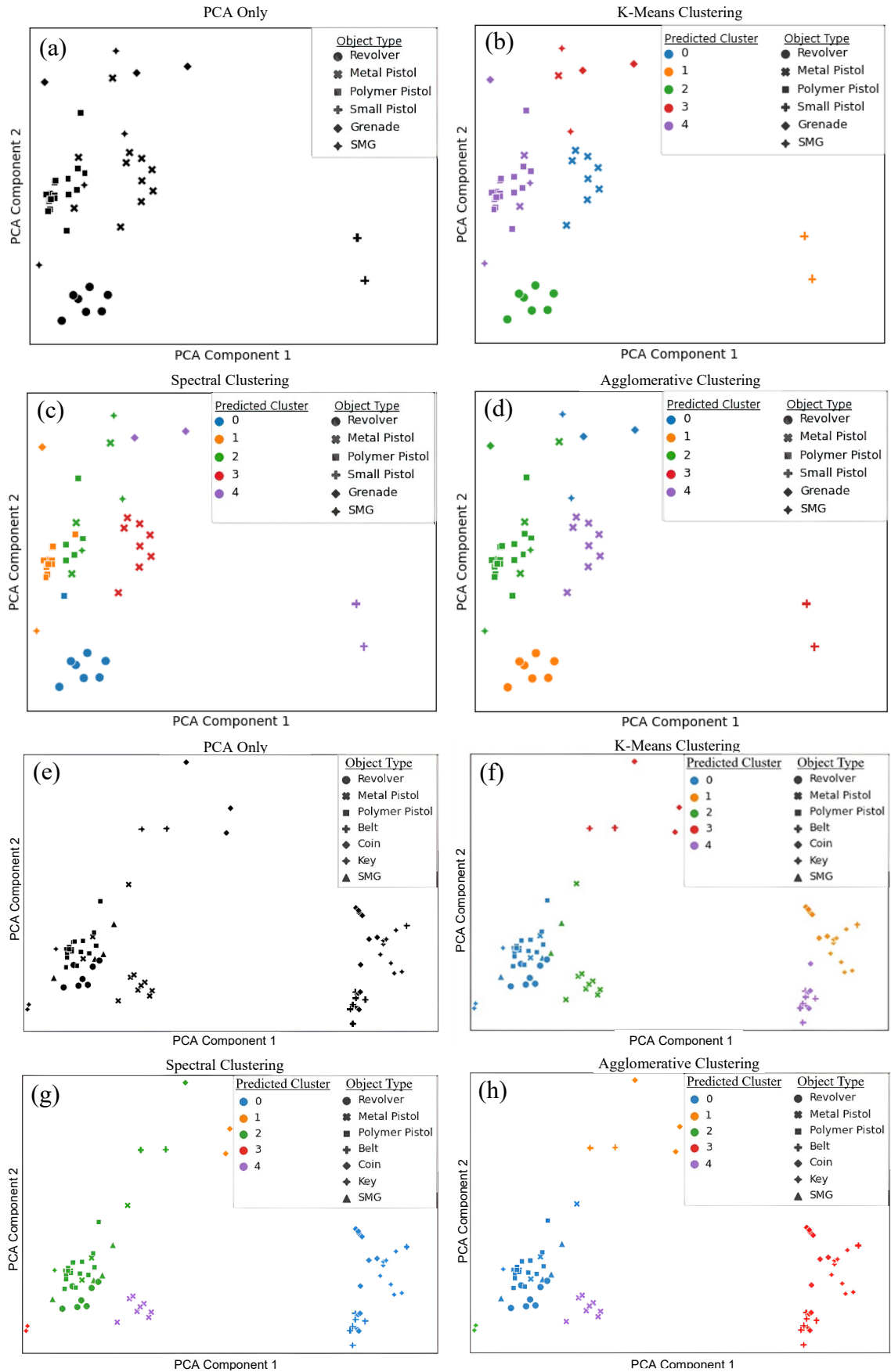


Figure 4-11 – PCA visualization and three different clustering algorithms applied to the datasets with 168 features per object; (a-d) is dataset 1 and (e-h) is dataset 2.

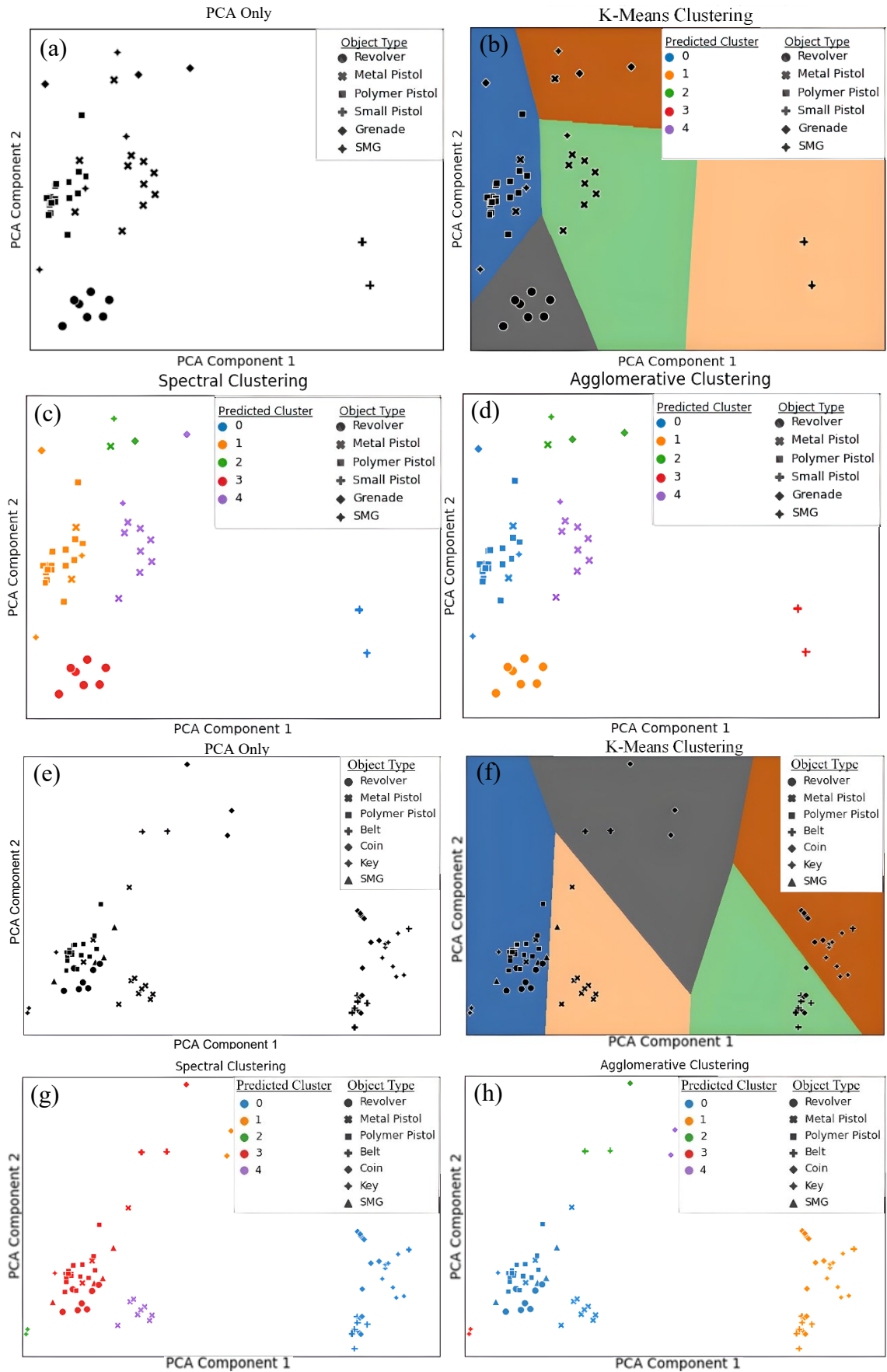


Figure 4-12 – PCA visualization and three different clustering algorithms applied to the datasets with 2 features per object; (a-d) is dataset 1 and (e-h) is dataset 2.

4.4. Measuring the Generalised MPT of Cone Shaped Targets

A case study was done using the instrument described in the previous chapter to measure the higher rank MPTs of metal targets. For this, a non-uniform magnetic field with a known strength is required. Although the instrument was designed to generate a uniform magnetic field at a specific region and the measurements to be done in that region, it is still possible to do measurements outside of this region for measuring higher rank MPT. Three cone shaped objects with three different materials (copper, brass, and stainless steel) were chosen to be used as the targets. A bespoke TOM was built for holding and rotating these cone shaped targets outside of the uniform magnetic field region, described in Section 3.4. These targets were first rotated outside of the uniform magnetic field region at several chosen positions. The rank 2 MPT of these targets were then measured by placing them in the uniform magnetic field region. Rank 3 MPT of the objects were then obtained by subtracting the rank 2 response from the response acquired from the non-uniform region. Figure 4-13 shows a subset of the results from this case study. The results indicate a close match between experimental and simulated rank 2 and rank 3 MPTs of the stainless-steel cone. Small differences between experimental and simulated data are due to the challenge of accurately modelling material properties of the stainless-steel. In Figure 4-13(c), the noise in experimental data is caused by the low SNR outside of the uniform magnetic field of the coil array, which was not optimised for this experiment. However, the general trend and the average magnitude of the responses are still very similar to the simulated data. This proved that, for the first time, the higher rank MPT (GMPT) of a metal object can be measured in practice. The work done for measuring GMPT of cone shaped objects has been further described in the peer reviewed published journal paper entitled "Measurement of GMPT Coefficients for Improved Object Characterisation in Metal Detection" and given in Publications – Publication 4 of this thesis.

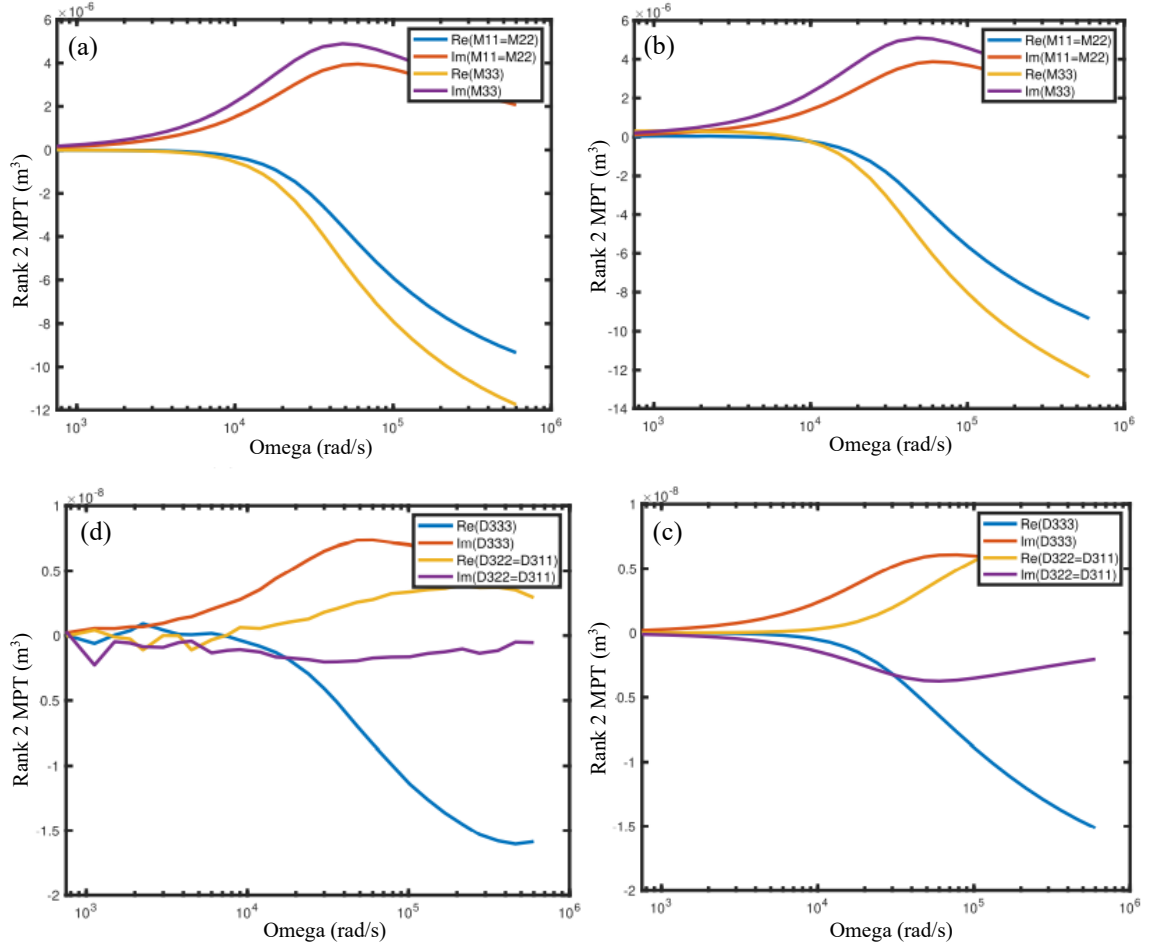


Figure 4-13 – Rank 2 and rank 3 MPT of the steel cone. (a)-(b) are the measured and simulated rank 2 MPT of the cone, respectively. (c)-(d) are the measured and simulated rank 3 MPT of the cone.

4.5. Summary

This chapter presented the results obtained from four case studies done using the instrument described in Chapter 3. Initially, rank 2 MPT of a set of British Pound and United States Dollar coins were measured and compared with previously published measured and simulated data. This proved the instrument's ability to accurately measure and replicate the rank 2 MPT of metal objects. The rank 2 MPT of four AP landmines and their metal components were later measured, for the first time. The study also identified which metal components of the landmines contributed to the magnetic response observed on the overall response of the landmines. Another study utilised both the small and the large coil arrays to collect rank 2 MPT data of a set of threat (e.g., firearms, knives) and non-threat (keys, belts and coins) objects. Clustering in the data was then evaluated by the use of unsupervised machine learning algorithms. The study concluded that rank 2 MPT of threat and non-threat objects could be clustered into separate groups.

Utilising this information to develop the next generation of walk-through metal detectors has the potential to speed up the security screening process in large venues in the future. Finally, rank 3 MPT of three cone shaped target objects were measured by placing them outside of the uniform magnetic field region of the coil array. This proved that higher order MPT of metal objects can, for the first time, be measured in practice. The knowledge gained from the higher rank MPT study can be applied for designing the next generation landmine detectors. A landmine detector capable of measuring the rank 2 MPT of target objects could utilise an MPT library of landmines and clutter for better classification. However, magnetic fields generated by metal detectors used in landmine detection are not uniform. This results in more contribution from the higher rank MPT of the target objects to the overall electromagnetic signature, which can decrease the accuracy of the target classification. A landmine detector with a known magnetic field could measure its position relative to the detected target to measure the higher rank MPT of that target, which can improve the target classification performance even further. To generate a higher rank MPT library of target objects, a robust methodology needs to be developed. This includes designing and building a coil array with known, non-uniform magnetic field, a TOM which can rotate the objects' in this non-uniform magnetic field, and a post-processing software which can automatically retrieve the higher rank MPT of the target objects.

5. Ground Penetrating Radar

This chapter describes the basic principles of Ground Penetrating Radar (GPR), discusses previous relevant work found via a comprehensive literature review, and presents the work undertaken involved in generating ML training datasets using simulation models of realistic GPR scenarios.

Section 5.1 briefly introduces GPR and its potential uses and limitations. Section 5.2 then describes the working principle of a typical GPR system. Previously published work on generating simulated or real GPR datasets and the application of ML classifiers are then discussed in Section 5.3. Section 5.4 describes the methodology for generating realistic simulation models involving landmines and clutter, which was done as part of this research. Finally, Section 5.5 provides a summary of the chapter with potential areas for future research.

5.1. Introduction

GPR is a non-destructive geophysical method which uses electromagnetic waves to investigate the subsurface. It can be used to extract features from the subsurface and ultimately can create an image to analyse or detect objects. In the context of landmine detection, GPR is an alternative methodology which operates at a higher frequency spectrum. This opens up the potential to characterise different components of the target landmines and clutter. Using the two methodologies at the same time can improve the classification performance and confidence. The GPR can detect dielectric discontinuities under the ground, which happens at the boundary of materials with different dielectric properties. This means that GPR can detect matter volumes of objects in the ground, for example, a landmine. However, rocks, water concentrations, air cavities such as burrows and other materials also cause dielectric discontinuities. Therefore, GPR, similar to metal detection, is also prone to clutter in the soil which causes FAR [76] - [81].

Similar to using smart classification algorithms (e.g., ANN) that utilise the MPT of target objects for metal detection, a large dataset of GPR signatures of landmines and clutter objects can be generated for training ML algorithms. However, collecting a large amount of real data is difficult as access to real landmines is limited. An alternative is to augment the real dataset with simulated data to achieve the dataset size required. However, it is important for the simulation models to represent real scenarios to achieve high

classification accuracy on real scenarios. If this is achieved, and in the context of dual mode landmine detection (MD and GPR), a lower false alarm rate from MD by utilising MPT and a lower false alarm rate from GPR by utilising ML algorithms could help achieve a very low overall false alarm rate for a dual mode landmine detector. This chapter describes an attempt to generate GPR simulation models which represent real life scenarios with the aim of training a ML classifier to improve target classification and reduce FAR, using a commercial Finite-Difference Time-Domain (FDTD) method simulation package called gprMax [82]. However, it is important to note that although, simulations are valuable for augmenting real datasets, they are not enough by themselves to train an ML classifier which would perform well on real data. This is because it is very difficult to generate complex simulation models that represent the amount of random noise generated in real life scenarios (e.g., by electronics, sensor head movement and clutter), as well as the amount of inhomogeneity in the soil. Some research work was also done on visualisation of the simulation models and the results generated, as it is important for understanding and optimising the results. The GPR scans were plotted using a custom Python script, while the simulation models were exported from the simulation software and visualised in ParaView [83], [84]. It is also important to note that to achieve a dual mode landmine detector with reduced FAR, the classification algorithms for both MD and GPR should be combined together with a higher-level decision algorithm. However, this is out of the scope of this research.

5.2. Principles of GPR

A GPR sends electromagnetic waves towards the ground with a frequency that can range between 1 MHz and 10 GHz. However, frequencies used in most applications are between 10 MHz and 3 GHz [76], [78]. When these waves encounter a boundary between two media with different dielectric constants or conductivities, they refract, reflect, diffract or scatter [85]. Examples to this can be the boundary between air and ground or between soil and rock. After emitting the source electromagnetic waves, GPR then listens to the waves which are scattered back, and the sensed waves are then recorded as time series data [76]. An example of a such time series recorded at a stationary position is shown in Figure 5-1, which is called an A-Scan. The A-scan shows the main components in the received signal, which are convolved together at the receiver.

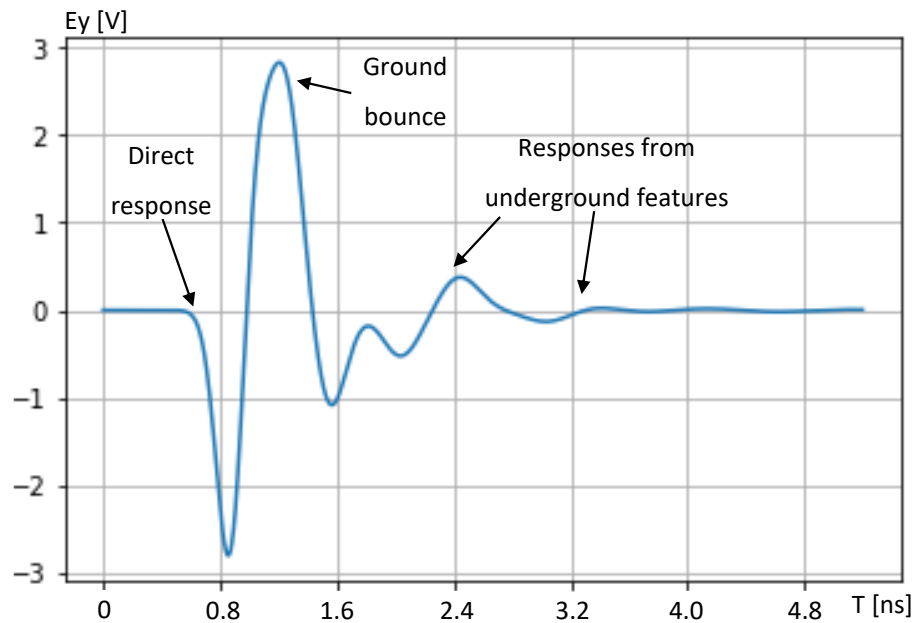


Figure 5-1 – An A-Scan recorded for around 5 nanoseconds, where the direct interaction between transmit and receive antennas, the wave bounce back from the air/ground boundary and the responses from the dielectric discontinuities in the soil are shown.

Figure 5-2 shows a B-Scan, which is made up of a series of A-Scans recorded over a certain distance. Recording a B-Scan allows more information to be captured about a target in the soil by revealing more features of the object from different positions. The horizontal lines between 1 and 2 nanoseconds in Figure 5-2 represent the direct response and the ground bounce whereas the parabolic shape below the horizontal lines are the waves reflected from the target object. When the sensor head is away from the object's position, the reflected waves take longer to come back and are also weaker. The reflected waves become stronger and take a shorter time to come back as the sensor head gets closer to the target object. This results in a parabolic shape on the B-Scan plot when there is a single target object in the ground.

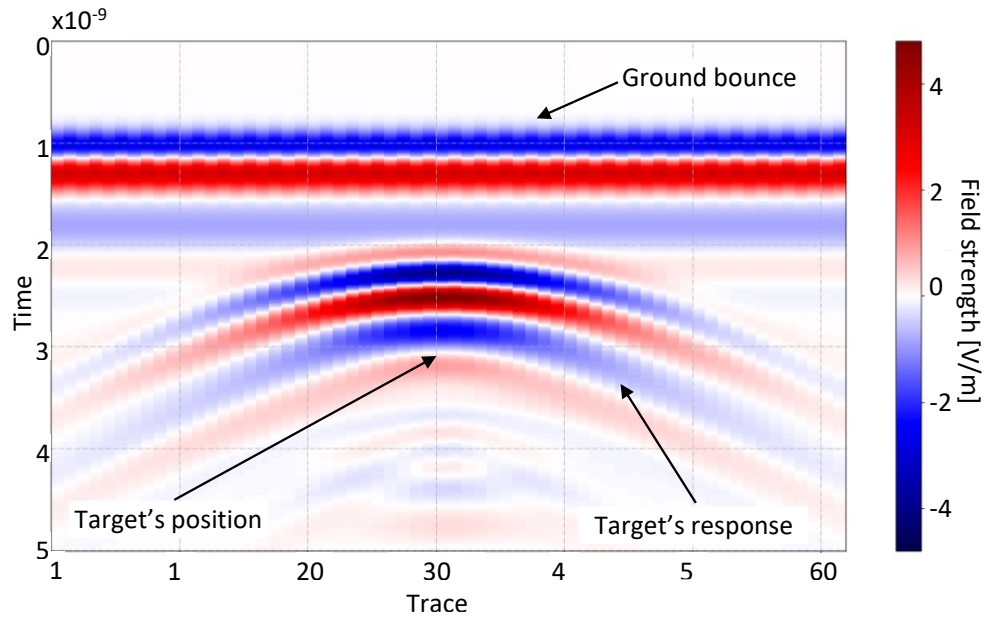


Figure 5-2 – A B-Scan made up of 62 A-Scans recorded on a straight line with 4 mm steps.

As the dielectric losses and conductivity of the soil increases, the penetration depth of the GPR decreases. This is because the ground absorbs more energy from the electromagnetic waves. In addition, the penetration range of GPR decreases as the centre frequency of the emitted waves increases. However, higher bandwidth increases the resolution and the features that can be extracted from the subsurface. Therefore, finding the optimal frequency range which gives the required penetration and resolution for a specific application is crucial [76], [86].

Although, GPR can use time or frequency domain techniques, the most common method is the time domain where series of electromagnetic pulses are radiated from the antennas. The amplitude of the radiated waves can range from 200 mV to 200 V and the pulse length from 0.2 to 50 nanoseconds. The pulse shape is generally similar to a differentiated Gaussian function where the centre frequency can be set depending on the application. A pulse with bandwidth of at least 25 percent of the centre frequency is called and Ultra-Wideband Radar (UWB). UWB radars have less range as their power spectrum is low. However, the pulses are spread across a large frequency spectrum, yielding higher resolution and making them suitable for applications which require low penetration depth but high resolution [87], [88]. The frequency domain technique varies the frequency of the waves while keeping the amplitude constant. This can be done by either stepping the wave frequency over time or stepping a carrier frequency of a continuous wave [89], [90].

5.3. Previous Work

This section provides an overview of previous work that has been published on generating GPR models of realistic scenarios in the context of humanitarian demining and application of ML classifiers to real and simulated datasets made of such models, which are relevant to the research in this thesis.

One relevant study to this research is [78] where simulated datasets of landmines and metal clutter were created using gprMax. These datasets were then used to train Deep Neural Networks (DNN) to discriminate between the targets. The simulations included landmine models buried in realistic soil models along with an uppermost rough surface or undulating. The DNN trained with the simulation data achieved a 98% detection rate with 10% FAR. The work on the simulation and the modelling used in their research and further work undertaken by the authors on the subject were also published in [91]-[96].

A real dataset consisting of GPR B-Scans were augmented using B-Scans obtained from gprMax simulations to train a Convolutional Neural Network (CNN) in [97]. A detection rate of 90% was achieved with 30% FAR. The downside of the used methodology is that any detected object is considered to be a landmine, with the assumption of most of the objects in a minefield are landmines. However, this can result in a much higher FAR when the trained classifier is used in the actual minefield with a lot of clutter in the soil.

The Finite-Difference Time-Domain (FDTD) method was used, similar to gprMax, to generate a synthetic GPR dataset with landmines in [98]. The dataset was post-processed using a Nonuniform Fast Fourier Transform (NUFFT) algorithm. The dataset was then fed to normalized energy and least-mean-square-based anomaly detectors for landmine detection. Using this methodology, the study was able to achieve around 90% detection rate was achieved with less than 20% FAR.

Wilson et al. used a dataset to test four different discrimination algorithms and evaluate their performance [99]. The dataset involved B-Scans collected by a NIITEK vehicle-mounted GPR array. The data was collected over 41,807 m² of ground and included 1,593 landmines. Before inputting the dataset to discrimination algorithms, a pre-screener was applied to the dataset to extract points of interest from the large amount of data. Approximately 90% probability of detection with 0.00054 false alarms per meter square was achieved by the discrimination algorithms.

A pre-processing algorithm called Drop-Off Minibatch Online Dictionary Learning (DOMINODL) was proposed for obtaining sparse representations of GPR data for speeding up Neural Network (NN) and improving classification performance [100]. A 98% correct classification of PMN and PMA-2 AP landmines were achieved using a dataset involving the landmines.

Data from GPR, MD and an Infrared (IR) camera were fused together using a two-level belief function in [101]. Target objects were classified into three categories using the MD data in the first level, which were low, high and no metal content object. In the second level, data from all sensors were utilised to classify the objects as threat or non-threat. The methodology was tested on a small dataset consisting of 28 threat and non-threat objects. It was concluded that the use of a two-level belief function increased the classification performance compared to using just MD with no classification algorithm. However, the size of the dataset was not sufficient to calculate the actual amount of performance increase between the methods.

An Electromagnetic Induction (EMI) sensor and a GPR were used to collect real data from two landmine detection test lanes in [102]. Classification performance of a number of machine learning algorithms such as Logistic Regression (LR), Random Forest (RF) and SVM were tested on the dataset. A probability of detection of 95%, with 0.0025 false alarms per meter square was achieved with RF. However, 100% probability of detection with 0.05 false alarms per meter square, was achieved using LR in conjunction with application of a feature extraction algorithm as a pre-processing method.

A test lane consisting of 26 AP landmines and 6 clutter was scanned in [103] using a multi sensor detector utilising MD, GPR and IR sensors. Performance of four data fusion algorithms were tested on the dataset for target classification. The data fusion algorithms used were Bayesian Reasoning, Dempster-Shafer, Fuzzy Probabilities and manually implemented rules. A 90% probability of detection at 4 false alarms per meter square was achieved using the manually implemented rules. The next best performing algorithm was the Fuzzy Probabilities algorithm.

A real GPR dataset consisting of 1771 threat alarms and 640 nonthreat alarms were used to test the performance of SVM and RF classifiers when a custom pre-processing algorithm called PatchSelect was used [104]. A 98% probability of detection at 0.003 false alarms per meter square was achieved using the PatchSelect pre-processing

algorithm together with the SVM classifier. Similarly, a real GPR dataset of buried landmine surrogates was built in a lab arrangement in [105]. The data was then used to train a Support Vector Machine (SVM) and a DNN. It was concluded that the DNN performed 10% better at target classification compared to the SVM. A detection rate of 90% was achieved with 25% FAR using the DNN.

A CNN was trained with a simulated GPR dataset consisting of 50,000 B-Scans of threat and non-threat targets in [106]. The trained CNN was then tested on a real dataset consisting of 9 threat and non-threat target objects. A 95% probability of detection at a 0.2 false alarms per meter square was achieved. Similarly, a real GPR dataset involving 11,952 landmines and 24,045 clutter was used to train a CNN classifier in [107]. Performance of the CNN was then evaluated using a test dataset involving 2,900 landmines and 3,954 clutter. The results show a 90% probability of detection with 0.2 false alarms per meter square. Another real GPR dataset consisting of B-Scans which do not involve landmines was used to train a CNN based Autoencoder in [108]. The Autoencoder was setup as an anomaly detection algorithm, which was trained using the GPR dataset without landmines. The Autoencoder was then tested using two datasets consisting of 17 landmines buried in a test lane, as anomalies. A 98% probability of detection with 0.2 false alarms per meter square or a 90% probability of detection with no false alarms were achieved.

The above shows that there is sufficient amount of research suggesting that the use of ML classifiers for landmine detection is a promising strategy. However, datasets used in virtually all the published literature are either small or existing datasets taken from a third party, which involve unknown parameters. This may cause data overfitting and result in the tested classifiers to achieve better than they would in real life situations across different soil types and scenarios. It is also important to note that most publications used real datasets for training and testing ML classifiers, rather than simulated data. This suggests that there is a general understanding in the literature that ML classifiers trained with simulated data may not perform well when introduced with real data. Therefore, the methodology used to generate simulated GPR datasets in the research presented in this thesis can be used to augment real datasets to build large datasets involving both simulated and real data. This can then help overcome the disadvantages of large, simulated datasets or small real datasets for training ML classifiers.

5.4. Simulation Models

By generating realistic models of AP landmines, clutter, and soil using gprMax, a simulated dataset was generated for training ML algorithms for classification. This was achieved by iteratively adding more complex features to an initial simple reference model (e.g., soil with homogenous materials and no clutter). The dataset was then conditioned by applying post processing of the data for better ML training results.

Landmine Models

Three AP landmines (PMA-1, PMA-2 and PMA-3) were modelled in gprMax. The landmines were chosen according to the availability of information about the internal components as well as their widespread use in the field [109]-[111]. A 1 mm resolution was used all landmine models.

The PMA-1 is a Yugoslavian anti-personnel landmine which uses 200 g of Trinitrotoluene (TNT) as explosive charge. It is mostly found in Namibia, Balkans, and Angola. It is 140 mm in length, 30 mm in height and 70 mm in width. The plastic case has a relative permittivity $\epsilon_r = 2.8$ and the TNT explosive $\epsilon_r = 6$ [109]. The simulation model of PMA-1 is shown in Figure 5-3 visualised using ParaView software [83], [84].

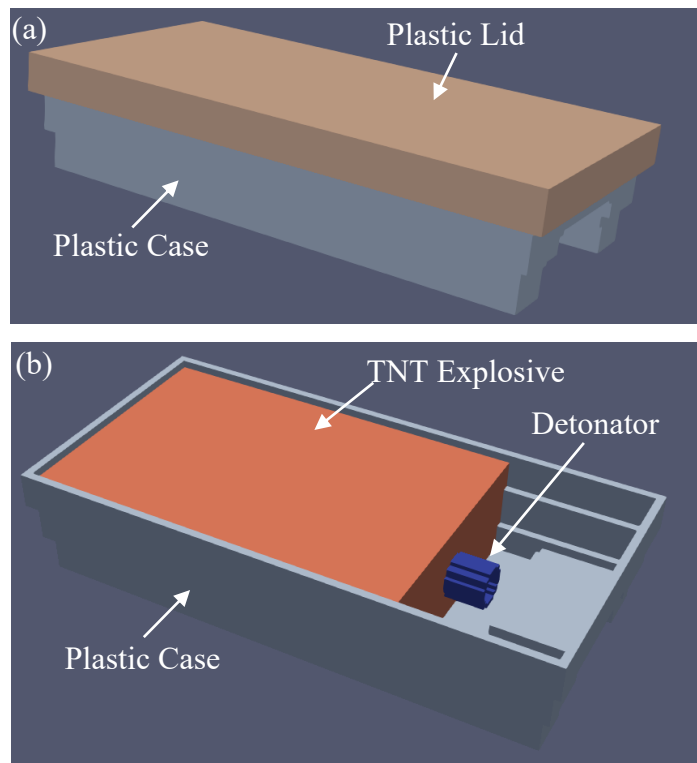


Figure 5-3 – Simulation model of a PMA-1 AP landmine. (a) is the landmine with the top lid closed and (b) the top lid open, revealing the components inside.

PMA-2 is also a Yugoslavian anti-personnel landmine which uses 95 g of TNT. It is found in Albania, Angola, Bosnia, Cambodia, Croatia, Serbia, Zimbabwe, and Namibia. It has a diameter of 68 mm and height of 61 mm. The relative permittivity used for the plastic case, the TNT explosive and the detonator fuse are the same as PMA-1 [110]. The simulation model of the PMA-2 is shown in Figure 5-4.

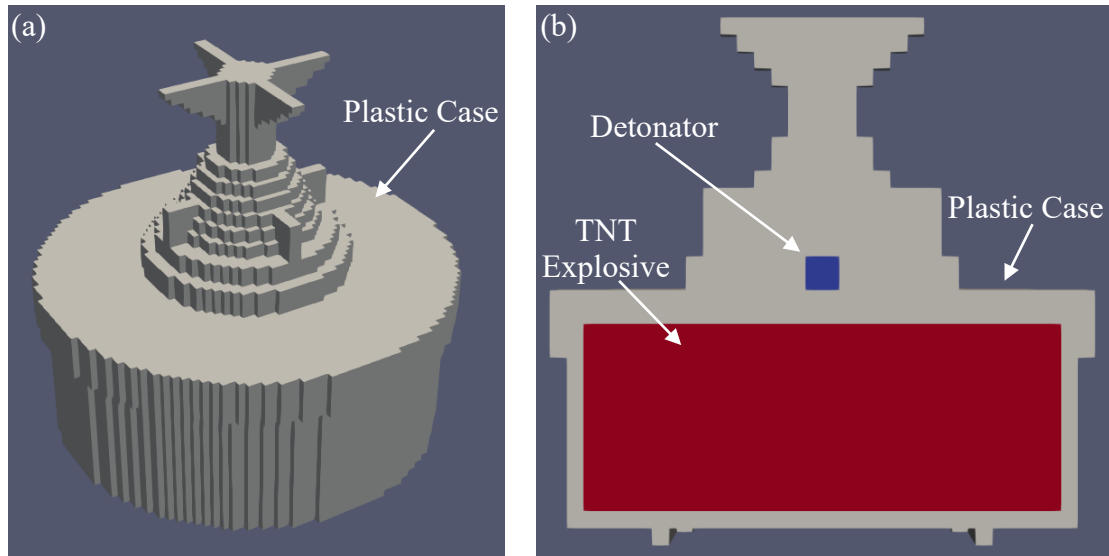


Figure 5-4 – Simulation model of a PMA-2 AP landmine. (a) is the landmine view from outside and (b) is the cross-sectional view from the side.

PMA-3 is also a Yugoslavian landmine with 35 g of TNT for the explosive. It is found in Albania, Bosnia, Cambodia, Chad, Chile, Croatia, Serbia, Lebanon, Namibia, and Peru. It has a diameter of 111 mm and height of 40 mm. The relative permittivity used for the plastic case, the TNT explosive and the detonator are the same as PMA-1 [111]. The lid on the top that covers the sides is made of rubber, with a relative permittivity $\epsilon_r = 3$.

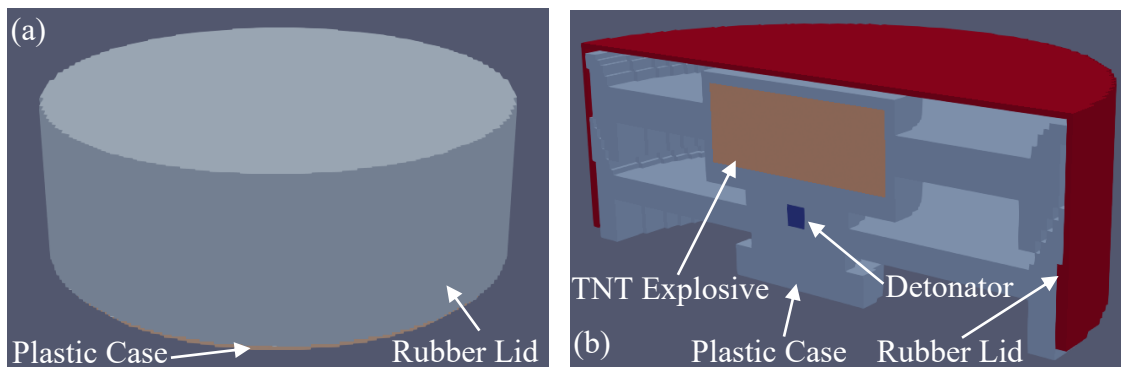


Figure 5-5 – Simulation model of a PMA-3 AP landmine. (a) is the landmine view from outside and (b) is the cross-sectional view from the side.

Clutter Models

Naturally occurring clutter in the soil include rocks, water concentrations, air cavities such as burrows and plant roots. In addition, shrapnel and bullet / bullet cartridges are sources of clutter in post conflict land. As the clutter shapes and sizes are random, basic shapes included in the simulation package (e.g., cube, triangle, sphere, cylinder) were used for generating these types of clutter. The size, shape, material and position of this type of clutter were also randomised when generating the models for the dataset, which is described in detail in Section 5.4. A model was built for a .222 Remington cartridge, which is representative of a typical metal clutter found in post-conflict land. The bullet and the cartridge case were modelled separately and as well as together as a whole. All three types were then used as clutter in the generated models. However, it is important to note that due to the resolution limit of the simulation software, which is 1 mm, it wasn't possible to correctly model the bullet head's shape. The models are shown in Figure 5-6.

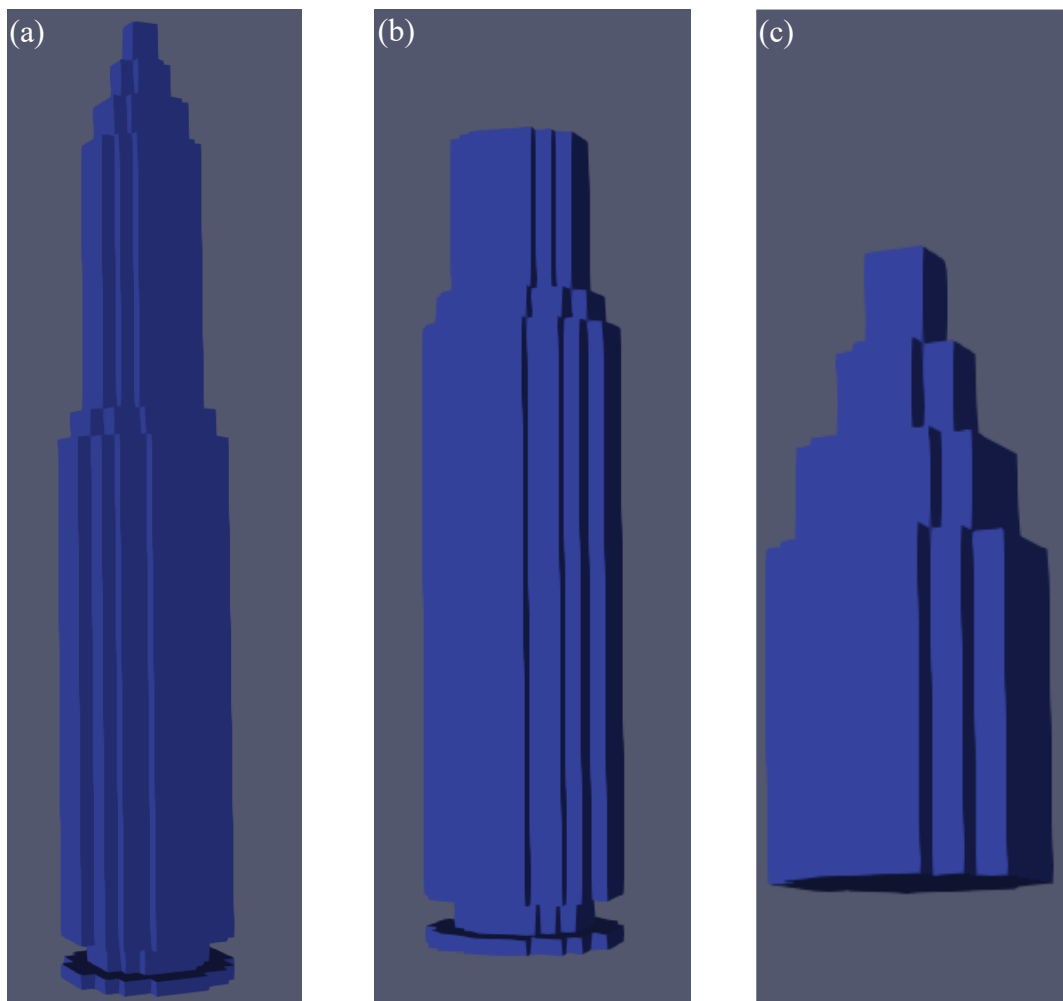


Figure 5-6 – Model of the 7.62×51 mm NATO standard ammunition cartridge. (a) is the unfired cartridge as a whole, (b) is the cartridge case and (c) is the bullet.

Soil Models

Inhomogeneous soil was modelled using a function in the simulation package which allows the use of a mixing model for soils, proposed by Peplinski et al. [112]. The function utilises fractals, allowing the use of orthogonal parallelepiped with fractal distributed properties, which are related to a material mixing model in the simulation model. Various parameters of the soil can be set inside the function, such as sand fraction, clay fraction, bulk density, density of the sand particles and the volumetric water fraction of the soil. In addition, varying surface roughness and grass can also be added to the soil using other functions in the simulation package. Two soil models generated using the simulation package, one with and one without clutter and grass, are shown in Figure 5-7. A cross-sectional snapshot of the GPR waves propagating through the model in Figure 5-7(b) is also shown in Figure 5-8.

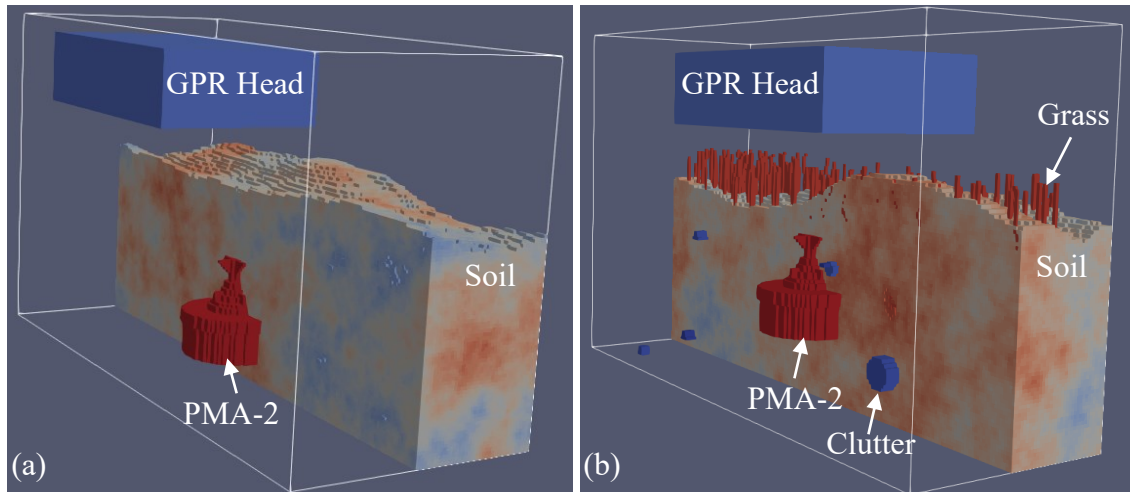


Figure 5-7 – Two soil models generated using gprMax. (a) is a soil model with inhomogeneous material distribution and rough surface. In addition to the features in (a), (b) also introduces clutter and grass.

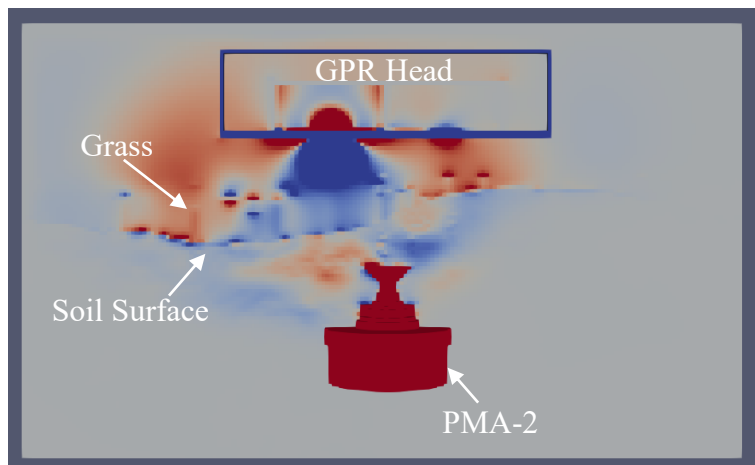


Figure 5-8 – A snapshot of the GPR waves propagating through a simulation model, where reflections from the grass, soil surface, and the PMA-2 landmine are visible.

Dataset

To generate the dataset, 500 simulation models were created per landmine, bullet and bullet cartridge. In addition, 500 simulation models were created with no target object but just clutter, to simulate no target scenarios. A B-Scan was run over the target object for each simulation model, resulting in a dataset with 3,000 B-Scans covering 6 target scenarios. 100 A-Scans with 4 mm steps on a straight line were recorded to form each B-Scan. To generate the 3,000 simulation models, a python script was used, which produced 500 random scenarios per target object. A number of model parameters were randomised in the script to make all models unique, such as soil moisture amount, number of grass shoots, shape, size, material and the number of clutter items. The main parameters for the simulation models are shown in Table IX below.

Table IX – Main parameters of the simulation models.

Variable	Randomised	Range	Variable	Randomised	Range
Soil Roughness	Yes	20 - 45 mm peak-to-peak	Clutter Position	Yes	Anywhere in Soil
Volumetric Water Fraction	Yes	0.01 - 0.1	Landmine Depth	Yes	1 – 5 cm
GPR Height	No	20 mm	Grass	Yes	Yes/No
Number of Clutter	Yes	2 - 10	Number of Grass Shoots	Yes	10 - 300
Clutter Shapes	Yes	Cube, Triangular Prism, Sphere, Cylinder	Landmine Orientation	Yes	0, ± 15 , ± 30 and ± 45 degrees
Clutter Materials	Yes	Rock, Plastic, PEC, Air	Clay/Sand Fractions	No	0.5/0.5
Clutter Length	Yes	4 – 8 mm	Bulk Density of Soil	No	2 g/cm ³
Clutter Radius	Yes	4 – 8 mm	Sand Particle Density	No	2.66 g/cm ³

The resulting B-Scans were further processed to aid the training of the ML algorithms. As the ground response dominates the B-Scans, the targets' responses are not visible on the B-Scan visualisations. Removing the ground response amplifies the target's response which can potentially help speed up and improve the performance of an ML classifier. To remove the ground response, the A-Scans at the start and at the end of the B-Scan were averaged and subtracted from the whole B-Scan. Although, this does not completely remove the ground response as the ground is uneven, it is generally mostly removed. To remove the remaining ground response and amplify the target object's response, a time varying gain can be applied to each A-Scan in the B-Scan. This attenuates the responses closer to the GPR head (e.g., the ground) and amplifies the ones farther (e.g., a landmine). Finally, the B-Scans are normalised to make the response magnitudes standard, which again may help improve classification performance. Visualisation of a B-Scan before and after post-processing are shown in Figure 5-9.

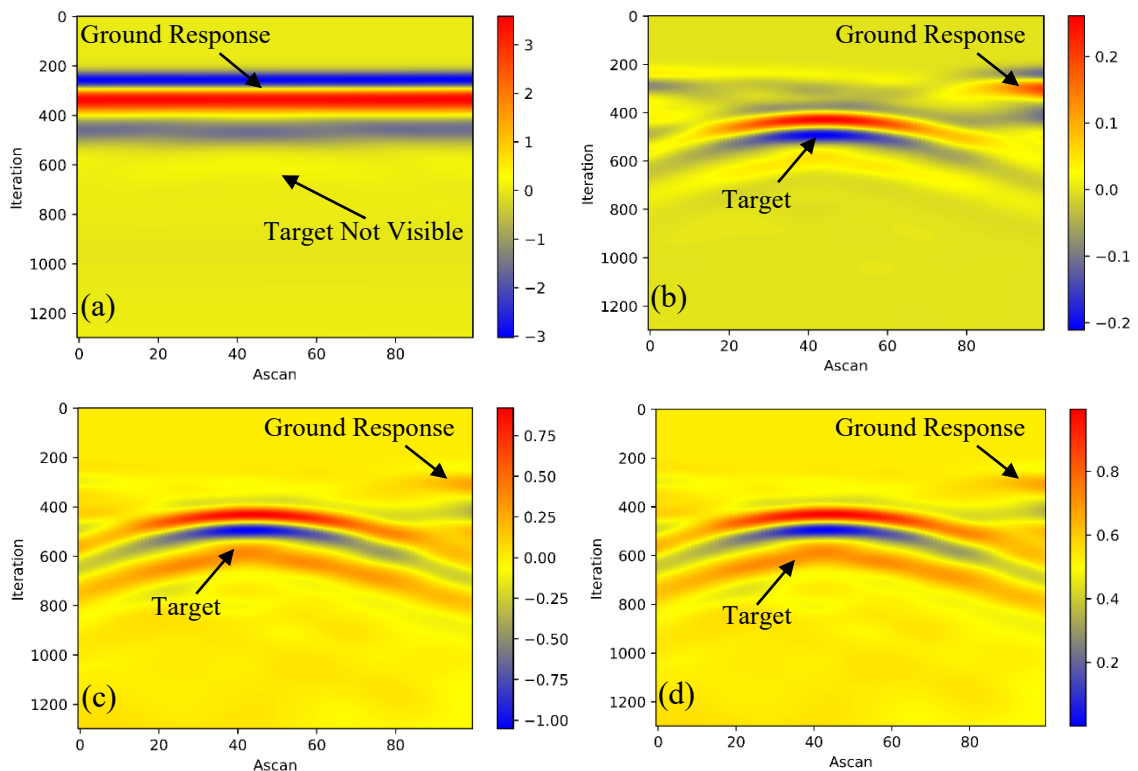


Figure 5-9 – Example B-Scan before and after applying post processing. (a) the raw B-Scan, (b) after background removal, (c) after applying time varying gain, and (d) after magnitude normalisation.

5.5. Summary and Future Work

The chapter discusses the working principles of GPR, its advantages and limitations. Use of real and synthetic GPR data for training of ML classifiers in the literature were also summarised, with discussion of the methodology used in each publication. The simulation methodology and the simulation models generated (e.g., AP landmines, clutter and inhomogeneous soil) were also described in detail. Using the methodology described, synthetic GPR datasets were generated with incremental complexity, which involved GPR B-Scans. Random clutter with random shape, material, size and position were included in the soil for increased complexity. The soil in the most complex dataset also contained random roughness, vegetation and moisture. The most complex dataset included 3000 B-Scans.

Even with all the complexity and randomness used in the simulation models, the data still does not involve enough details to reflect all real-life scenarios. This would possibly cause data overfitting during ML classifier training, causing a good classification accuracy on the data, where the same classifier would perform poorly in a real-life application. Some examples are the lack of real noise, fixed GPR head height, small number of target models, and the lack of soil type variation (percentage of sand and clay in the mixture is always the same). A preliminary test of DNN and CNN type ML classifiers confirmed this by achieving perfect classification performance on the most complex dataset. Although, it is possible to generate more complex simulation models with larger volume, resolution, variation and more complex features, the computational cost of the simulations quickly rises. Therefore, the augmentation of the dataset with real GPR data is necessary. This means that the dataset will be large, because of the simulated data, but will also include enough complexity and noise from real life scenarios which will prevent the overfitting of the dataset by the ML classifiers. This finding is also consistent with the literature, where mostly real data was used for ML classifier training and testing. This is also consistent with the work reported in Section 4.3 of this thesis when applying ML to real MPT data from metal detection systems. Namely, real data is an essential requirement in order to achieve meaningful output from ML algorithms. Taking this into account, it is anticipated that with the availability of real GPR data and the progress of computational technology, it is possible to generate a hybrid dataset involving real GPR data from different soil types and more complex simulation models. Therefore, an ML classifier can be trained to achieve high probability of detection and low false alarm rates on real data.

Methodology of using the polarizability tensor could also be utilised for the GPR applications in the future when the mathematical theory is in place. When such methodology is available, both the MPT and the GPR polarizability tensor signatures could be measured for a target object simultaneously using a dual mode landmine detector. This would allow the characterisation and classification of the buried target with much higher accuracy compared to conventional dual mode landmine detectors.

6. Conclusion and Future Work

6.1. Conclusion

The research presented in this thesis has given both a detailed background and a collection of peer-reviewed articles concerning MPT characterisation methods, machine learning and GPR simulation modelling. Overall, the research has taken forward ideas of using methods which can better provide discrimination between threat and non-threat items. The methods have been applied in the application areas of humanitarian demining and aiding the development of the next generation of smart WTMDs.

An instrument for measuring the MPT of metal objects was designed, constructed and evaluated. The instrument utilises either smaller or larger bespoke multi-coil arrays for measuring the MPTs of different sized metal objects. Each novel coil geometry generates a uniform magnetic field inside the coil array for measuring the rank 2 MPT of the target objects placed inside the coils. The small coil array was built with the motivation of measuring the rank 2 MPT of AP landmines, while the large coil array was built for measuring the rank 2 MPT of small to medium sized firearms. Portable system electronics to drive the coils and measure the transimpedance were designed and built. A control software with GUI for experiment control and automation was written, as well as a post-processing software for MPT inversion from multiple transimpedance measurements. Noise and drift performance as well as the measurement repeatability of the instrument were tested and reported. MPTs measured by the instrument were compared with previously published simulated and experimental data, which proved the instrument's ability to accurately characterise rank 2 MPTs of metal objects. The developed system was used during several measurement campaigns involving the characterisation of hundreds of metal objects in such a way as to build accurate data libraries of both threat and non-threat objects. Such data libraries are anticipated to be invaluable in furthering research in developing related and future metal detection systems e.g., the next generation of smart metal detection, Walk-Through Metal Detectors.

Three TOMs were built for measuring the MPT of different types of objects. A single axis TOM which can rotate objects around a horizontal axis with an estimated one-degree level of precision was built. This was used to measure rank 2 MPT of symmetrical and homogenous metal objects during the instrument's development stages.

A truncated Icosahedron shaped multi-axis TOM capable of orientating objects more fully in three-dimensional space was built. The geometry of the TOM had 32 faces made up of pentagons and hexagons, which provided 16 unique orientations due to the uniform magnetic field. The TOM was used for measuring the rank 2 MPT of non-symmetrical, irregular objects. A small, 3D printed version of the TOM was built for the small coil arrangement, while a large version was built using PBT pipe and 3D printed nodes for the large coil arrangement. The tI shaped TOM, together with the post-processing algorithm which carries out the MPT inversion is a novel aspect of this research. This methodology provides fast and reliable measurement of the rank 2 MPT of any metal object which can fit inside the TOM.

Another TOM was built for rotating cone shaped metal objects around a horizontal axis with one degree accuracy, outside the uniform magnetic field region of the small coil array. The TOM also enabled the adjustment of horizontal and vertical position of the cones inside the non-uniform magnetic field region. This enabled the exposure of the cone shaped metal objects to different regions of the non-uniform magnetic field. Using this methodology proved that, for the first time, the rank 3 MPT (GPMT) of a metal object could be measured.

Using the small tI shaped multi-axis TOM inside the small coil array, the rank 2 MPT of four AP landmines and their metal components were measured and published in the literature for the first time. The study compared the characteristics of the metal components and found that the springs and the firing pins in the AP landmines were responsible for the magnetic response of the four AP landmines. Furthermore, the study showed that rusting of the metal components had minimal effect on the overall rank 2 MPT of the AP landmines. This proved that the rank 2 MPT of a brand-new AP landmine still holds after the landmine has been buried in the soil for several years and the onset of component oxidation. The information from this study is crucial for reducing the FAR in the next generation of smart landmine detectors.

Using the large tI shaped multi-axis TOM inside the large coil array, the rank 2 MPT of 120 firearms were measured. The target objects included pistols, SMGs, grenades and unconventional firearm types. In addition, rank 2 MPT of 90 non-threat metal objects were measured. The target objects included coins, keys, belts, mobile phones, vapes, etc. Using the rank 2 MPT of threat and non-threat objects, two datasets were produced where

one of them included only threat objects, and the other one included both threat and non-threat objects. Clustering in the datasets were evaluated using three clustering algorithms (unsupervised Machine Learning). Different types of firearms were generally grouped into separate clusters in the dataset with only threat objects. Threat and non-threat objects were also grouped into separate clusters in the dataset with both threat and non-threat objects, with some of the non-threat objects clustered together with the threat ones. However, no threat objects were clustered together with the non-threat objects.

Using gprMax, simulation models of three AP landmines and a NATO standard ammunition were built. By using these models and realistic soil models with random surface and clutter, a dataset was created with 3000 simulated B-Scans. The soil model involved random number of grass shoots, clutter and random amount of moisture. The position and orientation of the target objects were also random. A preliminary classification test was conducted where a DNN and a CNN were trained and tested using the dataset and all targets were classified correctly. A possible reason for this is the ML classifiers overfitting the dataset, where the accuracy becomes so high as the train and test datasets use similar simulation models (e.g., same soil type). The same classifier would possibly not perform as well in a different soil type or on real data. Although, augmentation with real data is necessary for the simulated datasets to be useful, achieving a methodology for generating simulated datasets and training ML classifiers with such datasets are useful for the development of future landmine detectors.

The major achievements of this research can also be briefly summarised as below:

- Development of an instrument capable of measuring the rank 2 MPT of metal objects by utilising a novel coil array geometry to generate a precise uniform magnetic field.
- The instrument's details and the performance test results were published in the publication named "Measuring the Magnetic Polarizability Tensor Using an Axial Multi-Coil Geometry" in the IEEE Sensors Journal.
- A methodology was established for fast and reliable measurement of the rank 2 MPT of non-symmetrical metal objects by utilising a novel target orientation manipulator.

- This methodology and the rank 2 MPT of non-symmetrical test objects were submitted for publication in IEEE Sensors Journal with the name “Measuring the Magnetic Polarizability Tensor of Non-Symmetrical Metallic Objects”.
- Using the instrument and the methodology described in the above points, rank 2 MPT of four AP landmines and their metal components were measured, for the first time.
- These results were published and presented in the 2022 IEEE International Instrumentation and Measurement Technology Conference with the name “A Study on the Magnetic Polarizability Tensors of Minimum Metal Anti-Personnel Landmines”.
- Rank 3 MPT of three cone shaped test objects were measured by placing them in the non-uniform magnetic field region of the coil array. A bespoke target orientation manipulator was built for this study. The study proved, for the first time, that the higher rank MPT of metal objects can be experimentally measured.
- The results of this study was published in the IEEE Sensors Journal with the name “Measurement of GMPT Coefficients for Improved Object Characterisation in Metal Detection”.
- Using the instrument and the methodology described, two rank 2 MPT datasets involving threat (e.g., pistols, SMGs, knives) and non-threat (e.g., keys, coins, belts) objects were built. Unsupervised machine learning algorithms were then applied to the datasets to evaluate the clustering in the data. This study showed that the threat and non-threat objects can be grouped into separate clusters by the unsupervised machine learning algorithms. These results give the confidence to further expand this study to generate a large dataset involving threat and non-threat objects. Then, supervised machine learning classifiers can be trained using the dataset to improve classification and throughput in security screening applications.
- The results from this study was submitted (accepted) for publication in the IEEE Sensors Journal with the name “Classification of Threat and Non-Threat Objects Using the Magnetic Polarizability Tensor and a Large-Scale Multi-Coil Array”.

Overall, this research has mainly studied characterisation and classification techniques for both MD and GPR for dual mode humanitarian demining. However, emphasis was put on characterisation techniques for MD as per industrial partners' interests. The methodology established for fast and reliable measurement of the rank 2 MPT of metal objects is crucial for improving the pace of humanitarian demining by reducing FAR. This could be achieved by generating an MPT library of both landmines and common metal clutter using the established methodology. A standard data format for MPT is also needed for generating such library, which was established in this research for sharing the acquired data with the industrial partners. The work during the course of this research and reported in this thesis has made significant progress in creating such an MPT library of, in particular, threat objects which are difficult to acquire for MPT measurements e.g., firearms and landmines. A landmine detector utilising magnetic induction spectroscopy may then use this library to do better target classification. In addition, the same methodology can be used to generate an MPT library of threat and non-threat objects for better classification in WTMDs. A detector capable of measuring the MPT of metal objects on a person passing through can utilise this library for rejecting non-threat objects to increase the throughput of people. On the other hand, the methodology established for generating simulated GPR datasets for ML training could be utilised to augment real GPR datasets with realistic synthetic data. The resulting dataset could then be used to train high performing classifiers to reduce FAR. The better classification from both MD and GPR combined has a high potential to improve FAR and speed up the pace of humanitarian demining operations, which was the main motivation of this research.

6.2. Future Work

This thesis has considered both MD and GPR technologies. It is worth noting that over the past decade commercial systems have increasingly combined MD and GPR as dual mode detectors. This thesis has reported characterisation techniques for both MD and GPR as separate developments with Chapters 2-4 focusing on MD and Chapter 5 focusing on GPR, respectively. Clearly both MD and GPR techniques share the same foundations in Maxwell's equations. Therefore, a direction for future research may be to find synergies between these two methodologies exploiting their common physical basis. For instance, the ML approaches used for GPR in Chapter 5, which take into account complex ground effects, could be applied to the discrimination problem for MD, especially dealing

with uncooperative ground. Conversely, for GPR, a concise tensor like characterisation of target objects may also be beneficial. Hence, this thesis has considered these separate areas, but with the expectation of future research may eventually unite them as one continuum across the electromagnetic spectrum.

Larger coil arrays, possibly with different geometries could be built in the future for measuring the MPT of larger threat object, such as assault rifles or anti-tank landmines. WTMDs which only look for threat signatures like these could help the early detection of possible attacks in crowded areas. An MPT library of anti-tank landmines could also expand the future use of MPT in humanitarian demining to clearance of such threats. Future work could also include development of an automated TOM which would enable object rotation inside the coil arrays to further speed up the MPT measurement. This could help with the feasibility of generating a library involving threat and non-threat objects for MD applications, by reducing the amount of work required by the instrument operator. Measuring the MPT of larger metal objects would also require expanding the frequency spectrum to lower frequencies to be able to capture the important signature information. As metal detectors used in dual mode landmine detectors generally generate a non-uniform magnetic field, the contribution from higher rank MPT of target objects become more apparent in the electromagnetic signatures. Even though the landmine detector is capable of measuring the rank 2 MPT of the target object, the presence of the non-uniform magnetic field can result in a less accurate object characterisation, hence, worse classification accuracy. To solve this, an instrument capable of measuring the GMPT of metal targets with a robust and reliable measurement methodology could be developed. The instrument can then be used to generate a GMPT library of the target objects. The same methodology can then be adapted for the dual mode landmine detectors to enable the GMPT measurement of the target objects. This can lead to much better characterisation accuracy of the targets, hence, better classification accuracy.

The study on GPR datasets can further expand in the future by generating a real GPR dataset involving AP landmines and clutter in different soil mixtures. If a large enough dataset could be built, an ML classifier could be trained using just the real data for best performance. Otherwise, performance of an ML classifier trained with simulated data could be tested on the smaller real dataset. The real data could also be augmented with the simulated data to possibly achieve the best classification performance by reducing data overfitting.

References

- [1] International Campaign to Ban Landmines, “What is a Landmine?”, Technical Report, 2019.
- [2] The Geneva International Centre for Humanitarian Demining (GICHD), “Introduction and History of Mine Action,” Technical Report, 2014.
- [3] International Campaign to Ban Landmines, “Landmine Monitor 2021”, Technical Report, 2021.
- [4] Secretary-General, “Assistance in Mine Action: Report of the Secretary General (A/74/288),” United Nations, Technical Report, 2019.
- [5] International Campaign to Ban Landmines, “The Treaty”, [Online]. Available: <http://www.icbl.org/en-gb/the-treaty.aspx>
- [6] International Campaign to Ban Landmines, “The Treaty”, [Online]. Available: <http://www.icbl.org/en-gb/the-treaty/treaty-in-detail/treaty-text.aspx>
- [7] United Nations, “Convention on the Prohibition of the Use, Stockpiling, Production and Transfer of Anti-Personnel Mines and on Their Destruction,” Technical Report, 1997.
- [8] International Campaign to Ban Landmines, “Landmine Monitor 2019”, Technical Report, 2019.
- [9] International Campaign to Ban Landmines, “Landmine Monitor 2020”, Technical Report, 2020.
- [10] Guelle, D., Smith, A., Lewis, A. and Bloodworth, T., “Metal detector handbook for humanitarian demining,” *Luxembourg: Office for Official Publications of the European Communities*, 2003.
- [11] Tsipis, K. “Technological Innovation in Humanitarian Demining,” *Human Factors and Ergonomics Society*, SANTA MONICA, pp. 750-753, 1998.
- [12] Kopacek, P., “Humanitarian Demining for International Stability,” *IFAC Proceedings Volumes*, vol. 34, pp. 85-89, 2001.

- [13] Takahashi, K., Preetz, H. and Igel, J., "Soil properties and performance of landmine detection by metal detector and ground-penetrating radar — Soil characterisation and its verification by a field test," *Journal of Applied Geophysics*, vol. 73, pp. 368-377, 2011.
- [14] Das, Y., "Effects of soil electromagnetic properties on metal detectors," *IEEE Transactions on Geoscience and Remote Sensing*, vol. 44, no. 6, pp. 1444-1453, 2006.
- [15] Das, Y., "Effects of magnetic soil on metal detectors: preliminary experimental results," *Proceedings of SPIE Conference on Detection and Remediation Technologies for Mines and Minelike Targets XII*, vol. 6553, Orlando – USA, 2007.
- [16] Das, Y., "A preliminary investigation of the effects of soil electromagnetic properties on metal detectors," *Proceedings of SPIE Conference on Detection and Remediation Technologies for Mines and Minelike Targets IX*, vol. 5415, pp. 677–690, Orlando – USA, 2004.
- [17] Kasban, H., Zahran, O., Elaraby, S., El-Kordy, M. and Abd El-Samie, F., "A Comparative Study of Landmine Detection Techniques," *Sensing and Imaging: An International Journal*, vol. 11, pp. 89-112, 2010.
- [18] Smith, S., "Mine Detection Dogs at Work," *The Journal of Conventional Weapons Destruction*, vol. 5, 2001.
- [19] Hayter, D., "The Evolution of Mine Detection Dog Training," *The Journal of Conventional Weapons Destruction*, vol. 7, 2003.
- [20] Daniels, D., "Ground penetrating radar," 2nd edition, *London: The Institution of Electrical Engineers*, 2004.
- [21] Daniels, D., "A review of GPR for landmine detection," *Sensing and Imaging: An International Journal*, vol. 7, pp. 90-123, 2006.
- [22] Daniels, D. "EM Detection of Concealed Targets," *New Jersey: John Wiley & Sons, Inc*, 2010.

- [23] Kwon, O., Sim, J., “Effects of data set features on the performances of classification algorithms,” *Expert Systems with Applications*, vol. 40, pp.1847-1857, 2013.
- [24] Wilson, B.A., Ledger, P.D., Lionheart, W.R.B., “Identification of Metallic Objects using Spectral Magnetic Polarizability Tensor Signatures: Object Classification,” *International Journal for Numerical Methods in Engineering*, Accepted Manuscript, 2022.
- [25] Ledger, PD., and Lionheart, WRB., “Understanding the magnetic polarizability tensor,” *IEEE Transactions on Magnetics*, vol. 52. No. 5, pp. 1-16, 2016.
- [26] Ledger, PD., and Lionheart, WRB., “An Explicit Formula for the Magnetic Polarizability Tensor for Object Characterization,” *IEEE Transactions on Geoscience and Remote Sensing*, vol. 56, no. 6, pp. 3520- 3533, 2018.
- [27] Ledger, P., Lionheart, W., “Characterizing the shape and material properties of hidden targets from magnetic induction data,” *IMA Journal of Applied Mathematics*, vol. 80, pp. 1776-1798, 2015.
- [28] Ledger, P., Lionheart, W., "Magnetic polarizability tensors for low frequency object classification and detection," *International Applied Computational Electromagnetics Society Symposium - Italy (ACES)*, pp. 1-2, 2017.
- [29] Ledger, PD., and Lionheart, WRB., “The spectral properties of the magnetic polarizability tensor for metallic object characterisation,” *Mathematical Methods in the Applied Sciences*, vol. 43, no. 1, pp. 78-113, 2019.
- [30] Ledger, PD, Lionheart, WRB., “Generalised magnetic polarizability tensors,” *Mathematical Methods in the Applied Sciences*, vol. 41, pp. 3175– 3196, 2018.
- [31] Wilson, B. and Ledger, PD., “Efficient computation of the magnetic polarizability tensor spectral signature using proper orthogonal decomposition,” *International Journal for Numerical Methods in Engineering*, vol. 122 no. 8, pp.1940-1963, 2021.
- [32] Bell, TH., Barrow, BJ, Miller, JT, “Subsurface discrimination using electromagnetic induction sensors,” *IEEE Transactions Geoscience Remote Sensing*, vol. 39, no. 6, pp. 1286–1293, 2001.

- [33] Skitek, GG, Marshall, SV, "Biot-Savart Law, Ampere's Law, Curl Stokes' Theorem," *Electromagnetic Concepts and Applications*, pp. 216-220, 1987.
- [34] Kraus, JD, Fleisch, DA, "Electromagnetics with Applications," *McGraw-Hill Book*, p. 105, 1999.
- [35] Lorrain, P, Corson, DR, Lorrain, F, "Magnetic fields I " *Electromagnetic Fields and Waves*, WH Freeman & Co, 1998.
- [36] Bell, TH, Barrow, BJ, Miller, JT, "Subsurface Discrimination Using Electromagnetic Induction Sensors," *IEEE Geoscience and Remote Sensing*, vol. 39, pp. 1286-1293, 2001.
- [37] Abdelkerim, OA, "Magnetic Tensor Spectroscopy for Humanitarian Anti - Personnel Landmine Detection," PhD Thesis, The University of Manchester, 2015.
- [38] Fernandez, JP., Barrowes, BE., Grzegorzcyk, TM., Lhomme, N., O'Neill, K., Shubitidze, F., "A man-portable vector sensor for identification of unexploded ordnance," *IEEE Sensors Journal*, vol. 11, pp. 2542–2555, 2011.
- [39] Norton, SJ., Won, IJ., "Identification of buried unexploded ordnance from broadband electromagnetic induction data," *IEEE Transactions of Geoscience Remote Sensing*, vol. 39, pp. 2253–2261, 2001.
- [40] Grzegorzcyk, TM., Barrowes, BE., Shubitidze, F., Fernandez, JP., O'Neill, K., "Simultaneous identification of multiple unexploded ordnance using electromagnetic induction sensors," *IEEE Transactions of Geoscience Remote Sensing*, vol. 49, pp. 2507–2517, 2011.
- [41] Nelson, HH., McDonald, JR., "Multisensor towed array detection system for UXO detection," *IEEE Transactions on Geoscience and Remote Sensing*, vol. 39, pp. 1139-1145, 2001.
- [42] Marsh, LA., Ktistis, C., Järvi, A., Armitage, D., Peyton, AJ., "Three-dimensional object location and inversion of the magnetic polarizability tensor at a single frequency using a walk-through metal detector," *Measurement Science and Technology*, vol. 24, p. 045102, 2013.

- [43] Makkonen, J., Marsh, L.A., Vihonen, J., O'Toole, M.D., Armitage, D.W., Järvi, A., Peyton, A.J., Visa, A., "Determination of material and geometric properties of metallic objects using the magnetic polarizability tensor," *IEEE Sensors Applications Symposium (SAS)*, pp. 1-5, 2015.
- [44] Makkonen, J., Marsh, L., Vihonen, J., Järvi, A., Armitage, D., Visa, A., Peyton, A., "Improving reliability for classification of metallic objects using a WTMD portal," *Measurement Science and Technology*, vol. 26, p. 105103, 2015.
- [45] Makkonen, J., Marsh, L.A., Vihonen, J., Visa, A., Järvi, A., Peyton, A.J., "Classification of metallic targets using a single frequency component of the magnetic polarizability tensor," *Journal of Physics: Conference Series*, vol. 450, p. 012038, 2013.
- [46] Makkonen, J., Marsh, L.A., Vihonen, J., Järvi, A., Armitage, D., Visa, A., Peyton, A.J., "KNN classification of metallic targets using the magnetic polarizability tensor," *Measurement Science and Technology*, vol. 25, no. 5, pp. 055105, 2014.
- [47] Makkonen, J., "Classification of Metallic Targets Using a Walk-Through Metal Detection Portal," PhD. Dissertation, Tampere University of Technology, 2015.
- [48] O'Toole, M., Karimian, N., Peyton, A.J., "Classification of Nonferrous Metals Using Magnetic Induction Spectroscopy," *IEEE Transactions on Industrial Informatics*, vol. 14, no. 8, pp. 3477-3485, 2018.
- [49] Tao, Y., Yin, W., Zhang, W., Zhao, Y., Ktistis, C., Peyton, A.J., "A Very-Low-Frequency Electromagnetic Inductive Sensor System for Workpiece Recognition Using the Magnetic Polarizability Tensor," *IEEE Sensors Journal*, vol. 17, no. 9, pp. 2703-2712, 2017.
- [50] Marsh, L.A., Abdel Rehim, O.A., Tan, Y.M., O'Toole, M., Armitage, D.W., Peyton, A.J., "Design of electromagnetic sensor arrays optimised for inversion of the magnetic polarizability tensor," *IEEE Sensors Applications Symposium (SAS)*, 2015, pp. 1-4, 2015.
- [51] Ambrus, D., Vasic, D., Bilas, V., "Comparative Study of Planar Coil EMI Sensors for Inversion-Based Detection of Buried Objects," *IEEE Sensors Journal*, vol. 20, no. 2, pp. 968-979, 2020.

- [52] Zhao, Y., Yin, W., Ktistis, C., Butterworth, D., Peyton, A.J., "Determining the Electromagnetic Polarizability Tensors of Metal Objects During In-Line Scanning," *IEEE Transactions on Instrumentation and Measurement*, vol. 6, no. 5, pp. 1172-1181, 2016.
- [53] Dekdouk, B., Ktistis, C., Marsh, L., Armitage, D., Peyton, A.J., "Towards metal detection and identification for humanitarian demining using magnetic polarizability tensor spectroscopy," *Measurement Science and Technology*, vol. 26, no. 11, pp. 115501, 2015.
- [54] Ambruš, D., Vasić, D., Bilas, V., "Innovating on top of I&M fundamentals for safer humanitarian demining," *IEEE Instrumentation & Measurement Magazine*, vol. 23, no. 3, pp. 35-41, 2020.
- [55] Dalichaouch, Y., Whitecotton, B., McManus, T., Kuhn, S., Trammell, H., Shelby, R., Carin, L., "Wideband frequency response of low-metal mines," *Detection and Remediation Technologies for Mines and Minelike Targets IX*, vol. 5415, pp. 275-282, 2004.
- [56] Scott, W.R., "Broadband array of electromagnetic induction sensors for detecting buried landmines," *IEEE International Geoscience and Remote Sensing Symposium (IGARSS), Boston, MA, USA*, Jul. 2008, pp. II-375–II-378.
- [57] Scott, W.R., Larson, G.D., "Modeling the measured em induction response of targets as a sum of dipole terms each with a discrete relaxation frequency," *IEEE International Geoscience and Remote Sensing Symposium, Honolulu, HI, USA*, pp. 4188-419, 2010.
- [58] Larson, G.D., Scott, W.R., "Automated, non-metallic measurement facility for testing and development of electromagnetic induction sensors for landmine detection," *Detection and Sensing of Mines, Explosive Objects, and Obscured Targets XIV*, 2009.
- [59] Scott, W.R., Larson, G.D., "Measured dipole expansion of discrete relaxations to represent the electromagnetic induction response of buried metal targets," *Detection and Sensing of Mines, Explosive Objects, and Obscured Targets XV*, Article No. 76640E, 2010.

- [60] Scott, WR., McFadden, M., “Wideband measurement of the magnetic susceptibility of soils and the magnetic polarizability of metallic objects,” *IEEE International Geoscience and Remote Sensing Symposium, Munich, Germany*, pp. 3170–3173, 2012.
- [61] Rehim, OA., Davidson, JL., Marsh, LA., O'Toole, M., Armitage, D. and Peyton, AJ., “Measurement system for determining the magnetic polarizability tensor of small metal targets,” *IEEE Sensors Applications Symposium (SAS), Zadar*, pp. 1-5, 2015.
- [62] Rehim, OA., Davidson, JL., Marsh, LA., O'Toole, M., Peyton, AJ., “Magnetic polarizability tensor spectroscopy for low metal anti-personnel mine surrogates,” *IEEE Sensors Journal*, vol. 16, no. 10, pp. 3775–3783, 2016.
- [63] Davidson, JL., Rehim, OA., Hu, P., Marsh, LA., O'Toole, MD., Peyton, AJ., “On the magnetic polarizability tensor of US coinage,” *Measurement Science and Technology*, vol. 29, no. 3, 2018.
- [64] Amad, AAS., Ledger, PD., Betcke, T., Praetorius, D., “Accurate Benchmark Computations of the Polarizability Tensor for Characterising Small Conducting Inclusions,” arXiv preprint arXiv:2106.15157, 2021.
- [65] Ledger, P., Lionheart, W., Amad, A., “Characterisation of multiple conducting permeable objects in metal detection by polarizability tensors,” *Mathematical Methods in the Applied Sciences*, vol. 42, pp. 830-860, 2018.
- [66] Ledger, PD., Wilson, BA., Amad, AAS., Lionheart, WRB., “Identification of metallic objects using spectral magnetic polarizability tensor signatures: Object characterisation and invariants,” *International Journal for Numerical Methods in Engineering*, vol. 122, no. 15, pp. 3941–3984, 2021.
- [67] GICHD, Collaborative ORDNance Data Repository (CORD). [Online]. Available: <http://cord.gichd.org/ordnance?id=http%3A%2F%2Fcord.gichd.org%2Fontology%23Landmine4156>.
- [68] MQTT: The Standard for IoT Messaging. [Online]. Available: <https://mqtt.org/>
- [69] Wilson, BA., and Ledger, PD., “Efficient computation of the magnetic polarizability tensor spectral signature using proper orthogonal decomposition,”

International Journal for Numerical Methods in Engineering, vol. 122, no. 8, pp. 1940–1963, 2021.

- [70] Zaglmayr, S.: PhD thesis "High Order Finite Elements for Electromagnetic Field Computation", Johannes Kepler University Linz, 2006.
- [71] Schöberl, J.: "NETGEN - An advancing front 2D/3D-mesh generator based on abstract rules." *Computing and Visualization in Science*, vol. 1, pp. 41-52, 1997.
- [72] Schöberl, J.: "C++11 Implementation of Finite Elements in NGSolve", *ASC Report 30/2014, Institute for Analysis and Scientific Computing*, Vienna University of Technology, 2014.
- [73] EU. Commission Implementing Regulation (EU) 2015/1998 of 5 November 2015 Laying down Detailed Measures for the Implementation of the Common Basic Standards on Aviation Security. 2015.
- [74] NIJ Std 0602.01, "Walk-Through Metal Detectors for Use in Concealed Weapon and Contraband Detection," National Institute of Justice, Office of Science and Technology, Washington, DC 20531, January 2003.
- [75] Agruto, A.; Li, Y.; Tian, G.Y.; Bowring, N.; Lockwood, S. A Review of Concealed Weapon Detection and Research in Perspective. In Proceedings of the 2007 IEEE International Conference on Networking, Sensing and Control, London, UK, 15–17 April 2007; pp. 443–448.
- [76] Daniels, D. J., "Ground Penetrating Radar," *Stevenage: Institution of electrical engineers*, 2004.
- [77] Abujarad, F., "Ground Penetrating Radar Signal Processing for Landmine Detection," *Ph.D., Otto-von-Guericke-Universität Magdeburg*, 2007.
- [78] Giannakis, I., "Realistic Numerical Modelling of Ground Penetrating Radar for Landmine Detection," *Ph.D., University of Edinburgh*, 2016.
- [79] Kasban, H., Zahran, O., Elaraby, S., El-Kordy, M. and Abd El-Samie, F., "A Comparative Study of Landmine Detection Techniques," *Sensing and Imaging: An International Journal*, vol. 11, pp. 89-112, 2010.

- [80] Tsipis, K. "Technological Innovation in Humanitarian Demining," Human Factors and Ergonomics Society, SANTA MONICA, pp. 750-753, 1998.
- [81] Kopacek, P., "Humanitarian Demining for International Stability," IFAC Proceedings Volumes, vol. 34, pp. 85-89, 2001.
- [82] Warren, C., Giannopoulos, A., Giannakis, I., "gprMax: Open-source software to simulate electromagnetic wave propagation for Ground Penetrating Radar," *Computer Physics Communications*, vol. 209, pp. 163-170, 2016.
- [83] Ahrens, J., Geveci, B., Law, C., "ParaView: An End-User Tool for Large Data Visualization," *Visualization Handbook*, Elsevier, 2005.
- [84] Ayachit, U., "The ParaView Guide: A Parallel Visualization Application," *Kitware*, 2015.
- [85] Fitzpatrick, R., "Classical Electromagnetism," *Austin: The University of Texas*, 2014.
- [86] Jol, H., "Ground Penetrating Radar: Theory and Applications," *Oxford, UK: Elsevier Science*, 2009.
- [87] Immoreev, I., "Ultra-Wideband Radar Systems: Advantages and Disadvantages," *IEEE Conference on Ultra-Wideband Systems and Technologies*, 2002.
- [88] Radartutorial.eu, "Radar Basics – UWB - Radar," 2019. [Online] Available at: <http://www.radartutorial.eu/02.basics/UWB%20Radar.en.html> [Accessed June 2019].
- [89] Nicolaescu, I., "Stepped Frequency Continuous Wave Radar – Data Processing," *2. International Workshop on Advanced GPR*, Netherlands: IEEE, pp. 177-18, 2003.
- [90] Huici, M. A. G., "Accurate Ground Penetrating Radar Numerical Modeling for Automatic Detection and Recognition of Antipersonnel Landmines," *PhD. Germany: The University of Bonn*, 2012.
- [91] Warren, C., Giannopoulos, A., "Creating finite-difference time-domain models of commercial ground-penetrating radar antennas using Taguchi's optimization method," *Geophysics*, pp.37-47, 2011.

- [92] Giannakis, I., Giannopoulos, A., Warren, C., "Realistic FDTD GPR Antenna Models Optimized Using a Novel Linear/Nonlinear Full-Waveform Inversion," *IEEE Transactions on Geoscience and Remote Sensing*, 57, pp.1768-1778, 2019.
- [93] Warren, C., "Open-Source Software to Simulate Electromagnetic Wave Propagation for Ground Penetrating Radar," *Computer Physics Communications*, 2016.
- [94] Giannopoulos, A., "An advanced GPR modelling framework: the next generation of gprMax," *International Workshop on Advanced Ground Penetrating Radar (IWAGPR)*. Florence, Italy, 2015.
- [95] Giannakis, I., Giannopoulos A., Warren, C., "A Realistic FDTD Numerical Modeling Framework of Ground Penetrating Radar for Landmine Detection," *IEEE Journal of Selected Topics in Applied Earth Observations and Remote Sensing*, vol. 9, no. 1, pp. 37-51, 2016.
- [96] Giannakis, I., Giannopoulos A., Davidson, N., "Realistic modelling of ground penetrating radar for landmine detection using FDTD," *Proceedings of the 15th International Conference on Ground Penetrating Radar*, pp. 954-959, 2014.
- [97] Kafedziski, V., Pecov, S., Tanevski, D., "Detection and Classification of Land Mines from Ground Penetrating Radar Data Using Faster R-CNN," *26th Telecommunications Forum (TELFOR)*, pp. 1-4, 2018.
- [98] Song, J., Liu, Q. H., Torriane, P., Collins, L., "Two-dimensional and three-dimensional NUFFT migration method for landmine detection using ground-penetrating Radar," *IEEE Transactions on Geoscience and Remote Sensing*, vol. 44, no. 6, pp. 1462-1469, 2006.
- [99] Wilson, J., Gader, P., Lee, W., Frigui, H., Ho, K., "A Large-Scale Systematic Evaluation of Algorithms Using Ground-Penetrating Radar for Landmine Detection and Discrimination," *IEEE Transactions on Geoscience and Remote Sensing*, vol. 45, pp. 2560-2572, 2007.
- [100] Giovanneschi, F., Mishra, K. V., Gonzalez-Huici, M. A., Eldar Y. C., Ender, J. H. G., "Dictionary Learning for Adaptive GPR Landmine Classification," *IEEE*

Transactions on Geoscience and Remote Sensing, vol. 57, no. 12, pp. 10036-10055, 2019.

- [101] Milisavljevic N., Bloch, I., "Sensor fusion in anti-personnel mine detection using a two-level belief function model," *IEEE Transactions on Systems, Man, and Cybernetics, Part C (Applications and Reviews)*, vol. 33, no. 2, pp. 269-283, 2003.
- [102] Torrione, P., Morton Jr., K., "Sensor fusion approaches for EMI and GPR-based subsurface threat identification," *Detection and Sensing of Mines, Explosive Objects, and Obscured Targets XVI*, pp. 801720/1-15, 2011.
- [103] den Breejen, E., Schutte, K., "Sensor fusion for antipersonnel landmine detection: a case study," *Detection and Remediation Technologies for Mines and Minelike Targets IV*, Orlando, pp.1235-1245, 1999.
- [104] Reichman, D., Collins, L. and Malof, J., "On Choosing Training and Testing Data for Supervised Algorithms in Ground-Penetrating Radar Data for Buried Threat Detection," *IEEE Transactions on Geoscience and Remote Sensing*, vol. 56, pp. 497-507, 2018.
- [105] Smitha, N., Singh, V., "Target detection using supervised machine learning algorithms for GPR data," *Sensing and Imaging*, vol. 21, 2020.
- [106] Lameri, S., Lombardi, F., Bestagini, P., Lualdi, M., Tubaro, S., "Landmine detection from GPR data using convolutional neural networks," *25th European Signal Processing Conference (EUSIPCO)*. pp. 508-512, 2017.
- [107] Wilson, J., Toska, F., Levental, M., Dobbins, P., "A deep neural network model for hazard classification," *Artificial Intelligence and Machine Learning in Defence Applications*, pp. 1116903, 2019.
- [108] Bestagini, P., Lombardi, F., Lualdi, M., Picetti F., Tubaro, S., "Landmine Detection Using Autoencoders on Multipolarisation GPR Volumetric Data," *IEEE Transactions on Geoscience and Remote Sensing*, vol. 59, no. 1, pp. 182-195, 2021.
- [109] The Collaborative ORDNance (CORD) Data Repository, "PMA-1," [Online] Available at: <https://ordata.info/> [Accessed May 2019].

- [110] The Collaborative ORDNance (CORD) Data Repository, "PMA-2," [Online] Available at: <https://ordata.info/> [Accessed May 2019].
- [111] The Collaborative ORDNance (CORD) Data Repository, "PMA-3," [Online] Available at: <https://ordata.info/> [Accessed May 2019].
- [112] Peplinski, N. R., Ulaby, F. T., Dobson, M. C., "Dielectric properties of soils in the 0.3-1.3-GHz range," *IEEE Transactions on Geoscience and Remote Sensing*, vol. 33, no. 3, pp. 803-807, 1995.

Publications

This chapter presents publications where the author either led or made considerable contribution towards the reported work. Whether a publication is published, under review or accepted and pending publication at the time of the submission of this thesis is stated on the page before the paper. The contribution of the author towards the work for each paper, as well as how each paper relates to the objectives of the research are described below:

1. **Measuring the Magnetic Polarizability Tensor Using an Axial Multi-Coil Geometry:** This journal paper describes an instrument capable of measuring the rank 2 MPT of symmetrical metallic objects. The paper discusses the background mathematical theory, previous work measuring the rank 2 MPT and the instrument built including the coil array, system electronics and software. This work therefore satisfies the objectives 1, 2 and 3 of this research. The author was provided with a coil configuration design and a partially built coil array which were carried out as part of an MEng team project. The author reverse engineered and fully built the coil array. This involved modifying the parts which were not built as per the design documentation, rewiring, balancing, encapsulating and screening the coils, running performance tests and generally ensuring a durable coil array was built. The author also designed, simulated and built the system electronics, as well as the control and post-processing software. Finally, the author run the practical experiments for the results section of the paper.
2. **Measuring the Magnetic Polarizability Tensor of Non-Symmetrical Metallic Objects:** This journal paper describes a novel methodology which can be used with the instrument described in Publication 1 to measure the rank 2 MPT of non-symmetrical, irregular metallic objects. The paper describes a TOM which enables target orientations to give a wide interrogation of three-dimensional space, which better defines the inversion of the MPT problem, and the methodology required to acquire the full rank 2 MPT of the non-symmetrical objects. The author was initially provided with the TOM design with CAD drawings which were used by the author to 3D print and assemble the TOM. The paper describes the mathematical theory of rotations between different orientations of the TOM.

Finally, the author used this information to produce a post-processing software capable of calculating the rank 2 MPT from raw measurement data.

3. **A Study on the Magnetic Polarizability Tensors of Minimum Metal Anti-Personnel Landmines:** This conference paper presents and evaluates the rank 2 MPTs of four minimum metal anti-personnel landmines and their metal components measured during a measurement campaign at Fenix Insight Ltd in London. The author was responsible for running the practical experiments and evaluating the results. The author has also presented the work at the related conference as a poster.
4. **Measurement of GMPT Coefficients for Improved Object Characterisation in Metal Detection:** This journal paper describes the Generalised Magnetic Polarizability Tensor (GMPT) theory which includes higher rank MPT in the object characterisation. The paper then shows, for the first time, that GMPTs can be measured in practice. For this paper, the author was responsible for designing and manufacturing the TOM, which was used to rotate cone shaped metal objects outside of the uniform magnetic field region of the instrument described in the previous papers. The author also run the practical experiments which were used for the characterisation of the GMPTs of the cone shaped metal objects.
5. **Classification of Threat and Non-Threat Objects Using the Magnetic Polarizability Tensor and a Large-Scale Multi-Coil Array:** This paper describes a larger coil array which uses the same coil configuration with the coil array published in Publication 1. The coil array was built for measuring the rank 2 MPTs of small to medium sized firearms, such as pistols and SMGs. The large coil array was used during two measurement campaigns at the UK's National Firearms Centre (NFC) where rank 2 MPTs of around 120 threat objects were measured. The rank 2 MPTs of the threat objects were then combined with a number of non-threat object MPTs to generate two datasets. Unsupervised Machine Learning algorithms were then used to evaluate the clustering in the datasets. The author shared the workload of manufacturing the large coil array with the lead author of the paper, as well as the practical experiments run during the measurement campaigns at the NFC. The author also run the experiments for measuring the rank 2 MPTs of 90 non-threat objects. The author used the collected

data to generate two training datasets and applied a number of clustering algorithms (unsupervised machine learning) to the datasets for evaluating the clustering of the objects.

Publication 1

Özdeğer, T., Davidson, J. L., van Verre, W., Marsh, L. A., Lionheart, W. R. B., Peyton, A. J., "Measuring the Magnetic Polarizability Tensor Using an Axial Multi-Coil Geometry," *IEEE Sensors Journal*, vol. 21, no. 17, pp. 19322-19333, 2021. **Published.**

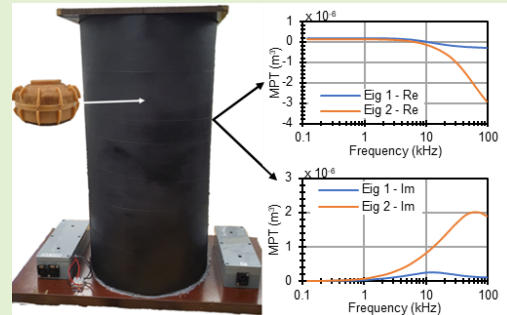
Doi: 10.1109/JSEN.2021.3088809.

Measuring the Magnetic Polarizability Tensor Using an Axial Multi-Coil Geometry

Toykan Özdeğer^{ID}, John L. Davidson^{ID}, Wouter van Verre^{ID}, Liam A. Marsh^{ID}, *Member, IEEE*, William R. B. Lionheart^{ID}, and Anthony J. Peyton^{ID}

Abstract—The Magnetic Polarizability Tensor (MPT) is a representative property of an electrically conducting or magnetic object that includes information about the object's characteristics such as, shape, size and material. The MPT is especially relevant to metal detection (MD) and can be used to improve MD performance by helping to distinguish between objects. This paper describes an instrument intended to measure the MPT of objects such as anti-personnel landmines and metallic clutter, up to 130 mm in diameter. The instrument uses a novel multi-coil geometry to generate a uniform electromagnetic field over the volume containing the test object to accurately determine the MPT. Performance tests of the system shows peak variance in the MPT is approximately 15 mm³. Typical experimental repeatability is better than one percent for tests involving copper disks. Additionally, simulated data as well as previously published simulated and experimental data are used as a validation method of the experimental results. Good agreement between these and the measured MPTs of example targets are seen, proving the system's capability of characterizing metallic objects.

Index Terms—Electromagnetic Induction Spectroscopy, Magnetic Polarizability Tensor, metal detection, metal classification.



I. INTRODUCTION

ANTI-PERSONNEL (AP) landmines continue to be a significant problem in post-conflict areas as they can remain armed long after the conflict has ended. Clearing an area of landmines is a slow and expensive process and so landmines may remain undisturbed for many years. This renders large areas of land unusable, preventing people from using this land for agriculture, social and economic activity, or housing. However, the biggest problem is that a landmine is victim activated and cannot distinguish between military personnel or civilians. Therefore, landmines in post-conflict areas mostly cause damage to non-military people [1], [2].

Manuscript received May 10, 2021; accepted May 28, 2021. Date of publication June 14, 2021; date of current version August 31, 2021. This work was supported in part by the Engineering and Physical Sciences Research Council under Grant EP/R002177 and in part by the Sir Bobby Charlton Foundation. The associate editor coordinating the review of this article and approving it for publication was Dr. Jürgen Kosel. (Corresponding author: Toykan Özdeğer.)

Toykan Özdeğer, John L. Davidson, Wouter van Verre, Liam A. Marsh, and Anthony J. Peyton are with the Department of Electrical and Electronics Engineering, The University of Manchester, Manchester M13 9PL, U.K. (e-mail: toykan.ozdeger@manchester.ac.uk; j.davidson-2@manchester.ac.uk; wouter.vanverre@manchester.ac.uk; liam.marsh@manchester.ac.uk; a.peyton@manchester.ac.uk).

William R. B. Lionheart is with the Department of Mathematics, The University of Manchester, Manchester M13 9PL, U.K. (e-mail: bill.lionheart@manchester.ac.uk).

Digital Object Identifier 10.1109/JSEN.2021.3088809

It is estimated that there are tens of millions of buried AP landmines worldwide, which means with the current rate of demining, it will take many years to clear all post-conflict areas of landmines [3], [4].

Metal detection (MD) has been the common way to detect landmines in humanitarian demining, which has more recently been augmented by ground penetrating radar (GPR). However, land in post-conflict areas usually have a high density of metallic clutter in the soil, which results in a high false alarm rate (FAR) from MD, which can hamper the demining process. In some fields, deminers can find 100 clutter objects for each landmine [5]. Clearly better differentiation would help.

The Magnetic Polarizability Tensor (MPT) is a representative electromagnetic object property, which depends on the size, material and shape of an object. Recent progress in mathematical theory has demonstrated that the MPT is the coefficient array in the first term in an asymptotic expansion of the perturbed field [6]–[9]. Although the motivation of this paper is toward humanitarian demining, the MPT and Electromagnetic Induction Spectroscopy have also been successfully applied widely in MD, for example to the detection of unexploded ordnance [10]–[12], walk-through metal detectors [13], metal recycling [14], workpiece recognition [15], non-destructive testing [16]–[18] and buried object detection [19]. MPT and broadband inductive sensing have also been previously proposed for landmine detection [20]–[25].

If an MPT library of landmines and common metallic clutter found in post-conflict areas are to be constructed, landmine detectors could utilize this library to reduce FAR and speed up the demining process, especially when coupled to secondary detection such as GPR.

Small-scale multiple coil arrangements have been reported in the area of induction spectrometry. For example, Goldfarb and Minervini [26] reported on the theory of mutual inductance applied to AC spectrometry for small cylindrical specimens. Additionally, West and Bailey [27] describe a simplistic six coil arrangement used for the measurement of the complex magnetic susceptibility of soils. However, those systems have not been used to produce absolute measurements of the MPT nor are of sufficient size to enable measurements to be taken on larger objects such as AP landmines.

Previously, Scott and Larson have established an experimental test facility [24], [25] which enables the measurement of the electromagnetic induction (EMI) response of target objects as a function of location and orientation. The facility includes a cart-based broadband EMI data collection system [28] and a laboratory-based positioner [29] with 3D automated translational and semi-automated rotational stages. Additionally, Scott and Larson developed dipole expansion and inversion techniques used to measure the magnetic susceptibility of soils and the polarizability of metallic objects [25], [30]. Reported targets have included coplanar metal loops, AP landmines and clutter items such as rifle cartridges and steel nails. Good agreement between measured and theoretical model parameters are presented for the case of single and triple conducting loop targets as a function of relaxation frequency.

At the University of Manchester, an MPT measurement system was previously built in [31], which was reported to characterize MPTs of AP landmine surrogates and small metal objects such as common clutter items found in post-conflict areas [32]. However, measurements from the coil arrangement were prone to drift, the system did not have a large region of uniform electromagnetic field for measuring larger AP landmines and was unable to characterize large objects due to the small size of the measurement space. Additionally, the previous system only utilized a simple target manipulator, which was unable to provide precise orientation of large targets.

This paper describes a new multi-coil arrangement with custom electronics system and software, which is better suited to the characterization of large objects such as landmines and landmine surrogates. A wider frequency spectrum was also used in the new system, extending to a lower frequency of 100 Hz, thereby improving the characterization of objects of lower conductivity and higher permeability. Commercial demining metal detectors do not presently provide direct MPT measurements. Additionally, although some experimental and laboratory-based systems [10]–[12], [28]–[30] have generated MPTs, these have often been for either large UXO type targets or for test objects which are difficult to replicate accurately in terms of size, shape, and material composition. Therefore, to assess the performance of the new system, we have compared the MPT data with previously obtained and published US coins MPT data from [33] and AP landmine MPT data from [32].

In this paper we start in Section II with describing the MPT, how it can be measured experimentally and the design of a coil arrangement for this purpose. Section III gives details of the experimental setup for the MPT measurement arrangement including the system electronics, controlling software for data acquisition and the target orientation manipulator. Section IV describes the methods used for characterization of the coils, assessment of overall system performance, setup calibration and acquisition of target data. Section V describes Finite Element Method (FEM) simulations of the coil arrangement and a sub-set of target objects. Section VI discusses the results of the coil characterization and system performance tests. The paper then shows the experimental results from the system and compares them with previously published measured and simulated data in section VII. Section VIII concludes the paper with a discussion of system potential and further work.

II. BACKGROUND

A. Magnetic Polarizability Tensor

Every conductive object gives a response to an applied electromagnetic field. In the eddy current approximation, the leading order term of the response is determined by the MPT of the object [34]. The MPT is an object specific property that depends on the shape, size, object's orientation and material composition. Consequently, when a metal detector generates an electromagnetic field near an object, the response that is measured by the receive coil is determined to a first approximation by the MPT [31]–[37]. The MPT in (1) is a 3×3 matrix of complex, frequency dependent coefficients. At a fixed frequency f , low enough for the eddy current approximation to be valid, the MPT matrix is symmetric and has six unique complex coefficients.

$$\mathbf{M}(f) = \begin{bmatrix} M'_{xx} + jM''_{xx} & M'_{xy} + jM''_{xy} & M'_{xz} + jM''_{xz} \\ M'_{yx} + jM''_{yx} & M'_{yy} + jM''_{yy} & M'_{yz} + jM''_{yz} \\ M'_{zx} + jM''_{zx} & M'_{zy} + jM''_{zy} & M'_{zz} + jM''_{zz} \end{bmatrix} \quad (1)$$

If constructing the MPT matrix by measurements, at least six complex suitably chosen measurements of the object are needed. However, in practice more orientations are used to improve accuracy [32]. The induced voltage V_{ind} in a receive coil, where I is the virtual electrical current in the receive coil satisfies (2). \mathbf{H} is the primary electromagnetic field as a vector representing the produced field by the coil in three-dimensional space, superscript T means transposed and subscript T and R correspond to transmit and receive coils, respectively.

$$V_{ind} \cong -j2\pi f \frac{\mu_0}{I} \mathbf{H}_T^T \mathbf{M} \mathbf{H}_R \quad (2)$$

To get coefficients in \mathbf{M} , multiple independent complex measurements of V_{ind} at each frequency are required for different transmitter and receiver field orientations to build a system of linear equations. To calculate all six unique components in the MPT matrix, the object should be rotated into at least six different orientations. By measuring V_{ind} and calculating alignment of \mathbf{H}_T and \mathbf{H}_R with the target, a linear equation for each orientation can be constructed using (2), where the only unknown is \mathbf{M} . Then, least squares method

can be used to calculate the MPT coefficients [38]. A nearly uniform electromagnetic field is needed near the object for this application as when non-uniform field is used, higher order terms in the asymptotic expansion also become apparent [9]. For calculating rotated electromagnetic fields of transmit and receive coils for each orientation, which are same for both coils if they are coaxial, rotation matrix can be used as in (3):

$$\mathbf{H}^1 = \mathbf{R} \mathbf{H}^0 \quad (3)$$

The MPT is frequency dependent, which means that measuring MPT at different frequencies provides a more detailed information set so a stronger basis for discrimination. However, the orientation dependency of the MPT makes it difficult to characterize a target object, where the orientation is unknown. Therefore, eigenvalues of the MPTs are used in classification, which are not orientation dependent. Eigenvalues of MPT are responses generated when the primary field is aligned with one of object's principal axes [39]. Diagonal matrix, Λ , in (4) shows eigenvalues of the MPT matrix \mathbf{M} .

$$\Lambda(f) = \begin{bmatrix} \Lambda_{xx}' + j\Lambda_{xx}'' & 0 & 0 \\ 0 & \Lambda_{yy}' + j\Lambda_{yy}'' & 0 \\ 0 & 0 & \Lambda_{zz}' + j\Lambda_{zz}'' \end{bmatrix} \quad (4)$$

B. Coil Design

To calculate the MPT of an object, the applied field needs to be accurately known. One of the key requirements of the system is to generate a parallel uniform magnetic field over a region of approximately 13 cm × 13 cm × 13 cm. This volume space being representative of a typical AP landmine or landmine surrogate [40]. To achieve uniformity over this volume the coil arrangement design is based on Helmholtz coil [41] principles and the application of the Biot-Savart Law.

According to Biot-Savart Law in (5), a magnetic field $\vec{\mathbf{B}}$ is produced when a current I passes through a conductor with linear segment $d\vec{\mathbf{L}}$, where $\vec{\mathbf{r}}^2$ is the displacement vector between point of observation and midpoint $\hat{\mathbf{r}}$:

$$\vec{\mathbf{B}} = \frac{\mu_0 I}{4\pi} \oint \frac{d\vec{\mathbf{L}} \times \hat{\mathbf{r}}}{\vec{\mathbf{r}}^2} \quad (5)$$

Circular coils could be represented by piecewise linear elements. The magnetic field generated by each coil segment can then be calculated using (5).

Individual coil arrangements of candidate systems were generated using bespoke MATLAB based code to calculate the field over the desired volume. Coil geometry variables included the number of coils, the coil positions and the number of turns. A bespoke optimizer algorithm utilizing the Biot-Savart Law and Helmholtz coil principles determined field distributions. The optimizer algorithm generated multiple geometries that could create a uniform field. One of the generated geometries from the optimizer was chosen that best satisfied the most appropriate practical coil arrangement.

III. EXPERIMENTAL SETUP

A. System Overview

The main system consists of three main parts, which are a coaxial coil arrangement, system electronics and control

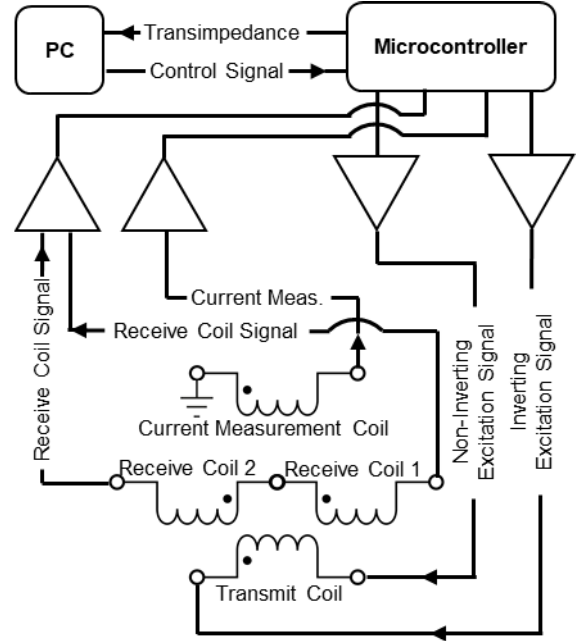


Fig. 1. System schematic showing signal routing between coils, electronics and the data acquisition PC.

software on a PC. The custom-made control software is used to transmit control signals e.g. frequency, amplitude and digital signal processing settings to a microcontroller. The microcontroller is then used to generate excitation signals for the power amplifiers driving the transmit coils. Measurement signals from the receive coils are filtered and amplified by bespoke receive electronics. These measurements are converted to transimpedance values by the microcontroller after applying digital signal processing (DSP) and sent to the PC. Value averaging and MPT inversion are then performed by the control software. The system schematic is shown in Fig. 1.

B. Coil Arrangement

The coil arrangement in Fig. 2 consists of a coaxial transmit coil with 240 mm diameter and two coaxial receive coils with 220 mm diameter. Additionally, a two-turn pick-up coil positioned at the base of the coils is used for current measurement. Position of the pick-up was deemed to give minimal interaction with target objects. Design of the coils are based on the method described in section II-B and the overall height of the resulting coil arrangement is 500 mm. The transmit coil is made up of 2.1 mm enamelled copper wire wound as nine separate coil sections (turns: 11:3:5:5:5:5:3:11) connected in series addition. The two receive coils are connected in series opposition with each coil made up of 1.2 mm PVC insulated wire wound as four coil sections (turn: 27:18:18:49:49:18:18:27). The coils are optimized for the range between 100 Hz to 100 kHz so the resonant frequencies of the transmit and receive coil impedances are outside of the operating frequency spectrum. All coils are wound around glass fibre reinforced plastic hollow cylinders and are encapsulated in epoxy resin. The arrangement is painted with conductive

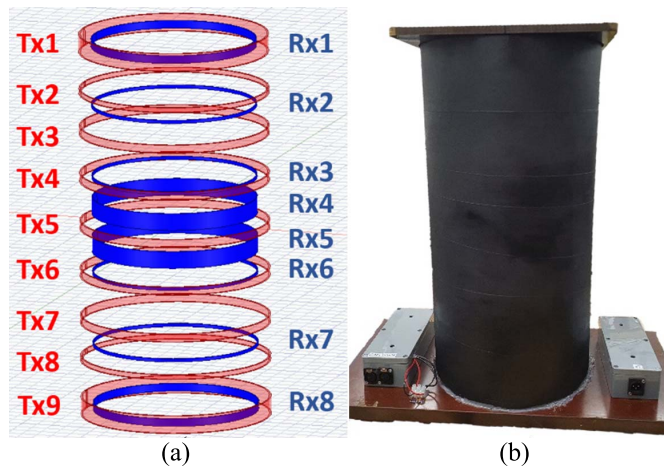


Fig. 2. The coil arrangement. Figure (a) is the schematic of the coil geometry and (b) the constructed coil arrangement.

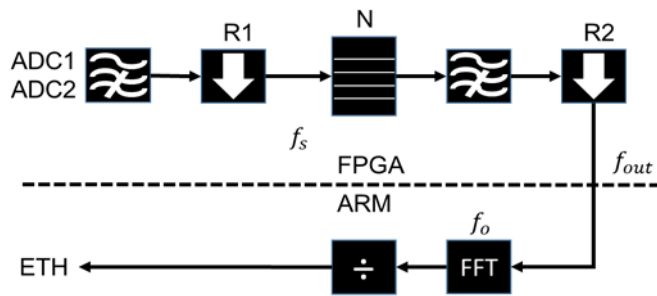


Fig. 3. Input data signal processing chain.

paint (surface resistivity: $55\Omega/\text{sq}/50$ microns) for electrostatic shielding.

C. Electronics

Main system electronics consists of transmit and receive electronics, power supply units and the microcontroller. The system is powered by two 18 V, 350 W power supply units (PSU) for the amplifiers and a 12 V, 80 W PSU for the microcontroller and electronics box cooling fans. A Red Pitaya model (STEMlab 125-14) is used as controller and signal processor for the system. The transmit electronics are implemented on a four-layer PCB and consists of an instrumentation amplifier, twenty power amplifiers and a band pass filter at the input for removing both AC and Digital-to-Analogue Converter's (DAC) switching noise. Half of the power amplifiers are configured as non-inverting while the rest are configured as inverting amplifiers. Each amplifier (Analog Devices LT 1210) is powered with ± 18 V and can output 32 V peak-to-peak voltage. By utilizing ten inverting and ten non-inverting configurations working in parallel in a differential configuration, the transmit circuit is able to output 64 V peak-to-peak at 10 A (640 W reactive power) to the transmit coil. Receive electronics consists of two identical circuits on two-layer PCBs, each consisting of an instrumentation amplifier (Analog Devices AD8429) and an active band-pass filter.

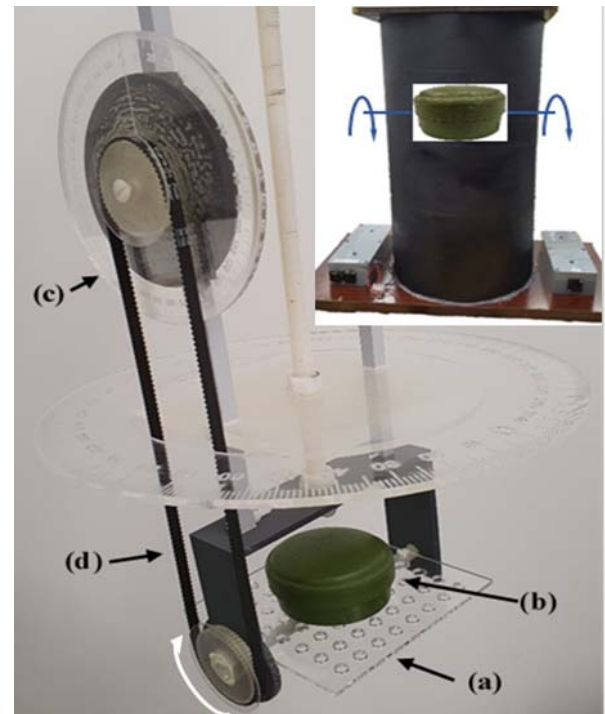


Fig. 4. Mechanical orientation manipulator 3D model showing (a) the target rotating plate, (b) Type 72A landmine surrogate, (c) measurement protractor and (d) the manually operated drive belt.

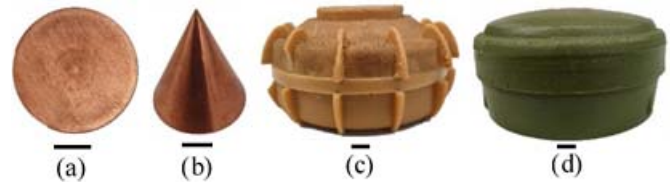


Fig. 5. Example target test objects showing copper disk, cone and AP landmine surrogates. Object (a) copper disk viewed from above and measuring 30 mm in diameter and 2 mm in thickness, (b) copper cone measuring 30 mm in height with a 30 mm diameter base, (c) TS-50 landmine surrogate and (d) Type 72A landmine surrogate. Black lines under each object represent a centimeter for scale.

D. Data Acquisition and Digital Signal Processing

The data acquisition and processing are performed by a Xilinx Zynq7000 system-on-chip (SoC), combining a dual-core ARM Cortex A7 processing and Xilinx 7-series FPGA. The SoC is mounted on a Red Pitaya, which also includes two 125 MSPS, 14-bit, Analogue-to-Digital Converter (ADC) channels and two DAC channels, also at 125 MSPS and 14-bits. The ADCs and DACs are interfaced with the FPGA fabric in the SoC, to ensure accurate timing between all four channels. The system is modified from one previously designed spectroscopic metal detector [42], [43]. The data processing on the SoC is split between the FPGA fabric and the ARM cores; the full processing chain is shown in Fig. 3 in block form.

The first step is a down sampling low-pass filter (with rate $R1$), followed by a step, which generates blocks with N samples. These blocks are then further down sampled (by a

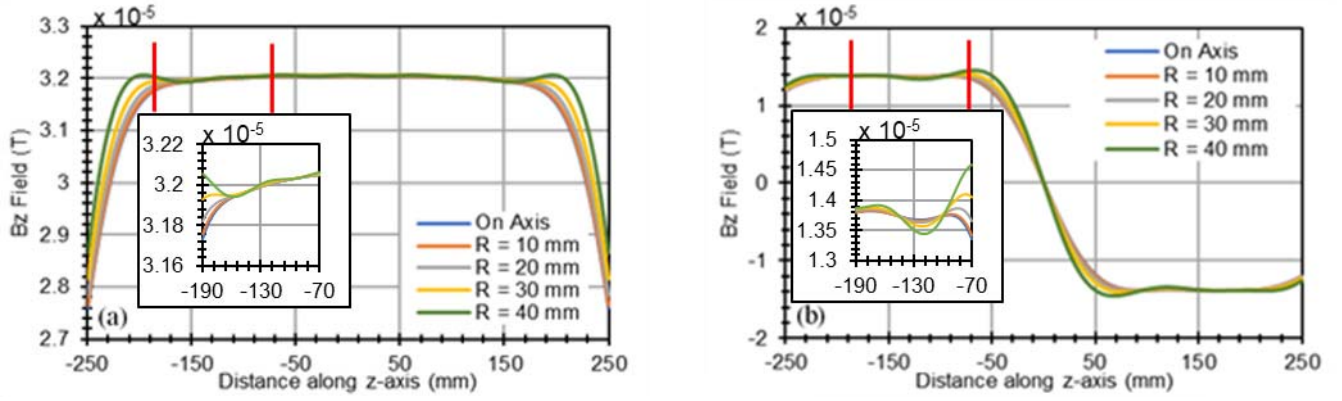


Fig. 6. Simulations of the magnetic field inside the coil system for the non-target case when transmit and receive coils are individually driven by an electric current; (a) transmit coil and (b) receive coil excitation. The measurement region is between the red vertical lines shown in the figure. The subplots within the figure show the field data within the measurement region at an enhanced scale.

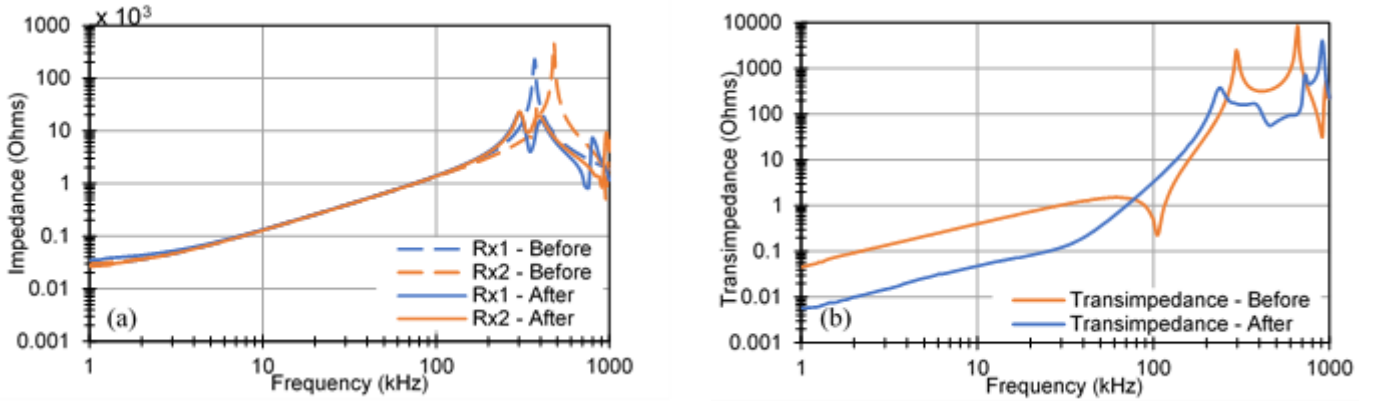


Fig. 7. (a) shows individual impedance curves of the receive coils before and after balancing the impedances while (b) shows the transimpedance between transmit coil and the receive coils, connected in series opposition, before and after the receive coils were balanced.

rate $R2$) and sent to the ARM cores. The samples are then transformed using an N -point RFFT and the harmonics of interest are extracted. The final output is calculated by dividing the extracted harmonics from $ADC1$ by $ADC2$, to calculate the transimpedance. The results are transmitted to the host PC via Ethernet, using Linux on the ARM processor. The effective sampling frequency, output data rate and the fundamental frequency of the system are given in (6), (7) and (8) respectively, where ADC frequency (f_{ADC}) is always 125 MSPS.

$$f_s = \frac{f_{ADC}}{R1} \quad (6)$$

$$f_{out} = \frac{f_s}{N \times R2} \quad (7)$$

$$f_0 = \frac{f_s}{N} \quad (8)$$

The output signal path consists of a lookup table in the FPGA (of length N) for the transmit signal, which is read at the sampling frequency f_s . The data can be output at this rate, or up sampled to f_{ADC} via a linear interpolator or cascaded integrator-comb filter, which can be configured at runtime. The parameters $R1$, $R2$ and N are also configurable at runtime, so that the sampling frequency, fundamental frequency and output frequencies can be configured depending on the

application needs. A low fundamental frequency reduces the acquisition speed of the system. Therefore, in this experiment the parameters $R1$ and N were changed as the frequency sweep progresses. This allows for granular sweep at low frequencies, while speeding up the acquisition rate at higher frequencies.

E. Control Software

The control software was written in Python 3.7 and allows the user to set experiment settings by a graphical user interface (GUI). The control of frequency sweeps, data logging and processing, MPT inversion and plotting are done automatically by the control software. The final output folder contains raw data, calibrated transimpedance values and MPT eigenvalues.

F. Target Orientation Manipulator

The custom-built target orientation manipulator shown in Fig. 4 is used to place and rotate objects in the coil arrangement, which has rotational precision of approximately 1° . It is manually operated and can rotate target objects around one axis. This means that only objects with symmetrical geometry can be measured as this methodology assumes the axis of rotation is aligned with an eigenvector of the object.

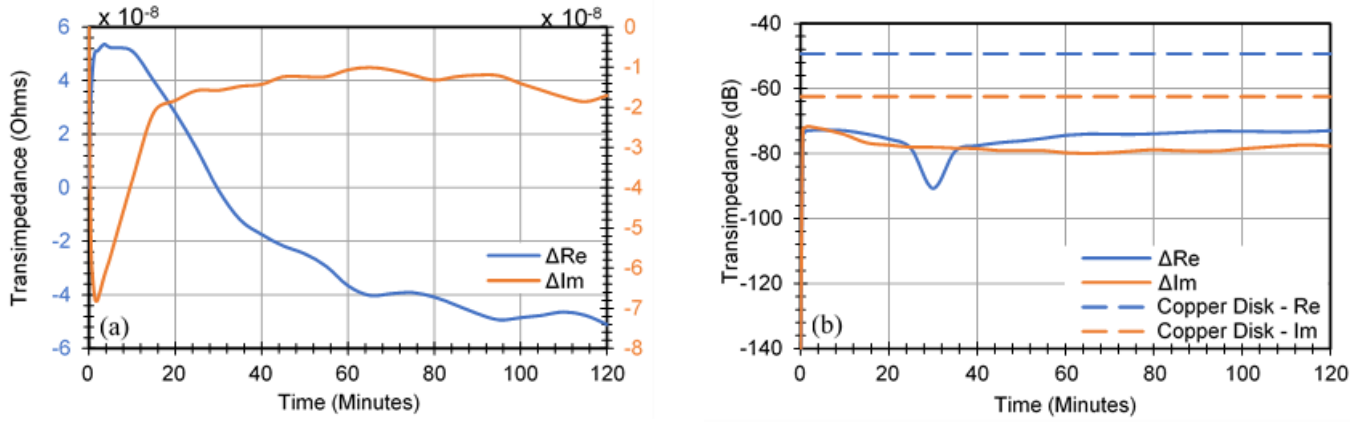


Fig. 8. Drift measurement data showing (a) the drift in measured real and imaginary transimpedance values plotted versus time and (b) absolutes of measured drift in real and imaginary transimpedance values in dB scale compared with the copper disk at 50 kHz.

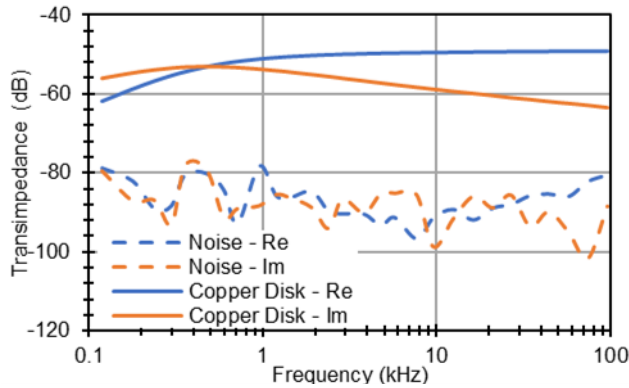


Fig. 9. Absolute of real and imaginary transimpedance values of example copper disk data compared with noise in dB scale.

IV. METHOD

An impedance analyser (*Solatron 1260A*) was used to measure the impedance characteristics of the coil arrangement. This was performed for the nine transmit coils connected in series wound in the same sense. This was also repeated for each receive coil. Impedance measurements were repeated five times to eliminate any error originating from noise contributions.

Before starting an experiment, all settings were set using the GUI and the system was left running for at least half an hour. This enabled the system to reach a steady-state temperature and minimize measurement drift caused by system temperature changes. Additionally, all experiments were performed in a temperature-controlled environment to prevent significant ambient temperature changes, in order to minimize thermal drift. A background measurement was first taken with no object in the coils. Then, this was subtracted from the measurements with the target object in the coils. After this, a NiZn ferrite rod (Ferroxcube ROD10/40-4B2-L) was placed in the coils for calibration as a pure real response is expected from the rod across the frequency range used. Phase correction for each frequency was done according to the ferrite rod's results using (9). The correction values were then restored and

applied to all subsequent target measurements.

$$Z_{Calibrated} = Z_0 \times \frac{e^{-j\theta}}{|Z_0|} \quad (9)$$

The noise floor of the system was quantified by performing measurements with no object in the coils and then subtracting the background field from the measurements. Measurement drift was quantified by measuring transimpedance with no target object in the coils over a defined time scale and using the same background subtraction method for all measurements. Experimental repeatability was evaluated by repeating the same measurement protocol with a copper disk for ten times over a period of 48 hours. Each separate measurement lasted one hour and was temporally spaced by approximately two hours.

MPTs were acquired by rotating each target object in the coils twenty-four times with fifteen-degree steps using the target orientation manipulator in Fig. 4. After each rotational increment, the background field subtraction was updated to further minimize drift and improve experimental repeatability. After all orientations were measured, the control software calculated the MPTs and output MPT eigenvalues and the associated plots. A subset of target objects is shown in Fig. 5. The landmine surrogates were provided by Fenix Insight UK.

V. COIL GEOMETRY MODELING AND SIMULATIONS

The simulation geometry comprised of an outer free-space region and the coil arrangement simplified into segmented 3D rings of the nine transmit and eight receive coils as shown in Fig. 2(a). Coil excitation used current distributions normalized to the transmit coil with the fewest number of turns. Simulations for comparison with experimental measurements involved the rotation of the target object positioned in the most sensitive and uniform field region of the coil arrangement. Target rotations used 15° increments from 0° to 345° at either single fixed frequencies or spectroscopically in the range of 10 Hz to 100 MHz in ten logarithmic increments per decade. For disk targets typical meshing involved a FEM model of approximately 150k tetrahedral elements in total per rotational geometry with between 12k to 20k elements

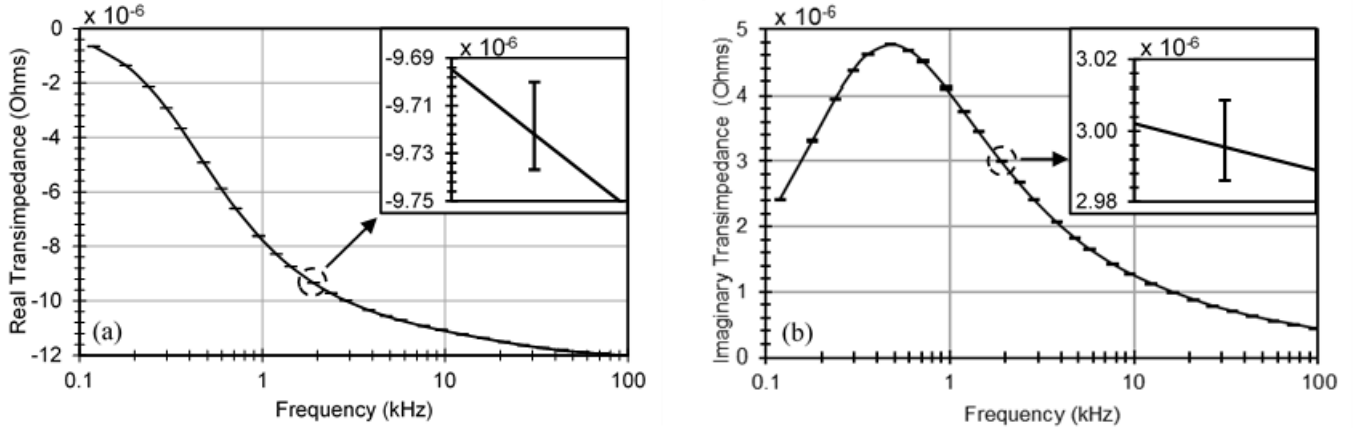


Fig. 10. Average of the transimpedance values of ten consecutive experiments with error bars showing the range of maximum and minimum values for each transimpedance. Plots show (a) real and (b) imaginary transimpedance values. The deviation in the data is approximately two orders of magnitude smaller compared with the absolute transimpedance values, which gives the appearance of single horizontal tick lines for the plotted error bars in the main plots. The upper right insert region in the plots shows the typical small deviation across the experiments, which is not easily discernible in the main plots. This is quantified in TABLE I.

per disk. This increasing to approaching 200k tetrahedral elements per whole FEM and approximately 30k elements for simulations involving cone targets. For the non-target case, 2D axial-symmetric- simulations were carried out to assess the field uniformity of the coil arrangement as shown in Fig. 6. The uniformity was verified by measuring the MPT of a stainless-steel ball bearing of 1 cm in diameter at various locations on and off-axis within the measurement region. The standard deviation of the MPT was found to be 30 mm³, which is the same order of magnitude as the noise floor. Simulations were performed using the FEM solver, *Maxwell*, (*Ansys Electromagnetics Suite, Release 19.2*).

VI. COIL CHARACTERIZATION AND SYSTEM PERFORMANCE

Although both receive coils were designed to be identical, in practice, their impedances across the adopted frequency range were not the same. Coil Rx1 was found to exhibit a resonance peak at 371 kHz, while coil Rx2 yielded a resonance peak at approximately 478 kHz, due to differing lengths and spacing of constituent wires. To reduce the resonance effects, a parallel capacitance of 15 pF was used. Additionally, a parallel resistance of 43 k Ω was added to coil Rx1 and 56 k Ω was added to coil Rx2. The effect of the additional passive components on linearity and resonance is shown in Fig. 7(a). The addition of the passive component networks has effectively increased the linearity towards the higher end of the operating frequency spectrum. The measured transimpedance between the transmit and the receive coils are shown in Fig. 7(b). As seen from the plot, the resonance frequency is approximately 250 kHz, which is above the maximum operating frequency of the system.

System performance was measured by evaluating measurement drift, the noise floor characteristics and experimental repeatability. From the measured drift curves shown in Fig. 8(a), it can be clearly seen that most of the drift happens in the first sixty minutes. The results of the drift measurement were then compared to the transimpedance measurements of the copper disk at 50 kHz, shown as straight dashed lines,

in Fig. 8(b). Time interval to update the background was determined by evaluating this figure. The measured noise floor was compared to transimpedance measurements of a copper disk having a diameter of 30 mm and thickness of 2 mm as shown in Fig. 9 in dB scale. As can be seen, there is a minimum of 20 dB difference between noise floor and signal across the measured frequency spectrum. In addition, the variance in MPT measurements is between -78 dB and -100 dB, which is approximately 15 mm³.

Quantification of experimental repeatability was evaluated by using the largest and smallest values of the MPT eigenvalues for a given frequency in normalized RMS error (NRMSE) as defined by (10). In the NRMSE equation, n is number of measurement frequencies, $Expt_i$ is the maximum or minimum transimpedance value at frequency i , $Expt(Avg)_i$ is the average of the transimpedance values for frequency i and $\overline{Expt(Avg)}$ is the average of average transimpedance values for all frequencies. Lower NRMSE values mean better experimental repeatability.

$$NRMSE = \frac{\sqrt{\frac{\sum_{i=1}^n (Expt_i - Expt(Avg)_i)^2}{n}}}{\overline{Expt(Avg)}} \quad (10)$$

TABLE I presents the NRMSE values for the copper disk. Fig. 10 also shows the variation of eigenvalues from all experiments for each frequency compared to the average using error bars, where most of the maximum and minimum values can only be discerned as a single line. This represents a typical result of only 0.54% average difference between maximum and minimum real transimpedance values and 0.62% imaginary transimpedance values across all frequencies, which indicates excellent experimental repeatability.

VII. RESULTS

MPTs of various objects were measured with the multi-coil arrangement and compared. A range of US Dollar coins were compared with simulations and measurements acquired from our previous measurement system, which were published in [32], [33]. Both simulations and previous measurements

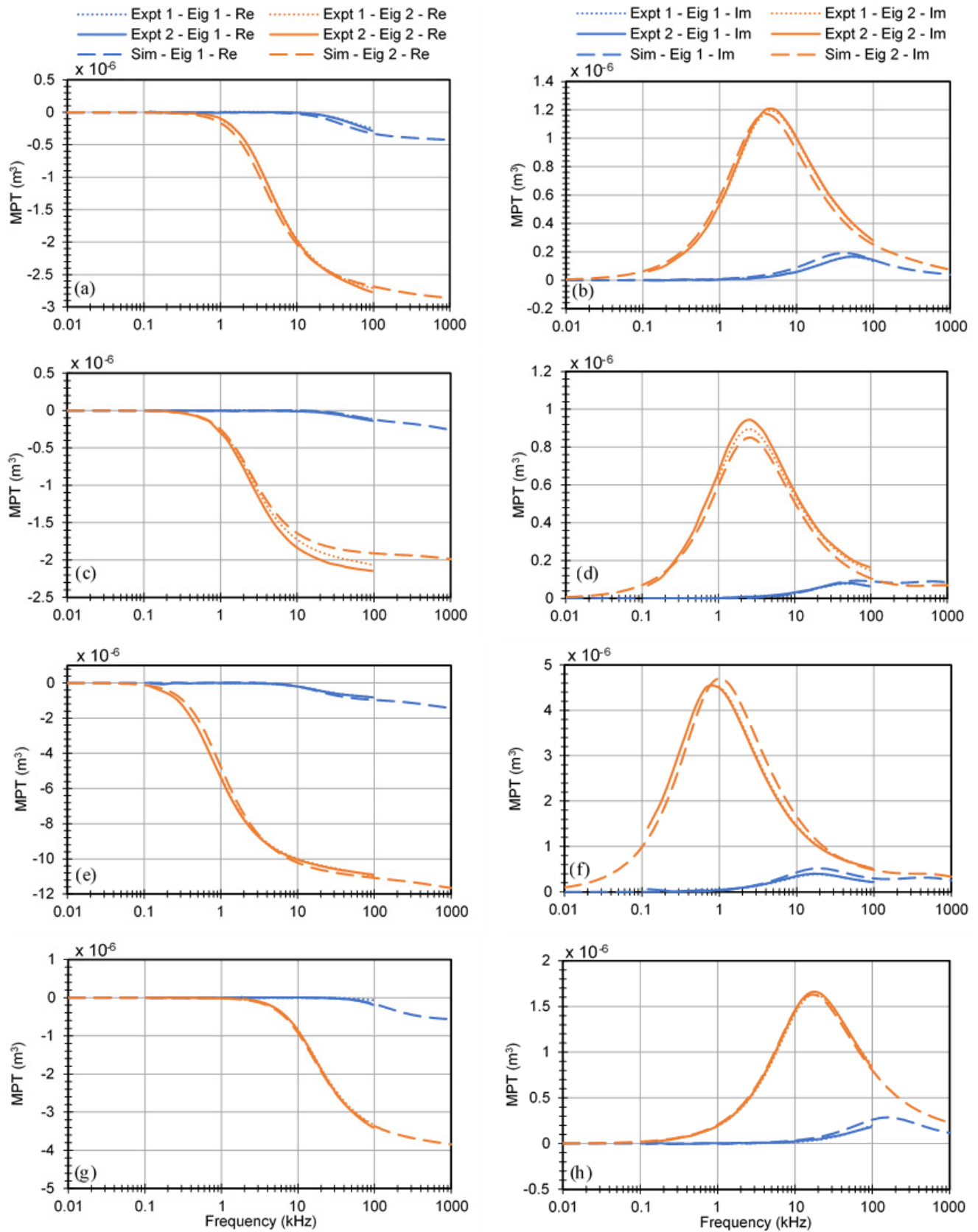


Fig. 11. Measured real and imaginary MPT eigenvalues for US coinage, compared with simulated and previously published MPT results are shown. Plots (a-b) one cent, (c-d) dime, (e-f) half dollar and (g-h) nickel. Expt 1 and Sim are values for experimental and simulated results from [33] while Expt 2 is experimental data from the new system.

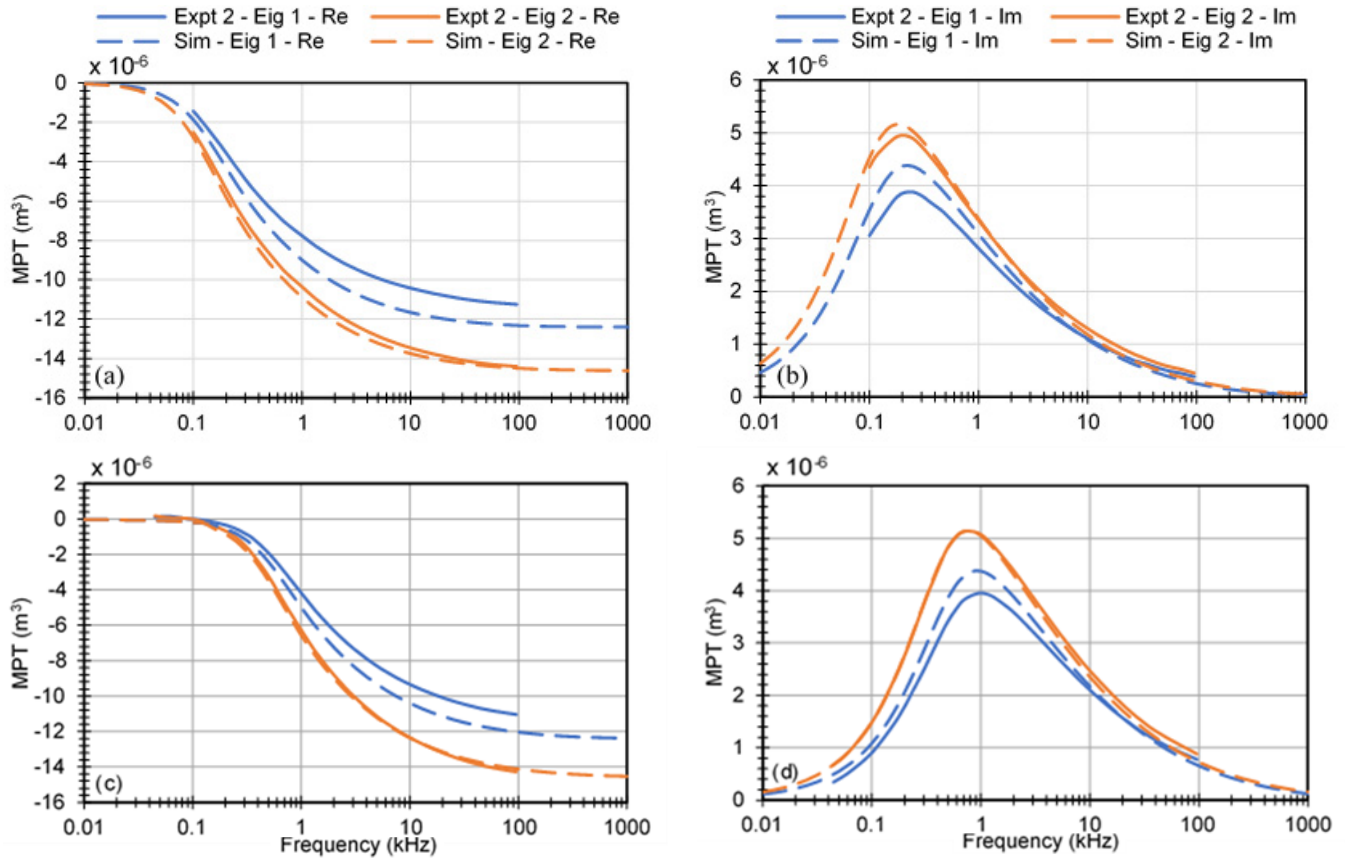


Fig. 12. Real and Imaginary MPT eigenvalues of two geometrically identical cones, which are 30 mm in both diameter and height. Plots (a-b) copper and (c-d) brass cones, respectively. Expt is experimental data from the new system and Sim is the simulated data. Conductivity of 58 MS/m and 13.9 MS/m were used for copper and brass cones, respectively.

TABLE I

NRMSE OF DIFFERENCES BETWEEN MAXIMUM AND MINIMUM TRANSIMPEDANCE EIGENVALUES COMPARED TO THE AVERAGE

	Real Eigenvalues		Imaginary Eigenvalues	
	Min	Max	Min	Max
Copper Disk	0.0017	0.0023	0.0033	0.0037

of objects' MPTs were used as a verification method of the system's ability to measure MPTs of objects, as MPTs are object specific and do not change depending on how they are obtained. Additionally, measured MPT's were compared with FEM simulations of copper and brass cones.

Fig. 11 shows objects measured, which are compared with both simulations and previous measurements, Fig. 12 shows objects measured, which are compared with simulations and Fig. 13 compares measured surrogate landmines with previous measurements. NRMSE values are shown for the experimental results in TABLE II compared with both previously published measured and simulated MPTs where available. NRMSE values comparing recent and past experimental data are shown in *Experimental Eigenvalues* column while the NRMSE values comparing recent experimental data with simulated data are shown in *Simulated Eigenvalues* column.

There is good agreement between experimental results for US coins with our previously published simulated and

TABLE II

NRMSE OF DIFFERENCES BETWEEN MEASURED MPT EIGENVALUES COMPARED TO THE PREVIOUSLY PUBLISHED MEASURED AND SIMULATED MPT EIGENVALUES

	Experimental Eigenvalues				Simulated Eigenvalues			
	Eigenvalue 1		Eigenvalue 2		Eigenvalue 1		Eigenvalue 2	
	Re	Im	Re	Im	Re	Im	Re	Im
One Cent	0.270	0.052	0.023	0.025	0.516	0.300	0.073	0.091
Nickel	3.290	0.138	0.044	0.025	0.367	0.535	0.046	0.042
Dime	0.618	0.061	0.059	0.066	0.755	0.304	0.146	0.142
Half Dollar	0.072	0.043	0.009	0.021	0.273	0.305	0.042	0.108
Copper Cone	N/A	N/A	N/A	N/A	0.117	0.127	0.033	0.057
Brass Cone	N/A	N/A	N/A	N/A	0.125	0.095	0.033	0.039
Type 72A	0.370	0.032	0.597	0.048	N/A	N/A	N/A	N/A
TS-50	4.863	0.278	0.250	0.105	N/A	N/A	N/A	N/A

experimental data. For example, for the one-cent coin, recent experimental data acquired from the multi-coil arrangement, labelled Expt 2 follow the same curve with previously published experimental data, labelled Expt 1. Magnitudes and the horizontal positions of loss-peaks are within two percent for both eigenvalues. Loss-peak magnitudes for simulation and

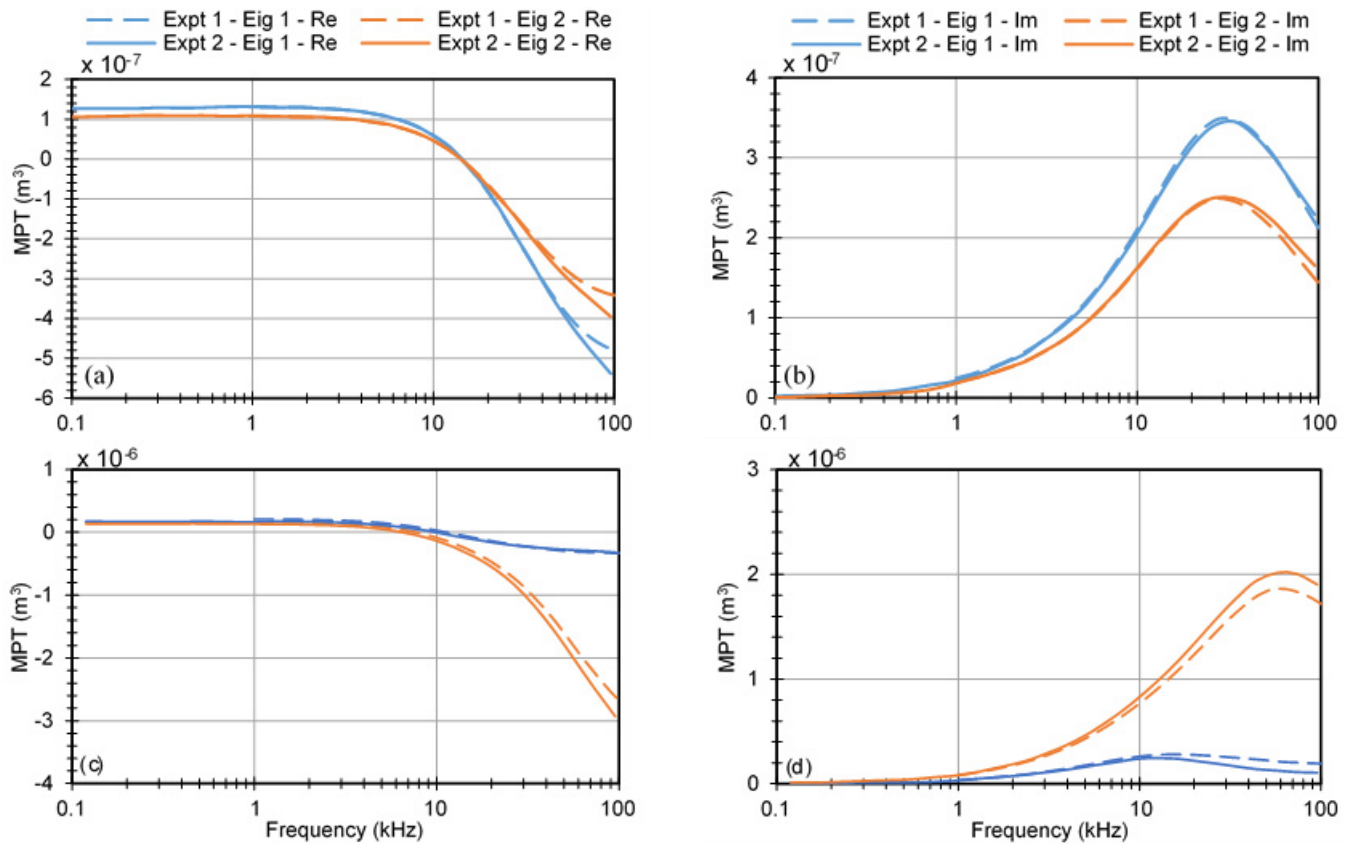


Fig. 13. Real and imaginary MPT eigenvalues of target anti-personnel landmines. Plot (a-b) Type-72A landmine surrogate and (c-d) TS-50 landmine surrogate. Expt 1 refers to previous experimental data from [32] and Expt 2 is for the experimental data from the new system.

experimental data are within twelve and three percent of each other for eigenvalue one and two, respectively.

Additionally, the magnitude of the measured MPT and frequency of the loss peak of the one cent coin are the same order of magnitude with the work of Scott and Larson [29]. However, a full comparison cannot be made as only five frequency points were presented in [29] while thirty are used in our system. Furthermore, [29] does not present full real and imaginary eigenvalue components which would allow for a direct comparison with our work.

The main source of error between experimental data collected with the new system and previous simulated data for US coins from [33] is due to simulation models assuming coins only to be simple cylinders with no attempt to describe additional geometrical features e.g. reeded edges, legend or design relief. Additionally, material composition of the coins was also assumed to be homogenous in simulations while this is not the case in physical reality, as coins are made of complex alloys. The inability of the FEM process to accurately describe the true physical and electrical nature of coins is more fully described in [33].

For cone shaped targets in Fig. 12 the overall agreement between experiment and simulation data are also generally good, with the FEM results validating the experimental data acquired from the coil arrangement. For example, for the copper cone, loss-peak magnitudes between experimental and simulated MPTs for eigenvalue 1 are within ten percent of each

other and are within five percent for eigenvalue 2. Position of the loss-peaks in the frequency spectrum are within ten percent of each other for eigenvalue 1 and seven percent for eigenvalue 2. Such differences are to be expected due to the FEM model only being an approximate geometrical representation of the actual physical coil arrangement in terms of e.g. conductor thickness, coil positions and diameters. Additionally, for computational simplicity, the FEM model describes both transmit and receive coils as simplified segmented polygons. Similarly, to constrain the meshing level within the FEM, targets such as cones have been simplified using rounded edges, which are not present in physical reality. Simplifications of this type are a necessary trade-off between modelling accuracy and the available computational resources.

There is also a good agreement between measured surrogate landmine MPTs with previously published measured data. Magnitudes and the horizontal positions of the loss-peaks are within two percent of each other for the Type-72A surrogate landmine and within five percent for the TS-50 surrogate landmine. There is an upward trend towards the end of the spectrum of real MPT eigenvalues measured by the previous system for Type-72A surrogate landmine. This is potentially caused by the generated magnetic field not being entirely uniform in the previous system for the volume covered by the landmine. In addition, the higher NRMSE values for real MPT eigenvalues for both landmines are caused by the MPT curves changing signs through the frequency spectrum.

VIII. CONCLUSION AND FUTURE WORK

A multi-coil arrangement system has been designed and constructed for accurately measuring MPTs of anti-personnel (AP) landmines and similar sized metallic objects. Noise and drift performance of the system in addition to experimental repeatability have been presented. Experimental results were compared with previously published simulated and experimental data, which proved the ability of the system for measuring MPTs of objects. This verified the ability of the system to measure MPTs accurately. The novelty of the presented coil arrangement is its ability to generate a primary field of sufficient uniformity to satisfy the rank-2 MPT dipole approximation described by (2) for three-dimensional target interrogation of large objects such as AP landmines.

Measuring MPTs of non-symmetrical objects by improving software and building a target orientation manipulator that can automatically rotate objects in three-dimensional space are the main areas of future work. This will then allow the building of a comprehensive MPT library containing anti-personnel landmines and common metallic clutter found in post-conflict areas. The future challenge will be to apply such a library initially to aid in the development of efficient metal detection algorithms and subsequently, to provide a real-time comparison within the field with metal detection technology capable of providing direct MPT measurements. However, to utilize the MPT in practical demining operations several challenges need to be addressed to discriminate between clutter items and AP landmines. In particular, multiple lateral sensor spacing needs to exist to correctly interrogate the target in three-dimensional space for MPT inversion. Additionally, highly magnetic soils pose a challenge for accurate MPT measurement due to the electromagnetic behaviour of soils [44]. The issues of lateral and multiple coil spacing has been described in [10], [12] and is the topic of ongoing research in [19]. Once these issues are further understood, laboratory-based instruments for accurately measuring MPTs such as the one presented in this paper, will be vital in aiding the reduction of false alarms in the field.

REFERENCES

- [1] *What Is a Landmine?* Int. Campaign Ban Landmines, Geneva, Switzerland, 2019.
- [2] *Facts About Landmines*, CARE, Noida, India, 2019.
- [3] *Landmine Monitor*, Int. Campaign Ban Landmines, Geneva, Switzerland, 2019.
- [4] *The Landmine History Page*, Fed. Amer. Scientists, Washington, DC, USA, 2019. [Online]. Available: <https://fas.org/asmp/campaigns/landmines/lmhistory.htm>
- [5] K. Tsipis, "Technological innovation in humanitarian demining," in *Proc. Hum. Factors Ergonom. Soc.*, Santa Monica, CA, USA, 1998, pp. 750–753.
- [6] P. D. Ledger and W. R. B. Lionheart, "Understanding the magnetic polarizability tensor," *IEEE Trans. Magn.*, vol. 52, no. 5, pp. 1–16, May 2016.
- [7] P. D. Ledger and W. R. B. Lionheart, "An explicit formula for the magnetic polarizability tensor for object characterization," *IEEE Trans. Geosci. Remote Sens.*, vol. 56, no. 6, pp. 3520–3533, Jun. 2018.
- [8] P. D. Ledger and W. R. B. Lionheart, "The spectral properties of the magnetic polarizability tensor for metallic object characterisation," *Math. Methods Appl. Sci.*, vol. 43, no. 1, pp. 78–113, Jan. 2020.
- [9] P. D. Ledger and W. R. B. Lionheart, "Generalised magnetic polarizability tensors," *Math. Methods Appl. Sci.*, vol. 41, no. 8, pp. 3175–3196, May 2018.
- [10] J. P. Fernandez, B. E. Barrowes, T. M. Grzegorzczak, N. Lhomme, K. O'Neill, and F. Shubitidze, "A man-portable vector sensor for identification of unexploded ordnance," *IEEE Sensors J.*, vol. 11, no. 10, pp. 2542–2555, Oct. 2011.
- [11] S. J. Norton and I. J. Won, "Identification of buried unexploded ordnance from broadband electromagnetic induction data," *IEEE Trans. Geosci. Remote Sens.*, vol. 39, no. 10, pp. 2253–2261, Oct. 2001.
- [12] T. M. Grzegorzczak, B. E. Barrowes, F. Shubitidze, J. P. Fernandez, and K. O'Neill, "Simultaneous identification of multiple unexploded ordnance using electromagnetic induction sensors," *IEEE Trans. Geosci. Remote Sens.*, vol. 49, no. 7, pp. 2507–2517, Jul. 2011.
- [13] J. Makkonen *et al.*, "KNN classification of metallic targets using the magnetic polarizability tensor," *Meas. Sci. Technol.*, vol. 25, no. 5, May 2014, Art. no. 055105.
- [14] M. D. O'Toole, N. Karimian, and A. J. Peyton, "Classification of nonferrous metals using magnetic induction spectroscopy," *IEEE Trans. Ind. Informat.*, vol. 14, no. 8, pp. 3477–3485, Aug. 2018.
- [15] Y. Tao, W. Yin, W. Zhang, Y. Zhao, C. Ktistis, and A. J. Peyton, "A very-low-frequency electromagnetic inductive sensor system for workpiece recognition using the magnetic polarizability tensor," *IEEE Sensors J.*, vol. 17, no. 9, pp. 2703–2712, May 2017.
- [16] J. García-Martín, J. Gómez-Gil, and E. Vázquez-Sánchez, "Non-destructive techniques based on eddy current testing," *Sensors*, vol. 11, no. 3, pp. 2525–2565, Feb. 2011.
- [17] L. U. Daura, G. Tian, Q. Yi, and A. Sophian, "Wireless power transfer-based eddy current non-destructive testing using a flexible printed coil array," *Phil. Trans. Roy. Soc. A, Math., Phys. Eng. Sci.*, vol. 378, no. 2182, Oct. 2020, Art. no. 20190579.
- [18] M. Lu *et al.*, "Determination of surface crack orientation based on thin-skin regime using triple-coil drive-pickup eddy-current sensor," *IEEE Trans. Instrum. Meas.*, vol. 70, Dec. 2021, Art. no. 6003509.
- [19] D. Ambrus, D. Vasic, and V. Bilas, "Comparative study of planar coil EMI sensors for inversion-based detection of buried objects," *IEEE Sensors J.*, vol. 20, no. 2, pp. 968–979, Jan. 2020.
- [20] Y. Zhao, W. Yin, C. Ktistis, D. Butterworth, and A. J. Peyton, "Determining the electromagnetic polarizability tensors of metal objects during in-line scanning," *IEEE Trans. Instrum. Meas.*, vol. 65, no. 5, pp. 1172–1181, May 2016.
- [21] B. Dekdouk, C. Ktistis, L. A. Marsh, D. W. Armitage, and A. J. Peyton, "Towards metal detection and identification for humanitarian demining using magnetic polarizability tensor spectroscopy," *Meas. Sci. Technol.*, vol. 26, no. 11, Nov. 2015, Art. no. 115501.
- [22] D. Ambrus, D. Vasic, and V. Bilas, "Innovating on top of I&M fundamentals for safer humanitarian demining," *IEEE Instrum. Meas. Mag.*, vol. 23, no. 3, pp. 35–41, May 2020.
- [23] Y. Dalichaouch *et al.*, "Wideband frequency response of low-metal mines," *Proc. SPIE, Detection Remediation Technol. Mines Minelike Targets IX*, vol. 5415, Sep. 2004, doi: [10.1117/12.547340](https://doi.org/10.1117/12.547340).
- [24] W. R. Scott and G. D. Lars, "Modeling the measured em induction response of targets as a sum of dipole terms each with a discrete relaxation frequency," in *Proc. IEEE Int. Geosci. Remote Sens. Symp.*, Honolulu, HI, USA, Jul. 2010, pp. 4188–4191.
- [25] G. D. Larson and W. R. Scott, Jr., "Automated, non-metallic measurement facility for testing and development of electromagnetic induction sensors for landmine detection," *Proc. SPIE, Detection Sens. Mines, Explosive Objects, Obscured Targets XIV*, vol. 7303, May 2009, Art. no. 73030X, doi: [10.1117/12.819855](https://doi.org/10.1117/12.819855).
- [26] R. B. Goldfarb and J. V. Minervini, "Calibration of AC susceptometer for cylindrical specimens," *Rev. Sci. Instrum.*, vol. 55, no. 5, pp. 761–764, May 1984.
- [27] G. F. West and R. C. Bailey, "An instrument for measuring complex magnetic susceptibility of soils," *Proc. SPIE, Detection Remediation Technol. Mines Minelike Targets X*, vol. 5794, Jun. 2005, doi: [10.1117/12.602992](https://doi.org/10.1117/12.602992).
- [28] W. R. Scott, "Broadband array of electromagnetic induction sensors for detecting buried landmines," in *Proc. IEEE Int. Geosci. Remote Sens. Symp. (IGARSS)*, Boston, MA, USA, Jul. 2008, pp. II-375–II-378.
- [29] W. R. Scott and G. D. Larson, "Measured dipole expansion of discrete relaxations to represent the electromagnetic induction response of buried metal targets," in *Detection and Sensing of Mines, Explosive Objects, and Obscured Targets XV*, 2010, Art. no. 76640E.
- [30] W. R. Scott and M. McFadden, "Wideband measurement of the magnetic susceptibility of soils and the magnetic polarizability of metallic objects," in *Proc. IEEE Int. Geosci. Remote Sens. Symp.*, Munich, Germany, Jul. 2012, pp. 3170–3173.
- [31] O. A. Abdel Rehim, J. L. Davidson, L. A. Marsh, M. D. O'Toole, D. W. Armitage, and A. J. Peyton, "Measurement system for determining the magnetic polarizability tensor of small metal targets," in *Proc. IEEE Sensors Appl. Symp. (SAS)*, Zadar, Croatia, Apr. 2015, pp. 1–5.

- [32] O. A. Abdel-Rehim, J. L. Davidson, L. A. Marsh, M. D. O'Toole, and A. J. Peyton, "Magnetic polarizability tensor spectroscopy for low metal anti-personnel mine surrogates," *IEEE Sensors J.*, vol. 16, no. 10, pp. 3775–3783, May 2016.
- [33] J. L. Davidson, O. A. Abdel-Rehim, P. Hu, L. A. Marsh, M. D. O'Toole, and A. J. Peyton, "On the magnetic polarizability tensor of US coinage," *Meas. Sci. Technol.*, vol. 29, no. 3, Mar. 2018, Art. no. 035501.
- [34] P. D. Ledger and W. R. B. Lionheart, "Characterizing the shape and material properties of hidden targets from magnetic induction data," *IMA J. Appl. Math.*, vol. 80, no. 6, pp. 1776–1798, 2015.
- [35] L. A. Marsh, C. Ktistis, A. Järvi, D. W. Armitage, and A. J. Peyton, "Three-dimensional object location and inversion of the magnetic polarizability tensor at a single frequency using a walk-through metal detector," *Meas. Sci. Technol.*, vol. 24, no. 4, Apr. 2013, Art. no. 045102.
- [36] L. A. Marsh, C. Ktistis, A. Järvi, D. W. Armitage, and A. J. Peyton, "Determination of the magnetic polarizability tensor and three dimensional object location for multiple objects using a walk-through metal detector," *Meas. Sci. Technol.*, vol. 25, no. 5, May 2014, Art. no. 055107.
- [37] B. Dekdouk, L. A. Marsh, D. W. Armitage, and A. J. Peyton, "Estimating magnetic polarizability tensor of buried metallic targets for land mine clearance," in *Ultra-Wideband, Short-Pulse Electromagnetics 10*, F. Sabath and E. Mokole, Eds. New York, NY, USA: Springer, 2014, doi: 10.1007/978-1-4614-9500-0_38.
- [38] A. Björck, *Numerical Methods in Matrix Computations*. Cham, Switzerland: Springer, 2016. [Online]. Available: <https://www.springer.com/gp/book/9783319050881>
- [39] T. H. Bell, B. J. Barrow, and J. T. Miller, "Subsurface discrimination using electromagnetic induction sensors," *IEEE Trans. Geosci. Remote Sens.*, vol. 39, no. 6, pp. 1286–1293, Jun. 2001.
- [40] GICHD. *Collaborative ORDNance Data Repository (CORD)*. Accessed: Apr. 10, 2021. [Online]. Available: <http://cord.gichd.org/ordnance?id=http%3A%2F%2Fcord.gichd.org%2Fontology%23Landmine4156>
- [41] E. L. Bronaugh, "Helmholtz coils for calibration of probes and sensors: Limits of magnetic field accuracy and uniformity," in *Proc. Int. Symp. Electromagn. Compat.*, Atlanta, GA, USA, 1995, pp. 72–76.
- [42] L. A. Marsh *et al.*, "Combining electromagnetic spectroscopy and ground-penetrating radar for the detection of anti-personnel landmines," *Sensors*, vol. 19, no. 15, p. 3390, Aug. 2019.
- [43] W. van Verre, L. A. Marsh, J. L. Davidson, E. Cheadle, F. J. W. Podd, and A. J. Peyton, "Detection of metallic objects in mineralized soil using magnetic induction spectroscopy," *IEEE Trans. Geosci. Remote Sens.*, vol. 59, no. 1, pp. 27–36, Jan. 2021.
- [44] Y. Das, "Effects of soil electromagnetic properties on metal detectors," *IEEE Trans. Geosci. Remote Sens.*, vol. 44, no. 6, pp. 1444–1453, Jun. 2006.



Toykan Özdeğer received the M.Eng. (Hons.) degree in electrical and electronics engineering from The University of Manchester in 2018, where he is currently pursuing the Ph.D. degree. From 2016 to 2017, he worked as an Instrumentation and Control Engineering Placement Student with Phillips 66 for one year during his degree. His research interests include machine learning, landmine detection, and metal characterization.



John L. Davidson received the B.Sc. (Hons.) degree in engineering physics and the Ph.D. degree in Mössbauer spectroscopy from Sheffield Hallam University (SHU) in 1993 and 1997, respectively. As a Research Fellow with the University of Southampton from 1998 to 2002, he developed an interest in electrostatics and electromagnetics. In 2002, he joined The University of Manchester initially working in the area of electrical impedance tomography applied to industrial and medical problems, and

more recently, in the area of electromagnetics. He has authored or coauthored more than 50 scientific publications. His current research interests include electromagnetic modeling, inverse problems, and magnetic induction sensor development. In 2008, he was awarded the Beloe Fellowship Award from Worshipful Company of Scientific Instrument Makers.



Wouter van Verre received the B.Eng. (Hons.) degree in electrical and electronics engineering and the Ph.D. degree in the use of electromagnetic methods for the detection of buried landmines from The University of Manchester in 2016 and 2021, respectively. He subsequently joined the EM Sensing Group, Department of Electrical and Electronic Engineering, The University of Manchester. His research interests include the use of metal detection in polar environments and MIMO ground-penetrating radar.



Liam A. Marsh (Member, IEEE) received the M.Eng. (Hons.) degree in electrical engineering and electronics from the Institute of Science and Technology, The University of Manchester, Manchester, U.K., in 2007, and the Ph.D. degree in electromagnetic tomography and people screening from The University of Manchester in 2011. He subsequently joined the Sensing, Imaging and Signal Processing Research Group, Department of Electrical and Electronic Engineering, The University of Manchester, as a Research Associate. In 2018, he was appointed as a Lecturer in Embedded Systems with The University of Manchester. His research interests include the development of electromagnetic sensor systems for security, landmine detection, and polar sensing.



William R. B. Lionheart received the B.Sc. degree in mathematics from The University of Warwick, U.K., in 1980, and the Ph.D. degree in electrical impedance tomography from Oxford Brookes University, U.K.

He is currently a Professor of Applied Mathematics with The University of Manchester, U.K., where he is involved in a wide range of inverse problems in medicine and industry, including electrical impedance tomography, magnetic induction tomography, x-ray and neutron

computed tomography, and position emission tomography. His interest in low-frequency electromagnetic imaging led to his involvement in civilian land mine clearance.



Anthony J. Peyton received the B.Sc. degree in electrical engineering and electronics from The University of Manchester in 1983 and the Ph.D. degree in medical instrumentation in 1986. After various positions in the scientific instrumentation industry and academia, he was appointed as a Professor in Electromagnetic Engineering in May 2004. He has over 30 years of experience in a diverse range of electromagnetic sensor systems and has been a principal investigator of numerous national, international and industry

funded projects. He has been the coauthor of over 160 international journal articles. His group work was extensively with industry in sectors, including non-destructive testing, security, medical, food quality, and humanitarian demining.

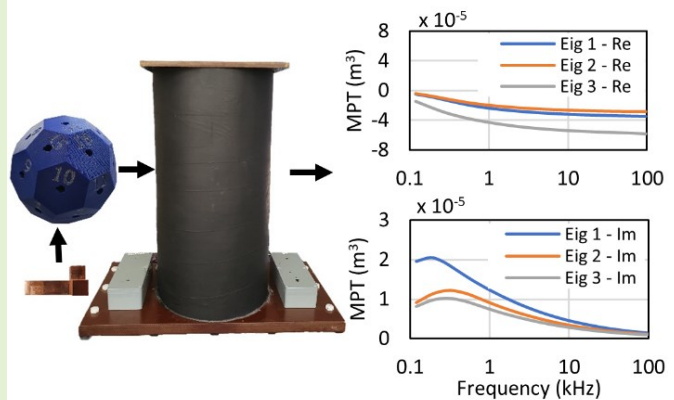
Publication 2

Özdeğer, T., Davidson, J. L., Ledger, P. D., Conniffe, D., Lionheart, W. R. B., Peyton, A. J., "Measuring the Magnetic Polarizability Tensor of Non-Symmetrical Metallic Objects," *IEEE Sensors Journal*, **Submitted, Under Review**.

Measuring the Magnetic Polarizability Tensor of Non-Symmetrical Metallic Objects

Toykan Özdeğer¹, John L Davidson², Paul D. Ledger³, Daniel Conniffe⁴,
William R B Lionheart⁵, Anthony J Peyton⁶

Abstract— The Magnetic Polarizability Tensor (MPT) is a representative electromagnetic property of a metallic object, which depends on the size, material, shape, and excitation frequency of the object. The MPT can be used to describe the response of metal detector systems and improve target classification performance in applications utilizing electromagnetic induction spectroscopy. However, for target characterization, a library of possible target objects needs to be created which can be used for training machine learning classifiers. To supplement and benchmark our existing library of simulated and measured MPT object characterizations, it is necessary to be able to measure object characterizations accurately and efficiently. This paper describes a novel method utilizing a truncated icosahedron shaped manipulator and procedure to measure MPT characterizations of non-symmetrical, irregular objects. This new method allows the measurement of the MPT of any appropriately sized object. The method also ensures the MPT characterizations are measured quickly and are well posed, without sacrificing accuracy. Performance of the method is validated by comparing experiment results acquired using the new method with experiment results acquired using a slower method for symmetrical objects as well as synthetic results generated using a commercial finite element package and an optimized dedicated open source MPT-Calculator package, which offers high accuracy and considerable computational advantages. Good agreement between the new method and the other three methods is seen. For all objects that have been characterized, MPT loss-peak magnitude and horizontal positions from all described methods are within five percent of each other at worst.



Index Terms— Electromagnetic Induction Spectroscopy, Magnetic Polarizability Tensor, Metal Detection, Metal Classification

I. INTRODUCTION

The Magnetic Polarizability Tensor (MPT) is a representative electromagnetic property of a metallic object, which depends on the size, material, shape, and excitation frequency of the object. Recent progress in mathematical theory

This paper was submitted for review on 07/03/22. Toykan Özdeğer, John Davidson, Daniel Conniffe, William R.B. Lionheart, and Anthony J. Peyton would like to thank the Engineering and Physical Sciences Research Council (Grant ref EP/R002177) and Sir Bobby Charlton Foundation for financial support. Paul D. Ledger would like to thank the Engineering and Physical Sciences Research Council (Grant refs EP/R002134/2, EP/V049453/1, and EP/V009028/1) for financial support.

Toykan Özdeğer, John Davidson, Daniel Conniffe, Anthony J. Peyton are with the Electrical and Electronic Engineering Department, The University of Manchester, Manchester, UK, M13 9PL (e-mail: toykan.ozdeger@manchester.ac.uk; J.Davidson-2@manchester.ac.uk; daniel.conniffe@manchester.ac.uk; a.peyton@manchester.ac.uk).

William R.B. Lionheart is with the Department of Mathematics, The University of Manchester, Manchester, UK, M13 9PL (e-mail: bill.lionheart@manchester.ac.uk).

Paul D. Ledger is with the Department of Mathematics, The University of Keele, Keele, UK (e-mail: p.d.ledger@keele.ac.uk).

has demonstrated that the MPT provides the object characterization in the leading order term of the asymptotic expansion of the perturbed magnetic field in the presence of a conducting permeable object [1]–[4]. The MPT along with Electromagnetic Induction Spectroscopy have been successfully applied in the area of metal detection e.g. the detection of unexploded ordnance [5]–[8], walk-through metal detectors [9], metal classification and recognition [10], [11], Non Destructive Testing (NDT) [12]–[14], and buried object detection [15]. MPT and broadband inductive sensing have also been previously proposed for landmine detection [16]–[24]. All these application areas have adopted some system-specific methodology to interrogate effectively the object of interest in three-dimensional space in order to calculate the MPT.

To measure the MPT of an object, its electromagnetic signature needs to be examined from several directions and with different applied field orientations. Several authors have described their system-specific methodology of experimentally determining the MPT. One particular approach is to use multiple coil arrangements. For example, the handheld sensor described in [5] uses five receive coils at different locations and

the whole sensor is moved around the target object to subject it to fields from different directions. A similar approach was taken in [6] by moving a handheld sensor (Geophex GEM-3) above the target to retrieve the MPT. However, the reported methodology only covers objects with symmetrical geometries. A non-linear inversion methodology was used in [7] by applying Gauss-Newton algorithm to data acquired from [5] and [8], where multiple coils are used. The multiple coil approach has also been used in walk-through metal detectors for determining the MPT e.g. Makkonen *et al* describes [9] a system used for object classification via determination of the spectroscopic tensor. In this case, a Levenberg–Marquardt algorithm was used to solve the optimization problem to arrive at the MPT from the Electromagnetic Induction (EMI) data where position and orientation of the target objects were not known. Another novel multiple coil arrangement has been reported in [11] which uses eight coils positioned in a circular array around the target object. The system was used for workpiece recognition by capturing electromagnetic characteristics of the target object at different angles at the same time as opposed to rotating the sensor or the object.

An alternative approach to using multiple coils is to either rotate or move the target object with respect to a known primary field thereby effectively interrogating the target in the three-dimensional field space. Scott and Larson [20], [21] describe a laboratory positioner with three automated translational stages, two automated rotational stages (yaw and pitch), and one manually adjusted roll stage. An EMI sensor array fixed to the positioner enables the measurement of the induction response of a target as a function of position. The system has been used to characterize targets such as AP landmines, rifle cartridges and steel nails and in [20] report MPT data generated using a dipole expansion and inversion technique [21] developed for the measurement of the magnetic susceptibility of soils and the polarizability of metallic objects. Objects were rotated in steps around the x-axis continuously where the rotation on other two axes were stepped once one rotation was complete around the x-axis. Each experiment lasted 19 hours caused by the large amount of data points. A least squares method was then used to arrive at the MPT characterizations of the target objects using responses from each orientation.

MPT calculation has also been applied to planar coil arrangements. Ambrus *et al* present simulated data from seven different planar coil geometries applied to test three different MPT inversion methods [15]. Optimized coil geometries ranged from single transmit and receive coil to single transmit and nine receive coils arranged in such a way as to best interrogate the target object space. Evaluated algorithms included non-linear least squares, conjugate gradient, Levenberg-Marquardt and Broyden-Fletcher-Goldfarb-Shannon (BFGS) methods applied to simulated buried cylindrical objects. Zhao *et al* [16] has also evaluated the performance of different inversion methods applied to different coil geometries and measurement protocols. Explored geometries included in-line axial scanning, multi-position measurements over a coplanar coils and target rotation within a balanced coaxial coil arrangement utilizing one transmit and two receive coils. A least squares inversion method was also applied in [17] to synthetic planar coil data to arrive at MPTs

and estimate object location in the application area of humanitarian demining. Application of a non-linear inversion method (not specified) was suggested for synthetic planar coil data taken at different locations compared to the object in [18] where the non-linearity of the problem was caused by the object's location being unknown.

Given an object's shape, size and material parameters the MPT of an object as a function of frequency (known as its spectral signature) can also be computed numerically using, for instance, the finite element method. To accelerate computations of the MPT spectral signature a proper orthogonal decomposition reduced order model with a-posteriori error estimates has been developed in the form of the open source MPT-Calculator software [25], which has been used to produce MPT spectral signatures of realistic threat objects [26] resulting in the open MPT-Library dataset. This approach employs a higher order Finite Element Method (FEM) accelerated by a reduced order model for rapid computation of the MPT spectral signatures. A comparison of different machine learning approaches has been presented in [27], with classification learnt from invariant MPT spectral signatures.

As outlined by the literature, accurate determination of the MPT depends upon many contributing factors including the sensor coil geometry, measurement protocol, acquired signal to noise level and appropriate selection of an inverse solution method. The interaction of these factors is not always well understood. Additionally, knowledge of how the target object interrogates the applied primary field space is a crucial requirement. For uniform fields and symmetrical objects this can be simplified by target rotations about simple orthogonal planes. For non-symmetrical targets, the interaction between applied field and target becomes more complex and simple rotations around orthogonal planes may either be insufficient to acquire an accurate MPT or become overly time consuming.

One of the motivations of MPT research is to develop a comprehensive library of objects in order to distinguish between threat and benign targets. For example, clutter items in post-conflict areas have a detrimental effect on the False Alarm Rate (FAR) in humanitarian demining [28]. If an MPT library of landmines and common metallic clutter found in post-conflict areas is to be constructed, landmine detectors could utilize this library to reduce FAR and speed up the demining process, especially when coupled to secondary detection such as GPR [28]. However, such a library could only be constructed with an efficient and fast method of characterizing objects.

In [22], an MPT measurement system utilizing a multi-coil arrangement with custom electronics and software is described. The system uses a wide frequency spectrum and is able to characterize large objects such as AP landmines, and landmine surrogates. However, the Target Orientation Manipulator (TOM) in [22] only rotates objects around one axis, therefore, only objects with symmetrical shape and homogeneous material distribution can be characterized, without multiple manual iterations. Consequently, we propose a new target rotational measurement protocol involving a set of orientations which are sufficient to acquire accurate MPTs.

This paper describes an efficient method utilizing a truncated icosahedron shaped TOM for characterizing MPTs of non-

symmetrical and non-homogeneous objects. Experimental data acquired using this novel TOM are compared with data acquired using the TOM in [22] for validation. The data is then further validated using synthetic data generated by a commercial FEM package and the open source MPT-Calculator simulation method described in [26].

In this paper, Section II describes the MPT, the underlying mathematical theory and how it can be related to real measurements. We also describe the geometry that we used for the TOM and why it is a well posed solution for non-symmetrical object characterization. Section III describes the experimental setup used for MPT measurement which involves the coil arrangement, system electronics, control software and the new target orientation manipulator. Section IV describes the experimental procedure followed to characterize MPT of target objects. Sections V and VI discuss the FEM and the MPT Calculator, respectively, which are used for generating synthetic data to validate experimental data. The experimental and synthetic data are then presented and compared in Section VII to prove the method's performance. Finally, Section VIII concludes the paper with a discussion of the experimental method's potential and further work.

II. BACKGROUND

A. Magnetic Polarizability Tensor

Our interest lies in characterizing hidden conducting permeable objects when the eddy current approximation of the Maxwell system, i.e. when the excitation frequency ω is small and conductivity σ_* of an object high (a more formal definition also involves the shape of the object [29] and its magnetic permeability μ_*). Given orthonormal coordinate basis vectors $\mathbf{e}_i, i = 1, 2, 3$, the complex symmetric rank 2 magnetic polarizability tensor (MPT)

$$\mathcal{M} = (\mathcal{M})_{ij} \mathbf{e}_i \otimes \mathbf{e}_j, \quad (1)$$

which is a function of the object's shape, its size α as well as μ_* , σ_* , ω , has been shown to provide object characterization information in the leading order term of an asymptotic expansion of the perturbed magnetic field in the form

$$(\mathbf{H}_\alpha - \mathbf{H}_0)(\mathbf{x})_i = (\mathbf{D}_x^2 G(\mathbf{x}, \mathbf{z}))_{ij} (\mathcal{M})_{jk} (\mathbf{H}_0(\mathbf{z}))_k + \mathbf{R}(\mathbf{x})_i \quad (2)$$

as $\alpha \rightarrow 0$. In the above, $G(\mathbf{x}, \mathbf{z}) = 1/(4\pi|\mathbf{x} - \mathbf{z}|)$ denotes the free space Laplace Green's function, $\mathbf{H}_0(\mathbf{z})$ the background field at the position of the object and $\mathbf{R}(\mathbf{x})$ a residual term with a known form, as shown by Ledger and Lionheart [1]-[4]. Furthermore, in these works, Ledger and Lionheart give several different equivalent expressions for computing $(\mathcal{M})_{jk}$ as a post-processing step once a vector valued transmission problem has been solved and explain its mathematical properties, including its behavior with ω .

In [2] Ledger and Lionheart explain the connection between (2) and the perturbed voltage measured by a metal detector for several practical scenarios. In the case of small coils placed a long way from the metal detector, the perturbed voltage is in the form $\mathbf{m} \cdot (\mathbf{H}_\alpha - \mathbf{H}_0)(\mathbf{x})$ where \mathbf{m} is the dipole moment of the measurement coil, while, for larger coils placed close to the object, then integrals of the form

$$\int_S \mathbf{n} \cdot (\mathbf{H}_\alpha - \mathbf{H}_0)(\mathbf{x}) d\mathbf{x} \quad (3)$$

over appropriate cross-sectional surfaces of measurement coils with unit normal \mathbf{n} predict the perturbed voltage. In both cases the perturbed voltage can be shown [2] to reduce to the form

$$\Delta V = \mathbf{H}_0^{Ms}(\mathbf{z}) \cdot (\mathcal{M} \mathbf{H}_0^{Tr}(\mathbf{z})) \quad (4)$$

where $\mathbf{H}_0^{Ms}(\mathbf{z})$ is the background field at the position of the object that would result if the measurement coil(s) is used an excitor and $\mathbf{H}_0^{Tr}(\mathbf{z}) = \mathbf{H}_0(\mathbf{z})$ is the background field resulting from the transmitting coil at the position of the object.

B. Truncated Icosahedron

The MPT has at most 6 independent complex coefficients and transforms under rotation as

$$(\mathcal{M})_{ij} = (\mathbf{R})_{ip} (\mathbf{R})_{jq} (\mathcal{M})_{pq} \quad (5)$$

where \mathbf{R} is the orthogonal rotation matrix describing the object transformation. To determine the MPT coefficients $(\mathcal{M})_{ij}$, it is important that measurements of ΔV are made at sufficiently many, appropriately chosen rotations of the object. Just choosing 6 randomly chosen rotations is not guaranteed to fully determine $(\mathcal{M})_{ij}$ unless the directions are independent. Furthermore, in order minimize measurement errors, many more than 6 directions and measurements are preferred. To ensure consistency and accuracy of measurements, as well as to accelerate MPT measurements, an approach whereby the rotations of the object can always be guaranteed to be the same is desired.

A truncated icosahedron (tI) [30], [31] as shown in Fig. 1 is an Archimedean polyhedral solid object with 32 faces comprising of 12 regular pentagons and 20 regular hexagons. Many will recognise the pattern of faces as being the same as used in a traditional football (soccer ball in the U.S.). The pentakis dodecahedron [32] is the dual polyhedron of the tI, the vertices of the former being projections of the face centres of the truncated icosahedron. For the unit case, these vertices are defined in Cartesian coordinates given by 12 cyclic permutations each of $(0, \pm 1, \pm \varphi)$ and $(\pm \varphi, \pm 1/\varphi, 0)$ and eight points defined by $(\pm 1, \pm 1, \pm 1)$ where φ is the golden ratio [33]. It is trivial to use these coordinates to define azimuth and polar angles of a conventional spherical coordinate system to define 32 rotation matrices (with one being the identity matrix) that reorientate the tI from a conical choice with *face 1* at its base, say, to situations where each of its other 31 faces are at its base. Importantly, these 32 orthogonal rotation matrices should be distinguished from the orthogonal matrices, which make up the rotation group and symmetry group of a tI, which have orders 60 and 120, respectively. In the case of rotation group, these comprises of the 60 rotation matrices for which the configuration of the tI is preserved. The symmetry group additionally includes the 60 orthogonal matrices corresponding to the tI symmetries.

We fix an object in the centre of a hollow tI so if the tI is rotated then the object will also be rotated by the same amount. By numbering the faces of the tI, it becomes a simple matter to manually reorientate the tI and, hence the object, according to each of the face of the tI. The flat faces of the tI reduces considerably the uncertainty in the rotations, as explicit rotation

matrices are known that reorientate the tI according to its different faces. Additionally, if an object is positioned in the center of the tI, then we can use the symmetry of \mathcal{M} and the form of (4) to reduce the number of faces that need to be considered from 32 to 16 as follows. Considering two opposite faces of the tI, with centers $f_n = -f_{n+16}$, their associated orthogonal reflection matrix is $R = -I$, where I is the identity matrix. Then, using (5), $\mathcal{M}' = \mathcal{M}$ and, hence, opposite faces do not provide additional information. For other non-opposite faces, the Rodriguez rotation formula can be used to obtain the orthogonal rotation matrix R between faces, which, using (5), leads to $\mathcal{M}' \neq \mathcal{M}$ for a general object. This information, together with form of the measurements in (4), can be used to build an overdetermined system of linear equations for the 6 unknown MPT coefficients at each frequency, which is solved using least squares. The use of the tI thereby guarantees that the directions are independent and provide a simple method to ensure consistency and accuracy of the directions and orientations used for the measurements.

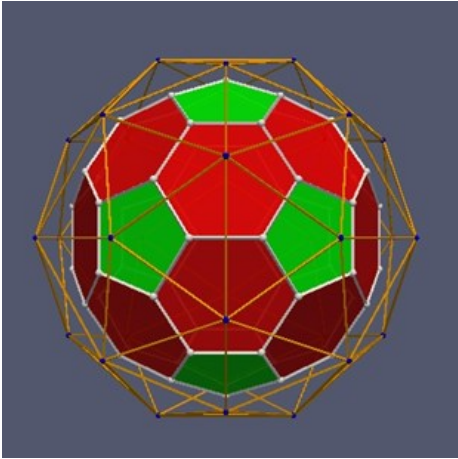


Fig. 1. The truncated icosahedron shown with red hexagon and green pentagon faces within its dual polyhedron shape of the pentakis dodecahedron represented as a wire frame.

III. EXPERIMENTAL SETUP

A. System Overview

A description of the main system used was previously published in [22], which consists in three main parts: a control software on a PC, system electronics, and a coaxial coil arrangement. The control software communicates with the microcontroller of the system electronics bidirectionally by sending signals to control the output amplitude, frequency, data acquisition settings, and receiving the measured transimpedance between transmit and receive coils. Post-processing of the data is also done by the control software, which outputs MPT eigenvalues.

The microcontroller (Red Pitaya – STEMLab 125-14) sends excitation signals to 20 transmit amplifiers according to the experiment settings and acquires signals from two input amplifiers, one for receive coil voltage and one for transmit coil current. Half of the transmit amplifiers are configured as inverting, while the rest are as non-inverting. The transmit amplifier circuit can provide a 64 V sine wave output at 10 A.

The coaxial coils shown in Fig. 2 consists of an outer transmit coil (240 mm in diameter), made up of nine individual sections, and two inner identical receive coils (220 mm in diameter) connected in series opposition, each made up of four individual coil sections. The coils were designed using Helmholtz coils principle and the application of the Biot-Savart Law to achieve a uniform magnetic field inside the coils. There is a two-turn current pick-up coil placed at the bottom of the coil arrangement, which acts as the current sensor of the system. Overall height of the coil arrangement is 500 mm.

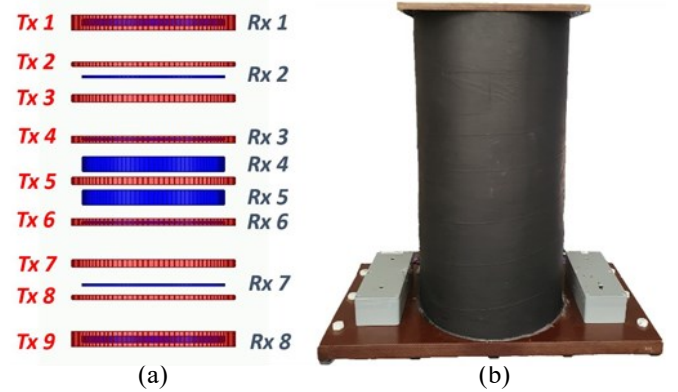


Fig. 2. The coil arrangement. (a) showing alignment of the coils and (b) showing the constructed coil arrangement, encapsulated in epoxy resin [22].

B. Target Orientation Manipulator

A custom-built, tI shaped target orientation manipulator (TOM) shown in Fig. 3 is used to rotate objects in three-dimensional space. The TOM is 3D printed using polylactic acid (PLA) filament and has a diameter of 150 mm and a 10 mm wall thickness. As target objects can be rotated around all three axes using this method, objects without symmetrical geometries and homogeneous materials can be characterized. Each face of the TOM has a keyed hole in the middle. These -

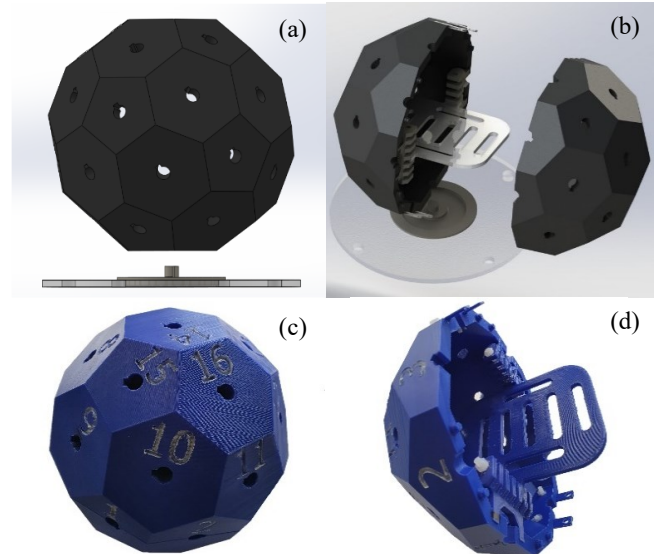


Fig. 3. Computer Aided Design (CAD) models and built version of the Target Orientation Manipulator. (a) and (c) showing closed CAD and built versions. (b) and (d) showing CAD and built versions where the two halves are separated.

are used to place the faces on a custom-made table with a keyed seat, which helps control the horizontal position and keeps rotation around the vertical axis fixed for consistency. The manipulator is built in two halves to allow access to the internal object mounting plate. Vertical position of the mounting plate can be adjusted to ensure the target object is centralised on the vertical axis of the manipulator. Target objects are securely fixed in the TOM using a combination of adhesive tape and adhesive putty.

IV. METHOD

The system was set up and left running for at least half an hour before an experiment to ensure a steady-state system temperature was reached. Additionally, all experiments were done in a temperature-controlled area to minimize any potential measurement drift caused by system temperature variation. At the start of each experiment, measurements were taken with no object present in the coils to serve as a background reference. This was stored and subtracted from the measurements acquired with the target object in the coils. Phase correction was then done by using a NiZn ferrite rod as a pure real (reactive) response is expected across the operating frequency spectrum. The required correction values were then stored and applied to all subsequent measurements with target objects in the coils. MPT characterization of a target object was acquired by placing the target object inside the TOM and rotating it by placing the TOM in turn on each of its 16 faces thereby giving 16 unique and independent object orientations. Additionally, the background was measured after every two target orientations to further minimize any experimental error due to measurement drift. MPT characterization of each object was then calculated by the control software and presented in the form of MPT eigenvalues. The target objects are shown in Fig. 4. All objects were CNC machined from copper stock material to a tolerance better than 50 microns.

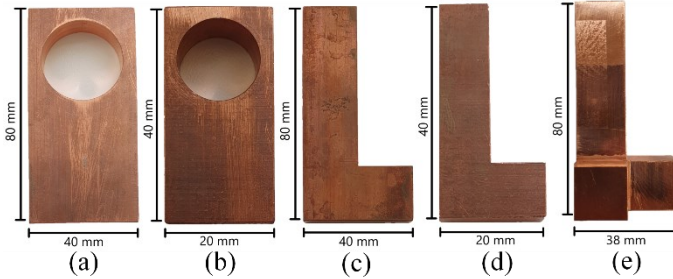


Fig. 4. Example target objects showing copper cuboid with a hole, 'L' shape and three legged 'L' shape. Object (a) and (b) copper cuboids with a hole, (c) and (d) copper 'L' shapes, (e) three legged 'L' shape. All five objects have a thickness of 10 mm where the three legged 'L' shape's third leg is 19 mm.

V. FINITE ELEMENT METHOD

Simulations were performed using the commercial FEM (Finite Element Method) solver, *Maxwell*, (*Ansys Electromagnetics Suite, Release 19.2*). The simulation geometry comprised of an outer free-space region and a three-dimensional simplified model of the segmented coil arrangement as described in [22]. Test objects were modelled using a commercial CAD package prior to importing into the Ansys Electromagnetics suite and the modelled coil geometry.

Simulations for comparison with experimental measurements involved positioning each target within the uniform field region of the modelled coils at defined angular orientations in relation to the normals of the central faces of the truncated icosahedron described in Section IIB. Polar and azimuth angles of a spherical coordinate system as shown in Fig. 5(a) were used to describe the target under test. Simulations were carried out for the 16 independent face-defined truncated icosahedron orientations of each test object. Fig. 5(b) shows an example orientation of a test object within a detailed part of the modelled coil arrangement. Each target orientation involved simulations over the frequency sweep range of 100 Hz to 100 kHz in ten logarithmic increments per decade. All test objects were modelled using a conductivity of pure copper defined as 5.8×10^7 S/m by the International Annealed Copper Standard (IACS). Typical meshing involved a FEM model of approximately 150k tetrahedral elements in total per orientation geometry with between 15k to 25k elements per test object.

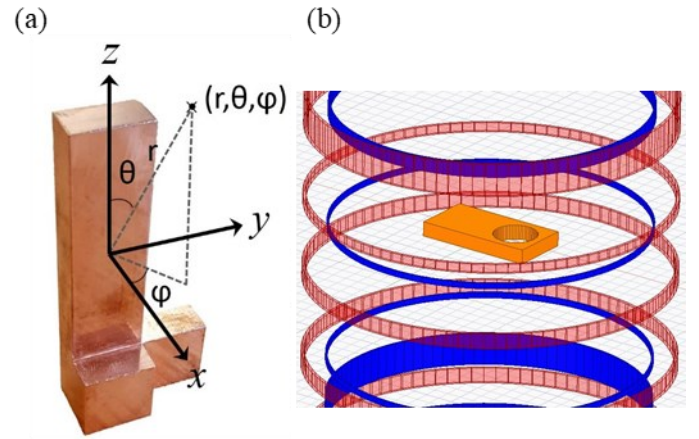


Fig. 5. FEM modelling of test objects showing (a) adopted orientation coordinate system and (b) example test object within the coil geometry at one of the independent face-defined truncated icosahedron orientations.

VI. MPT-CALCULATOR

The MPT calculator software employs the NGSolve FEM library [34]-[36] to provide accurate high-order finite element solutions to vectorial transmission problems from which the MPT coefficients $(\mathcal{M})_{ij}$ follow in a post-processing step [3]. To accelerate the computation of the MPT spectral signature, which would otherwise require full FEM solves for each frequency of interest, a reduced order model (ROM) is employed to predict the full signature from a small number of solution snapshots at different frequencies at reduced computational cost. The reduced order model benefits from a-posteriori error estimates, which the MPT spectral signature predicted by the ROM with respect to signature that would be obtained from full FEM solves at each frequency. For full details see [25].

VII. RESULTS

MPTs of various objects were measured using the new target orientation manipulator. The results were compared with MPTs acquired from FEM simulations, MPT calculator software, and measurements that used the previous TOM. Because MPTs are

object specific, the other methods were used as a verification of the new method's ability to characterize MPTs of objects correctly.

Fig. 6 shows the MPT of a copper disk, which is compared with FEM simulations and measurements from the previous TOM. Fig. 7 shows measured target objects compared with FEM simulations, measurements done with the previous TOM and values from the MPT Calculator algorithm. Fig. 8 shows

MPT of a copper 'L' shape with a third leg where all three legs are at different lengths. This makes it the most non-symmetrical object between the ones interrogated in this paper with six independent MPT coefficients.

There is a good agreement between experimental results acquired using the new and previous TOMs. For all target objects in both Fig. 6 and Fig. 7, data acquired using the new TOM, labelled as Expt 2, follow a similar curve with data -

TABLE I

NRMSE of differences between measured MPT eigenvalues compared to MPT eigenvalues generated using the MPT-Calculator algorithm.

	<i>MPT-Calculator vs. New TOM</i>						<i>MPT-Calculator vs. Previous TOM</i>					
	Eigenvalue 1		Eigenvalue 2		Eigenvalue 3		Eigenvalue 1		Eigenvalue 2		Eigenvalue 3	
	Re	Im	Re	Im	Re	Im	Re	Im	Re	Im	Re	Im
Small 'L' Shape	0.033	0.024	0.022	0.015	0.029	0.018	0.035	0.040	0.025	0.029	0.027	0.030
Large 'L' Shape	0.027	0.029	0.032	0.029	0.026	0.024	0.023	0.035	0.030	0.038	0.023	0.034
Small Cuboid with Hole	0.027	0.015	0.022	0.014	0.018	0.024	0.024	0.027	0.020	0.027	0.021	0.033
Large Cuboid with Hole	0.025	0.049	0.022	0.027	0.024	0.024	0.025	0.054	0.019	0.031	0.020	0.026
Three Legged 'L' Shape	0.024	0.036	0.030	0.032	0.025	0.040	N/A	N/A	N/A	N/A	N/A	N/A

TABLE II

NRMSE of differences between measured MPT eigenvalues compared to MPT eigenvalues generated using the FEM simulations.

	<i>FEM vs. New TOM</i>						<i>FEM vs. Previous TOM</i>					
	Eigenvalue 1		Eigenvalue 2		Eigenvalue 3		Eigenvalue 1		Eigenvalue 2		Eigenvalue 3	
	Re	Im	Re	Im	Re	Im	Re	Im	Re	Im	Re	Im
Small 'L' Shape	0.046	0.062	0.028	0.054	0.031	0.053	0.048	0.078	0.031	0.064	0.031	0.062
Large 'L' Shape	0.030	0.071	0.056	0.088	0.039	0.083	0.028	0.080	0.054	0.096	0.037	0.093
Small Cuboid with Hole	0.024	0.071	0.032	0.067	0.030	0.057	0.024	0.077	0.032	0.078	0.035	0.067
Large Cuboid with Hole	0.027	0.105	0.049	0.120	0.055	0.123	0.028	0.110	0.045	0.126	0.050	0.124
Three Legged 'L' Shape	0.035	0.078	0.060	0.087	0.030	0.105	N/A	N/A	N/A	N/A	N/A	N/A

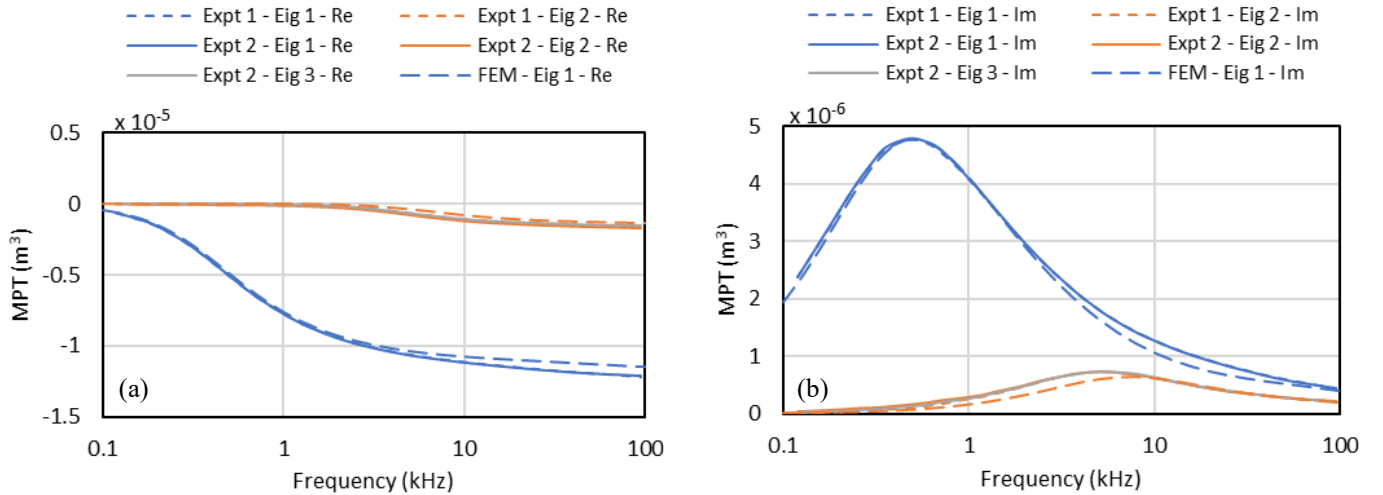


Fig. 6. Real and imaginary MPT eigenvalues for a copper disk with 30 mm in diameter and 2.15 mm thickness measured using the new object orientation manipulator, compared with measurements using previous object orientation manipulator and FEM simulations. "Expt 1" represents values from experiments done using the previous TOM while "Expt 2" represents values taken using the new one. "FEM" represents values from FEM simulations. Plots show (a) real and (b) imaginary MPT eigenvalues.

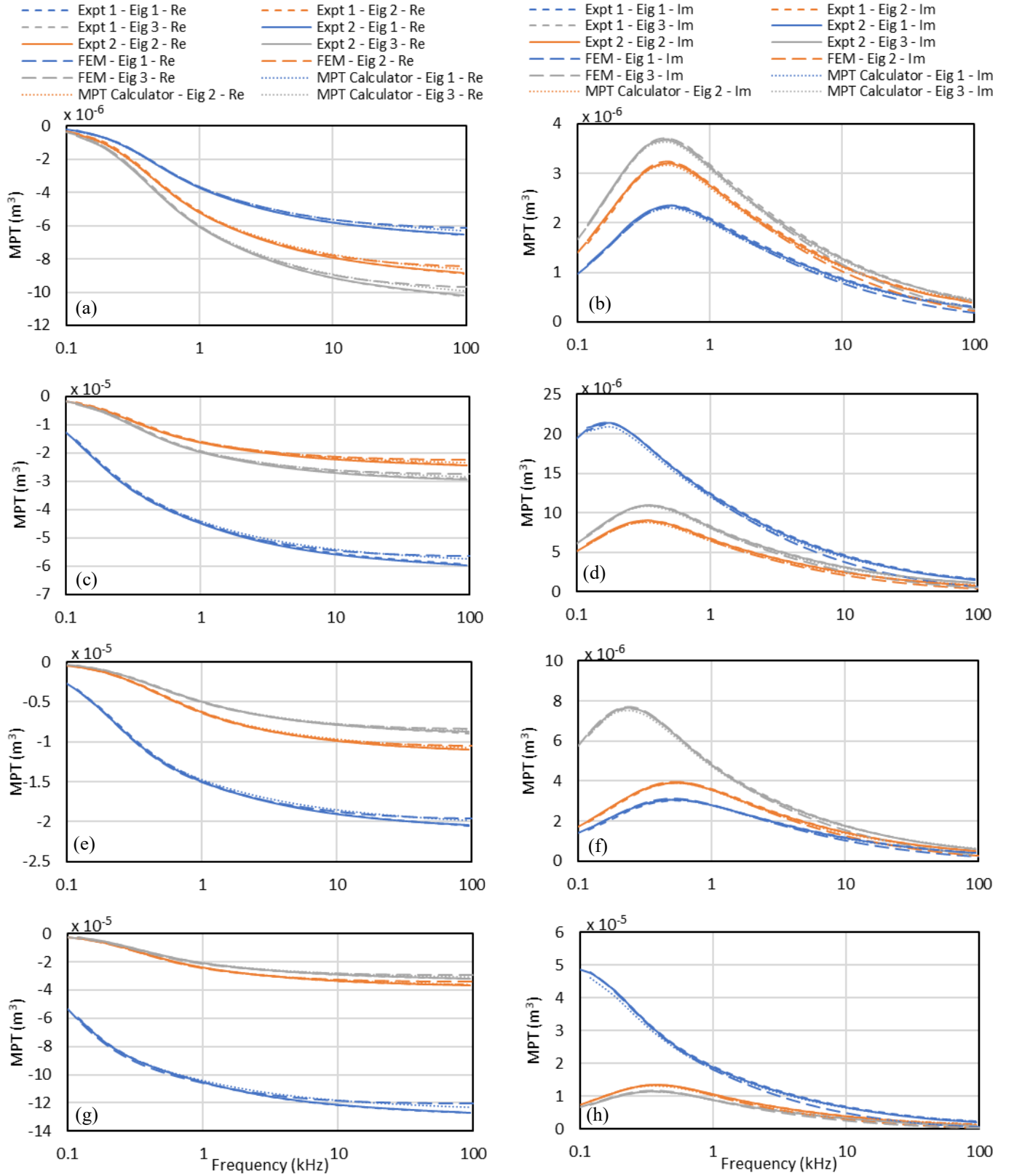


Fig. 7. Measured real and imaginary MPT eigenvalues of target objects, compared with results from FEM simulations, MPT Calculator and measurements using the previous TOM. Plots (a-b) small 'L' shape, (c-d) large 'L' shape, (e-f) small cuboid with hole, (g-h) large cuboid with hole. "Expt 1" represents values from experiments done using the previous TOM while "Expt 2" represents values taken using the new one. "FEM" represents values from FEM simulations while "MPT Calculator" represents values acquired using the MPT Calculator.

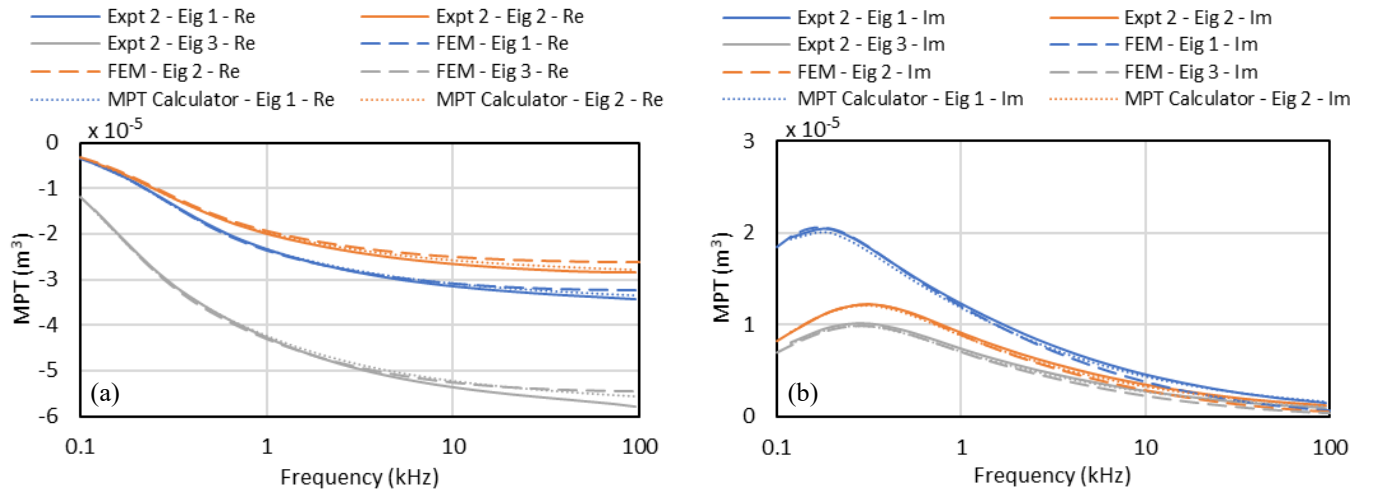


Fig. 8. Real and imaginary MPT eigenvalues for a three legged 'L' shape measured using the new object orientation manipulator, compared with results from FEM simulations and MPT Calculator. "Expt 2" represents values taken using the new TOM. "FEM" represents values from FEM simulations while "MPT Calculator" represents values acquired using the MPT Calculator. Plots show (a) real and (b) imaginary MPT eigenvalues.

acquired using the previous TOM, labelled as Expt 1. Loss-peak magnitude and horizontal positions are within less than one percent of each other. In addition, for all target objects shown in Fig. 7 and Fig. 8, MPT loss-peak magnitude and horizontal positions for new and previous TOMs, FEM simulations and MPT Calculator are within five percent of each other at worst.

The main source of error between the data from new and previous TOMs is the orientation accuracy of the previous TOM, which is around 1 degree, whereas we estimate the new TOM's orientation accuracy to be better than 1 degree. The error in orientation of an object when placed on the previous TOM also contributes to errors, as objects are not 100% symmetrical and perfectly homogeneous materials. However, these errors do not matter for the new TOM methodology, as the objects are characterized in all three dimensions. In addition to the previous approach being unable to characterize non-symmetrical objects where principal axes of the object are not obvious, it is also less accurate compared to the new TOM method when the principal axes are obvious. This is quantified in TABLE I and TABLE II, where Normalised Root Mean Square Error (NRMSE) between data generated by MPT-Calculator algorithm and FEM simulations are compared with experimental data acquired by using both TOMs. For all target objects considered in TABLE I and TABLE II, NRMSE values for data acquired using the new TOM are generally lower than the previous TOM, meaning that the new method is more accurate. NRMSE has previously been used as an analysis method for results comparison and has been described in more detail in [22], [37].

VIII. CONCLUSION AND FUTURE WORK

A truncated icosahedron shaped target orientation manipulator was designed and constructed for fast and accurate measurement of MPT characterizations. The manipulator was tested in a previously built and reported system which the performance is known. Modifications were made on the post-processing algorithm to take the rotation matrices between truncated icosahedron's faces into account. Experimental

results acquired using the new target orientation manipulator methodology was compared with previously reported experimental results as well as synthetic data acquired using FEM and custom MPT-Calculator algorithms. This verified the method's ability to measure MPT characterizations of non-symmetrical, irregular metal objects accurately. The novelty of the new method is the truncated icosahedron shaped target orientation manipulator combined with the required measurement system and processing algorithms, making it a complete, measurement ready system capable of measuring rank-2 MPT characterizations. We hope to report results from this system on targets of interest for applications including humanitarian demining and security screening in the near future.

IX. REFERENCES

- [1] Ledger, PD., and Lionheart, WRB., "Understanding the magnetic polarizability tensor," *IEEE Transactions on Magnetics*, vol. 52, No. 5, pp. 1-16, 2016.
- [2] Ledger, PD., and Lionheart, WRB., "An Explicit Formula for the Magnetic Polarizability Tensor for Object Characterization," *IEEE Transactions on Geoscience and Remote Sensing*, vol. 56, no. 6, pp. 3520-3533, 2018.
- [3] Ledger, PD., and Lionheart, WRB., "The spectral properties of the magnetic polarizability tensor for metallic object characterisation," *Mathematical Methods in the Applied Sciences*, vol. 43, no. 1, pp. 78-113, 2019.
- [4] Ledger, PD, Lionheart, WRB., "Generalised magnetic polarizability tensors," *Mathematical Methods in the Applied Sciences*, vol. 41, pp. 3175-3196, 2018.
- [5] Fernandez, JP., Barrowes, BE., Grzegorzczak, TM., Lhomme, N., O'Neill, K., and Shubitidze, F., "A Man-Portable Vector Sensor for Identification of Unexploded Ordnance," *IEEE Sensors Journal*, vol. 11, no. 10, pp. 2542-2555, 2011.
- [6] Norton SJ., and Won, JJ., "Identification of buried unexploded ordnance from broadband electromagnetic induction data," *IEEE Transactions on Geoscience and Remote Sensing*, vol. 39, no. 10, pp. 2253-2261, 2001.
- [7] Grzegorzczak, TM., Barrowes, BE., Shubitidze, F., Fernandez, JP., and O'Neill, K., "Simultaneous Identification of Multiple Unexploded Ordnance Using Electromagnetic Induction Sensors," *IEEE Transactions on Geoscience and Remote Sensing*, vol. 49, no. 7, pp. 2507-2517, 2011.
- [8] Nelson, HH., and McDonald, JR., "Multisensor towed array detection system for UXO detection," *IEEE Transactions on Geoscience and Remote Sensing*, vol. 39, no. 6, pp. 1139-1145, 2001.

- [9] Makkonen, J., Marsh, L., Vihonen, J., Järvi, A., Armitage, D., Visa, A. and Peyton, A., "KNN classification of metallic targets using the magnetic polarizability tensor," *Measurement Science and Technology*, vol. 25, no. 5, pp. 055105, 2014.
- [10] O'Toole, M., Karimian, N. and Peyton, A., "Classification of Nonferrous Metals Using Magnetic Induction Spectroscopy," *IEEE Transactions on Industrial Informatics*, vol. 14, no. 8, pp. 3477-3485, 2018.
- [11] Tao, Y., Yin, W., Zhang, W., Zhao, Y., Ktistis, C., and Peyton, A.J., "A Very-Low-Frequency Electromagnetic Inductive Sensor System for Workpiece Recognition Using the Magnetic Polarizability Tensor," *IEEE Sensors Journal*, vol. 17, no. 9, pp. 2703-2712, 2017.
- [12] García-Martín, J., Gómez-Gil, J. and Vázquez-Sánchez, E., "Non-Destructive Techniques Based on Eddy Current Testing," *Sensors*, vol. 11, no. 3, pp. 2525-2565, 2011.
- [13] Daura, L., Tian, G., Yi, Q. and Sophian, A., "Wireless power transfer-based eddy current non-destructive testing using a flexible printed coil array," *Philosophical Transactions of the Royal Society A: Mathematical, Physical and Engineering Sciences*, vol. 378, no. 2182, p. 20190579, 2020.
- [14] Lu, M., Meng, X., Huang, R., Chen, L., Tang, Z., Li, J., Peyton, A. and Yin, W., "Determination of Surface Crack Orientation Based on Thin-Skin Regime Using Triple-Coil Drive-Pickup Eddy-Current Sensor," *IEEE Transactions on Instrumentation and Measurement*, vol. 70, pp. 1-9, 2021.
- [15] Ambrus, D., Vasic, D. and Bilas, V., "Comparative Study of Planar Coil EMI Sensors for Inversion-Based Detection of Buried Objects," *IEEE Sensors Journal*, vol. 20, no. 2, pp. 968-979, 2020.
- [16] Zhao, Y., Yin, W., Ktistis, C., Butterworth, D. and Peyton, A., "Determining the Electromagnetic Polarizability Tensors of Metal Objects During In-Line Scanning," *IEEE Transactions on Instrumentation and Measurement*, vol. 6, no. 5, pp. 1172-1181, 2016.
- [17] Dekdouk, B., Ktistis, C., Marsh, L., Armitage, D. and Peyton, A., "Towards metal detection and identification for humanitarian demining using magnetic polarizability tensor spectroscopy," *Measurement Science and Technology*, vol. 26, no. 11, pp. 115501, 2015.
- [18] Ambruš, D., Vasić, D., and Bilas, V., "Innovating on top of I&M fundamentals for safer humanitarian demining," *IEEE Instrumentation & Measurement Magazine*, vol. 23, no. 3, pp. 35-41, 2020.
- [19] Dalichaouch, Y., Whitecotton, B., McManus, T., Kuhn, S., Trammell, H., Shelby, R. and Carin, L., "Wideband frequency response of low-metal mines," *Detection and Remediation Technologies for Mines and Minelike Targets IX*, vol. 5415, pp. 275-282, 2004.
- [20] Scott, W.R., and Larson, G.D., "Modeling the measured em induction response of targets as a sum of dipole terms each with a discrete relaxation frequency," *IEEE International Geoscience and Remote Sensing Symposium*, Honolulu, HI, USA, pp. 4188-419, 2010.
- [21] Larson, G.D., and Scott, W.R., "Automated, non-metallic measurement facility for testing and development of electromagnetic induction sensors for landmine detection," *Detection and Sensing of Mines, Explosive Objects, and Obscured Targets XIV*, 2009.
- [22] Özdeğer, T., Davidson, J.L., Van Verre, W., Marsh, L.A., Lionheart, W.R.B., and Peyton, A.J., "Measuring the Magnetic Polarizability Tensor Using an Axial Multi-Coil Geometry," in *IEEE Sensors Journal*.
- [23] Rehim, O., Davidson, J.L., Marsh, L.A., O'Toole, M., Armitage, D. and Peyton, A., "Measurement system for determining the magnetic polarizability tensor of small metal targets," *IEEE Sensors Applications Symposium (SAS)*, Zadar, pp. 1-5, 2015.
- [24] Rehim, O., Davidson, J.L., Marsh, L.A., O'Toole, M. and Peyton, A., "Magnetic Polarizability Tensor Spectroscopy for Low Metal Anti-Personnel Mine Surrogates," *IEEE Sensors Journal*, vol. 16, no. 10, pp. 3775-3783, 2016.
- [25] Wilson, B.A., and Ledger, P.D., "Efficient computation of the magnetic polarizability tensor spectral signature using proper orthogonal decomposition," *Int. J. Numer. Methods Eng.*, vol. 122, no. 8, pp. 1940-1963, 2021.
- [26] Ledger, P.D., Wilson, B.A., Amad, A.A.S., and Lionheart, W.R.B., "Identification of metallic objects using spectral magnetic polarizability tensor signatures: Object characterisation and invariants," *Int. J. Numer. Methods Eng.*, vol. 122, no. 15, pp. 3941-3984, 2021.
- [27] Wilson, B.A., Ledger, P.D., and Lionheart, W.R.B., "Identification of metallic objects using spectral magnetic polarizability tensor signatures: Object classification," *International Journal for Numerical Methods in Engineering*, Accepted Author Manuscript, 2022.
- [28] Tsipis, K., "Technological Innovation in Humanitarian Demining," *Human Factors and Ergonomics Soc*, SANTA MONICA, 1998, pp. 750-753.
- [29] Schmidt, K., Sterz, O., and Hiptmair, R., "Estimating the eddy-current modeling error," *IEEE Transactions on Magnetics* 44, vol. 6, pp. 686-689, 2008.
- [30] Coxeter, H.S.M., Longuet-Higgins, M.S., and Miller, J.C.P., "Uniform Polyhedra," *Phil. Trans. Roy. Soc. London Ser. A* 246, pp. 401-450, 1954.
- [31] Cundy, H., and Rollett, A., "Stellated Archimedean Polyhedra," *Mathematical Models*, 3rd edition, pp. 123-128 and Table II following p. 144, 1989.
- [32] Wenninger, M., "Dual Models," *Cambridge University Press*, MR 0730208, 1983.
- [33] Catalan, E., "Mémoire sur la Théorie des Polyèdres," *Journal de l'École Polytechnique*, vol. 24, pp. 1-71, 1865.
- [34] Zaglmayr, S.: PhD thesis "High Order Finite Elements for Electromagnetic Field Computation", Johannes Kepler University Linz, 2006.
- [35] Schöberl, J.: "NETGEN - An advancing front 2D/3D-mesh generator based on abstract rules." *Computing and Visualization in Science*, vol. 1, pp. 41-52, 1997.
- [36] Schöberl, J.: "C++11 Implementation of Finite Elements in NGSolve", *ASC Report 30/2014*, Institute for Analysis and Scientific Computing, Vienna University of Technology, 2014.
- [37] Davidson, J., Abdel-Rehim, O., Hu, P., Marsh, L., O'Toole, M. and Peyton, A., "On the magnetic polarizability tensor of US coinage," *Measurement Science and Technology*, vol. 29, no. 3, pp. 035501, 2018.

Publication 3

Özdeğer, T., Ledger, P. D., Peyton, A. J., "A Study on the Magnetic Polarizability Tensors of Minimum Metal Anti-Personnel Landmines," *2022 IEEE International Instrumentation and Measurement Technology Conference (I2MTC)*, pp. 1-6, 2022.
Published.

Doi: 10.1109/I2MTC48687.2022.9806662.

A Study on the Magnetic Polarizability Tensors of Minimum Metal Anti-Personnel Landmines

Toykan Özdeğer

Department of Electrical and
Electronics Engineering

University of Manchester

Manchester, United Kingdom

ORCID ID: 0000-0002-9039-4626

Paul D. Ledger

School of Computing and Mathematics
Keele University

Keele, United Kingdom

ORCID ID: 0000-0002-2587-7023

Anthony J. Peyton

Department of Electrical and
Electronics Engineering

University of Manchester

Manchester, United Kingdom

ORCID ID: 0000-0002-5740-348X

Abstract— The Magnetic Polarizability Tensor (MPT) is a characterization of a metal object with coefficients that depend on the object's shape, size, material, and excitation frequency. This property can be utilized to minimize false alarm rates and improve target classification on landmine detectors capable of measuring MPT spectral signatures of target objects. This paper studies such characterizations of four landmines and their components for the first time. The MPT signatures of their components were then compared with each other. It was found that firing pins and springs in most landmines were responsible for the magnetic aspect of the landmine's MPT.

Keywords— *Electromagnetic Induction Spectroscopy, Magnetic Polarizability Tensor, Metal Detection, Metal Classification, Humanitarian Demining*

I. INTRODUCTION

Humanitarian Demining is a demanding process. One of the main causes of this is the metallic clutter within the soil in most post-conflict areas, which causes a high false alarm rate (FAR) in Metal Detection (MD). MD being the most common way of detecting landmines in humanitarian demining, a high FAR slows down the process. In some areas, only one percent of the detected objects are landmines, while the remaining is metallic clutter [1]-[3]. MD has recently been augmented with Ground Penetrating Radar (GPR) to reduce FAR caused by the metallic clutter [4]. However, GPR is also prone to false alarms caused by inhomogeneities in the soil, such as moisture, vegetation, burrows, and stones. In addition, it is difficult to detect flush buried landmines using GPR as they can be lost in the large response caused by the ground bounce from the emitted radar signals.

The Magnetic Polarizability Tensor (MPT) is a characterization of a metal object that depends on the object's shape, size, materials, and exciting frequency. It applies in the eddy current regime where object conductivities are high, and frequencies are low. See [5] for details of how the applicability of the eddy current model can be estimated. A rigorous mathematical theory has been established that shows that the rank 2 MPT is complex symmetric, with coefficients \mathcal{M}_{ij} , and provides the object description in equation (1). This formula describes the leading order term in an asymptotic expansion of the perturbed magnetic field $(\mathbf{H}_\alpha - \mathbf{H}_0)(\mathbf{x})$ at position \mathbf{x} in the presence of a small object at position \mathbf{z} placed in a time varying background field \mathbf{H}_0 [6], [7].

$$(\mathbf{H}_\alpha - \mathbf{H}_0)(\mathbf{x})_j = (\mathbf{D}_x^2 G(\mathbf{x}, \mathbf{z}))_{jm} \mathcal{M}_{mi} (\mathbf{H}_0(\mathbf{z}))_i + (\mathbf{R}(\mathbf{x}))_j \quad (1)$$

In the above, $G(\mathbf{x}, \mathbf{z})$ is the free space Laplace Green's function and $\mathbf{R}(\mathbf{x})$ denotes the residual. Furthermore, there is an explicit formula for \mathcal{M}_{ij} and hence, the MPT can be computed numerically [8]-[10]. Recent research has suggested using the MPT to distinguish between and classify metal objects [11], which can be extended to landmines. Electromagnetic Induction Spectroscopy and the MPT have also been suggested and applied previously for metal recycling [12], walk-through metal detectors [13], and detection of unexploded ordnance [14]-[16]. If a library of MPT characterizations of common landmines could be generated, a metal detector capable of measuring MPTs could utilize the library to classify objects and reduce FAR. Previously, an instrument capable of characterizing MPTs of metal objects up to 130 mm in diameter was built and reported by our team in [17]. In this paper, we utilize this system to characterize four landmines and their metal components. We then study their MPT eigenvalues as they are invariant of object orientation and provide possible features for object classification.

II. EXPERIMENTAL SETUP

The experimental setup consists of three main parts, a coaxial coil arrangement, system electronics and control software. Choosing a uniform \mathbf{H}_0 means $\mathbf{R}(\mathbf{x})$ vanishes in (1), which makes it easier to determine the MPT coefficients from measurements of $(\mathbf{H}_\alpha - \mathbf{H}_0)(\mathbf{x})$ taken in the form of voltages in measurement coils.

The coaxial coils in Fig. 1 are designed using an optimization algorithm utilizing Helmholtz Coil principles to have a uniform electromagnetic field inside the coils. The transmit coil of the arrangement has a 240 mm diameter and is made up of nine individual coil sections (turns: 11:3:5:5:5:5:5:3:11) connected in series addition, which are used to generate \mathbf{H}_0 . There are two receive coils, each made up of four coil sections (turns: 27:18:18:49:49:18:18:27) and are 220 mm in diameter. The two, four coil sections are connected in series opposition to have no output when there is no target object placed in the arrangement. There is an additional two-turn pick-up coil at the bottom of the coil arrangement for measuring the current. The placement of the coil is chosen to have minimal interaction with the target objects placed in the coils. The total height of the coil arrangement is 500 mm. The coils are wound around hollow fiberglass tubes and are encapsulated in epoxy resin for thermal and mechanical stability. The coils are optimized to operate between 100 Hz and 100 kHz. Therefore, resonant

The authors would like to thank the Engineering and Physical Sciences Research Council (Grant ref EP/R002177) and Sir Bobby Charlton Foundation for financial support of this research. P.D. Ledger gratefully acknowledges the financial support received from EPSRC in the form of grants EP/V049453/1 and EP/V009028/1.

frequencies of the coils' impedances are designed to be outside of the operating spectrum. The lower and higher frequency limits are chosen to capture the necessary spectral characteristics of anti-personnel landmines. Outside the operating spectrum, spectral response of most anti-personnel landmines moves towards their asymptote, where the response is mostly flat.

System electronics are controlled by the control software and are used to drive the coils and take measurement inputs. It consists of a transmit electronics, receive electronics, a microcontroller (Red Pitaya – STEMLab 125-14) and power supplies. The system is powered by two 18 V, 350 W power supply units (PSU) for the amplifiers and a 12 V, 80 W PSU for the microcontroller and electronics box cooling fans.

The transmit electronics are mainly made up of twenty power amplifiers and their complementary components implemented on a four-layer PCB. Half of the amplifiers are configured as non-inverting and the other half as inverting. Together, the transmit power amplifiers output a sine wave with 10 Amps maximum at 64 Volts. An intermediate instrumentation amplifier with a gain of 32 is used between the output of the microcontroller and the power amplifiers, amplifying the ± 1 V output of the microcontroller to ± 32 V.

There are two receive amplifier circuits for current and voltage measurement made up of instrumentation amplifiers and band pass filters. The band pass filters have a lower cut off frequency of 70 Hz to eliminate AC power noise and a higher cut of frequency of 120 kHz to remove any noise introduction from signals outside of the operating spectrum, including from digital-to-analogue converter (DAC) switching noise. The microcontroller is used as signal excitation source for the transmit electronics which also acquires generated signal from the receive electronics. The microcontroller has a maximum input voltage of ± 1 V. The maximum voltage output from the receive coils were found to be less than 200 mV with the test objects used in [17], so gain of the instrumentation amplifier for receive voltage measurement was set to 5. The output voltage can also be reduced if there is any saturation at the receive electronics. The maximum voltage from the current measurement coil was measured to be ± 400 mV, so gain of the instrumentation amplifier for current measurement was set to 2.

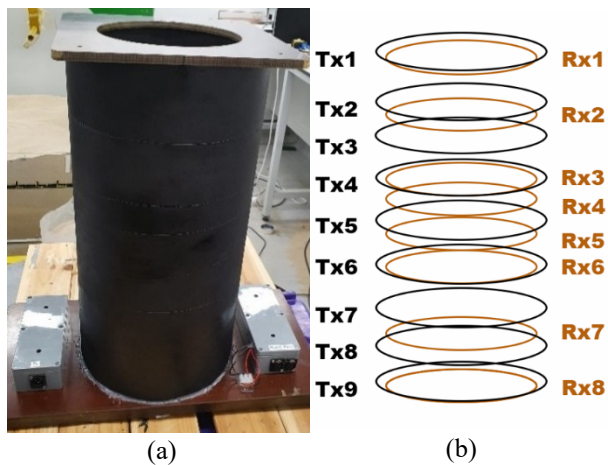


Fig. 1 - Coaxial coil arrangement of the system. (a) is the completed coil arrangement encapsulated in epoxy and fiberglass tubes. (b) is the geometry showing relative positions of individual coil sections to each other.

Data acquisition and processing is done by a Xilinx Zynq7000 system-on-chip (SoC), which is mounted on the microcontroller. It has two 14-bit, 125 MSPS analogue-to-digital converters (ADC) that are used for the voltage and current measurements. The 14-bit resolution approximately translates to a voltage resolution of 122 μ V. The SoC also has two 14-bit, 125 MSPS DACs, which one of them is used for the transmit amplifier excitation source.

Experiment settings, calibration, data logging and processing are handled by the control software of the system. It communicates with the microcontroller in real time and controls frequency and amplitude of the generated signal. Post-processing of the data is also done by the control software. MPT eigenvalues are the final output from the software, at the end of an experiment.

Performance of the system was tested and evaluated in detail in [17]. Experiment repeatability was tested by characterizing a copper disk 30 mm in diameter and 2 mm in thickness 10 times. For this experiment, we can estimate, at the 95% confidence level, that our sample size of 10 measurements is sufficient to predict the (population) mean value of the real and imaginary parts of \mathcal{M}_{ij} lies within 1% of its sample mean value at each frequency.

III. METHOD

Experiment settings were set in the control software before each experiment. The system was then left running for more than an hour to warm up. This ensured the system reached its steady-state temperature to minimize measurement drift caused by system temperature change. First, a NiZn ferrite rod was measured which has a pure real response across the operating spectrum. This was then used as reference for phase calibration of the experiment results.

For each experiment, the target object was placed in the coils at sixteen unique, pre-determined orientations, which were same for all experiments. For each orientation, a number of frequency sweeps (set in the experiment settings) were done and averaged for improved signal-to-noise ratio (SNR). Although, six unique orientations are enough for measuring rank 2 MPT of an object, using sixteen independent orientations results in an overdetermined system with sixteen linear equations which reduces measurement errors. The MPT coefficients of an object then follow from solving a least square method using the perturbed voltage measurements. The eigenvalues of the real and imaginary part of the MPTs were then calculated and plotted versus frequency.

The perturbed voltage measurements were obtained by taking a background field measurement without an object and subtracting this from the measurement with the object present. To reduce uncertainty, after each measurement at an orientation, the background measurement was taken again and updated. The system has a high thermal and mechanical stability (caused by being encapsulated in epoxy resin), which further ensured that any small drift caused by a temperature change was also eliminated. Another source of uncertainty in the experiments is the error in the orientation. This is caused by small shape imperfections of the target orientation manipulator used, which is manufactured using a combination of laser-cut and 3D printed parts. The orientation error has been found to be less than 1 degree and the error introduced to the MPT measurements by this is within the noise floor of the experiments. This means, no significant error is introduced to the experiments by the

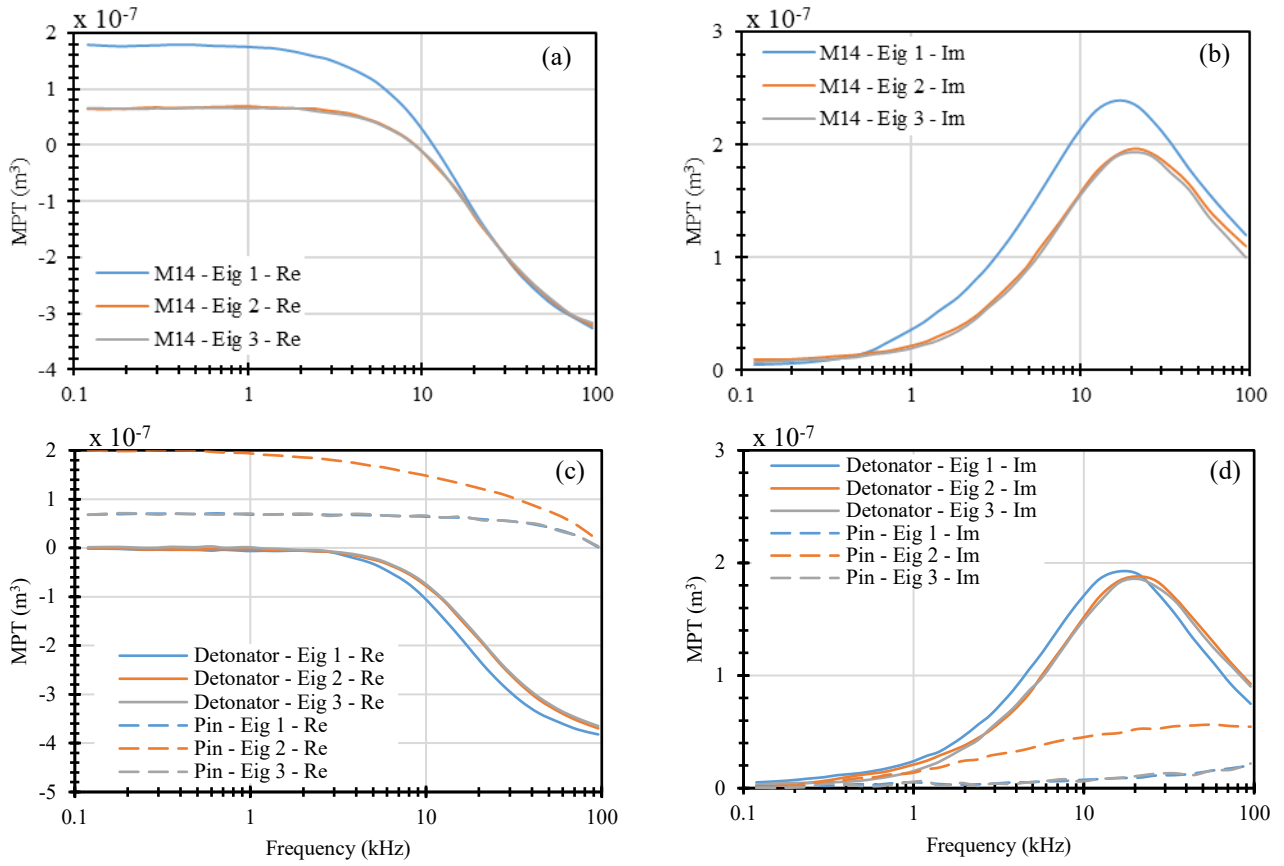


Fig. 2 – Real and imaginary MPT eigenvalues of M14 anti-personnel landmine and its components. (a-b) are M14 anti-personnel landmine. (c-d) are detonator and pin of M14.

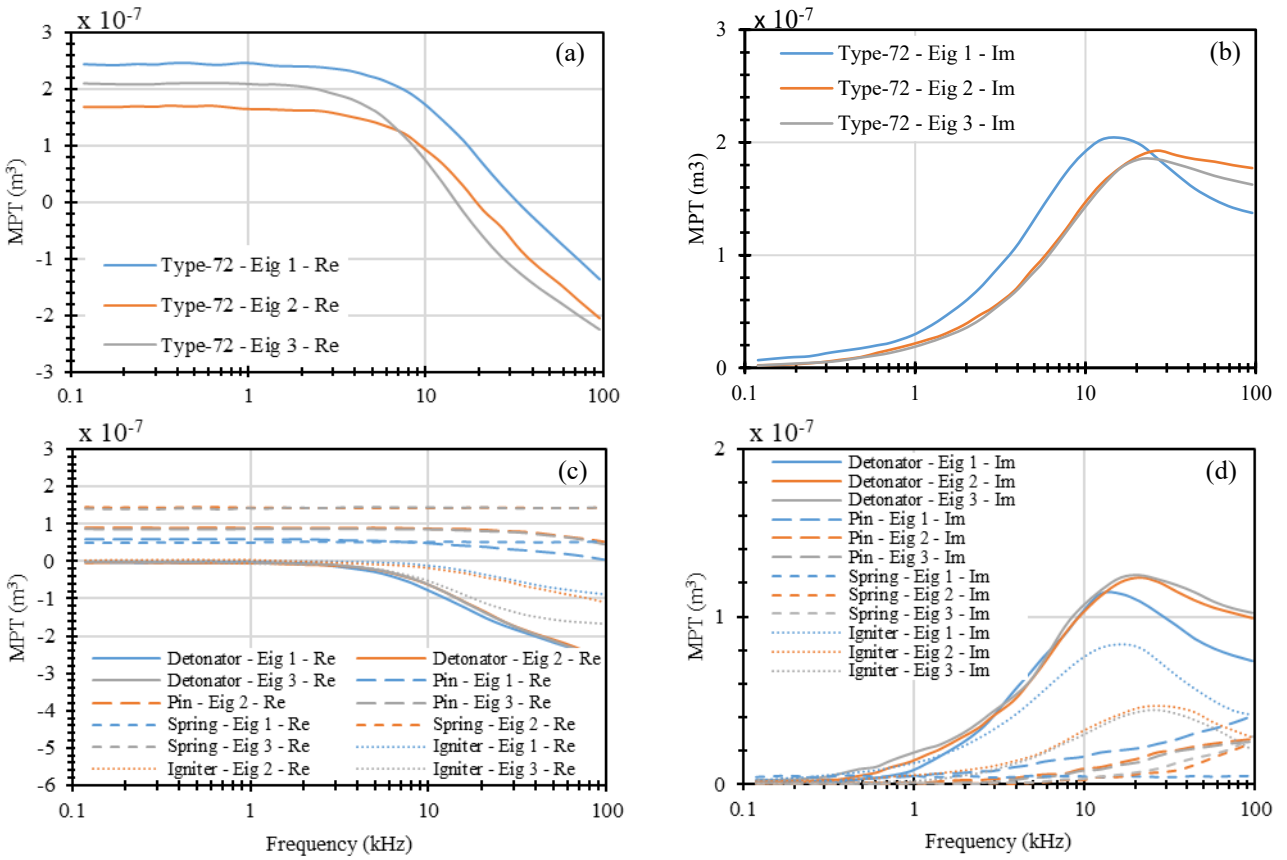


Fig. 3 – Real and imaginary MPT eigenvalues of Type-72 anti-personnel landmine and its components. (a-b) are Type-72 anti-personnel landmine. (c-d) are detonator, pin, spring, and igniter of Type-72.

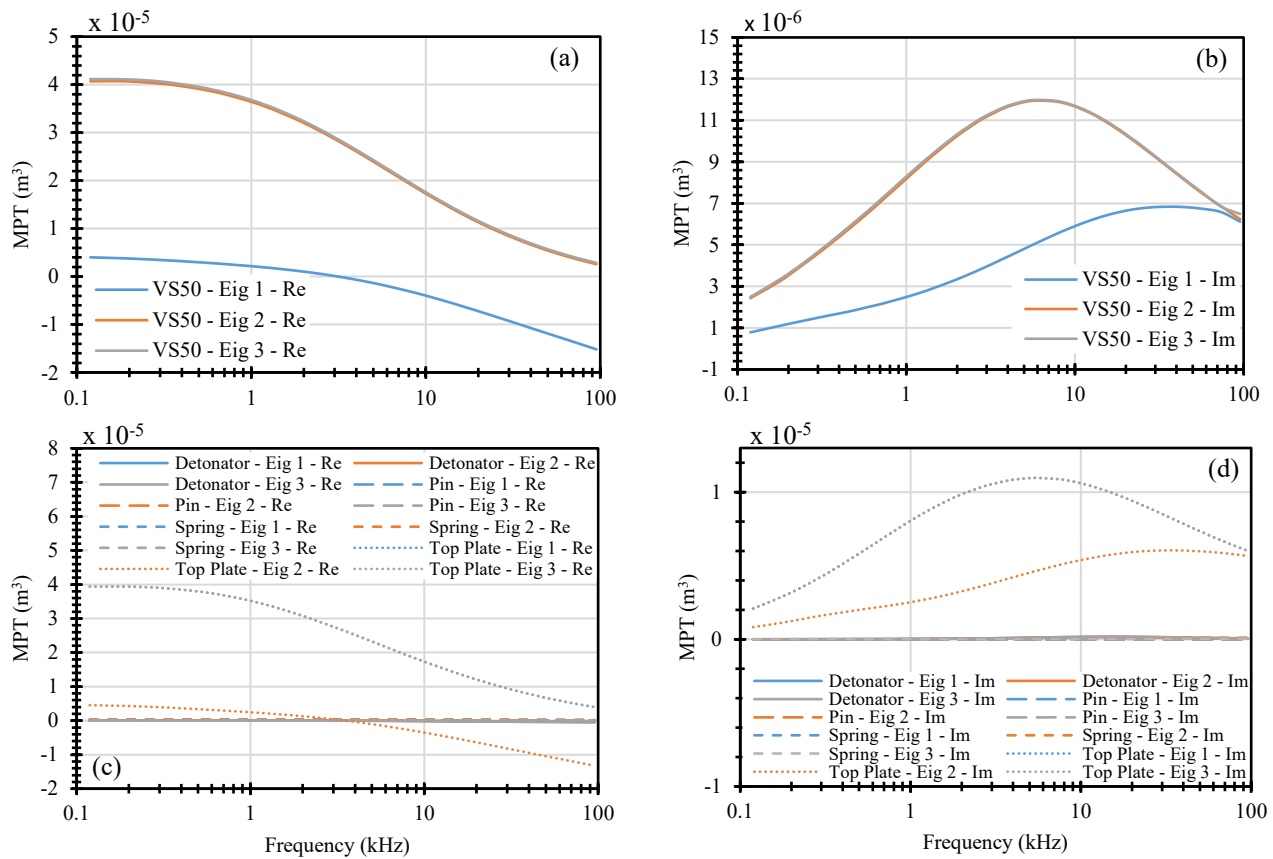


Fig. 4 – Real and imaginary MPT eigenvalues of VS50 anti-personnel landmine and its components. (a-b) are VS50 anti-personnel landmine. (c-d) are detonator, pin, spring, and top plate of VS50.

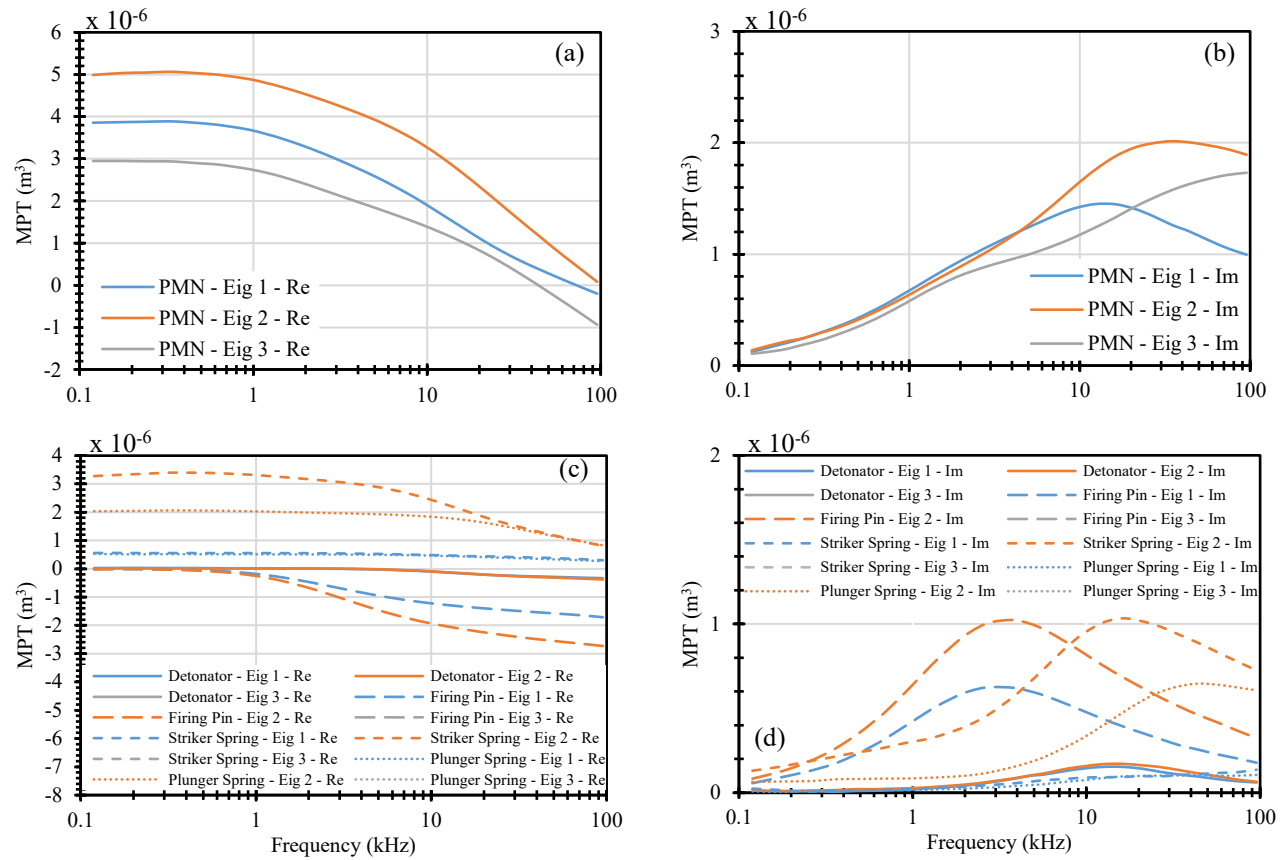


Fig. 5 – Real and imaginary MPT eigenvalues of PMN anti-personnel landmine and its components. (a-b) are PMN anti-personnel landmine. (c-d) are detonator, pin, striker spring, plunger spring and igniter of PMN.

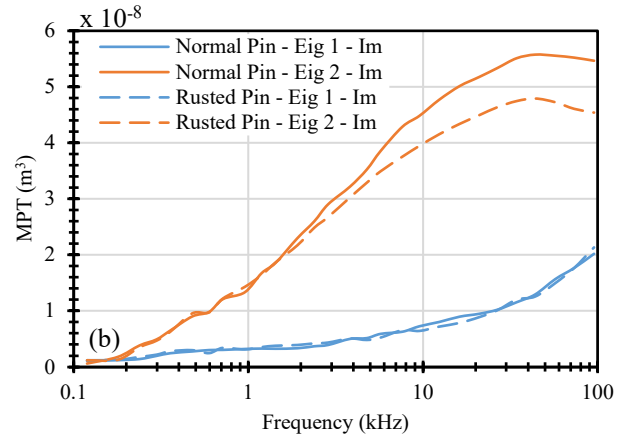
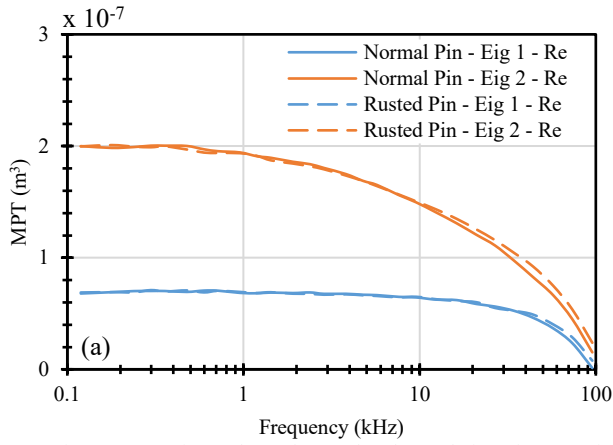


Fig. 6 – MPT eigenvalues of normal and rusted pins of M14 anti-personnel landmine. (a) is real and (b) is imaginary MPT eigenvalues.

object orientation errors. The main source of error in the experiments is measurement noise. SNR can differ depending on the target object's response size at different frequencies. A test was run using a copper disk 30 mm in diameter and 2 mm in thickness where the SNR was found to be 100 at worst. However, SNR can be improved where necessary by simply increasing the amount of signal averaging with a trade-off of increasing the amount of time it takes to run the experiment. Overall, error from measurement drift, measurement noise and orientation errors combined only start to be apparent below 20 mm³, which has found to perform well for landmine characterization.

IV. RESULTS

The study covers MPT characterizations of four anti-personnel landmines and their components, which were supplied by Fenix Insight Ltd. The landmines and their components are shown in TABLE I.

Real and imaginary MPT eigenvalues of four landmines and their individual components are shown in Fig. 2-5. For all four landmines, the spring was ferrous, as well as the firing pin except for the PMN. This can be concluded from the lower frequency asymptote of real MPT eigenvalues being above 0 m³ for these components. MPT eigenvalues of VS50 were dominated by its top plate, which is larger than the other components. PMN and VS50 had around 10 and 100 times larger response compared to M14 and Type-72, respectively. This is due to PMN and VS50 having larger components compared to the others. This means that PMN and VS50 are potentially more detectable and can be distinguished from the background response much easier compared to M14 and Type-72. For M14, the difference between the MPT eigenvalue response for new and rusted ignition pins was also compared in Fig. 6. This is motivated by the fact that landmine components may rust if left buried for a long time. While the real MPT eigenvalues had negligible difference on this scale, imaginary MPT eigenvalue 2 for rusted pin was smaller towards higher end of the spectrum compared to the normal pin. The difference was around ten times smaller than imaginary MPT eigenvalue 2 of the landmine. Therefore, it is likely to be difficult to discriminate in real world data in the field with more noise. However, this means that rusting of the components may not have a large impact of the landmine's MPTs, which reduces any possibility of false classification of targets due to rusting.

TABLE I
Characterized anti-personnel landmines.

Name	Image	Metal Components
M14		Detonator, Pin
Type-72		Detonator, Spring, Igniter, Pin
VS50		Detonator, Spring, Pin, Top Plate
PMN		Detonator, 2 Springs, Firing Pin, Lid Strap

V. CONCLUSION AND FUTURE WORK

Four landmines and their components were characterized using the MPT measurement system described in [17]. Eigenvalues of the rank 2 MPT characterizations of these between 100 Hz and 100 kHz were reported. In addition, rusting of the firing pin was found to have minimal impact on the overall landmine MPT characterization. This shows that rank 2 MPT characterizations of new landmines remain valid for characterizing landmines buried underground, which may have rusted components. Characterizing higher rank MPTs of metal objects, including landmines, is ongoing research. This can further improve classification and reduce FAR for landmine detectors without uniform electromagnetic field. Another ongoing research is to use the acquired landmine and metal clutter (ongoing) MPT object characterizations in realistic soil models. A large dictionary of simulated MPT characterizations of security threat objects has already been

created and used to train machine learning algorithms for classification purposes [5], [11]. In future work, we will extend this library to include simulated and measured MPT characterizations of landmine components. Trained Machine learning algorithms' performance of identifying landmines and reducing FAR can then be tested in the field using metal detectors utilizing electromagnetic induction spectroscopy.

ACKNOWLEDGMENT

The authors would like to thank Fenix Insight Ltd for providing access to the landmines characterized in this paper.

VI. REFERENCES

- [1] International Campaign to Ban Landmines, "What is a Landmine?", 2019, Accessed November 2021, <http://www.icbl.org/en-gb/problem/what-is-a-landmine.aspx>.
- [2] International Campaign to Ban Landmines, "Landmine Monitor", 2019, Accessed November 2021, <http://www.icbl.org/en-gb/resources/landmine-monitor.aspx>.
- [3] International Campaign to Ban Landmines, "A History of Landmines", Accessed November 2021, <http://www.icbl.org/en-gb/problem/a-history-of-landmines.aspx>.
- [4] Tsipis, K. "Technological Innovation in Humanitarian Demining," *Human Factors and Ergonomics Soc*, SANTA MONICA, pp. 750-753, 1998.
- [5] Ledger, P.D., Wilson, B.A., Amad, A.A.S., Lionheart, W.R.B., "Identification of metallic objects using spectral MPT signatures: Object characterization and invariants," *International Journal for Numerical Methods in Engineering*, vol. 122, pp. 3941-3984, 2021.
- [6] Ledger, P.D., Lionheart, W.R.B., "The spectral properties of the magnetic polarizability tensor for metallic object characterization," *Math Meth Appl Sci*, vol. 43, pp. 78–113, 2020.
- [7] Ledger, P.D., Lionheart, W.R.B., "Characterizing the shape and material properties of hidden targets from magnetic induction data," *IMA Journal of Applied Mathematics*, vol. 80, no. 6, pp. 1776–1798, 2015.
- [8] Wilson, B.A., Ledger, P.D., "Efficient computation of the magnetic polarizability tensor spectral signature using proper orthogonal decomposition," *International Journal for Numerical Methods in Engineering*, vol. 122, pp. 1940–1963, 2021.
- [9] Ledger, P.D., Lionheart, W.R.B., "An Explicit Formula for the Magnetic Polarizability Tensor for Object Characterization," *IEEE Transactions on Geoscience and Remote Sensing*, vol. 56, no. 6, pp. 3520-3533, 2018.
- [10] Ledger, P.D., Lionheart, W.R.B., "Understanding the magnetic polarizability tensor," *IEEE Transactions on Magnetics*, vol. 52, No. 5, pp. 1-16, 2016.
- [11] Wilson, B.A., Ledger, P.D., Lionheart, W.R.B., "Identification of Metallic Objects using Spectral Magnetic Polarizability Tensor Signatures: Object Classification," *International Journal for Numerical Methods in Engineering*, Accepted Author Manuscript, 2022.
- [12] O'Toole, M., Karimian, N., Peyton, A.J., "Classification of Nonferrous Metals Using Magnetic Induction Spectroscopy," *IEEE Transactions on Industrial Informatics*, vol. 14, no. 8, pp. 3477-3485, 2018.
- [13] Makkonen, J., Marsh, L., Vihonen, J., Järvi, A., Armitage, D., Visa, A., Peyton, A.J., "KNN classification of metallic targets using the magnetic polarizability tensor," *Measurement Science and Technology*, vol. 25, no. 5, pp. 055105, 2014.
- [14] Fernandez, J.P., Barrowes, B. E., Grzegorzczak, T. M., Lhomme, N., O'Neill, K., Shubitidze, F., "A Man-Portable Vector Sensor for Identification of Unexploded Ordnance," *IEEE Sensors Journal*, vol. 11, no. 10, pp. 2542-2555, 2011.
- [15] Norton, S.J., Won, I.J., "Identification of buried unexploded ordnance from broadband electromagnetic induction data," *IEEE Transactions on Geoscience and Remote Sensing*, vol. 39, no. 10, pp. 2253-2261, 2001.
- [16] Grzegorzczak, T. M., Barrowes, B. E., Shubitidze, F., Fernandez, J.P., O'Neill, K., "Simultaneous Identification of Multiple Unexploded Ordnance Using Electromagnetic Induction Sensors," *IEEE Transactions on Geoscience and Remote Sensing*, vol. 49, no. 7, pp. 2507-2517, 2011.
- [17] Özdeğer, T., Davidson, J.L., van Verre, W., Marsh, L.A., Lionheart, W.R.B., Peyton, A.J., "Measuring the Magnetic Polarizability Tensor

Using an Axial Multi-Coil Geometry," *IEEE Sensors Journal*, vol. 21, no. 17, pp. 19322-19333, 2021.

Publication 4

Özdeğer, T., Ledger, P. D., Lionheart, W. R. B., Davidson, J. L., Peyton, A. J., "Measurement of GMPT Coefficients for Improved Object Characterisation in Metal Detection," *IEEE Sensors Journal*, vol. 22, no. 3, pp. 2430-2446, 2022. **Published.**

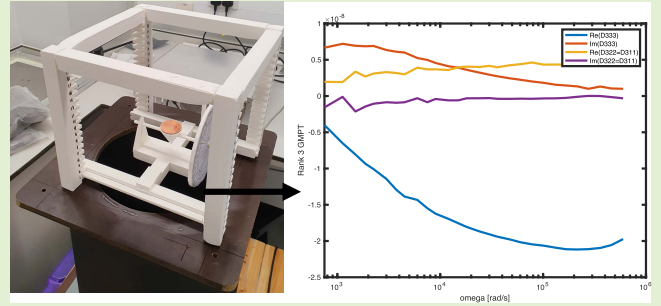
Doi: 10.1109/JSEN.2021.3133950.

Measurement of GMPT Coefficients for Improved Object Characterisation in Metal Detection

T. Özdeğer¹, P. D. Ledger², W. R. B. Lionheart³, J. L. Davidson⁴, and A. J. Peyton⁵

Abstract—Magnetic polarizability tensors (MPTs) have become popular for characterising conducting permeable objects and assisting with the identification of hidden objects in metal detection for applications in security screening, humanitarian demining and scrap sorting. A rigorous mathematical justification of the complex symmetric rank 2 MPT object characterisation has been established based on the leading order term in an asymptotic expansion of the perturbed field for small objects. However, the accuracy of an MPT object characterisation is limited by the tensor's small number of independent coefficients. By considering higher order terms in the asymptotic expansion, generalised magnetic polarizability tensors (GMPTs) have been introduced and the purpose of this work is to show that GMPT coefficients can, for the first time, be measured in practice. GMPTs offer the possibility to better discriminate between objects and, hence, the potential for better classification and identification, overcoming the limitations of a rank 2 MPT object characterisation. In a metal detector, the low-frequency background fields generated by a set of coils is almost always non-uniform and using GMPTs allow us to make a virtue of this. In this work we include both measurements and simulations to demonstrate the advantages that using GMPTs offer over using an MPT characterisation alone.

Index Terms—Electromagnetic induction spectroscopy, magnetic polarizability tensor, metal detection, metal classification.



I. INTRODUCTION

MAGNETIC polarizability tensors (MPTs) have become popular for characterising conducting permeable objects and assisting with the identification of hidden objects in metal detection for applications in security screening, humanitarian demining and scrap sorting e.g. [1], [2], [9]–[11], [19]–[21], [23], [30]–[32], [35]. A rigorous mathematical theory has been established for the complex

symmetric rank 2 MPT characterisation of a small highly conducting permeable isolated object in a non-conducting background. It has been shown that the MPT forms the object description in the leading order term of an asymptotic expansion of the perturbed magnetic field $(\mathbf{H}_a - \mathbf{H}_0)(\mathbf{x})$ as the object size $\alpha \rightarrow 0$ [4], [12]. The expansion holds at positions \mathbf{x} away from the object. Furthermore, for objects with rotational and reflectional symmetries, it has been established that the number of independent complex coefficients in the MPT can be much smaller than 6 [12]. The leading order term in the asymptotic expansion of $(\mathbf{H}_a - \mathbf{H}_0)(\mathbf{x})$ as $\alpha \rightarrow 0$ and an MPT object characterisation has been generalised for multiple and inhomogeneous objects in [16]. Considerable benefits have been seen to be offered by exploiting the spectral behaviour of the MPT coefficients, known as its spectral signature, which provides much richer information than the MPT at a single frequency. This has been understood theoretically [15], efficient algorithms have been developed to compute the MPT spectral signature [33] and these have been applied to compute libraries of MPT spectral signature object characterisations [17]. Machine learning approaches for object classification based on measured and simulated libraries of MPT spectral signatures have also been developed in [19], [20] and [34], respectively.

A complete asymptotic expansion of the perturbed magnetic field $(\mathbf{H}_a - \mathbf{H}_0)(\mathbf{x})$ as $\alpha \rightarrow 0$ has been derived in [14],

Manuscript received November 2, 2021; revised November 26, 2021; accepted December 2, 2021. Date of publication December 8, 2021; date of current version January 31, 2022. The work of T. Özdeğer was supported in part by the Engineering and Physical Sciences Research Council (EPSRC) U.K. under the Research Grant EP/R002177 and in part by the Sir Bobby Charlton Foundation. The work of P.D. Ledger was supported by EPSRC under the Research Grant EP/R002134/2, Grant EP/V049453/1, and Grant EP/V009028/1. The work of W. R. B. Lionheart was supported in part by EPSRC under Grant EP/V049496/1 and Grant EP/V009109/1 and in part by the Royal Society through the Royal Society Wolfson Research Merit Award. The associate editor coordinating the review of this article and approving it for publication was Prof. Chao Tan. (Corresponding author: P. D. Ledger.)

T. Özdeğer, J. L. Davidson, and A. J. Peyton are with the Department of Electrical and Electronic Engineering, The University of Manchester, Manchester M13 9PL, U.K.

P. D. Ledger is with the School of Computing and Mathematics, Keele University, Staffordshire ST5 5BG, U.K. (e-mail: p.d.ledger@keele.ac.uk).

W. R. B. Lionheart is with the Department of Mathematics, The University of Manchester, Manchester M60 1QD, U.K.

Digital Object Identifier 10.1109/JSEN.2021.3133950

which generalises the earlier results in [4], [12]. In this expansion, new object characterisations called generalised magnetic polarizability tensors (GMPTs) have been introduced, building on the MPT object characterisation in the leading order term. The purpose of this work is to show that GMPT coefficients can be measured in practice for the first time. GMPTs offer significant advantages over small object characterisations using the leading order rank 2 MPT descriptions currently used in metal detection. Specifically:

- 1) Offering the possibility to better discriminate between objects and, hence, offer the potential for better classification and identification, overcoming the limitations of characterising objects using just 6 complex coefficients in a rank 2 MPT description (a simple example of which is to tell which way a cone is pointing).
- 2) In a metal detector, the low-frequency background fields \mathbf{H}_0 generated by a set of coils is almost always non-uniform and using GMPTs allow us to make a virtue of this overcoming the assumption that \mathbf{H}_0 is uniform over the object in a rank 2 description (hence also achieving better 1.).

GMPTs are more complicated than the generalised polarizability tensors (GPT) derived by Ammari and Kang [6] for characterising low conducting inclusions in a scalar electrical impedance tomography (EIT) problem. They have interesting mathematical properties, which we plan to catalogue in a forthcoming work.

The novelties of this work can be summarised as follows: We show, for the first time, that GMPT coefficients and their spectral signature can be obtained in practice from measurements of $(\mathbf{H}_\alpha - \mathbf{H}_0)(\mathbf{x})$ for a multiple coil arrangement using a novel object manipulation device. The resulting measured GMPT spectral signatures we obtain are in good agreement with the simulated GMPT spectral signatures that we calculate from numerical simulations using finite elements. We illustrate that including the GMPT object characterisation information is important to accurately predict $(\mathbf{H}_\alpha - \mathbf{H}_0)(\mathbf{x})$ whenever the background field is non-uniform.

The work is organised as follows: We begin with some notation in Section II. Next, in Section III, we review the complete asymptotic expansion of $(\mathbf{H}_\alpha - \mathbf{H}_0)(\mathbf{x})$ as $\alpha \rightarrow 0$ and restrict consideration to terms associated with rank 2 MPT and rank 3 GMPT object characterisations. Then, in Section IV, we apply the asymptotic expansion to a mathematical model of the physical multiple coil arrangement that will be used to generate \mathbf{H}_0 and to measure $(\mathbf{H}_\alpha - \mathbf{H}_0)(\mathbf{x})$ in the form of a transimpedance measurement. In Section V, we describe how the transimpedance measurements can be used to determine the MPT and GMPT coefficients by rotating the object in a uniform and then non-uniform \mathbf{H}_0 using an object manipulation device and, in Section VI, we explain how the MPT and GMPT coefficients and their spectral signatures can be predicted numerically. Section VII presents a series of results that compare our measurements and simulations, which demonstrate that GMPT coefficients and their spectral signature can be obtained in practice and that they have an important role to play in predicting $(\mathbf{H}_\alpha - \mathbf{H}_0)(\mathbf{x})$ if \mathbf{H}_0 is

non-uniform. We finish, in Section VIII with some concluding remarks.

II. NOTATION

We denote by \mathbf{e}_k the unit basis vector associated with the k th coordinate direction in a standard orthonormal coordinate system $\mathbf{x} = (x_1, x_2, x_3)$ and, hence, the k th component of a vector field \mathbf{v} is given by $\mathbf{e}_k \cdot \mathbf{v} = (\mathbf{v})_k = v_k$. We will often use Einstein index summation notation so that a vector can be described as $\mathbf{v} = v_k \mathbf{e}_k$ and a rank 2 tensor using a calligraphic font as $\mathcal{M} = \mathcal{M}_{kj} \mathbf{e}_k \otimes \mathbf{e}_j$ where summation is implied over the repeated indices in each case. We will use a Gothic font for higher order tensors so that a rank 3 can be described as $\mathfrak{D} = \mathfrak{D}_{ijk} \mathbf{e}_i \otimes \mathbf{e}_j \otimes \mathbf{e}_k$. The imaginary unit is defined as $i := \sqrt{-1}$ and we will also use the notation $\|u\|_{L^2(\theta)} := \left(\int_0^{2\pi} |u(\theta)|^2 d\theta \right)^{1/2}$ to denote the L^2 norm of u over the angles $0 \leq \theta \leq 2\pi$.

III. COMPLETE ASYMPTOTIC EXPANSION

In [14] Ledger and Lionheart proved the result stated in Theorem 1 below, for describing the magnetic field perturbation $(\mathbf{H}_\alpha - \mathbf{H}_0)(\mathbf{x})$ at a position \mathbf{x} due to the presence of a highly conducting object B_α with conductivity σ_* and permeability μ_* in a non-conducting background with conductivity $\sigma = 0$ and the permeability of free space μ_0 . The result is applicable away from the object when the eddy current approximation of Maxwell's equations applies [3], which means the excited angular frequency $\omega = 2\pi f$ (with f measured in Hz) of the background field \mathbf{H}_0 is low and σ_* is high. Additionally, the topology of the object B_α and its size α limits the applicability of the eddy current model, with the eddy current model breaking down for a horse shoe shaped conductor at lower frequencies compared to a solid object of the same size due to capacitive coupling effects [26]. The description $B_\alpha := \alpha B + \mathbf{z}$ means that the object can be described by a non-dimensional object B placed at the origin, scaled by a size parameter α and translated by \mathbf{z} .

Theorem 1: The magnetic field perturbation in the presence of a small conducting object $B_\alpha = \alpha B + \mathbf{z}$ for the eddy current model when $\nu := \omega \sigma_* \mu_0 \alpha^2$ is order one and \mathbf{x} is away from the location \mathbf{z} of the inclusion is completely described by the asymptotic formula

$$\begin{aligned}
 (\mathbf{H}_\alpha - \mathbf{H}_0)(\mathbf{x})_i &= \sum_{m=0}^{M-1} \sum_{p=0}^{M-1-m} (\mathbf{D}_x^{2+m} G(\mathbf{x}, \mathbf{z}))_{[i, K(m+1)]} \\
 &\quad \mathfrak{M}_{K(m+1)J(p+1)}(\mathbf{D}_z^p(\mathbf{H}_0(\mathbf{z})))_{J(p+1)} \\
 &\quad + (\mathbf{R}(\mathbf{x}))_i, \tag{1} \\
 J(p+1) &:= [j, J(p)] = [j, j_1, j_2, \dots, j_p], \\
 K(m+1) &:= [k, K(m)] = [k, k_1, k_2, \dots, k_m],
 \end{aligned}$$

with $|\mathbf{R}(\mathbf{x})| \leq C \alpha^{3+M} \|\mathbf{H}_0\|_{W^{M+1, \infty}(B_\alpha)}$, $G(\mathbf{x}, \mathbf{z}) := 1/(4\pi|\mathbf{x} - \mathbf{z}|)$. In the above, $J(p)$ and $K(m)$ are p - and m -tuples of integers, respectively, with each index taking values 1, 2, 3, and Einstein index summation is implied over

$K(m+1)$ and $J(p+1)$. Also

$$(D_x^{2+m}G(\mathbf{x}, \mathbf{z}))_{[i, K(m+1)]} = \left(\prod_{\ell=1}^m \partial_{x_{k_\ell}} \right) (\partial_{x_k} (\partial_{x_i} (G(\mathbf{x}, \mathbf{z})))),$$

$$(D_z^p(H_0(\mathbf{z})))_{J(p+1)} = \left(\prod_{\ell=1}^p \partial_{z_{j_\ell}} \right) (H_0(\mathbf{z}) \cdot \mathbf{e}_j),$$

and the coefficients of a rank $2 + p + m$ generalised magnetic polarizability tensor (GMPT) are defined by

$$\mathfrak{M}_{K(m+1)J(p+1)} := -\mathfrak{C}_{K(m+1)J(p+1)} + \mathfrak{N}_{K(m+1)J(p+1)}, \quad (2)$$

where

$$\begin{aligned} \mathfrak{C}_{K(m+1)J(p+1)} &:= -\frac{i\nu\alpha^{3+m+p}(-1)^m}{2(m+1)!p!(p+2)}\mathbf{e}_k \\ &\cdot \int_B \boldsymbol{\xi} \times ((\Pi(\boldsymbol{\xi}))_{K(m)}(\boldsymbol{\theta}_{J(p+1)} + (\Pi(\boldsymbol{\xi}))_{J(p)}\mathbf{e}_j \times \boldsymbol{\xi})) d\boldsymbol{\xi}, \end{aligned} \quad (3a)$$

$$\begin{aligned} \mathfrak{N}_{K(m+1)J(p+1)} &:= \left(1 - \frac{\mu_0}{\mu_*}\right) \frac{\alpha^{3+m+p}(-1)^m}{p!m!}\mathbf{e}_k \\ &\cdot \int_B (\Pi(\boldsymbol{\xi}))_{K(m)} \left(\frac{1}{p+2} \nabla_\xi^\perp \times \boldsymbol{\theta}_{J(p+1)} + (\Pi(\boldsymbol{\xi}))_{J(p)}\mathbf{e}_j \right) d\boldsymbol{\xi}. \end{aligned} \quad (3b)$$

In the above, $\boldsymbol{\theta}_{J(p+1)}$ satisfy the transmission problem

$$\begin{aligned} \nabla_\xi^\perp \times \mu_*^{-1} \nabla_\xi^\perp \times \boldsymbol{\theta}_{J(p+1)} - i\omega\sigma_*\alpha^2 \boldsymbol{\theta}_{J(p+1)} \\ - i\omega\sigma_*\alpha^2 (\Pi(\boldsymbol{\xi}))_{J(p)}\mathbf{e}_j \times \boldsymbol{\xi} = \mathbf{0} \quad \text{in } B, \end{aligned} \quad (4a)$$

$$\nabla_\xi^\perp \cdot \boldsymbol{\theta}_{J(p+1)} = 0 \quad \text{in } \mathbb{R}^3 \setminus B \quad (4b)$$

$$\nabla_\xi \times \mu_0^{-1} \nabla_\xi \times \boldsymbol{\theta}_{J(p+1)} = \mathbf{0} \quad \text{in } \mathbb{R}^3 \setminus B, \quad (4c)$$

$$[\mathbf{n} \times \boldsymbol{\theta}_{J(p+1)}]_\Gamma = \mathbf{0} \quad \text{on } \Gamma := \partial B, \quad (4d)$$

$$\begin{aligned} [\mathbf{n} \times \mu_*^{-1} \nabla_\xi \times \boldsymbol{\theta}_{J(p+1)}]_\Gamma &= -(p+2)[\mu_*^{-1} \Gamma \\ &\cdot (\mathbf{n} \times \mathbf{e}_j (\Pi(\boldsymbol{\xi}))_{J(p)})] \quad \text{on } \Gamma, \end{aligned} \quad (4e)$$

$$\int_\Gamma \mathbf{n} \cdot \boldsymbol{\theta}_{J(p+1)} d\boldsymbol{\xi} = 0, \quad (4f)$$

$$\boldsymbol{\theta}_{J(p+1)} = O(|\boldsymbol{\xi}|^{-1})$$

$$\text{as } |\boldsymbol{\xi}| \rightarrow \infty, \quad (4g)$$

$(\Pi(\boldsymbol{\xi}))_{J(p)} := \prod_{\ell=1}^p \check{\zeta}_{j_\ell} = \check{\zeta}_{j_1} \check{\zeta}_{j_2} \cdots \check{\zeta}_{j_p}$ and in the case $J(p) = \emptyset$ then $(\Pi(\boldsymbol{\xi}))_{J(p)} = 1$.

Note that, compared to [14], we have chosen to simplify the notation so that $\check{\mathfrak{C}}$ is now written as \mathfrak{C} and $\check{\mathfrak{M}}$ as \mathfrak{M} . Furthermore, in this work, we will restrict consideration to objects with $\mu_* = \mu_0$ so that $\mathfrak{N}_{K(m+1)J(p+1)} = 0$ and consider

the case of $M = 2$. This means the asymptotic expansion we will consider includes the terms

$$\begin{aligned} (H_\alpha - H_0)(\mathbf{x})_i &= (D_x^2 G(\mathbf{x}, \mathbf{z}))_{ik} \mathcal{M}_{kj}(H_0(\mathbf{z}))_j \\ &+ \frac{1}{8} (D_x^3 G(\mathbf{x}, \mathbf{z}))_{ikk_1} \mathfrak{D}_{kk_1 j}(H_0(\mathbf{z}))_j \\ &- \frac{1}{6} (D_x^2 G(\mathbf{x}, \mathbf{z}))_{ik} \mathfrak{D}_{kjj_1} (D_z(H_0(\mathbf{z})))_{jj_1} \\ &+ (\mathbf{R}(\mathbf{x}))_i, \end{aligned} \quad (5)$$

with $|\mathbf{R}(\mathbf{x})| \leq C\alpha^5 \|\mathbf{H}_0\|_{W^{3,\infty}(B_\alpha)}$ describing the behaviour of the residual. In the above, the coefficients $\mathcal{M}_{kj} \equiv \mathfrak{M}_{kj}$ are associated with a complex symmetric rank 2 MPT characterisation $\mathcal{M} = \mathcal{M}_{kj} \mathbf{e}_k \otimes \mathbf{e}_j$, which follows since \mathfrak{M}_{kj} reduces to the rank 2 MPT coefficients \mathcal{M}_{kj} previously considered in [12], [13], [15], [16] where it has been shown that $\mathcal{M}_{kj} = \mathcal{M}_{jk}$. The coefficients $\mathfrak{D}_{kk_1 j}$ and \mathfrak{D}_{kjj_1} are associated with scaled rank 3 GMPT characterisations

$$\mathfrak{D} = \mathfrak{D}_{kk_1 j} \mathbf{e}_k \otimes \mathbf{e}_{k_1} \otimes \mathbf{e}_j, \quad \mathfrak{D} = \mathfrak{D}_{kjj_1} \mathbf{e}_k \otimes \mathbf{e}_j \otimes \mathbf{e}_{j_1}, \quad (6)$$

where

$$\mathfrak{D}_{K(m+1)J(p+1)} := (-1)^m 2(m+1)!p!(p+2) \mathfrak{C}_{K(m+1)J(p+1)}. \quad (7)$$

Furthermore, for $\mu_* = \mu_0$, the GMPT has the following symmetry

$$\mathfrak{D}_{K(m+1)J(p+1)} = \mathfrak{D}_{J(p+1)K(m+1)}, \quad (8)$$

which does not follow from reciprocity and is somewhat involved to prove. The proof will form part of a forthcoming work on the mathematical properties of GMPTs.

The coefficients \mathcal{M}_{kj} are independent of the choice of origin for $\boldsymbol{\xi}$ [4], [5], [16] and, hence, the MPT object characterisation is independent of the object's position. However, in common with GPTs for the EIT problem [6], the coefficients $\mathfrak{D}_{kk_1 j}$ of the scaled rank 3 GMPT depend on the choice of origin for $\boldsymbol{\xi}$. For this work, we choose the origin to be the object's centroid (centre of mass assuming uniform density).

Using \mathcal{M} alone to characterise objects has limitations since, at most, an object is characterised by 6 complex coefficients as a function of ω . However, for objects with rotational and/or reflectional symmetries the number of independent coefficients is much fewer and this makes it difficult to discriminate between objects in object classification and to determine which way an object (such as a cone) is pointing. By additionally using \mathfrak{D} provides up to an additional 11 complex coefficients as a function of ω , which can aid with discriminating between objects when undertaking classification. Although, for objects with mirror and/or reflectional symmetries, the number of independent coefficients of \mathfrak{D} also reduces. In the following we explain how the MPT and GMPT coefficients can be measured and simulated in practice.

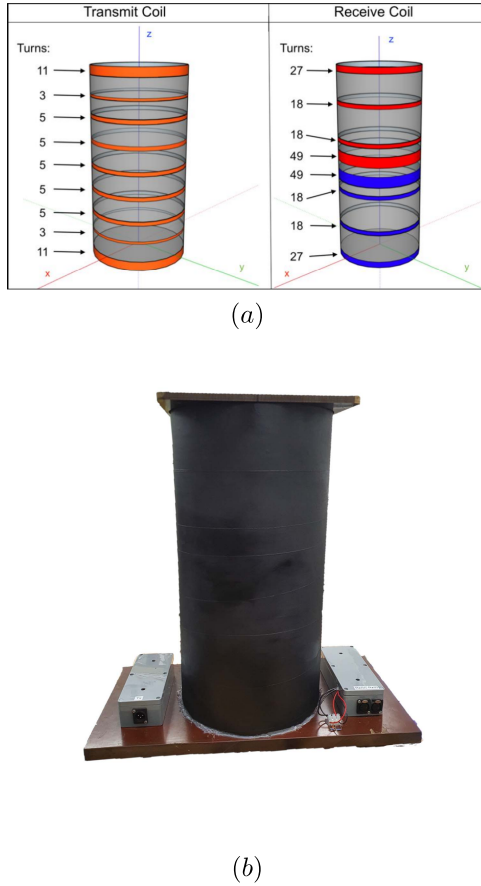


Fig. 1. Configuration of the multiple transmit and receive coil arrangement showing (a) turns in each coil and (b) the actual coil array.

IV. MATHEMATICAL MODEL OF THE COIL ARRANGEMENT

The induced voltage in a coil C with a single clockwise winding, for an object positioned at \mathbf{z} , can be expressed as

$$\begin{aligned} V^{\text{ind}} &= \int_C (\mathbf{E}_a - \mathbf{E}_0)(\mathbf{x}) \cdot \boldsymbol{\tau} d\mathbf{x} \\ &= \int_S \nabla \times (\mathbf{E}_a - \mathbf{E}_0)(\mathbf{x}) \cdot \mathbf{n} d\mathbf{x} \\ &= i\omega\mu_0 \int_S (\mathbf{H}_a - \mathbf{H}_0)(\mathbf{x}) \cdot \mathbf{n} d\mathbf{x}, \end{aligned} \quad (9)$$

where $C = \partial S$, $\boldsymbol{\tau}$ is the unit tangent to C and \mathbf{n} is the unit normal to S . Upon substitution of (1), the evaluation of V^{ind} reduces to performing integrals of components of $(\mathbf{D}_x^{2+m} G(\mathbf{x}, \mathbf{z}))$ with respect to \mathbf{x} over the surface S .

The particular coil configuration considered is shown in Fig. 1 and consists of 8 receive (Rx) coils and 9 transmit (Tx) coils coaxially arranged in a vertical stack so that $\mathbf{n} = \mathbf{e}_3$ in (9). Coils Rx1-Rx4 are wound in a clockwise orientation while coils Rx5-Rx9 are wound in an anticlockwise orientation. Defining

$$w(n) = \begin{cases} 1 & n = 1, \dots, 4 \\ -1 & n = 5, \dots, 8, \end{cases} \quad (10)$$

then the induced voltage is given by the sum

$$V^{\text{ind}} = i\omega\mu_0 \sum_{n=1}^8 \frac{w(n)N_{\text{Rx}}(n)}{L_{\text{Rx}}(n)} \int_{S_{\text{Rx}}(n)} (\mathbf{H}_a - \mathbf{H}_0)(\mathbf{x}) \cdot \mathbf{e}_3 d\mathbf{x}, \quad (11)$$

where $S_{\text{Rx}}(n)$, $N_{\text{Rx}}(n)$ and $L_{\text{Rx}}(n)$ are the enclosed surface, number of turns and length of the n th Rx coil, respectively. The background field \mathbf{H}_0 at the position \mathbf{z} that is created by the Tx coils can be expressed as the sum

$$\begin{aligned} \mathbf{H}_0(\mathbf{z}) &= \mathbf{H}_0^{\text{Tx}}(\mathbf{z}) \\ &= \sum_{n=1}^9 \mathbf{H}_{\text{coil}}(N_{\text{Tx}}(n), I_{\text{Tx}}(n), L_{\text{Tx}}(n), R_{\text{Tx}}(n), \\ &\quad z_1 \mathbf{e}_1 + z_2 \mathbf{e}_2 + (z_3 - L_{\text{Tx}}(n)/2 - p_{\text{Tx}}(n)) \mathbf{e}_3), \end{aligned} \quad (12)$$

where $N_{\text{Tx}}(n)$, $I_{\text{Tx}}(n)$, R_{Tx} , L_{Tx} are the number of turns, current flowing, radius and length of the n th Tx coil, respectively and $p_{\text{Tx}}(n)$ describes the vertical position (base) of the n th Tx coil. In addition, if $\mathbf{z} \parallel \mathbf{e}_3$, we have the well known form

$$\begin{aligned} \mathbf{H}_{\text{coil}}(N, I, L, R, z) \\ = \frac{NI}{2L} \left(\frac{\frac{L}{2R} - \frac{z_3}{R}}{\sqrt{1 + (\frac{L}{2R} - \frac{z_3}{R})^2}} + \frac{\frac{L}{2R} + \frac{z_3}{R}}{\sqrt{1 + (\frac{L}{2R} + \frac{z_3}{R})^2}} \right) \mathbf{e}_3, \end{aligned}$$

for the background field on axis resulting from a solenoid. Off-axis, the representation of \mathbf{H}_{coil} is also known analytically [7]. For the coil arrangement considered, the details are provided in Table I so that the overall height of the arrangement is 500 mm. The non-uniformity of the background field \mathbf{H}_0^{Tx} exterior to the coil array is illustrated in the finite element simulation shown in Fig. 2 (a), which is in close agreement with the analytical model, as Fig. 2 (b) shows.

Furthermore, introducing

$$(\mathbf{H}_0^{\text{Rx}}(\mathbf{z}))_k := \sum_{n=1}^8 \frac{w(n)N_{\text{Rx}}(n)}{L_{\text{Rx}}(n)} \int_{S(n)} \mathbf{D}_x^2 G(\mathbf{x}, \mathbf{z})_{3k} d\mathbf{x}, \quad (13)$$

for the background field that would be produced by the Rx coils if excited by a unit current source at position \mathbf{z} then it is easy to show that

$$\begin{aligned} (\mathbf{D}_z(\mathbf{H}_0^{\text{Rx}}(\mathbf{z}))_{kk_1}) \\ := \sum_{n=1}^8 \frac{w(n)N_{\text{Rx}}(n)}{L_{\text{Rx}}(n)} \int_{S(n)} (\mathbf{D}_z(\mathbf{D}_x^2 G(\mathbf{x}, \mathbf{z})))_{3kk_1} d\mathbf{x} \\ = - \sum_{n=1}^8 \frac{w(n)N_{\text{Rx}}(n)}{L_{\text{Rx}}(n)} \int_{S(n)} (\mathbf{D}_x^3 G(\mathbf{x}, \mathbf{z}))_{3kk_1} d\mathbf{x}. \end{aligned} \quad (14)$$

By substituting (5) into (11), replacing $\mathbf{H}_0(\mathbf{z})$ by the expression given in (12) and using (13) and (14), it can be shown that V^{ind} takes the simple form

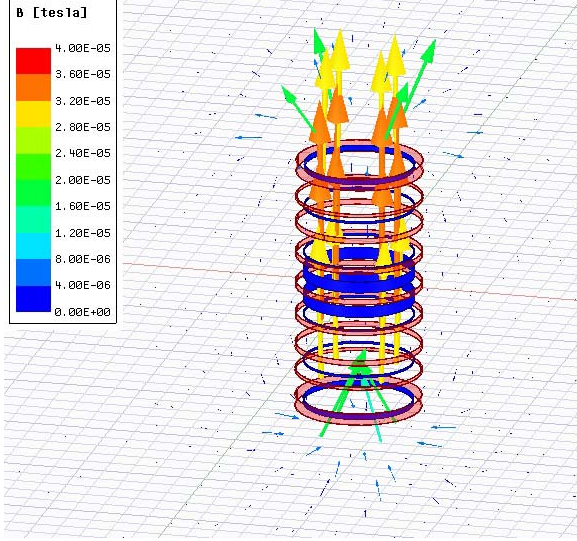
$$V^{\text{ind}} = V_2^{\text{ind}}(\mathcal{M}) + V_3^{\text{ind}}(\mathcal{D}) + V_r^{\text{ind}}, \quad (15)$$

where $V_2^{\text{ind}}(\mathcal{M})$ denotes the rank 2 contribution, $V_3^{\text{ind}}(\mathcal{D})$ denotes the rank 3 contribution and $V_r \leq C\alpha^5 \|\mathbf{H}_0\|_{W^{3,\infty}(B_a)}$ denotes the residual, which, as we will see, will be small

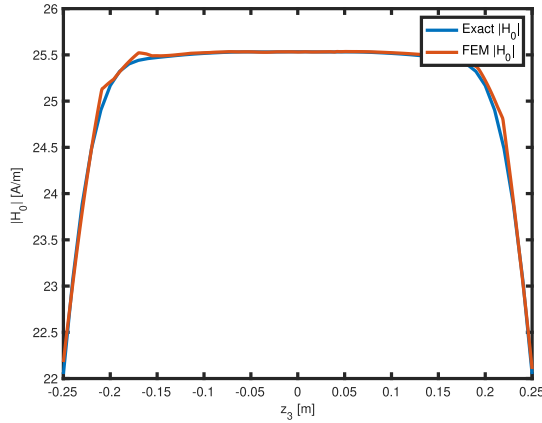
TABLE I
PARAMETERS DESCRIBING THE MULTIPLE COIL ARRANGEMENT

$N_{Rx}(n)$	27	18	18	49	49	18	18	27
$L_{Rx}(n)$ (mm)	10	4	4	22	22	4	4	10
$p_{Rx}(n)$ (mm)	234	155	61	14	-36	-65	-159	-244
$R_{Rx}(n)$ (mm)	220	220	220	220	220	220	220	220

$I_{Tx}(n)N_{Tx}(n)$ (A)	3.67	1	1.67	1.67	1.67	1.67	1.67	1	3.67
$L_{Tx}(n)$ (mm)	23.1	6.3	10.5	10.5	10.5	10.5	10.5	6.3	23.1
$p_{Tx}(n)$ (mm)	226.9	172.6	119.1	57.25	-5.25	-67.75	-129.6	-178.9	-250
$R_{Tx}(n)$ (mm)	240	240	240	240	240	240	240	240	240



(a)



(b)

Fig. 2. Illustration of the background field showing (a) the simulated field lines of $\mathbf{B}_0^{\text{Tx}} = \mu_0 \mathbf{H}_0^{\text{Tx}}$ around the coil array using a finite element model and (b) $|\mathbf{H}_0^{\text{Tx}}(\mathbf{z})|$ evaluated for positions \mathbf{z} along the axis of the coil array where $\mathbf{z} \parallel \mathbf{e}_3$ comparing (12) with a finite element model of the coil array.

for the problems we will consider. Explicitly, for the case considered in this work,

$$\begin{aligned}
 V_2^{\text{ind}}(\mathcal{M}) &:= i\omega\mu_0(\mathbf{H}_0^{\text{Rx}}(\mathbf{z}))_i \mathcal{M}_{ij}(\mathbf{H}_0^{\text{Tx}}(\mathbf{z}))_j \\
 V_3^{\text{ind}}(\mathcal{D}) &:= i\omega\mu_0 \left(-(\mathbf{D}_z(\mathbf{H}_0^{\text{Rx}}(\mathbf{z})))_{kk_1} \mathfrak{M}_{kk_1j}(\mathbf{H}_0^{\text{Tx}}(\mathbf{z}))_j \right. \\
 &\quad \left. + (\mathbf{H}_0^{\text{Rx}}(\mathbf{z}))_k \mathfrak{M}_{kjj_1}(\mathbf{D}_z(\mathbf{H}_0^{\text{Tx}}(\mathbf{z})))_{jj_1} \right) \\
 &= i\omega\mu_0 \left(-\frac{1}{8}(\mathbf{D}_z(\mathbf{H}_0^{\text{Rx}}(\mathbf{z})))_{kk_1} \mathfrak{D}_{kk_1j}(\mathbf{H}_0^{\text{Tx}}(\mathbf{z}))_j \right.
 \end{aligned} \tag{16a}$$

$$\begin{aligned}
 & -\frac{1}{6}(\mathbf{H}_0^{\text{Rx}}(\mathbf{z}))_k \mathfrak{D}_{kjj_1}(\mathbf{D}_z(\mathbf{H}_0^{\text{Tx}}(\mathbf{z})))_{jj_1} \Big) \\
 &= -i\omega\mu_0 \mathfrak{D}_{kk_1j} \left(\frac{1}{8}(\mathbf{D}_z(\mathbf{H}_0^{\text{Rx}}(\mathbf{z})))_{kk_1}(\mathbf{H}_0^{\text{Tx}}(\mathbf{z}))_j \right. \\
 &\quad \left. + \frac{1}{6}(\mathbf{H}_0^{\text{Rx}}(\mathbf{z}))_j(\mathbf{D}_z(\mathbf{H}_0^{\text{Tx}}(\mathbf{z})))_{kk_1} \right), \tag{16b}
 \end{aligned}$$

where $\mu_* = \mu_0$ has been assumed and the symmetry condition (8) has been used in the latter result.

We observe that $V_3^{\text{ind}}(\mathcal{D})$ provides a natural extension of the familiar $V_2^{\text{ind}}(\mathcal{M})$ term for a rank 3 GMPT object characterisation. For an object placed on axis and in the centre of the coil arrangement, $\mathbf{H}_0^{\text{Tx}}(\mathbf{z})$ is near uniform and the contribution V_2^{ind} dominates, while V_3^{ind} is negligible. However, for an object placed outside of the coil arrangement $\mathbf{H}_0^{\text{Tx}}(\mathbf{z})$ is non-uniform and $\|\mathbf{D}_z(\mathbf{H}_0^{\text{Tx}}(\mathbf{z}))\|$ can become large. Indeed, if $\mathbf{H}_0^{\text{Tx}}(\mathbf{z})$ is strongly non-uniform, $V_3^{\text{ind}}(\mathcal{D})$ becomes increasingly important and can dominate over $V_2^{\text{ind}}(\mathcal{M})$.

If an object B is rotated by an angle θ about a coordinate axis, its transformation can be described by $B' = \mathbf{R}(\theta)(B)$ where $\mathbf{R}(\theta)$ is an orthogonal rotation matrix. Accordingly, the coefficients of \mathcal{M} and \mathcal{D} transform as

$$\mathcal{M}'_{ij} = (\mathbf{R})_{ip}(\mathbf{R})_{jq}\mathcal{M}_{pq}, \tag{17a}$$

$$\mathfrak{D}'_{ijk} = (\mathbf{R})_{ip}(\mathbf{R})_{jq}(\mathbf{R})_{kr}\mathfrak{D}_{pqr}. \tag{17b}$$

Then, by replacing \mathcal{M}_{ij} by \mathcal{M}'_{ij} and \mathfrak{D}_{kk_1j} by \mathfrak{D}'_{kk_1j} in (16), we obtain $V_2^{\text{ind}}(\mathcal{M}, \theta)$ and $V_3^{\text{ind}}(\mathcal{D}, \theta)$ for the rank 2 and rank 3 contributions to $V^{\text{ind}}(\theta)$ as a function of object rotation angle.

Throughout, we will normalise the presented results of V^{ind} by ωi and we will refer to $\text{Re}(V^{\text{ind}}/(\omega i))$ as the reactive and $\text{Im}(V^{\text{ind}}/(\omega i))$ as the resistive components of the transimpedance, respectively.

V. MEASUREMENT OF TENSOR COEFFICIENTS

The procedure for measuring the coefficients of \mathcal{M} and \mathcal{D} for a given object αB breaks down in to first determining those of \mathcal{M} and then those of \mathcal{D} for each excitation frequency of interest. We describe each of these steps separately in the following.

A. Measuring the Coefficients of the Rank 2 MPT

If the object's position \mathbf{z} is chosen to be along the axis of the coil array, such that $\mathbf{z} \parallel \mathbf{e}_3$, and if z_3 is chosen within the volume of the coil array, away from its ends, $\mathbf{H}_0^{\text{Tx}}(\mathbf{z})$ is near uniform. For the coil array described in Table I, this occurs when $-0.155 \text{ m} \leq z_3 \leq 0.155 \text{ m}$, as shown in Fig. 2 (b). Hence, for objects placed in such locations, V_3^{ind} does not



Fig. 3. Target orientation manipulator capable of rotating objects around one axis.

contribute to V^{ind} and the measurements $V^{\text{ind, meas}}(\theta)$ can be used to determine \mathcal{M}_{ij} . Noting that $V_2^{\text{ind}}(\mathcal{M}, \theta)$ is linear in the coefficients of \mathcal{M} , and that these are independent of the object's position, we can determine \mathcal{M}_{ij} as the solution to the least squares problem

$$\min_{\mathcal{M}_{ij}} |g(\theta_n, \mathcal{M})|^2 = \min_{\mathcal{M}_{ij}} \sum_{n=1}^{N_\theta} \left| V^{\text{ind, meas}}(\theta_n) - V_2^{\text{ind}}(\mathcal{M}, \theta_n) \right|^2,$$

where N_θ is the total number of angles θ_n considered. This process is repeated for each excitation frequency of interest leading to the object's measured MPT spectral signature. Consideration must be given to the number of angles as well as to the number of rotation axes considered [13], [25] to ensure that all the independent coefficients of \mathcal{M} are properly found.

In practice, the above process is achieved by placing the objects at the aforementioned location and by performing rotations using the bespoke target orientation manipulator shown in Fig. 3. Using this apparatus, objects are rotated about different coordinate axes with a fixed degree increment. For each orientation, a frequency sweep between f_{\min} and f_{\max} is performed and V^{ind} for each frequency recorded. The control of system electronics and the data acquisition during the experiments is done automatically.

B. Measuring the Coefficients of \mathfrak{D}

Once the coefficients of \mathcal{M} are found, we can then determine the coefficients of \mathfrak{D} by placing the object at a position \mathbf{z} where the background field $\mathbf{H}_0^{\text{Tx}}(\mathbf{z})$ is non-uniform. This is achieved by placing the object on the axis of the coil array with $z_3 > 0.155$ m, performing rotations about different coordinate axes and solving the least squares problem

$$\begin{aligned} \min_{\mathfrak{D}_{kk_1j}} \sum_{n=1}^{N_\theta} |h(\theta_n, \mathcal{M}, \mathfrak{D})|^2 \\ = \min_{\mathfrak{D}_{kk_1j}} \sum_{n=1}^{N_\theta} \left| V^{\text{ind, meas}}(\theta_n) - V_2^{\text{ind}}(\mathcal{M}, \theta_n) - V_3^{\text{ind}}(\mathfrak{D}, \theta_n) \right|^2, \end{aligned} \quad (18)$$

for \mathfrak{D}_{kk_1j} for each frequency of interest leading to the object's measured GMPT spectral signature. Note that $V_3^{\text{ind}}(\mathfrak{D}, \theta_n)$ is linear in the unknown \mathfrak{D}_{kk_1j} and that $V_2^{\text{ind}}(\mathcal{M}, \theta_n)$ can be evaluated since the coefficients of \mathcal{M} have been found previously and the object position \mathbf{z} has been chosen. As in Section V-A, important consideration must be given to N_θ and the choice of θ_n [13].

Given that the object is positioned manually, its position \mathbf{z} is only known approximately. If we know that the object is placed on the e_3 axis, an improved estimate of its vertical elevation z_3 can be found by solving the minimisation problem

$$\min_{z_3} \sum_{n=1}^{N_\theta} \left| V^{\text{ind, meas}}(\theta_n) - V_2^{\text{ind}}(\mathcal{M}, \theta_n, z_3) \right|^2, \quad (19)$$

for the global minimum z_3 , where we have emphasised that V_2^{ind} also depends on z_3 . Once this improved estimate is found, it can be used in (18) to aid with determining \mathfrak{D}_{kk_1j} .

In practice, the above process is achieved by placing objects in the non-uniform part of the field by using the mechanical arrangement in Fig. 4. The same approach of incrementing the rotation by fixed angle increment and sweeping through the frequencies f_{\min} and f_{\max} , as described in Section V-A, is performed. However, the apparatus shown in this figure allows the object to be placed in different positions in both vertical and horizontal direction for each experiment. In particular, the apparatus allows the vertical position of an object to be adjusted in 10 mm steps using the slots on the arrangement. The object's horizontal position can be also adjusted in 10 mm steps on both the x_1 and x_2 axes by placing the arrangement into pre-marked positions on the lid of the coil arrangement.

VI. PREDICTING THE TENSOR COEFFICIENTS USING NUMERICAL SIMULATIONS

The numerical prediction of the coefficients of \mathcal{M} and \mathfrak{D} for a chosen object αB follows a similar procedure to that described previously for the computation of the coefficients of the rank 2 MPT [12], [13]. This involves approximating the solution $\boldsymbol{\theta}_{J(p+1)}$ to the transmission problem (4) by constructing weak discrete finite element approximations using an $\mathbf{H}(\text{curl})$ conforming discretisation, which is appropriate for this problem, where the both mesh spacing h and element order q^1 can be refined in order to improve the accuracy of the numerical solution. The Coulomb gauge $\nabla \cdot \boldsymbol{\theta}_{J(p+1)} = 0$ has been circumvented by numerical regularisation [18]. We use the NGSolve finite element library [27]–[29] for the numerical computations presented in this work.

Following the computation of $\boldsymbol{\theta}_{J(p+1)}$ for frequencies of interest between f_{\min} and f_{\max} , the coefficients of \mathcal{M} and \mathfrak{D} are obtained by a simple post-processing involving integrals over B using (3) leading to the object's simulated MPT and GMPT spectral signatures. We remark that this computation could be accelerated by using a proper orthogonal decomposition (POD) based reduced order model in a similar manner to [33].

¹We use q rather than the usual p to denote the element order avoid confusion with tensor indices

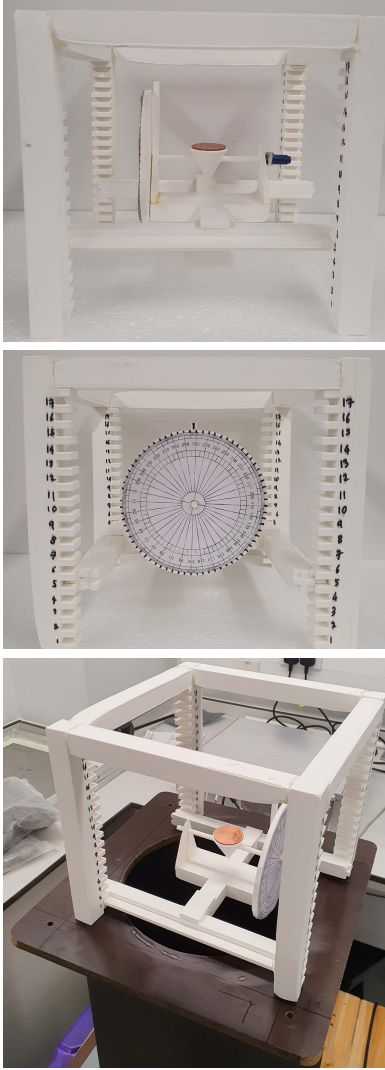


Fig. 4. Target orientation manipulator capable of rotating objects around one axis at different vertical and horizontal positions.

VII. RESULTS

We will focus on the situation where αB is chosen to be slightly truncated copper, brass and stainless steel cones, in turn. Cones have been chosen, since, while they have a rotational and mirror symmetries, they still have non-zero rank 3 GMPT coefficients and can be used to illustrate the improvements offered over using MPTs alone for object characterisation. The sizes of each of the truncated cones are identical and have the dimensions of bottom radius 7.5 mm, top radius 0.5 mm and a height of 15 mm, hence we set $\alpha = 0.001$ m and B to be the non-dimensional truncated cone with bottom radius 7.5, top radius 0.5 and height 15. The materials of the cones are provided in Table II. While approximate measurements of the conductivity of the cones specimens have been made using a 4 terminal resistivity measurement, the reference values are still believed to be more accurate than these and, hence, have been employed in the simulations.

We have chosen the cone's canonical orientation such that the vertex of the cone is aligned with the e_3 direction and

the base of the cone lies in the (x_1, x_2) plane. This means that the cone has a rotational symmetry about the x_3 axis and has reflectional symmetries about the x_1 and x_2 axes. Using this information, we deduce that the 2 non-zero independent coefficients of the complex symmetric \mathcal{M} are $\mathcal{M}_{11} = \mathcal{M}_{22}$ and \mathcal{M}_{33} [12]. In similar way, we deduce that the 4 non-zero independent coefficients of \mathcal{D} are $\mathcal{D}_{223} = \mathcal{D}_{113}$, $\mathcal{D}_{232} = \mathcal{D}_{131}$, $\mathcal{D}_{322} = \mathcal{D}_{311}$ and \mathcal{D}_{333} . By further noting the symmetry property (8), we find that this reduces to just 2 non-zero independent coefficients $\mathcal{D}_{223} = \mathcal{D}_{113} = \mathcal{D}_{322} = \mathcal{D}_{311}$ and \mathcal{D}_{333} .

Given the reduced number of independent coefficients of \mathcal{M} and \mathcal{D} for our chosen cones, placing the object on the x_3 axis and performing rotations about either the x_1 , or, equivalently the x_2 , axis are sufficient to determine the 2 non-zero independent coefficients of each of these tensors.

A. Copper Cone

By following the procedure described in Section V-A, we position the copper cone at $z = (0, 0, 0.15)$ m so that it lies in a uniform $\mathbf{H}_0^{\text{Tx}}(z)$ and measure $V^{\text{ind, meas}}(\theta)$ as we rotate the cone by an angle θ about the x_1 axis. We choose this position as the pseudo field generated by the receive coils (if they were used as transmit coils) is most uniform at $z = (0, 0, 0.15)$ m and $z = (0, 0, -0.15)$ m. While midpoint of the transmit coil is at $z = (0, 0, 0)$ m, the receive coils do not have sensitivity at this location, and we choose $z = (0, 0, 0.15)$ m as this easier to access than $z = (0, 0, -0.15)$ m. For further details, see Figure 6 in [25]. We set $N_\theta = 72$ and choose $\theta_n = n\Delta\theta = 2n\pi/N_\theta$ radians so that measurements are made at 5 degree increments. We use this measurement to determine $\mathcal{M}_{11} = \mathcal{M}_{22}$ and \mathcal{M}_{33} for 28 frequencies between 119.25 Hz and 95400 Hz leading to the object's measured MPT spectral signature. Then, following the measurement of the coefficients of \mathcal{M} , we follow the procedure in Section V-B and move the cone to $z = (0, 0, 0.343)$ m where $\mathbf{H}_0^{\text{Tx}}(z)$ is non-uniform. Again we measure $V^{\text{ind, meas}}(\theta)$ as we rotate the cone by an angle θ about the x_1 axis. We make $N_\theta = 72$ measurements and follow the procedure described in Section V-B to determine $\mathcal{D}_{223} = \mathcal{D}_{113} = \mathcal{D}_{322} = \mathcal{D}_{311}$ and \mathcal{D}_{333} for the same 28 frequencies between $f_{\min} = 119.25$ Hz and $f_{\max} = 95400$ Hz leading to the object's GMPT spectral signature.

To obtain the object's MPT and GMPT spectral signatures numerically, we follow the procedure in Section VI and generate a mesh of 98419 unstructured tetrahedra to discretise the cone object B and fill the space to a truncated boundary in the form of the box $[-1000, 1000]^3$. By performing p -refinement, we find that order $q = 3$ elements lead to convergence of the tensor coefficients $\mathcal{M}_{11} = \mathcal{M}_{22}$, \mathcal{M}_{33} , $\mathcal{D}_{223} = \mathcal{D}_{113} = \mathcal{D}_{322} = \mathcal{D}_{311}$ and \mathcal{D}_{333} for frequencies between $f_{\min} = 119.25$ Hz and $f_{\max} = 95400$ Hz.

In Fig. 5, we show a comparison of the computed and measured MPT and GMPT spectral signatures where excellent agreement is observed for the computed and measured MPT spectral signatures and good agreement is observed for the computed and measured GMPT spectral signatures. The closer agreement between the spectral signatures for the simulations and measured MPT \mathcal{M} , compared to the GMPT \mathcal{D} is to be

TABLE II
MATERIAL PROPERTIES FOR THE COPPER, BRASS AND STAINLESS STEEL CONES

Material	μ_*	Reference σ_* (S/m)	Measured σ_* (S/m)	Simulations σ_* (S/m)
Copper	μ_0	5.95×10^7 [22]	7.63×10^7	5.95×10^7
Brass	μ_0	1.44×10^7 [24]	1.38×10^7	1.44×10^7
Stainless steel	μ_0	1.45×10^6 [8]	1.36×10^6	1.45×10^6

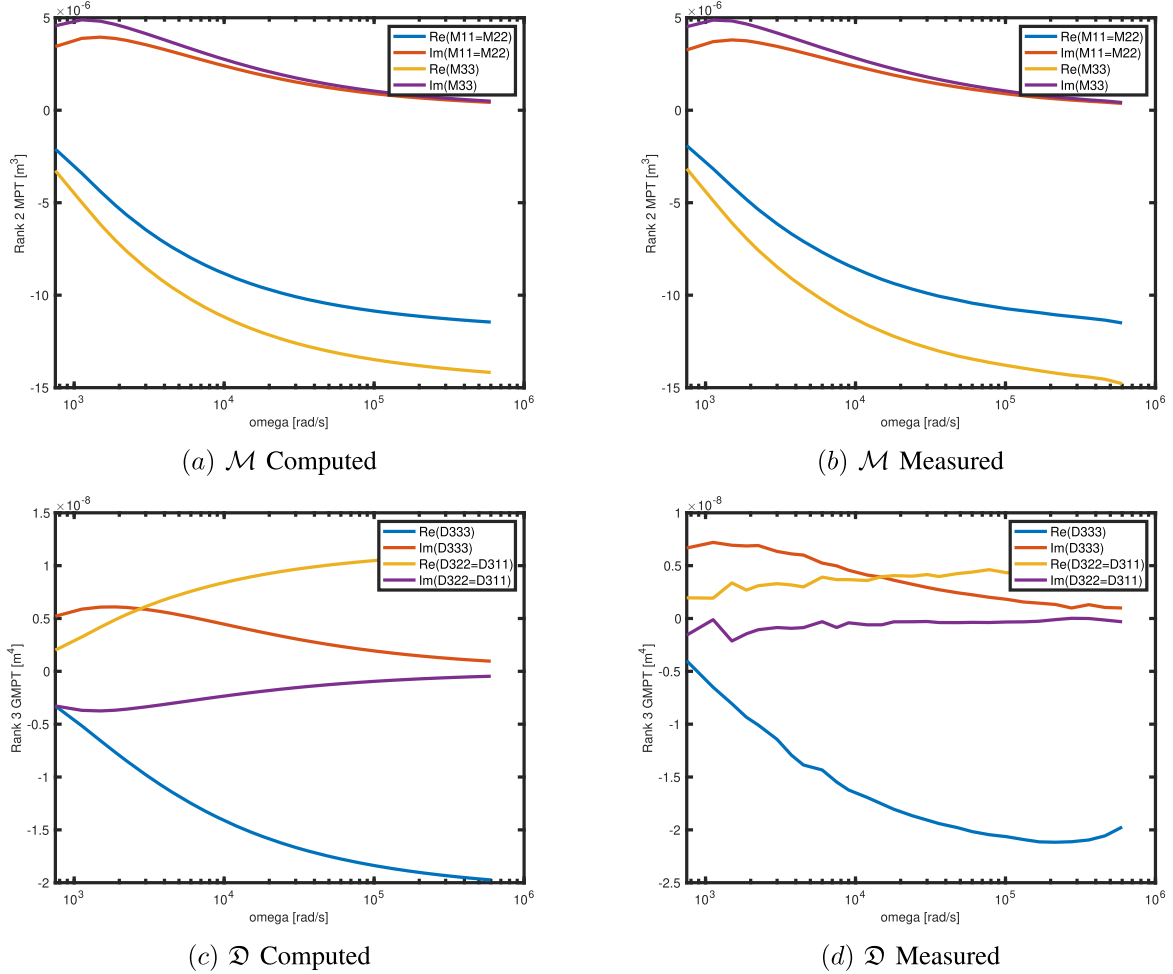


Fig. 5. Copper cone showing: spectral signature corresponding to (a) computed coefficients of \mathcal{M} and (b) measured coefficients of \mathcal{M} , (c) computed coefficients of \mathcal{D} and (d) measured coefficients of \mathcal{D} .

expected given that the coefficients of \mathcal{M} are two orders of magnitude larger than those of \mathcal{D} , which makes them easier to measure. The maximum difference between the measured and simulated \mathcal{M} coefficients over the frequencies of interest is around 0.8%, which can largely be attributed to noise and measurement errors in the system with any discretisation errors being much smaller. While the shape of the GMPT spectral signatures is well captured by the measurements, the accuracy of the smaller, and harder to measure, \mathcal{D} coefficients over the frequencies of interest is lower, with differences ranging from 1% to 25% for \mathcal{D}_{333} . We explain the reasons for the larger differences in Section VII-D. One noticeable difference between the simulations and measurements is the frequency at which the curves for $\text{Re}(\mathcal{D}_{322}) = \text{Re}(\mathcal{D}_{311})$ and $\text{Im}(\mathcal{D}_{333})$ cross. Even from the limited range of frequencies considered, we can see that both the real parts of the coefficients of

\mathcal{M} and \mathcal{D} illustrate a sigmoid behaviour with $\log \omega$ while the imaginary parts of the coefficients of \mathcal{M} and \mathcal{D} have single local maxima/minima with $\log \omega$, which is reminiscent of the spectral behaviour of the MPT that has already been understood theoretically [15].

To illustrate the importance of including both the $V_2^{\text{ind}}(\mathcal{M})$ and $V_3^{\text{ind}}(\mathcal{D})$ to predict V^{ind} when the object is located outside of the coil arrangement, we compare, in Fig. 6, the measured transimpedance $V^{\text{ind, meas}}(\theta)$ with $V_2^{\text{ind}}(\mathcal{M}, \theta)$ and $V_2^{\text{ind}}(\mathcal{M}, \theta) + V_3^{\text{ind}}(\mathcal{D}, \theta)$, each as a function of rotation angle θ about the x_1 axis, for different frequencies of excitation for an object at the position $\mathbf{z} = (0, 0, 0.343)$ m using the simulated MPT and GMPT spectral signatures. In each case, we see the superior performance of $V_2^{\text{ind}}(\mathcal{M}, \theta) + V_3^{\text{ind}}(\mathcal{D}, \theta)$ to predict $V^{\text{ind, meas}}(\theta)$ compared to using $V_2^{\text{ind}}(\mathcal{M}, \theta)$ alone for an object at this position, for all frequencies considered.

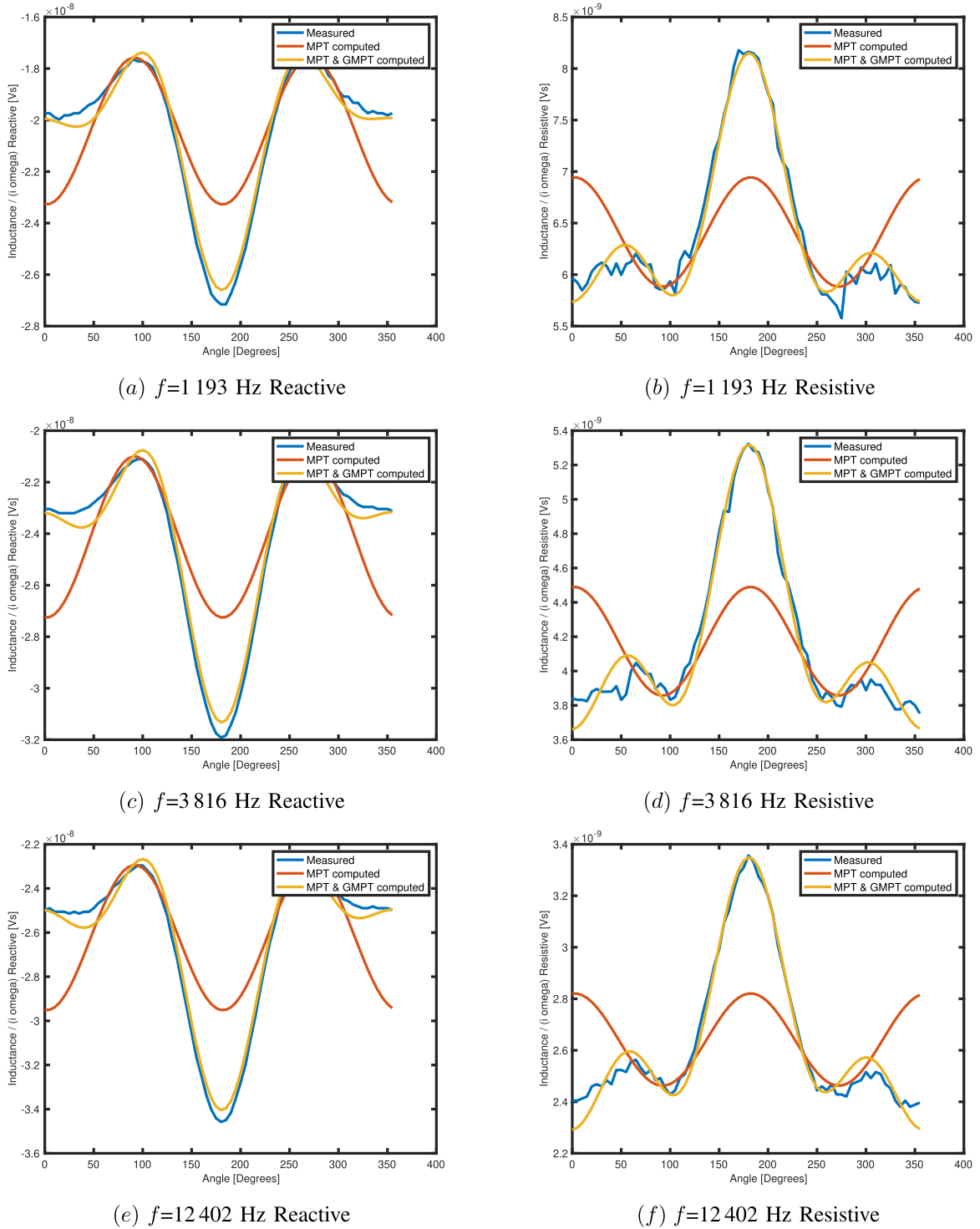


Fig. 6. Copper cone positioned in a non-uniform field at position $\mathbf{z} = (0,0,0.343)$ m comparing the reactive and resistive parts of $V^{\text{ind, meas}}(\theta)$, $V_2^{\text{ind}}(\mathcal{M}, \theta)$ and $V_2^{\text{ind}}(\mathcal{M}, \theta) + V_3^{\text{ind}}(\mathcal{D}, \theta)$, each normalised by ωi , showing (a) $f = 1193$ Hz Reactive, (b) $f = 1193$ Hz Resistive, (c) $f = 3816$ Hz Reactive, (d) $f = 3816$ Hz Resistive, (e) $f = 12402$ Hz Reactive and (f) $f = 12402$ Hz Resistive.

Next, we compare the performance of using the simulated and measured MPT and GMPT coefficients to predict $V^{\text{ind}}(\theta)$ at different frequencies for a cone located at $\mathbf{z} = (0, 0, 0.343)$ m. To do this, we compare, in Fig. 7, the reactive and resistive parts of the following residuals $V^{\text{ind, meas}}(\theta) - V_2^{\text{ind}}(\mathcal{M}, \theta)$, $V^{\text{ind, meas}}(\theta) - V_2^{\text{ind}}(\mathcal{M}^{\text{meas}}, \theta)$, $V_3^{\text{ind}}(\mathcal{D}^{\text{meas}}, \theta)$ and $V_3^{\text{ind}}(\mathcal{D}, \theta)$, where \mathcal{M} and \mathcal{D} indicate the simulated MPT and GMPT tensors and $\mathcal{M}^{\text{meas}}$ and $\mathcal{D}^{\text{meas}}$ the corresponding

measured tensors. We observe good agreement between the different residuals indicating that using either both the simulated MPT and GMPT coefficients or both the measured MPT and GMPT coefficients provide a good prediction of $V^{\text{ind}}(\theta)$ at this location.

To confirm that $V_2^{\text{ind}}(\mathcal{M}, \theta)$ and $V_3^{\text{ind}}(\mathcal{D}, \theta)$ do provide the dominant contributions to $V^{\text{ind, meas}}(\theta)$, and that other higher order terms do not play a significant role, we express

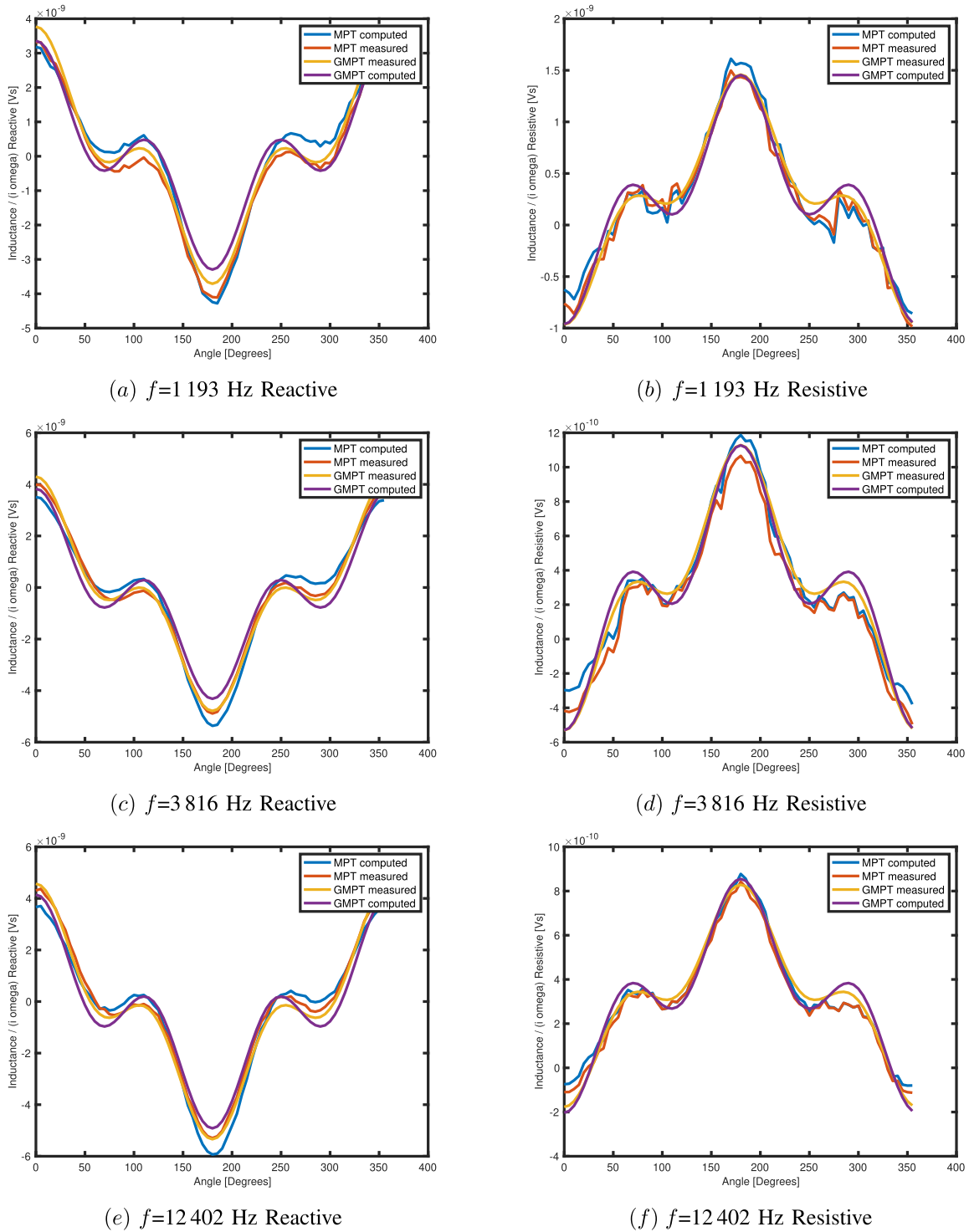


Fig. 7. Copper cone positioned in a non-uniform field at position $\mathbf{z} = (0,0,0.343)$ m comparing the reactive and resistive parts of $V_{\text{ind, meas}}(\theta) - V_2^{\text{ind, meas}}(\mathcal{M}, \theta)$, $V_2^{\text{ind, meas}}(\theta) - V_2^{\text{ind}}(\mathcal{M}^{\text{meas}}, \theta)$, $V_3^{\text{ind}}(\mathcal{D}^{\text{meas}}, \theta)$ and $V_3^{\text{ind}}(\mathcal{D}, \theta)$, each normalised by ωi , showing (a) $f = 1193$ Hz Reactive, (b) $f = 1193$ Hz Resistive, (c) $f = 3816$ Hz Reactive, (d) $f = 3816$ Hz Resistive, (e) $f = 12402$ Hz Reactive and (f) $f = 12402$ Hz Resistive.

$V_{\text{ind, meas}}(\theta)$ in the form

$$V_{\text{ind, meas}}(\theta) = \sum_{n=-K}^K c_n e^{in\theta},$$

and use a fast Fourier transform to determine the amplitudes $|c_n|$. Considering the products of rotation matrices in (17)

that describe how the coefficients of \mathcal{M} and \mathcal{D} transform under object rotation and writing powers of cosine and sine functions in terms of multiple angles, e.g. $\cos^2 \theta = (1 + \cos(2\theta))/2$, $\cos^3 \theta = (3 \cos \theta + \cos(3\theta))/4$ and $\cos^4 \theta = (3 + 4 \cos(2\theta) + \cos(4\theta))/8$, we conclude that, if $V_{\text{ind, meas}}(\theta)$ can be described by a rank 2 tensor description, it will have c_n being non-zero for $n = 0, \pm 2$ while, if it additionally contains

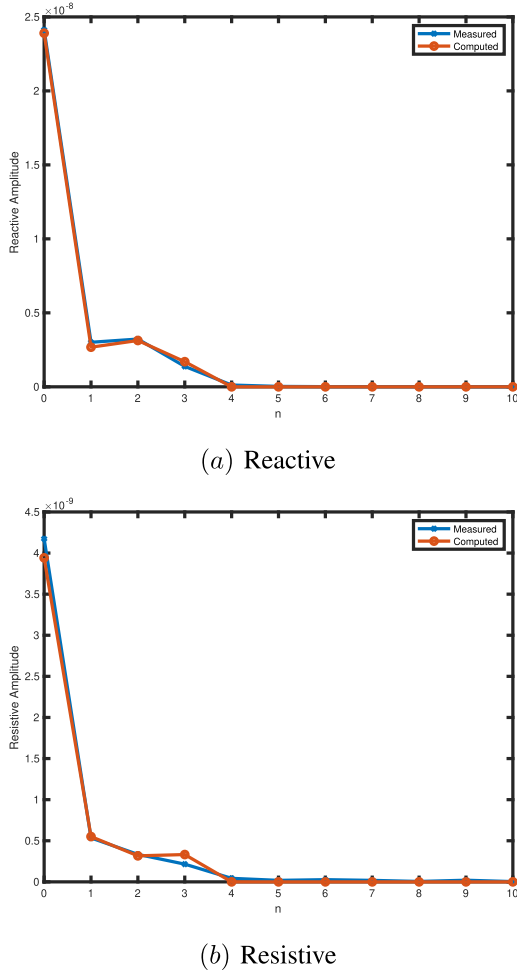


Fig. 8. Copper cone positioned in a non-uniform field at position $\mathbf{z} = (0, 0, 0.343)$ cm showing the Fourier coefficients in the expansion of the (a) reactive and (b) resistive parts of $V^{\text{ind, meas}}(\theta)$ for the case of $f = 1193$ Hz.

terms associated with a rank 3 description, then, c_n for $n = \pm 1, \pm 3$ will also be non-zero. Furthermore, if $V^{\text{ind, meas}}(\theta)$ additionally contains terms associated with a rank 4 description, then, c_n for $n = \pm 4$ will also be non-zero (since in this case there would be a product of 4 rotation matrices). In Fig. 8, we show the results of applying this to the case of the cone located at $\mathbf{z} = (0, 0, 0.344)$ m and $f = 1193$ Hz and remark that the results for other locations exterior to the coil array and other frequencies are similar. We observe that $V^{\text{ind, meas}}(\theta)$ has dominant contributions associated with $n = 0, \pm 1, \pm 2, \pm 3$, which is consistent with a rank 3 tensor description being able to fully describe its behaviour. Also shown is the corresponding result for $V_2^{\text{ind}}(\mathcal{M}, \theta) + V_3^{\text{ind}}(\mathcal{D}, \theta)$, which also has dominant contributions associated with $n = 0, \pm 1, \pm 2, \pm 3$, as expected.

To illustrate the importance of including both the $V_2^{\text{ind}}(\mathcal{M})$ and $V_3^{\text{ind}}(\mathcal{D})$ to predict V^{ind} at different object locations, we compare, in Fig. 9, the measured transimpedance $V^{\text{ind, meas}}(\theta)$ with $V_2^{\text{ind}}(\mathcal{M}, \theta)$ and $V_2^{\text{ind}}(\mathcal{M}, \theta) + V_3^{\text{ind}}(\mathcal{D}, \theta)$, each as a function of rotation angle θ about the x_1 axis, for different object locations and a fixed frequency of $f = 3816$ Hz using the simulated MPT and GMPT spectral signatures.

As previously observed for the fixed position of in $\mathbf{z} = (0, 0, 0.343)$ m in Fig. 6, we see that including the term $V_3^{\text{ind}}(\mathcal{D}, \theta)$ is important to accurately predict V^{ind} at different object locations. Note the results presented in Fig. 9 use a larger angle increment of $\Delta\theta = 2\pi/24$ radians, corresponding to 15 degrees, compared to those presented in Fig. 6 in order to reduce the cost of the measurements and, hence, the curves appear less smooth than before, but the conclusion remains unchanged. In a similar manner to Fig. 7, we show in Fig. 10 the corresponding transimpedance residuals for different object locations where we once again observe good agreement between the residual predicted by the simulated and measured MPT and GMPT coefficients.

Further to the results shown in Fig. 9 and 10, the accuracies according to the error measures

$$e_2^{\text{reactive}}(\mathcal{M}) = \frac{\|\text{Re}(V^{\text{ind, meas}}(\theta) - V_2^{\text{ind}}(\mathcal{M}, \theta))\|_{L^2(\theta)}}{\|\text{Re}(V^{\text{ind, meas}}(\theta))\|_{L^2(\theta)}}, \quad (20a)$$

$$e_2^{\text{resistive}}(\mathcal{M}) = \frac{\|\text{Im}(V^{\text{ind, meas}}(\theta) - V_2^{\text{ind}}(\mathcal{M}, \theta))\|_{L^2(\theta)}}{\|\text{Im}(V^{\text{ind, meas}}(\theta))\|_{L^2(\theta)}}, \quad (20b)$$

$$e_3^{\text{reactive}}(\mathcal{M}, \mathcal{D}) = \frac{\|\text{Re}(V^{\text{ind, meas}}(\theta) - V_2^{\text{ind}}(\mathcal{M}, \theta) - V_3^{\text{ind}}(\mathcal{D}, \theta))\|_{L^2(\theta)}}{\|\text{Re}(V^{\text{ind, meas}}(\theta))\|_{L^2(\theta)}}, \quad (20c)$$

$$e_3^{\text{resistive}}(\mathcal{M}, \mathcal{D}) = \frac{\|\text{Im}(V^{\text{ind, meas}}(\theta) - V_2^{\text{ind}}(\mathcal{M}, \theta) - V_3^{\text{ind}}(\mathcal{D}, \theta))\|_{L^2(\theta)}}{\|\text{Im}(V^{\text{ind, meas}}(\theta))\|_{L^2(\theta)}}, \quad (20d)$$

for a fixed frequency of $f = 3816$ Hz and the copper cone at different positions according to the simulated and measured coefficients of \mathcal{M} and \mathcal{D} are shown in Tables III and IV, respectively. These indicate that the accuracy of the transimpedance is improved from around 10% when only the MPT is used to around 2% when either the simulated or measured GMPTs are included for all object locations considered. We have seen that \mathcal{D} can be obtained from the measurements $V^{\text{ind, meas}}(\theta)$ if the object is placed in the non-uniform field and including $V_3^{\text{ind}}(\mathcal{D})$ is important whenever \mathbf{H}_0 is non-uniform. Importantly, as remarked in Section III, \mathcal{D} provides additional complex coefficients as a function of frequency in addition to those in \mathcal{M} that can aid with object discrimination when performing object classification. Next we consider a brass and then a steel cone.

B. Brass Cone

We repeat the procedures described in Section V-A to measure $\mathcal{M}_{11} = \mathcal{M}_{22}$ and \mathcal{M}_{33} at 28 frequencies between $f_{\min} = 119.25$ Hz and $f_{\max} = 95400$ Hz leading to the brass cone's measured MPT spectral signature. Then, we repeat the procedure in Section V-B to measure $\mathcal{D}_{223} = \mathcal{D}_{113} = \mathcal{D}_{322} = \mathcal{D}_{311}$ and \mathcal{D}_{333} for the same 28 frequencies between $f_{\min} = 119.25$ Hz and $f_{\max} = 95400$ Hz leading to the

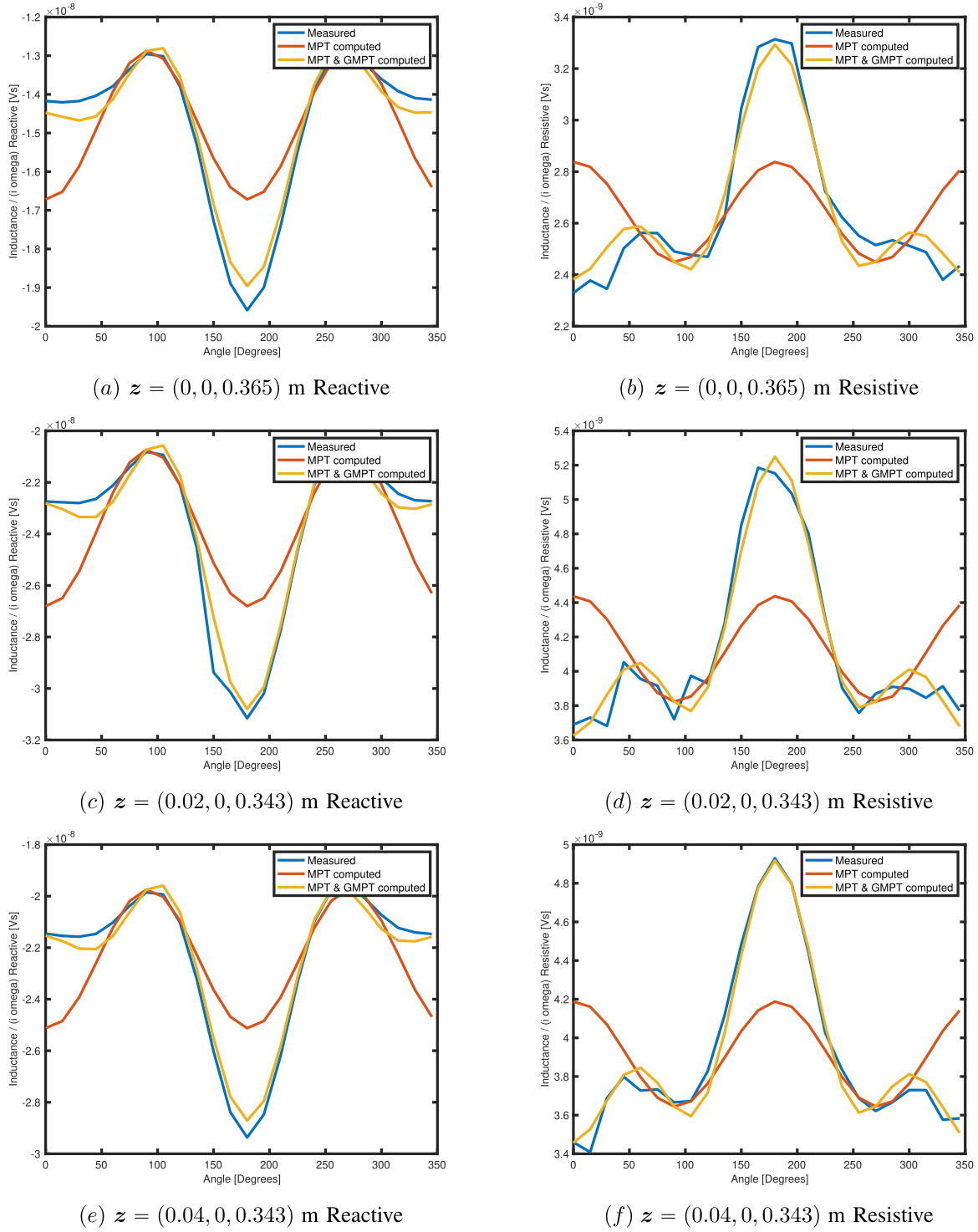


Fig. 9. Copper cone positioned in a non-uniform field comparing the reactive and resistive parts of $V_3^{\text{ind, meas}}(\theta)$, $V_2^{\text{ind}}(\mathcal{M}, \theta)$ and $V_2^{\text{ind}}(\mathcal{M}, \theta) + V_3^{\text{ind}}(\mathcal{D}, \theta)$, each normalised by ωi , for a fixed frequency of $f = 3816$ Hz showing (a) $z = (0, 0, 0.365)$ m Reactive, (b) $z = (0, 0, 0.365)$ m Resistive, (c) $z = (0.02, 0, 0.343)$ m Reactive, (d) $z = (0.02, 0, 0.343)$ m Resistive, (e) $z = (0.04, 0, 0.343)$ m Reactive and (f) $z = (0.04, 0, 0.343)$ m Resistive.

brass cone's measured GMPT spectral signature. To obtain the object's MPT and GMPT spectral signatures numerically, we follow the procedure in Section VI and employ the same discretisation used previously for the copper cone to simulate the coefficients $\mathcal{M}_{11} = \mathcal{M}_{22}$, \mathcal{M}_{33} , $\mathcal{D}_{223} = \mathcal{D}_{113} = \mathcal{D}_{322} = \mathcal{D}_{311}$ and \mathcal{D}_{333} for frequencies between $f_{\min} = 119.25$ Hz and $f_{\max} = 95\,400$ Hz for the brass cone.

In Fig. 11, we show a comparison of the computed and measured MPT and GMPT spectral signatures for the brass cone where excellent agreement is observed for the computed and measured MPT spectral signatures and good agreement is observed for the computed and measured GMPT spectral signatures. Again note that the non-zero independent coefficients of \mathcal{D} are 2 orders of magnitude smaller than those of

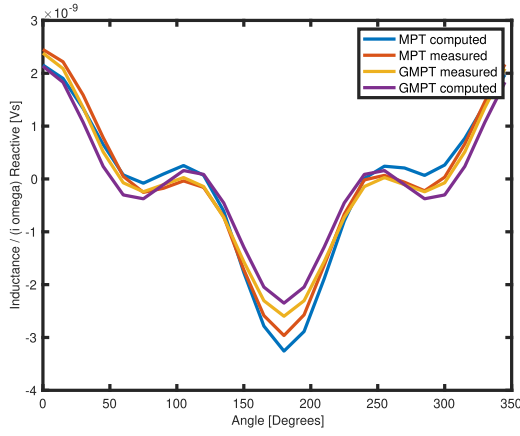
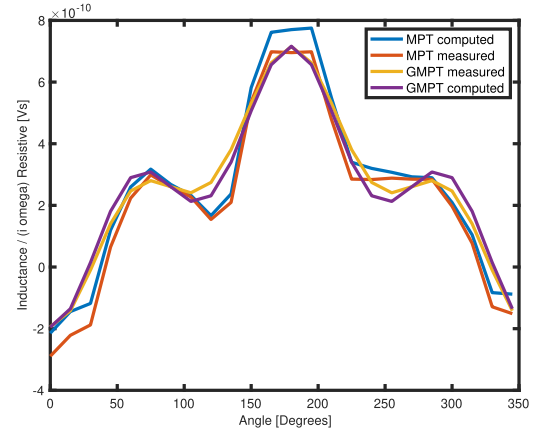
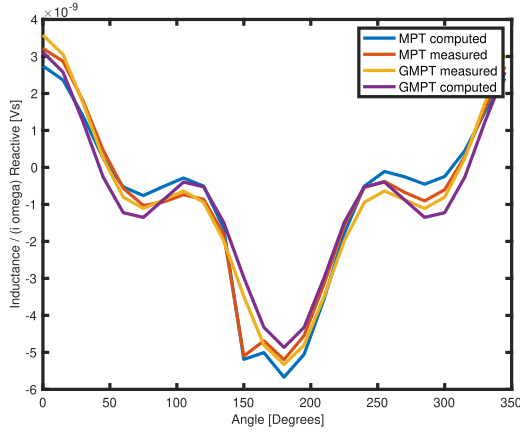
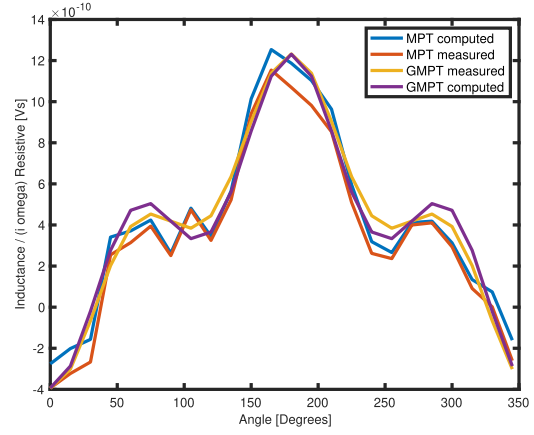
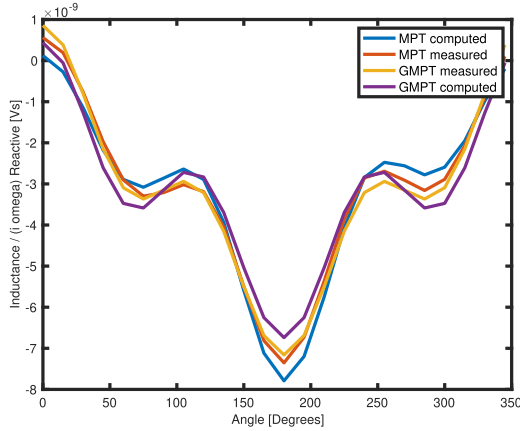
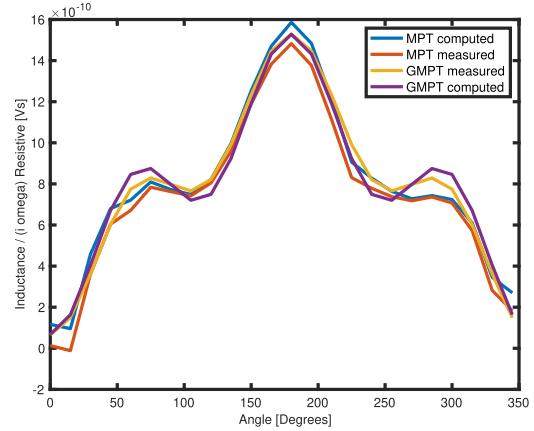
(a) $z = (0, 0, 0.365)$ m Reactive(b) $z = (0, 0, 0.365)$ m Resistive(c) $z = (0.02, 0, 0.343)$ m Reactive(d) $z = (0.02, 0, 0.343)$ m Resistive(e) $z = (0.04, 0, 0.343)$ m Reactive(f) $z = (0.04, 0, 0.343)$ m Resistive

Fig. 10. Copper cone positioned in a non-uniform field comparing the reactive and resistive parts of $V_3^{\text{ind, meas}} - V_2^{\text{ind}}(\mathcal{M})$, $V_3^{\text{ind, meas}} - V_2^{\text{ind}}(\mathcal{M}^{\text{meas}})$, $V_3^{\text{ind}}(\mathcal{D}^{\text{meas}})$ and $V_3^{\text{ind}}(\mathcal{D})$, each normalised by ωi , for a fixed frequency of $f = 3816$ Hz showing (a) $z = (0, 0, 0.365)$ m Reactive, (b) $z = (0, 0, 0.365)$ m Resistive, (c) $z = (0.02, 0, 0.343)$ m Reactive, (d) $z = (0.02, 0, 0.343)$ m Resistive, (e) $z = (0.04, 0, 0.343)$ m Reactive and (f) $z = (0.04, 0, 0.343)$ m Resistive.

\mathcal{M} and, hence, we should not expect them to be measured as accurately as those of \mathcal{M} , with the difference between the measured and computed MPT and GMPTs being similar to those for the copper cone. A similar noticeable difference between the simulations and measurements to the copper cone is the frequency at which the curves for $\text{Re}(\mathcal{D}_{322}) = \text{Re}(\mathcal{D}_{311})$ and $\text{Im}(\mathcal{D}_{311})$ cross. Also, in a similar manner to Fig. 5,

we observe that the coefficients of both the real parts of the coefficients of \mathcal{M} and \mathcal{D} show a sigmoid behaviour with $\log \omega$ while the coefficients of the imaginary parts of the coefficients of \mathcal{M} and \mathcal{D} have single local maxima/minima with $\log \omega$.

Comparable curves to those produced in Fig. 6-10 have also been found for the brass cone and similar agreements can be drawn for this object. Hence, we only provide the tabular

TABLE III

COPPER CONE POSITIONED IN A NON-UNIFORM FIELD COMPARING THE ERROR MEASURES DEFINED IN (20) FOR COMPUTED \mathcal{M} AND \mathcal{D} TENSORS, A FIXED FREQUENCY OF $f = 3816$ HZ AND DIFFERENT OBJECT LOCATIONS

z (m)	$e_2^{\text{reactive}}(\mathcal{M})$	$e_2^{\text{resistive}}(\mathcal{M})$	$e_3^{\text{reactive}}(\mathcal{M}, \mathcal{D})$	$e_3^{\text{resistive}}(\mathcal{M}, \mathcal{D})$
(0,0,0.343)	0.096309	0.097819	0.017664	0.021213
(0,0,0.365)	0.096627	0.103190	0.023734	0.026163
(0,0,0.382)	0.092338	0.090466	0.025041	0.021797
(0.02,0,0.343)	0.097654	0.101031	0.023663	0.022160
(0.04,0,0.343)	0.092492	0.098122	0.017634	0.016462

TABLE IV

COPPER CONE POSITIONED IN A NON-UNIFORM FIELD COMPARING THE ERROR MEASURES DEFINED IN (20) FOR MEASURED \mathcal{M} AND \mathcal{D} TENSORS, A FIXED FREQUENCY OF $f = 3816$ HZ AND DIFFERENT OBJECT LOCATIONS

z	$e_2^{\text{reactive}}(\mathcal{M}^{\text{meas}})$	$e_2^{\text{resistive}}(\mathcal{M}^{\text{meas}})$	$e_3^{\text{reactive}}(\mathcal{M}^{\text{meas}}, \mathcal{D}^{\text{meas}})$	$e_3^{\text{resistive}}(\mathcal{M}^{\text{meas}}, \mathcal{D}^{\text{meas}})$
(0,0,0.343)	0.097677	0.12152	0.017625	0.020402
(0,0,0.365)	0.097935	0.14225	0.018959	0.023640
(0,0,0.382)	0.093599	0.16891	0.020277	0.021123
(0.02,0,0.343)	0.098964	0.14300	0.023077	0.022878
(0.04,0,0.343)	0.093994	0.22635	0.018504	0.013540

TABLE V

BRASS CONE POSITIONED IN A NON-UNIFORM FIELD COMPARING THE ERROR MEASURES DEFINED IN (20) FOR COMPUTED \mathcal{M} AND \mathcal{D} TENSORS, A FIXED FREQUENCY OF $f = 3816$ HZ AND DIFFERENT OBJECT LOCATIONS

z	$e_2^{\text{reactive}}(\mathcal{M})$	$e_2^{\text{resistive}}(\mathcal{M})$	$e_3^{\text{reactive}}(\mathcal{M}, \mathcal{D})$	$e_3^{\text{resistive}}(\mathcal{M}, \mathcal{D})$
(0,0,0.343)	0.113650	0.104790	0.047887	0.023568
(0,0,0.361)	0.108850	0.102740	0.042399	0.026610
(0,0,0.381)	0.094877	0.090336	0.031265	0.023487
(0.02,0,0.341)	0.094400	0.101360	0.025379	0.019437
(0.04,0,0.336)	0.103850	0.102580	0.027634	0.020289

TABLE VI

BRASS CONE POSITIONED IN A NON-UNIFORM FIELD COMPARING THE ERROR MEASURES DEFINED IN (20) FOR MEASURED \mathcal{M} AND \mathcal{D} TENSORS, A FIXED FREQUENCY OF $f = 3816$ HZ AND DIFFERENT OBJECT LOCATIONS

z	$e_2^{\text{reactive}}(\mathcal{M}^{\text{meas}})$	$e_2^{\text{resistive}}(\mathcal{M}^{\text{meas}})$	$e_3^{\text{reactive}}(\mathcal{M}^{\text{meas}}, \mathcal{D}^{\text{meas}})$	$e_3^{\text{resistive}}(\mathcal{M}^{\text{meas}}, \mathcal{D}^{\text{meas}})$
(0,0,0.343)	0.113610	0.117590	0.040301	0.021583
(0,0,0.361)	0.111670	0.120900	0.036134	0.024457
(0,0,0.381)	0.096422	0.120910	0.022136	0.016521
(0.02,0,0.341)	0.096394	0.113750	0.035334	0.020949
(0.04,0,0.336)	0.104000	0.115820	0.033121	0.023151

summaries in Tables V and VI, which illustrate comparable accuracies for the simulated and measured coefficients of \mathcal{M} and \mathcal{D} for the brass cone positioned at different locations compared to those shown in Tables III and IV.

C. Steel Cone

We repeat the procedures described in Section V-A to measure $\mathcal{M}_{11} = \mathcal{M}_{22}$ and \mathcal{M}_{33} at 28 frequencies between $f_{\min} = 119.25$ Hz and $f_{\max} = 95400$ Hz leading to the steel cone's measured MPT spectral signature. Then, we repeat the procedure in Section V-B to measure $\mathcal{D}_{223} = \mathcal{D}_{113} = \mathcal{D}_{322} = \mathcal{D}_{311}$ and \mathcal{D}_{333} for the same 28 frequencies between $f_{\min} = 119.25$ Hz and $f_{\max} = 95400$ Hz leading to the steel cone's measured GMPT spectral signature. To obtain the object's MPT and GMPT spectral signatures numerically we employ the same discretisation as before and repeat the process described for the copper and brass cones.

In Fig. 12 we show a comparison of the computed and measured MPT and GMPT spectral signatures for the steel

cone where excellent agreement is observed for the computed and measured MPT spectral signatures and good agreement is observed for the computed and measured GMPT spectral signatures. Again note that the non-zero independent coefficients of \mathcal{D} are 2 orders of magnitude smaller than those of \mathcal{M} and, hence, we should not expect them to be measured as accurately as those of \mathcal{M} , in this case the minimum difference between the measured and computed MPT coefficients is much less than 1% and the minimum differences between measurement and simulations for \mathcal{D}_{333} is 5% while for \mathcal{D}_{322} it is 9.7%. In a similar manner to Fig. 5 and 11, we can see that the coefficients of both the real parts of \mathcal{M} and \mathcal{D} illustrate a sigmoid behaviour with $\log \omega$ while the coefficients of the imaginary parts of \mathcal{M} and \mathcal{D} have single local maxima/minima with $\log \omega$.

In a similar manner to the brass cone, we only provide the tabular summaries in Tables VII and VIII, which illustrate comparable accuracies for the simulated and measured coefficients of \mathcal{M} and \mathcal{D} for the steel cone positioned at different locations.

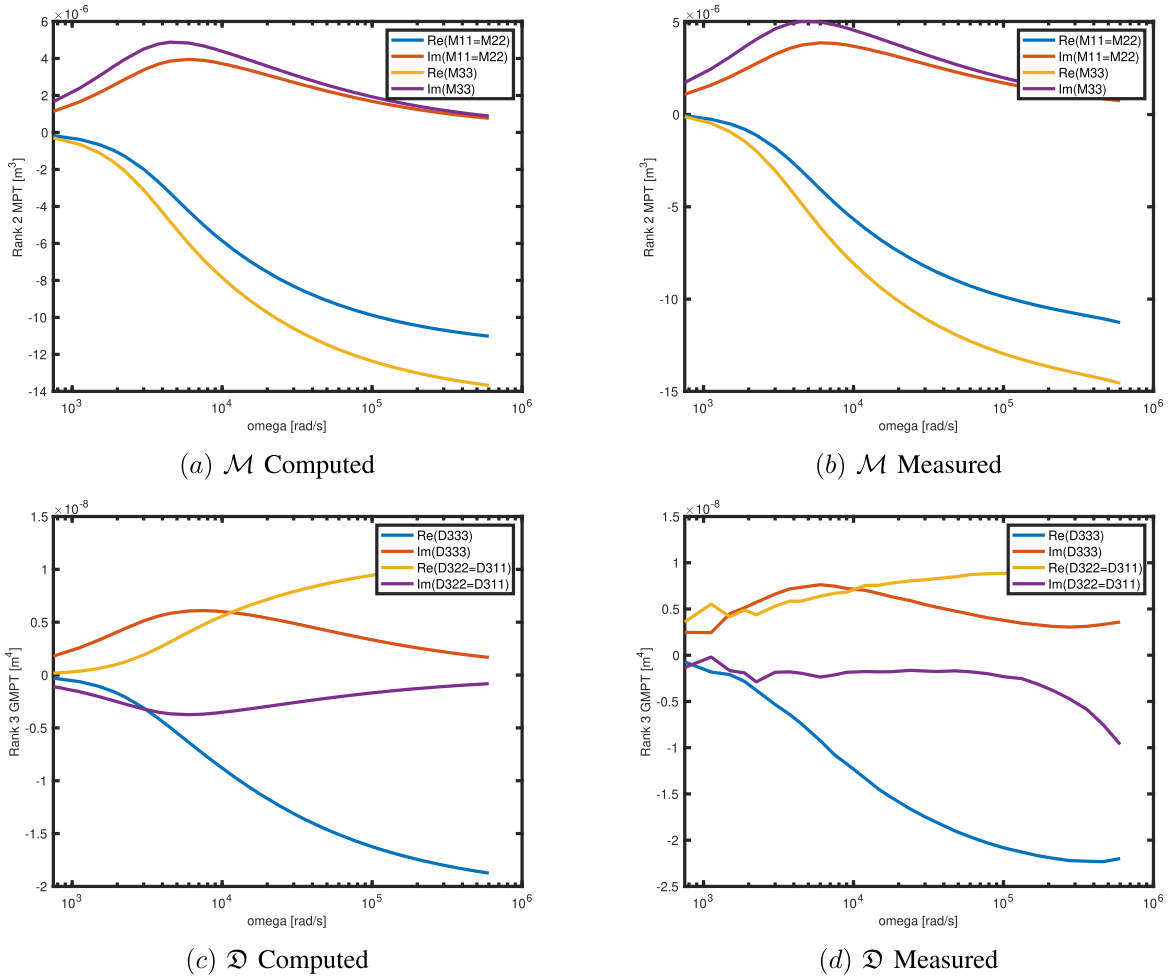


Fig. 11. Brass cone showing: spectral signatures corresponding to (a) computed coefficients of \mathcal{M} and (b) measured coefficients of \mathcal{M} , (c) computed coefficients of \mathcal{D} and (d) measured coefficients of \mathcal{D} .

TABLE VII

STEEL CONE POSITIONED IN A NON-UNIFORM FIELD COMPARING THE ERROR MEASURES DEFINED IN (20) FOR COMPUTED \mathcal{M} AND \mathcal{D} TENSORS, A FIXED FREQUENCY OF $f = 3816$ HZ AND DIFFERENT OBJECT LOCATIONS

z	$e_2^{\text{reactive}}(\mathcal{M})$	$e_2^{\text{resistive}}(\mathcal{M})$	$e_3^{\text{reactive}}(\mathcal{M}, \mathcal{D})$	$e_3^{\text{resistive}}(\mathcal{M}, \mathcal{D})$
(0,0,34.3)	0.096921	0.092994	0.024522	0.021665
(0,0,36.1)	0.095550	0.089722	0.030501	0.027052
(0,0,38.1)	0.099927	0.085682	0.052521	0.033339
(2,0,34.1)	0.103670	0.090383	0.056694	0.022046
(4,0,33.7)	0.097569	0.093506	0.024934	0.023298

TABLE VIII

STEEL CONE POSITIONED IN A NON-UNIFORM FIELD COMPARING THE ERROR MEASURES DEFINED IN (20) FOR MEASURED \mathcal{M} AND \mathcal{D} TENSORS, A FIXED FREQUENCY OF $f = 3816$ HZ AND DIFFERENT OBJECT LOCATIONS

z	$e_2^{\text{reactive}}(\mathcal{M}^{\text{meas}})$	$e_2^{\text{resistive}}(\mathcal{M}^{\text{meas}})$	$e_3^{\text{reactive}}(\mathcal{M}^{\text{meas}}, \mathcal{D}^{\text{meas}})$	$e_3^{\text{resistive}}(\mathcal{M}^{\text{meas}}, \mathcal{D}^{\text{meas}})$
(0,0,34.3)	0.097585	0.100140	0.019174	0.031757
(0,0,36.1)	0.095101	0.102820	0.012218	0.029557
(0,0,38.1)	0.100400	0.100500	0.046089	0.032477
(2,0,34.1)	0.103190	0.096255	0.056485	0.030406
(4,0,33.7)	0.097142	0.097605	0.024977	0.022437

D. Accuracy of MPT and GMPT Measurements

The high level of accuracy in the measured MPT coefficients has been achieved as the multi-coil arrangement was originally designed and built to characterise objects by their

rank 2 MPTs. The design, experimental repeatability and accuracy of the system has been reported in [25]. In this work, we have extended our original measurement system to allow, for the first time, the measurement of the rank 3 GMPT

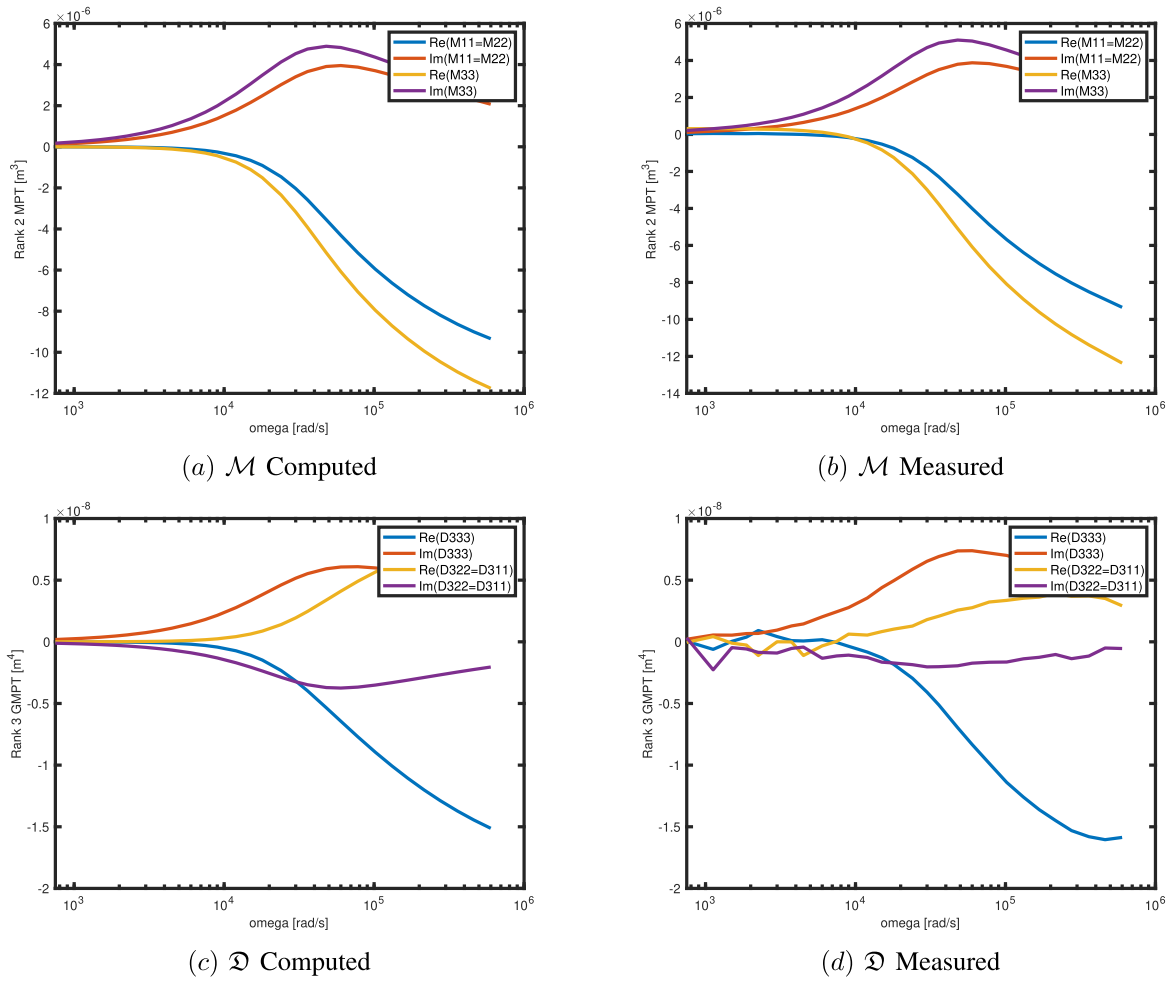


Fig. 12. Steel cone showing: (a) computed coefficients of \mathcal{M} and (b) measured coefficients of \mathcal{M} , (c) computed coefficients of \mathcal{D} and (d) measured coefficients of \mathcal{D} .

coefficients by placing the object in the non-uniform \mathbf{H}_0 field outside of the bore of the coil arrangement. There are several potential sources of error in the GMPT measurements. Firstly, the bore of the measurement apparatus is electrostatically shielded to remove any capacitive coupling of a target object to the coils. However, this is not the case when the target object is placed outside of the bore where \mathbf{H}_0 is non-uniform. This is further complicated when the object is rotated as the capacitive coupling may be different for different orientations. This results in experimental error that is observed in the higher frequencies in the measured spectrum. Secondly, the measurement system was designed to be sensitive across the bore where \mathbf{H}_0 is uniform, which means high signal-to-noise ratio (SNR) in this area. However, the SNR starts to get smaller as the target object moves away from where $\mathbf{H}_0(\mathbf{z})$ is uniform. This means there may be errors in the experimental results introduced by measurement noise. Thirdly, the apparatus was built to ensure a precise position and orientation manipulation, these manipulations will contain inaccuracies, which result in differences in $\mathbf{H}_0(\mathbf{z})$ as well as the rotational configuration of the object compared to the analytical model. Moreover, any small imperfections of the coils, which do not affect rank 2 MPT characterisation results in the uniform

field, may become more apparent in measurements outside of this region. Fourthly, a four-wire resistivity measurement was used to characterise resistivity of the cones. However, these may have small errors in the results meaning the materials modelled may be slightly different in simulations. While these sources of errors are not significant individually, the smaller rank 3 GMPT coefficients and the cumulative sum of these errors, leads to greater inaccuracies in their measurement when compared to those of the MPT. To improve the accuracy of GMPTs significantly would require the design of a new coil arrangement that is optimised to produce non-uniform \mathbf{H}_0 fields, which can be predicted with a high level of accuracy, and address the points raised above.

VIII. CONCLUSION

In this work we have explained the limitations of using an MPT spectral signature alone to characterise objects since the object is then characterised by just 6 complex coefficients as a function of ω . For objects with rotational and/or reflectional symmetries the number of independent coefficients is much fewer and this makes it difficult to discriminate between objects in object classification and to determine which way an object is pointing. Using GMPTs provides additional complex

coefficients as a function of ω , which can aid with discriminating between objects and, hence, they have the potential to improve classification. We have shown, for the first time, that GMPT coefficients and their spectral signature can be obtained in practice from measurements of $(\mathbf{H}_\alpha - \mathbf{H}_0)(\mathbf{x})$ from a coil arrangement. The resulting measured GMPT spectral signature we have obtained are in good agreement with the simulated GMPT spectral signatures we found from numerical simulations using finite elements, while the larger measured MPTs that exhibit a very high level of accuracy. We have illustrated that including the GMPT object characterisation information is important to accurately predict $(\mathbf{H}_\alpha - \mathbf{H}_0)(\mathbf{x})$ whenever the background field is non-uniform for a sequence of copper, brass and steel cones placed at different locations. Our future work includes designing and building a new measurement system that can achieve greater accuracy of GMPT coefficients.

In this work, we have limited consideration to objects with $\mu_* = \mu_0$ and to the cone geometry. For magnetic objects, \mathfrak{N} can not be neglected and includes important characterisation information. Furthermore, many practical objects have fewer (or no) symmetries compared to the cone, which increases the number of MPT and GMPT coefficients needed to characterise the object. The effect of an object's symmetry group on GMPT coefficients will be the subject of a forthcoming work.

REFERENCES

- [1] O. A. Abdel-Rehim, J. L. Davidson, L. A. Marsh, M. D. O'Toole, and A. J. Peyton, "Magnetic polarizability tensor spectroscopy for low metal anti-personnel mine surrogates," *IEEE Sensors J.*, vol. 16, no. 10, pp. 3775–3783, May 2016.
- [2] D. Ambruš, D. Vasić, and V. Bilas, "Robust estimation of metal target shape using time-domain electromagnetic induction data," *IEEE Trans. Instrum. Meas.*, vol. 65, no. 4, pp. 795–807, Apr. 2016.
- [3] H. Ammari, A. Buffa, and J. C. Nédélec, "A justification of eddy currents model for the Maxwell equations," *SIAM J. Appl. Math.*, vol. 60, no. 5, pp. 1805–1823, 2000.
- [4] H. Ammari, J. Chen, Z. Chen, J. Garnier, and D. Volkov, "Target detection and characterization from electromagnetic induction data," *J. Math. Pures Appl.*, vol. 101, no. 1, pp. 54–75, Jan. 2014.
- [5] H. Ammari, J. Chen, Z. Chen, D. Volkov, and H. Wang, "Detection and classification from electromagnetic induction data," *J. Comput. Phys.*, vol. 301, pp. 201–217, Nov. 2015.
- [6] H. Ammari and H. Kang, *Polarization and Moment Tensors with Applications to Inverse Problems and Effective Medium Theory*. New York, NY, USA: Springer-Verlag, 2007.
- [7] E. E. Callaghan and S. H. Maslen, "The magnetic field of a finite solenoid," NASA, Washington, DC, USA, Tech. Note D-465, 1960.
- [8] Wikipedia Contributors. *Electrical Resistivity and Conductivity, Wikipedia, The Free Encyclopedia*. Accessed: Jun. 25, 2021. [Online]. Available: https://en.wikipedia.org/wiki/Electrical_resistivity_and_conductivity
- [9] J. L. Davidson, O. A. Abdel-Rehim, P. Hu, L. A. Marsh, M. D. O'Toole, and A. J. Peyton, "On the magnetic polarizability tensor of U.S. Coinage," *Meas. Sci. Technol.*, vol. 29, no. 3, Mar. 2018, Art. no. 035501.
- [10] B. Dekdouk, C. Ktistis, L. A. Marsh, D. W. Armitage, and A. J. Peyton, "Towards metal detection and identification for humanitarian demining using magnetic polarizability tensor spectroscopy," *Meas. Sci. Technol.*, vol. 26, no. 11, 2015, Art. no. 115501.
- [11] N. Karimian, M. D. O'Toole, and A. J. Peyton, "Electromagnetic tensor spectroscopy for sorting of shredded metallic scrap," in *Proc. IEEE SENSORS*, Oct. 2017, pp. 1–3.
- [12] P. D. Ledger and W. R. B. Lionheart, "Characterizing the shape and material properties of hidden targets from magnetic induction data," *IMA J. Appl. Math.*, vol. 80, no. 6, pp. 1776–1798, 2015.
- [13] P. D. Ledger and W. R. B. Lionheart, "An explicit formula for the magnetic polarizability tensor for object characterization," *IEEE Trans. Geosci. Remote Sens.*, vol. 56, no. 6, pp. 3520–3533, Jun. 2018.
- [14] P. D. Ledger and W. R. B. Lionheart, "Generalised magnetic polarizability tensors," *Math. Methods Appl. Sci.*, vol. 41, no. 8, pp. 3175–3196, May 2018.
- [15] P. D. Ledger and W. R. B. Lionheart, "The spectral properties of the magnetic polarizability tensor for metallic object characterisation," *Math. Methods Appl. Sci.*, vol. 43, no. 1, pp. 78–113, Jan. 2020.
- [16] P. D. Ledger, W. R. B. Lionheart, and A. A. S. Amad, "Characterisation of multiple conducting permeable objects in metal detection by polarizability tensors," *Math. Methods Appl. Sci.*, vol. 42, no. 3, pp. 830–860, Dec. 2018.
- [17] P. D. Ledger, B. A. Wilson, A. A. S. Amad, and W. R. B. Lionheart, "Identification of metallic objects using spectral magnetic polarizability tensor signatures: Object characterisation and invariants," *Int. J. Numer. Methods Eng.*, vol. 122, no. 15, pp. 3941–3984, Aug. 2021.
- [18] P. D. Ledger and S. Zaglmayr, "hp-finite element simulation of three-dimensional eddy current problems on multiply connected domains," *Comput. Methods Appl. Mech. Eng.*, vol. 199, pp. 3386–3401, Dec. 2010.
- [19] J. Makkonen *et al.*, "KNN classification of metallic targets using the magnetic polarizability tensor," *Meas. Sci. Technol.*, vol. 25, no. 5, 2014, Art. no. 055105.
- [20] J. Makkonen *et al.*, "Improving reliability for classification of metallic objects using a WTMD portal," *Meas. Sci. Technol.*, vol. 26, no. 10, Oct. 2015, Art. no. 105103.
- [21] L. A. Marsh, C. Ktistis, A. Järvi, D. W. Armitage, and A. J. Peyton, "Three-dimensional object location and inversion of the magnetic polarizability tensor at a single frequency using a walk-through metal detector," *Meas. Sci. Technol.*, vol. 24, no. 4, Apr. 2013, Art. no. 045102.
- [22] C. R. Nave. *Resistivity and Temperature Coefficient at 20 Degrees C, Hyper Physics*. Accessed: Jun. 25, 2021. [Online]. Available: <http://hyperphysics.phy-astr.gsu.edu/hbase/Tables/rstiv.html>
- [23] S. J. Norton and I. J. Won, "Identification of buried unexploded ordnance from broadband electromagnetic induction data," *IEEE Trans. Geosci. Remote Sens.*, vol. 39, no. 10, pp. 2253–2261, Oct. 2001.
- [24] Electronics Notes. *Electrical Resistivity Table for Common Materials*. Accessed: Jun. 25, 2021. [Online]. Available: https://www.electronics-notes.com/articles/basic_concepts/resistance/electrical-resistivity-table-materials.php
- [25] T. Ozdeger, J. L. Davidson, W. van Verre, L. A. Marsh, W. R. B. Lionheart, and A. J. Peyton, "Measuring the magnetic polarizability tensor using an axial multi-coil geometry," *IEEE Sensors J.*, vol. 21, no. 17, pp. 19322–19333, Sep. 2021.
- [26] K. Schmidt, O. Sterz, and R. Hiptmair, "Estimating the eddy-current modeling error," *IEEE Trans. Magn.*, vol. 44, no. 6, pp. 686–689, Jun. 2008.
- [27] J. Schöberl, "NETGEN an advancing front 2D/3D-mesh generator based on abstract rules," *Comput. Vis. Sci.*, vol. 1, no. 1, pp. 41–52, Jul. 1997.
- [28] J. Schöberl, "C++11 implementation of finite elements in NGSolve," Inst. Anal. Sci. Comput., Vienna Univ. Technol., Vienna, Austria, Tech. Rep. ASC Rep. 30/2014, 2014.
- [29] J. Schöberl and S. Zaglmayr, "High order Nédélec elements with local complete sequence properties," *COMPEL-Int. J. Comput. Math. Electr. Electron. Eng.*, vol. 24, no. 2, pp. 374–384, Jun. 2005.
- [30] W. R. Scott and G. D. Larson, "Measured dipole expansion of discrete relaxations to represent the electromagnetic induction response of buried metal targets," in *Proc. SPIE, Detection Sensing Mines, Explosive Objects, Obscured Targets XV*, vol. 7664, FL, USA, 2010, Art. no. 76640E.
- [31] W. R. Scott, "Broadband array of electromagnetic induction sensors for detecting buried landmines," in *Proc. IEEE Int. Geosci. Remote Sens. Symp. (IGARSS)*, Boston, MA, USA, Jul. 2008, pp. 375–378.
- [32] W. R. Scott and M. McFadden, "Wideband measurement of the magnetic susceptibility of soils and the magnetic polarizability of metallic objects," in *Proc. IEEE Int. Geosci. Remote Sens. Symp.*, Jul. 2012, pp. 3170–3173.
- [33] B. A. Wilson and P. D. Ledger, "Efficient computation of the magnetic polarizability tensor spectral signature using proper orthogonal decomposition," *Int. J. Numer. Methods Eng.*, vol. 122, no. 8, pp. 1940–1963, Apr. 2021.
- [34] B. A. Wilson, P. D. Ledger, and W. R. B. Lionheart, "Identification of metallic objects using spectral magnetic polarizability tensor signatures: Object classification," 2021, *arXiv:2110.06624*.
- [35] Y. Zhao, W. Yin, C. Ktistis, D. Butterworth, and A. J. Peyton, "Determining the electromagnetic polarizability tensors of metal objects during in-line scanning," *IEEE Trans. Instrum. Meas.*, vol. 65, no. 5, pp. 1172–1181, May 2016.

Publication 5

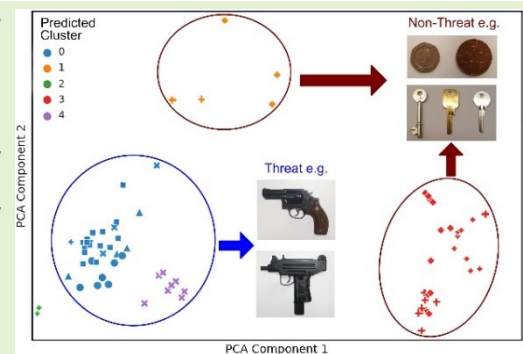
Davidson, J. L., **Özdeğer, T.**, Conniffe, D., Murray-Flutter, M., Peyton, A. J.,
"Classification of Threat and Non-Threat Objects Using the Magnetic Polarizability
Tensor and a Large-Scale Multi-Coil Array," *IEEE Sensors Journal*, **Accepted.**

Classification of Threat and Non-Threat Objects Using the Magnetic Polarizability Tensor and a Large-Scale Multi-Coil Array

John L Davidson^{id}, Toykan Özdeğer^{id}, Daniel Conniffe,
Mark Murray-Flutter and Anthony J Peyton^{id}

Abstract—This paper describes the development of a large-scale multi-coil arrangement capable of characterizing the Magnetic Polarizability Tensor (MPT) of large threat objects such as firearms. The system has been applied to the measurement of a comprehensive range of weapons made available by the National Firearms Centre of the UK. For comparison, a number of non-threat items such as metallic belt buckles, keys and coins have also been characterized. Clear differences in the magnitude and spectroscopic response of the MPT data for different firearm types and non-threat items are presented. The application of unsupervised Machine Learning (ML) algorithms to MPT data of threat and non-threat objects enable a better understanding of target object classification. The presented results are encouraging as they demonstrate the ability of the MPT used in combination with the adopted classification algorithms to robustly discriminate between threat and non-threat objects.

Index Terms—Magnetic Polarizability Tensor, Metal Detection, Machine Learning, Metal Classification



I. INTRODUCTION

Gun and knife crime are a serious global problem. For example, according to the Centers for Disease Control and Prevention's (CDC) National Center for Health Statistics [1] in 2020 in the US, gun related killings amounted to 19,384 people. This equates to 53 firearm related homicides each day in the US. Additionally, according to the FBI [2], there were 345 mass shooting incidents in the United States between 2000-2020, resulting in more than 1,024 deaths and 1,828 injuries. The deadliest attack, in Las Vegas in 2017 resulted in the death of 60 people and left 500 wounded. Although, less severe, there were in the UK 35 firearms related homicides in the year ending March 2021 with an additional 5,682 reported offences involving firearms [3]. Additionally, knife crime in the UK is a significant issue with over 47,000 offences in 2019 in England and Wales [4] involving knife or sharp implements resulting in 285 recorded homicides. Globally, high populated areas such as sports stadia, arenas, transportation hubs, shopping centers and other places such as music venues, schools and nightclubs

This paper was submitted for review on xx/xx/xxxx. John Davidson, Toykan Özdeğer, Daniel Conniffe, Mark Murray-Flutter and Anthony J. Peyton would like to thank Innovate UK (Grant ref 39814), the Engineering and Physical Sciences Research Council (Grant ref EP/R002177) and Sir Bobby Charlton Foundation for financial support.

Toykan Özdeğer, John Davidson, Dan Conniffe, Anthony J. Peyton are with the Electrical and Electronic Engineering Department, The University of Manchester, Manchester, UK, M13 9PL (e-mail: J.Davidson-2@manchester.ac.uk; toykan.ozdeger@manchester.ac.uk daniel.conniffe@manchester.ac.uk; a.peyton@manchester.ac.uk).

Mark Murray-Flutter is with the Royal Armouries, Leeds, UK (e-mail: mark.murray-flutter@armouries.org.uk).

represent potential targets for mass killings, gun and knife crime. Consequently, early recognition of threat objects e.g. metal detection methods may help to reduce the number of offences involving guns and knives.

In recent years, a number of different technologies have been developed to detect threat objects at security checkpoints [5]. For metallic objects, walk-through metal detectors (WTMD) have become the primary method used in security screening [6-7]. Typical threat items include concealed guns and knives. However, existing WTMD fail to accurately discriminate between threat items and harmless metallic objects such as belt buckles, keys, coins, watches, jewelry, and mobile phones. WTMDs are commonly used in environments such as airports, public buildings, prisons and, more recently, train stations, shopping centers and sports stadium events where the efficient throughput of people during the screening process is of considerable concern. To prevent constant false alarms, people are often required to remove metallic objects prior to WTMD screening. However, this disrupts throughput, increases delays, queuing time and public frustration. Additionally, false alarms also necessitate manual pat-down security checks which require a large number of staff to administer and further slow the screening process down significantly. Ideally, WTMD screening is required, which is able to reliably discriminate between genuine threat and non-threat items in near real time to reduce the need for metallic object removal, thereby increasing throughput.

The Magnetic Polarizability Tensor (MPT) is a representative electromagnetic property of a metallic object, which depends on the size, material, shape, and excitation

frequency of the object [8]-[10]. The MPT has been successfully applied in the area of metal detection e.g. the detection of unexploded ordnance [11]-[14], metal recognition and classification [15]-[16], Non Destructive Testing [17]-[19], buried object detection [20] and anti-personnel landmine characterisation [21]-[23]. In the area of WTMD, intelligent solutions using the MPT are being sought in order to decrease false alarm rates thereby increasing screening throughput. For example, Kauppila et al. [24] describe the concept of a WTMD able to generate mutually orthogonal homogeneous magnetic fields in such a way that the measured dipole moments allow for the classification of small items using a time series of eigenvalues of the MPT. The study presented simulated and proof of concept data showing the possibility of classifying unknown items in the WTMD to harmless and dangerous with a high degree of accuracy (approaching 90%). Extending on this work, Makkonen et al [25] applied a K-nearest-neighbour (KNN) based classifier algorithm to data acquired from a modified commercial WTMD with MPT data of metallic objects such as knives, shoe shanks and belts. The algorithm classified objects into 13 classes and distinguished several similar objects within each class. The presented results showed a typical success rate of over 95% for recognizing threats, and over 85% for correct classification. Furthermore, Makkonen et al increased the accuracy of the metal object classification using a novel application of a Levenberg-Marquardt algorithm reported in [26] by rejecting noisy and unreliable MPT data. Further studies have used Artificial Neural Network (ANN) methods to discriminate between threat and non-threat items. For example, Elgwell et al. [27] used a method based on the decay rates of induced currents in small threat objects. Al-Qubba et al. [28] constructed a giant magneto-resistive sensor and applied ANN and machine learning to recognise weapon and common daily non-threat items. Kottler et al [29] used a modified WTMD and analysed the magnetic spectrum generated when a person passes the WTMD. Many of the studies in the reported literature are promising, however, virtually all studies to date, have generally only considered small sample sets of threat items or are very sensitive to measurement noise.

This paper describes a novel large scale multi-coil geometry arrangement capable of measuring the MPT of small to medium sized firearms. For comparison, sample non-threat items provide additional data for testing the effectiveness of unsupervised machine learning algorithms for discriminating between the tested threat and non-threat items. In this paper, Section II describes the background to the MPT and unsupervised machine learning algorithms. Section III describes the experimental setup used for MPT measurements which involves a multi-coil arrangement and a new target orientation manipulator capable of housing the firearms of interest. Section IV gives details of the MPT measurement method, data sets used for testing of unsupervised machine learning algorithms and the associated data pre-processing and visualization methods. Section V gives further details of the tested threat and non-threat objects. Section VI presents example results and discusses the effectiveness of the tested algorithms. Finally, Section VII concludes the paper with a discussion of the potential of the adopted algorithms as object classifiers within the context of security screening.

II. BACKGROUND

A. Magnetic Polarizability Tensor

The MPT is a function of frequency and depends on the object's shape, material properties and its orientation in relation to an applied primary magnetic field. Mathematical descriptions of the MPT and, more generally, the perturbation of magnetic fields due to magnetic and conducting objects can be found in the pure and applied mathematics literature e.g. [8]-[10]. However, a simplified engineering approach to describing the rank 2 MPT considers the representation of metallic responses as point dipoles. This approach has been presented in several publications for time and frequency domain systems [11]-[13] and has previously been adopted for object classification using WTMD [25], [26]. For conciseness, a brief summary of the key equations describing the MPT are presented in this paper whilst complete derivations can be found in the provided references. The MPT itself is a complex -dependent quantity which is commonly expressed as a 3x3 matrix of the following structure:

$$\mathbf{M}(f) = \begin{bmatrix} M'_{xx} + jM''_{xx} & M'_{xy} + jM''_{xy} & M'_{xz} + jM''_{xz} \\ M'_{xy} + jM''_{xy} & M'_{yy} + jM''_{yy} & M'_{yz} + jM''_{yz} \\ M'_{xz} + jM''_{xz} & M'_{yz} + jM''_{yz} & M'_{zz} + jM''_{zz} \end{bmatrix} \quad (1)$$

At a fixed frequency f , low enough for the eddy current approximation to be valid then the MPT matrix in (1) is symmetric and has six unique complex coefficients. The complex nature of the MPT yields the implicit frequency dependence. Additionally, the MPT is orientation dependent and, therefore, a change in the orientation of the object in relation to the applied primary field will result in a change in the MPT. If constructing the MPT matrix by measurements, at least six complex and suitably chosen measurements of the object are needed. However, in practice more orientations are used to better pose the inverse problem and improve accuracy by reducing the effects of noise in the measurement data.

The induced voltage, V_{ind} , on the receive coil of an electromagnetic sensor, where I is the virtual current in the receive coil, can be shown to satisfy the following:

$$V_{ind} \cong -j2\pi f \frac{\mu_0}{I} \mathbf{H}_T^T \mathbf{M} \mathbf{H}_R \quad (2)$$

where \mathbf{H}_T is the primary electromagnetic field produced by a transmitting coil in three-dimensional space. The field quantity, \mathbf{H}_R is the incident magnetic field on the receive coil and f is the frequency at which the magnetic field is varying. Therefore, by measuring V_{ind} and calculating \mathbf{H}_T and \mathbf{H}_R at the target for defined unique orientations, then it is possible to build a system of linear equations constructed using (2). For the rank 2 MPT approximation, a near uniform electromagnetic field is required and the application of a rotation matrix, R based on Euler's theorem using (3) can be used to give an eigenvalue matrix which is orientation independent of the MPT:

$$\mathbf{M} = R \cdot \mathbf{\Lambda} \cdot R^T \quad (3)$$

where $\mathbf{\Lambda}$ is the diagonal matrix:

$$\mathbf{\Lambda}(f) = \begin{bmatrix} \Lambda'_{xx} + j\Lambda''_{xx} & 0 & 0 \\ 0 & \Lambda'_{yy} + j\Lambda''_{yy} & 0 \\ 0 & 0 & \Lambda'_{zz} + j\Lambda''_{zz} \end{bmatrix} \quad (4)$$

The eigenvalue matrix shown in (4) is frequency dependent, meaning that measuring the MPT at different frequencies provides a more detailed information set so a stronger basis for discrimination and any subsequent application of classification algorithms. This spectroscopic nature of the MPT and the associated eigenvalue matrix is inter-dependent with the object's shape, size, conductivity and permeability as described by Rehim *et al.* [23] and Ledger *et al.* [39]. This makes the MPT a potentially useful tool for the identification and classification of threat and non-threat objects within a security screening environment.

B. Unsupervised Machine Learning Algorithms

Machine Learning (ML) algorithms can be divided into three categories as *supervised*, *semi-supervised* and *unsupervised* ML algorithms [32]-[34]. Supervised ML algorithms require a labelled dataset which can be used to "train" the algorithm. A separate, smaller dataset can then be used to test the performance of the trained ML algorithm. Performance of a supervised ML algorithm is dependent on the size of the dataset used to train the algorithm. If a small dataset is used, it is very easy for the algorithm to "overfit" that specific dataset and not perform well when new data is introduced. On the other hand, unsupervised ML algorithms use unlabelled datasets to generate a labelled dataset as the result. Because of that, it is not easy to evaluate the performance of an unsupervised ML algorithm. However, unsupervised ML algorithms are useful for finding clusters or patterns in the data which may not be obvious. In addition, unsupervised ML algorithms can be used with small datasets and still provide valuable output.

To evaluate the possibility of classifying target objects using machine learning, unsupervised ML algorithms were applied to object MPT data. Normally, a supervised ML algorithm, such as a Deep Neural Network (DNN), would be deployed to classify targets in a complete system. However, due to the small size of the collected data (<100 samples), unsupervised ML algorithms were applied to evaluate and prove that the different types of samples in the dataset form clusters. If there are clusters in the data, this means a supervised ML algorithm can be trained with a large dataset of the same data type to classify the samples into those clusters. Therefore, this reported study aims to show that datasets generated using the data described in Sections IV and V exhibit clustering [35]-[36] within the measured data.

III. EXPERIMENTAL SETUP

A. System Overview

The main system comprises of three main parts; a large-scale coaxial multi-coil arrangement, custom made electronics and control software on a PC. The bespoke control software is used to set transmit control signals, e.g. frequency, signal amplitudes and digital signal processing (DSP) settings to a dedicated microcontroller (Red Pitaya – STEMLab 125-14). The microcontroller generates the requested excitation signals to a set of twenty power amplifiers (Analog Devices LT 1210) configured to produce 64 V peak-to-peak sine wave at 10 A to the transmit coil. Measurement signals from the receive coils are amplified and filtered by custom-made electronics controlled via the DSP of the microcontroller. Signal averaging of the acquired

measurements are performed in the control software prior to MPT inversion in accordance with Eq. (2). Full details of the custom-made electronics and data acquisition methods can be found in previous publications [30] and [37].

B. Large-Scale Multi-Coil Arrangement

The geometry of the coil arrangement is based on an approximate two factor scale up of the multiple coil array described by Ozdeger *et al.* [30]. The coil arrangement consists of spatially segmented coils corresponding to a coaxial transmit coil with 495 mm internal diameter and two receive coils each with 430 mm internal diameters. The transmit coil is made up of 12 AWG PVC insulated copper wire wound as nine separate coil sections (turns: 11:3:5:5:5:5:3:11) connected in series addition. The two receive coils are connected in series opposition in two symmetrical halves, with each coil made up of 14 AWG PVC insulated wire wound as eight separate coil sections (turns: 27:18:18:49:49:18:18:27). All coils are wound on 6 mm thickness flexible MDF former tubes which are held in position with top and bottom recessed MDF plates held in compression via three rigid polypropylene rods. Additional MDF annuli rings provide structural support of each MDF former tube. The coils are held in position using annuli rings and glass fibre reinforced tape. A final outermost tube provides further structural reinforcement and protects all coils and lead out wiring from the external environment. The external height of the coil arrangement is 1.1 m with an outermost diameter of 0.8 m. The overall mass is approximately 40 kg. The coil arrangement is supported using a bespoke MDF platform having an integrated operator step. A major role of the platform is the minimisation of potential coil unbalancing or saturation effects as a consequence of any unknown embedded and hidden metallic floor structures. An innermost tube of 1 mm thickness ABS sheeting painted with conductive paint (surface resistivity: 55 Ω /sq/ 50 microns thickness) provides electrostatic shielding. The coils are optimized for the range between 100 Hz to approximately 80 kHz; this frequency range being outside any coil resonant frequencies but within the frequency range of the driving and measurement electronics [30]. The design concept and constructed coil arrangement is shown in Fig. 3.

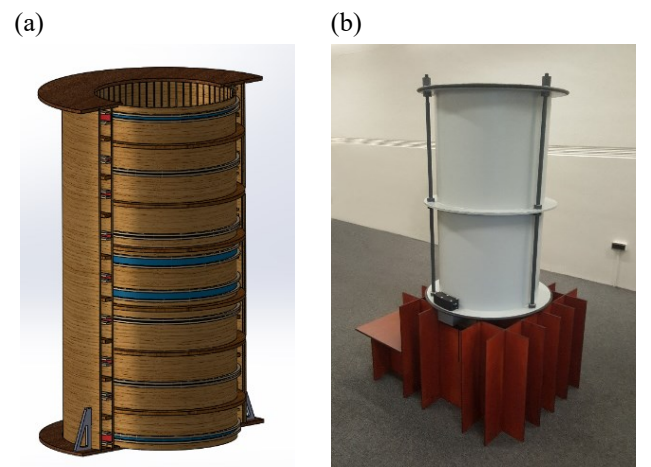


Fig. 1. The large-scale coil arrangement showing; (a) design concept cut away along with simplified inner receive coil and (b) constructed coil arrangement on the bespoke mounting platform.

C. Target Orientation Manipulator

A bespoke Target Orientation Manipulator (TOM) based on an open framed truncated Icosahedron (tI) enables test object rotation in three-dimensional space. The tI is constructed from a combination of 3D printed polylactic acid (PLA) nodes connected with sections of 15 mm diameter polybutylene pipe. The TOM allows for test objects to be rotated in such a way that provides unique independent orientations for the subsequent calculation of the magnetic polarizability tensor. The use of the tI method enables non-symmetrical target objects to be measured and has been described in more detail elsewhere [37]. The TOM uses a height adjustable internal MDF object mounting plate which can be accessed either by the temporary removal of a small section of the tI or by the direct placement of the object of interest onto the plate via one of the open faces of the tI. Target objects are securely fixed in the TOM using appropriate combinations of hook and loop type fasteners or adhesive tape. The TOM is approximately 360 mm in diameter and the use of numbered nodes along with a bespoke keyed seating arrangement within the coil arrangement allows for accurate and consistent positioning of each target in the measurement system. The TOM is shown in Fig. 4.

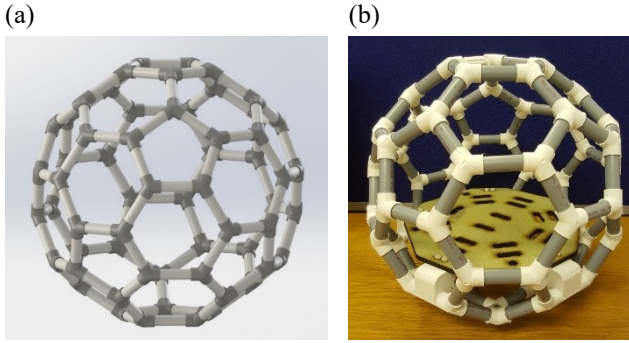


Fig. 4. CAD model and built version of the large-scale TOM; (a) design concept and (b) constructed TOM with mounting plate. The TOM is approximately 360 mm in diameter.

IV. METHOD

A. Magnetic Polarizability Tensor Measurement

The experimental setup described in Section III was used to characterise the rank 2 MPT of target objects. Experiment settings were set using the Graphical User Interface (GUI) on the computer before each experiment and the system was left to run until it reached the steady-state temperature. In addition, the instrument was also used in a temperature-controlled area to minimise the measurement drift caused by any temperature changes on the coils or the electronics. Phase and amplitude correction was achieved with a NiZn ferrite rod, which gives a pure real response through the instrument's operating frequency spectrum. A background measurement was recorded with no object inside the coils. The system was also calibrated against a copper reference target, see next paragraph. Then, the object was placed inside a truncated icosahedron shaped target orientation manipulator and was put into 16 unique orientations inside the coils. A measurement was taken at each orientation and the experiment was finalized with a measurement of the background again. After the background measurements were subtracted from the 16 measurements with object present, 16 linear equations were constructed using the orientation information and the measured voltages. A Least Squares

Method was then used to obtain the 6 unique components of the rank 2 MPT. The method of data capture has been described in more detail in [37].

The threat objects were characterized using the larger coil arrangement reported in this paper whereas the smaller non-threat objects were characterized using the smaller coil arrangement reported in [30]. To ensure both the larger and the smaller coil arrangements resulted in the same MPTs, well-defined and previously measured standard copper test pieces were characterized using both the larger and the smaller coil arrangements. The results were then compared to quantify the error present in measurements between the two coil arrangements. It was found that for the standard test pieces, the MPT eigenvalues characterized by the two coil arrangements were within one percent of each other at worst.

B. Datasets

Two datasets were generated using MPT data from measurements taken at the UK's National Firearms Centre and measurements from the University of Manchester laboratories. One of the datasets involved several types of firearms which were expected to form clusters in terms of the types of the firearms. Further details of the firearms tested are given in Section V. The other dataset involved a subset of the firearms from the first dataset, as well as a set of non-threat objects. Both datasets and the object types they include are shown in Table I.

Table I – Object types involved in the datasets generated. Numbers in each cell under the dataset columns indicate the number of specific objects in that particular sub-group of the dataset.

	<i>Dataset 1</i>	<i>Dataset 2</i>
Metal Frame Pistol	11	11
Polymer Frame Pistol	18	18
Revolver	7	7
Mini Pistol	2	-
Sub-Machine Gun (SMG)	4	4
Grenade	4	-
Key	-	12
Coin	-	13
Belt	-	11
<i>Total Number of Objects</i>	<i>46</i>	<i>76</i>

The only difference between Dataset 1 and Dataset 2, in addition to the inclusion of non-threat items, is the removal of the grenade data from Dataset 2. This was because of the inert materials in the grenades filled to replace the explosives were not known, meaning it was not clear if the inert grenades were completely representative of the live weapons. Although 7 clustering algorithms were initially tested, K-Means Clustering, Spectral Clustering and Agglomerative Clustering algorithms were found to be the better performers amongst the others. Therefore, they were used to evaluate the clustering in the datasets. The number of clusters specified for the clustering algorithms was set to 5, which was found to give the best performance for the used datasets and clustering algorithm combination.

C. Pre-Processing of the Datasets.

For each object, three eigenvalues of the complex rank 2 MPT across the frequency spectrum were recorded, resulting in 168 features/data points (real and imaginary values of three eigenvalues across 28 frequencies). Using the complex MPT eigenvalues, MPT invariants were calculated as described in [38]-[39] which resulted in the same number of features per object. Using the MPT invariants instead of the MPT eigenvalues eliminates classification issues arising from the arbitrary allocation of eigenvalues.

The number of features per object were reduced from 168 to 2 by using Principal Component Analysis (PCA), which was found to still hold 95% of the information of the data. The data was also normalized so that the minimum and maximum values of each object's features were between 0 and 1. This eliminated the possibility of any bias happening by the response size of each object e.g., response size of an SMG compared to a key. Although, the response size of an object is a feature, and should be used in a commercially deployed system, it is not possible to visualise the data and test for clustering without the normalization. Otherwise, all the smaller objects would just appear as a dot on the plots. Both datasets with reduced dimensions and the original datasets with 168 features were used to test the clustering in the data, meaning that a total of 4 datasets were used.

V. TESTED OBJECTS

A range of small to medium sized firearms provided by the UK's National Firearms Centre at the Royal Armouries were characterized using the large-scale multi-coil arrangement. The selected firearms ranged in size from typical self-loading handguns and revolvers to the larger machine pistol (MP) and submachine gun (SMG) weapons such as a Mini-Uzi 9 mm MP model measuring approximately 350 mm in length with the folding stock collapsed. Examples of firearms from the same manufacturer (and model) but with different frame materials were also tested. The selected firearms are representative of approximately two thirds of the 3 million pistols and revolvers that enter circulation in the US market each year. In addition to the tested firearms, a small number of inert filled hand fragmentation grenades typically used for drill purposes by military purposes were tested. A summary of the tested threat objects is shown in Table II. Additionally, examples of tested firearms are shown in Fig. 5.

Table II – Summary of tested threat objects.

Group / Type	Details / Manufacturers
Glock Group	9m Self Loading Polymer Framed
Miscellaneous 9 mm Pistols	Smith and Wesson, Heckler and Koch, Beretta, Jennings Firearms
Revolver Group	Colt, Webley, Smith and Wesson,. 38 and.45 Calibers
MP/SMG	Uzi, MAC-10 & 11, CZ Scorpion, Steyr Arms
Pistol Pairs	Same manufacturer (and model); different material finishes Sig Sauer, Smith and Wesson, Ruger
Grenades	Drill type with inert filling e.g. Arges Type HG84, 'Mills' British No. 5



Fig. 5. Example tested firearm types; (a) polymer framed self-loading pistol (Glock 43), (b) metal framed handgun (Beretta 92FS), (c) revolver (Smith and Wesson, model 547) and (d) Uzi 9 mm MP

A set of non-threat objects were characterized for comparison with the threat objects. These included coins, keys and metallic belt buckles. Coins consisted of both a mint condition uncirculated 2004 set of US coins and currently in circulation UK coins, minted circa 2015. Keys typical of the type used in UK and European mortice locks along with domestic door keys were also characterized. Keys were chosen to be representative of the keys carried by people prior to WTMD screening. Material types covered a range of carbon steel, stainless steel, brass and brass-nickel combinations typically used in key manufacture. Examples of the tested non-threat objects are shown in Fig. 6.

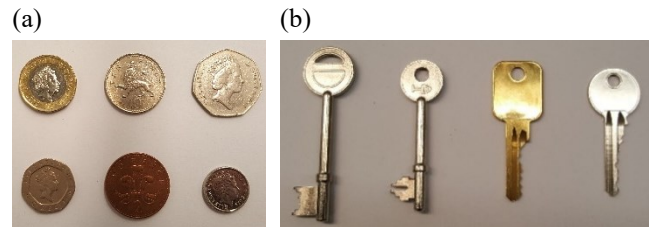


Fig. 6. Example benign test objects; (a) subset of circulated British coins (circa 2015) and (b) typical UK mortice and domestic door keys.

VI. RESULTS AND DISCUSSION

Fig. 7 shows typical eigenvalue MPT data associated with example threat and non-threat items detailed in Section V. The observations made on the eigenvalues of the measured objects show both a rich detail in the spectroscopic response and significant differences between different object types. For example, Fig. 7(a-b) shows clear differences in data magnitude and spectroscopic response for polymer framed, metal framed and revolver firearm types. The highest magnitude eigenvalue is associated with the revolver which is consistent with this firearm having the most metallic content of the presented data in this subplot. The asymmetrical shapes of the firearms result in the observed three different eigenvalue tensors. However, for all presented firearm types, the first eigenvalue shows a stronger level of dominance corresponding to an axial direction along the barrel length of each firearm.

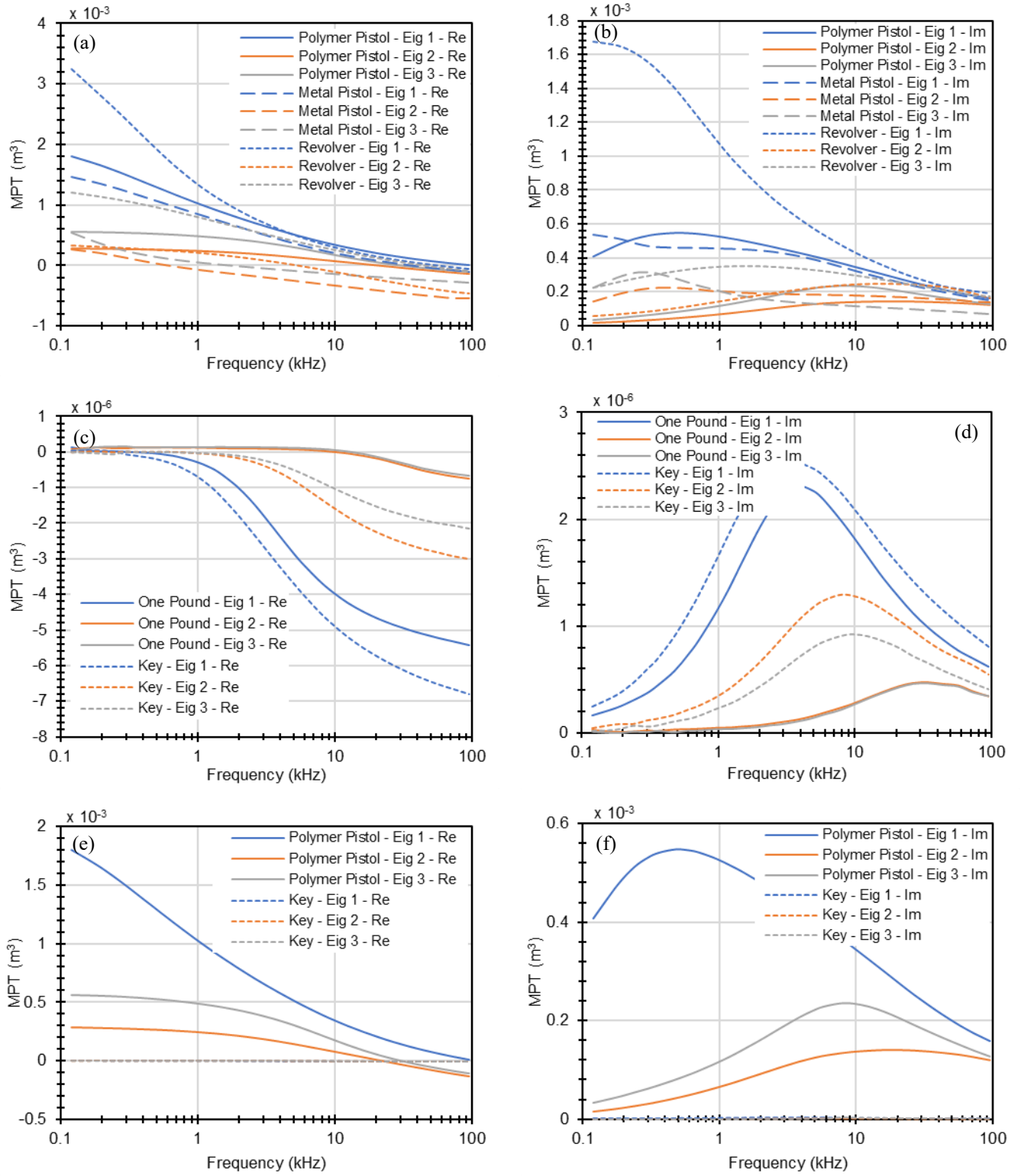


Fig. 7. Real (Left Hand Side) and imaginary (Right Hand Side) eigenvalue MPT data for example tested objects; (a)-(b) polymer (Glock 17) and metal framed pistols (Sig Sauer 9mm P225) and revolver (Colt 0.455), (c)-(d) one pound coin and domestic key, (e)-(f) polymer pistol and domestic key.

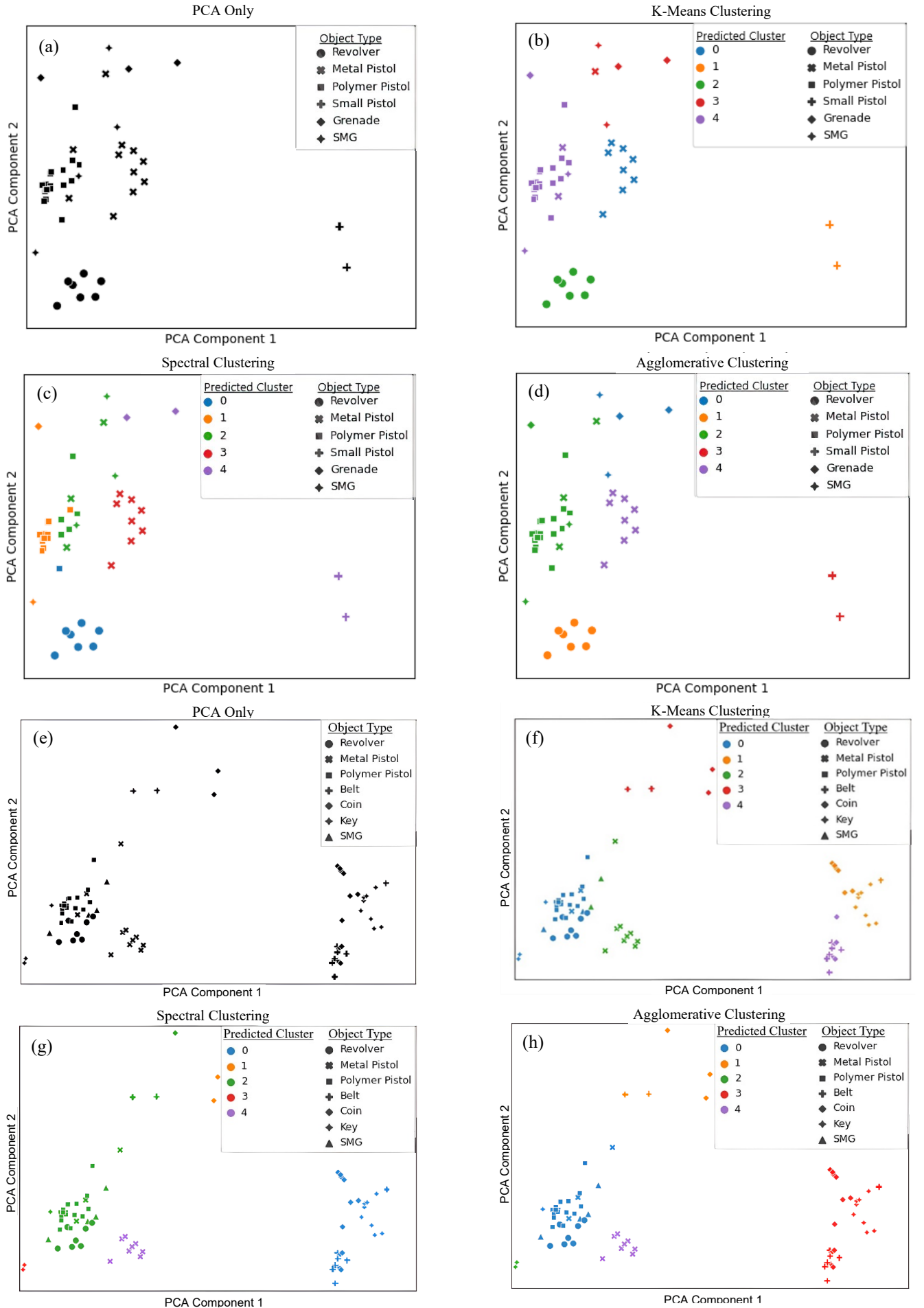


Fig. 8. PCA visualization and three different clustering algorithms applied to the datasets described in sections IV and V; (a-d) is dataset 1 and (e-h) is dataset 2.

Fig. 7(c-d) shows typical eigenvalue MPT data for a coin and a mortice lock key. The data are approximately three orders of magnitude smaller than the firearms of Fig. 7(a-b); this being consistent with the smaller relative sizes and the lower metallic content compared with the firearms. Additionally, for the coin, the first eigenvalue is strongly dominant compared with the two smaller repeated eigenvalues consistent of the MPT nature of a largely non-magnetic disk [31]. A comparison of the relative magnitude differences between a typical non-threat object and a polymer framed pistol is shown in Fig. 7(e-f). Although, polymer framed, the tested Glock 17 (third generation), still uses a substantial amount of metallic material in the barrel, slide, spring and the partial steel lining of the magazine. This is consistent with the observation of the positive real component in the eigenvalues at frequencies below 10 kHz suggesting a relative permeability greater than 1 indicative of a material such as a ferrous steel.

Clustering in the data was tested using 2 datasets and 3 Unsupervised ML algorithms for clustering. A subset of the clustering results is shown in Fig. 8. Each dataset had a version where the number of dimensions or features for each sample was reduced to 2 using PCA, and also another version with the full 168 dimensions. As the clustering algorithms performed better on the datasets with 168 dimensions, only the results for those datasets are shown in Fig. 8.

Main clusters in Dataset 1 were recognised by the clustering algorithms where all three algorithms have placed most object types into separate clusters. Two SMGs and grenades were clustered either into a separate cluster or together with the polymer framed pistols by all three algorithms. Most threat and non-threat objects were in separate clusters in Dataset 2. This can be clearly observed for the application of the Spectral and Agglomerative clustering algorithms which broadly shows threat objects grouped towards the bottom and LHS of the data plots. Although, some non-threat, ferrous objects were clustered as threats in some situations, no threat objects were clustered as non-threat, meaning that the algorithms did not produce any false negative classification. For example, two ferrous coins were clustered together with the threat objects in Fig. 8(f) and two different coins and a belt were again clustered together with the threat items in Fig. 8(g). The false classification rate of non-threat objects as threats would reduce significantly if the responses were not normalised, as most non-threat objects are smaller in size, compared to the threat objects in the datasets used. However, as described in Section IV-C, normalization of the data was a necessity for this specific application. The metal framed pistols were again clustered separately to polymer framed pistols. However, the cluster with polymer framed pistols also included revolvers and SMGs in the same cluster for this dataset. This is likely due to this dataset having non-threat objects (e.g., coins, keys) with very different characteristics to the firearms, which means that two different pistols styles look much more similar to each other compared to a pistol and a coin. Although a supervised machine learning algorithm trained with a large dataset would still be able to classify different types of firearms and non-threat objects at the same time, it would still have a higher accuracy of classifying threat and non-threat objects compared to discriminating between individual different types of threat objects. Consequently, a large response size difference between a threat and a non-

threat object in non-normalized data could be an important and useful feature, in addition to other characteristic differences.

VII. CONCLUSION AND FUTURE WORK

In this paper, we have described the development of a large-scale multi-coil arrangement capable of characterizing the MPT of large threat objects such as firearms. A novel aspect has been the measurement of a comprehensive range of weapons made available by the National Firearms Centre at the Royal Armouries in the UK. The resulting absolute MPT data will serve as a highly valuable library resource for the development of the next generation of WTMDs. Additionally, the results shown in this paper demonstrate that the tested clustering algorithms are capable of classifying threat objects in a consistent manner. Crucially, irrespective of algorithm type, the classification methods clearly demonstrate the ability to distinguish between firearms and non-threat objects. The presented classification methods are invariant to the orientation of the object tested being based on the measured absolute MPT values. The combination of high quality MPT data libraries and robust classification algorithms are a crucial aspect in aiding the development of newer, smarter WTMDs in such a way which will enable better discrimination between threat and non-threat objects.

VIII. REFERENCES

- [1] <https://wisqars.cdc.gov/data/explore-data/home>
- [2] *Active Shooter Incidents in the United States in 2020*, Federal Bureau of Investigation, U.S. Department of Justice, Washington, D.C, published 2021.
- [3] UK Office for National Statistics – Crime in England and Wales: <https://www.ons.gov.uk/peoplepopulationandcommunity/crimeandjustice/bulletins/crimeinenglandandwales/yearendingdecember2021#offences-involving-firearms>
- [4] Allen G, Audickas L, Loft P, Bellis A. *Knife Crime in England and Wales. Technical Report SN4304*; Briefing Paper London: House of Commons Library; 2019.
- [5] Agruto, A.; Li, Y.; Tian, G.Y.; Bowring, N.; Lockwood, S. A Review of Concealed Weapon Detection and Research in Perspective. In Proceedings of the 2007 IEEE International Conference on Networking, Sensing and Control, London, UK, 15–17 April 2007; pp. 443–448.
- [6] EU. Commission Implementing Regulation (EU) 2015/1998 of 5 November 2015 Laying down Detailed Measures for the Implementation of the Common Basic Standards on Aviation Security. 2015. Available online: <https://op.europa.eu/en/publication-detail/-/publication/c38f361d-8a99-11e5-b8b7-01aa75ed71a1>
- [7] NIJ Std 0602.01, “Walk-Through Metal Detectors for Use in Concealed Weapon and Contraband Detection,” National Institute of Justice, Office of Science and Technology, Washington, DC 20531, January 2003.
- [8] Ammari H, Chen J, Chen Z, Garnier J, Volkov D. Target detection and characterization from electromagnetic induction data. *Journal de Mathématiques Pures et Appliquées*. 2014;101(1):54-75.
- [9] Ledger, PD., and Lionheart, WRB., “Understanding the magnetic polarizability tensor,” *IEEE Transactions on Magnetics*, vol. 52. No. 5, pp. 1-16, 2016.
- [10] Ledger, PD., and Lionheart, WRB., “The spectral properties of the magnetic polarizability tensor for metallic object characterisation,” *Mathematical Methods in the Applied Sciences*, vol. 43, no. 1, pp. 78-113, 2019.
- [11] Fernandez, JP., Barrowes, BE., Grzegorzczak, TM., Lhomme, N., O'Neill, K., and Shubitidze, F., “A Man-Portable Vector Sensor for Identification of Unexploded Ordnance,” *IEEE Sensors Journal*, vol. 11, no. 10, pp. 2542-2555, 2011.
- [12] Norton SJ., and Won, JJ., “Identification of buried unexploded ordnance from broadband electromagnetic induction data,” *IEEE Transactions on Geoscience and Remote Sensing*, vol. 39, no. 10, pp. 2253-2261, 2001.

- [13] Grzegorzczuk, TM., Barrowes, BE., Shubitidze, F., Fernandez, JP., and O'Neill, K., "Simultaneous Identification of Multiple Unexploded Ordnance Using Electromagnetic Induction Sensors," *IEEE Transactions on Geoscience and Remote Sensing*, vol. 49, no. 7, pp. 2507-2517, 2011.
- [14] Nelson, HH., and McDonald, JR., "Multisensor towed array detection system for UXO detection," *IEEE Transactions on Geoscience and Remote Sensing*, vol. 39, no. 6, pp. 1139-1145, 2001.
- [15] Tao, Y., Yin, W., Zhang, W., Zhao, Y., Ktistis, C., and Peyton, AJ., "A Very-Low-Frequency Electromagnetic Inductive Sensor System for Workpiece Recognition Using the Magnetic Polarizability Tensor," *IEEE Sensors Journal*, vol. 17, no. 9, pp. 2703-2712, 2017.
- [16] O'Toole, M., Karimian, N. and Peyton, A., "Classification of Nonferrous Metals Using Magnetic Induction Spectroscopy," *IEEE Transactions on Industrial Informatics*, vol. 14, no. 8, pp. 3477-3485, 2018.
- [17] García-Martín, J., Gómez-Gil, J. and Vázquez-Sánchez, E., "Non-Destructive Techniques Based on Eddy Current Testing," *Sensors*, vol. 11, no. 3, pp. 2525-2565, 2011.
- [18] Daura, L., Tian, G., Yi, Q. and Sophian, A., "Wireless power transfer-based eddy current non-destructive testing using a flexible printed coil array," *Philosophical Transactions of the Royal Society A: Mathematical, Physical and Engineering Sciences*, vol. 378, no. 2182, p. 20190579, 2020.
- [19] Lu, M., Meng, X., Huang, R., Chen, L., Tang, Z., Li, J., Peyton, A. and Yin, W., "Determination of Surface Crack Orientation Based on Thin-Skin Regime Using Triple-Coil Drive-Pickup Eddy-Current Sensor," *IEEE Transactions on Instrumentation and Measurement*, vol. 70, pp. 1-9, 2021.
- [20] Ambrus, D., Vasic, D. and Bilas, V., "Comparative Study of Planar Coil EMI Sensors for Inversion-Based Detection of Buried Objects," *IEEE Sensors Journal*, vol. 20, no. 2, pp. 968-979, 2020.
- [21] Scott, WR., and Larson, GD., "Modeling the measured em induction response of targets as a sum of dipole terms each with a discrete relaxation frequency," *IEEE International Geoscience and Remote Sensing Symposium*, Honolulu, HI, USA, pp. 4188-419, 2010.
- [22] Larson, GD., and Scott, WR., "Automated, non-metallic measurement facility for testing and development of electromagnetic induction sensors for landmine detection," *Detection and Sensing of Mines, Explosive Objects, and Obscured Targets XIV*, 2009.
- [23] Rehim, O., Davidson, JL., Marsh, LA., O'Toole, M. and Peyton, A., "Magnetic Polarizability Tensor Spectroscopy for Low Metal Anti-Personnel Mine Surrogates," *IEEE Sensors Journal*, vol. 16, no. 10, pp. 3775-3783, 2016.
- [24] Kauppila, J.; Ala-Kleemola, T.; Vihonen, J.; Jylhä, J.; Ruotsalainen, M.; Järvi, A.; Visa, A. Classification of items in a walk-through metal detector using time series of eigenvalues of the polarizability tensor. In Proceedings Detection and Sensing of Mines, Explosive Objects, and Obscured Targets XIV; SPIE: Orlando, FL, USA, 2009; Volume 7303, pp. 1-15.
- [25] Makkonen, J., Marsh, L., Vihonen, J., Järvi, A., Armitage, D., Visa, A. and Peyton, A., "KNN classification of metallic targets using the magnetic polarizability tensor," *Measurement Science and Technology*, vol. 25, no. 5, pp. 055105, 2014.
- [26] Makkonen, J., Marsh, L., Vihonen, J., Järvi, A., Armitage, D., Visa, A. and Peyton, A., "Improving reliability for classification of metallic objects using a WTMD portal," *Measurement Science and Technology*, vol. 26, no. 10, pp. 105103, 2015.
- [27] Elgwell, A.; Harmer, S.W.; Bowring, N.J.; Shaofer, Y. Resolution of Multiple Concealed Threat Objects Using Electromagnetic Pulse Induction. *Prog. Electromagn. Res. M* 2012, 26, 55-68.
- [28] Al-Qubba, A.R.; Al-Shiha, A.; Tian, G.Y. Threat Target Classification Using ANN and SVM Based on a New Sensor Array System. *Prog. Electromagn. Res. B* 2014, 61, 69-85.
- [29] Kottler, D.K.; Roybal, L.G.; Polk, R.E. Detection and classification of concealed weapons using a magnetometer-based portal. In Proceedings Sensors, and Command, Control, Communications, and Intelligence (C3I) Technologies for Homeland Defense and Law Enforcement; SPIE: Orlando, FL, USA, 2009; Volume 4708, pp. 1-8.
- [30] Özdeğer, T., Davidson, JL., Van Verre, W., Marsh, LA., Lionheart, WRB., and Peyton, AJ., "Measuring the Magnetic Polarizability Tensor Using an Axial Multi-Coil Geometry," in *IEEE Sensors Journal*. vol. 21, no. 17, pp. 19322-19333, 1 Sept. 1, 2021, doi: 10.1109/JSEN.2021.3088809.
- [31] Davidson, J., Abdel-Rehim, O., Hu, P., Marsh, L., O'Toole, M. and Peyton, A., "On the magnetic polarizability tensor of US coinage," *Measurement Science and Technology*, vol. 29, no. 3, pp. 035501, 2018.
- [32] Rui Xu and D. Wunsch, "Survey of clustering algorithms," in *IEEE Transactions on Neural Networks*, vol. 16, no. 3, pp. 645-678, 2005.
- [33] Rokach, L. (2009). A survey of Clustering Algorithms. In: Maimon, O., Rokach, L. (eds) Data Mining and Knowledge Discovery Handbook. Springer, Boston.
- [34] Xu, D. and Tian, Y., 2015. A Comprehensive Survey of Clustering Algorithms. *Annals of Data Science*, 2(2), pp.165-193.
- [35] Rodriguez, M., Comin, C., Casanova, D., Bruno, O., Amancio, D., Costa, L. and Rodrigues, F., Clustering algorithms: A comparative approach. *PLoS ONE*, 2019 14(1) DOI: 10.1371/journal.pone.0210236
- [36] Greene, D., Cunningham, P., Mayer, R. (2008). Unsupervised Learning and Clustering. In: Cord, M., Cunningham, P. (eds) Machine Learning Techniques for Multimedia. Cognitive Technologies. Springer, Berlin, Heidelberg.
- [37] Özdeğer, T., Davidson, JL., Ledger, PD., Conniffe, D., Lionheart, WRB., and Peyton, AJ., "Measuring the Magnetic Polarizability Tensor of Non-Symmetrical Metallic Objects, submitted, IEEE Sensors Journal, 2022.
- [38] Ledger, PD., Wilson BA., Amad, AAS., Lionheart, WRB., "Identification of metallic objects using spectral magnetic polarizability signatures: Object characterisation and invariants," *International Journal for Numerical Methods in Engineering*, vol. 122, no. 15, pp. 3941-3984, 2021.
- [39] Wilson BA., Ledger, PD., Lionheart, WRB., "Identification of metallic objects using spectral magnetic polarizability signatures: Object classification," *International Journal for Numerical Methods in Engineering*, vol. 123(9) pp. 2076-2111, 2022. doi: 10.1002/nme.6927